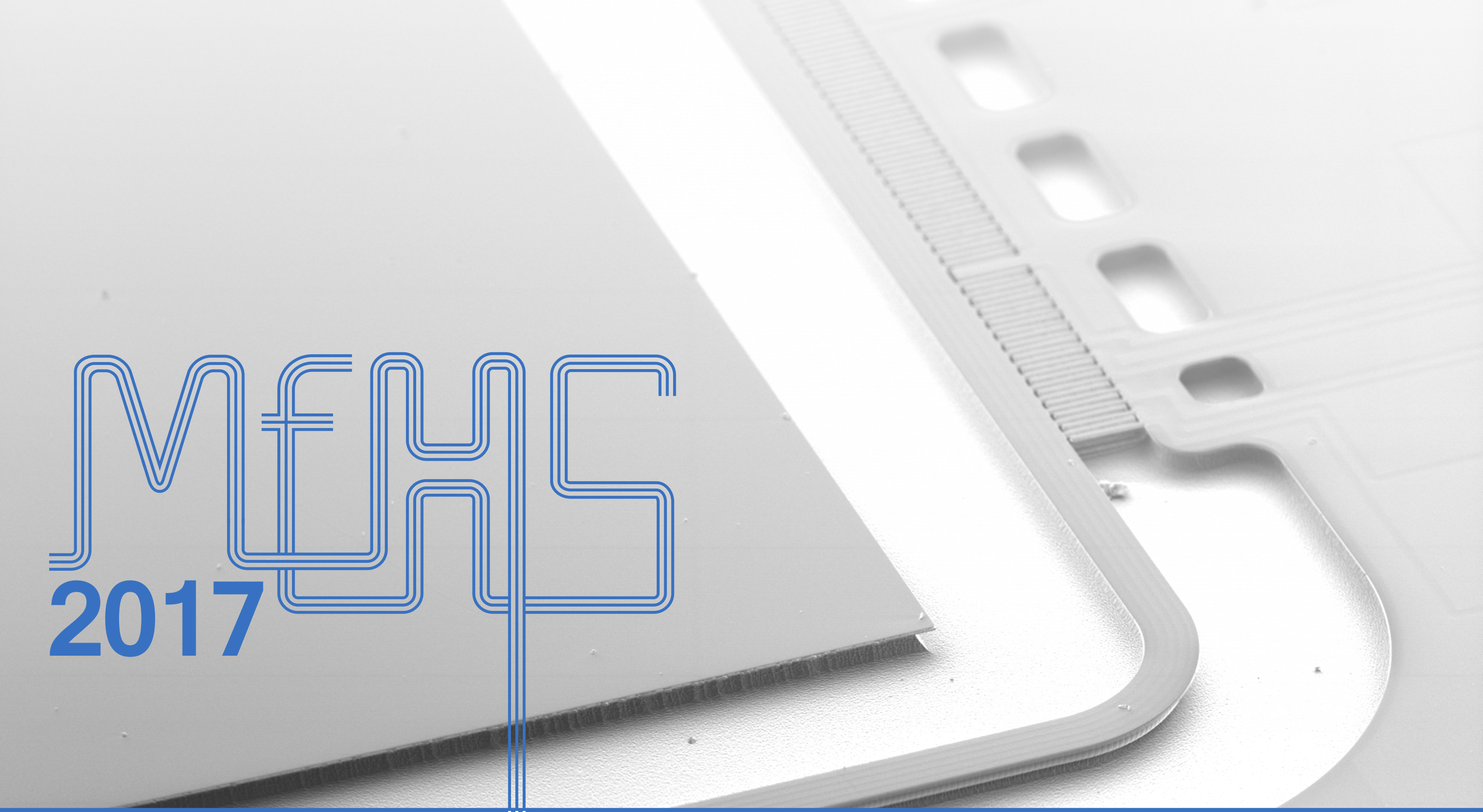

MFHS
2017

Conference Proceedings

The 3rd Conference on MicroFluidic Handling Systems

4-6 October 2017

Enschede
The Netherlands

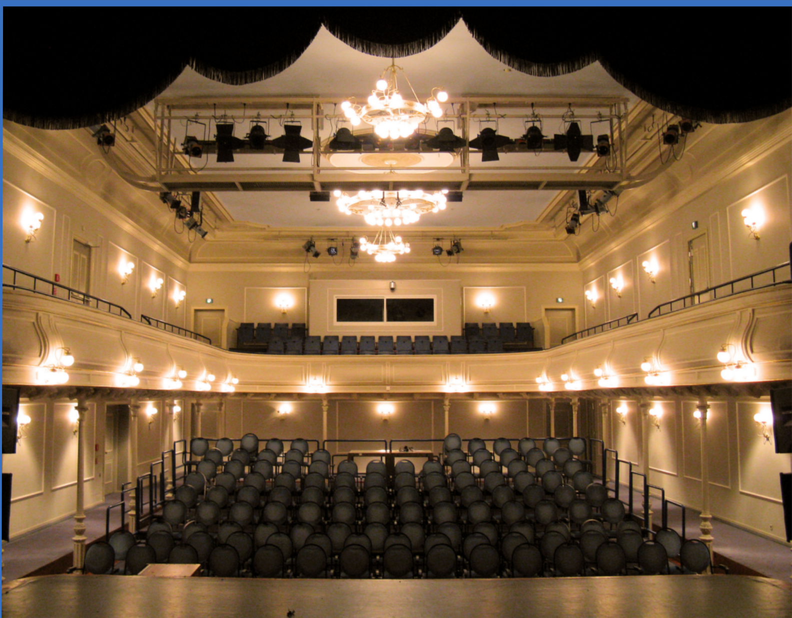

Conference: The 3rd Conference on MicroFluidic Handling Systems (MFHS 2017).
Dates: 4-6 October 2017.
Chairs: Joost Lötters and Gerald Urban.
Technical program committee: Ellis Meng, Shuichi Shoji, Jens Ducrée, Wouter van der Wijngaart, Bernhard Jakoby, Nico de Rooij, Peter Koltay, Andreas Ernst, Andreas Manz, Jankees Hogendoorn, Paddy French, Remco Wiegerink, Niels Tas.
Sponsors: University of Twente, MESA+, Bronkhorst High-Tech, Krohne, Innovative Sensor Technology IST AG, Fluigent, BioFluidiX, MDPI Micromachines, TNO, LioniX, Kloé, Micronit Microtechnologies, Truedyne, Axetris and Hahn-Schickard.
Location: De Kleine Willem, Langestraat 45, 7511 HB Enschede, The Netherlands.
Organization: Remco Wiegerink, Susan Janse, Dennis Alveringh. Jarno Groenesteijn, Henk-Willem Veltkamp, Yiyuan Zhao, Remco Sanders, Yaxiang Zeng and Thomas Schut.
Proceedings: Dennis Alveringh.

Welcome to the 3rd International Conference on MicroFluidic Handling Systems

Dear colleagues,

We are pleased to welcome you to the 3rd International Conference on MicroFluidic Handling Systems (MFHS 2017) in Enschede, as a follow-up to the successful first two conferences in Enschede in 2012 and in Freiburg in 2014.

Worldwide, accurate handling – i.e. analysis, dosage, measurement and control – of small and extremely small mass flow rates of both gases and liquids is becoming more and more important, driven by numerous applications. Examples of economically and societally relevant applications are e.g. improvement of medical infusion pump systems, increasing the efficiency of processes that extract oil from oil wells (enhanced oil recovery), systems that measure the energy content (calorific value or Wobbe Index) of natural gas and bio-gas, monitoring of ground water pollution and the production of pharmaceuticals by means of flow chemistry.

Whether in analytical instrumentation, flow chemistry, energy, semiconductor industry, food and beverage or life sciences – microfluidic handling systems are facing three major trends: (1) a need for accurate measurement and calibration facilities; (2) a need for complete functional systems rather than for the individual components, and (3) commercialisation of academic research results. In the future, the impact of this field of research may become bigger and potentially large target markets may arise, especially when spin-off companies start manufacturing and selling their products, systems or pilot plants.

The MFHS 2017 focuses mainly on the technology, components, devices and systems that enable the application in microfluidic systems. It provides an excellent opportunity to bring together scientists and engineers from academia, research institutes and companies to present and discuss the latest results in the field of microfluidic handling systems. The conference goals are to stimulate interaction and knowledge exchange between the delegates in a friendly atmosphere. The most recent developments in the field of microfluidic sensors, actuators, interfaces, fluidic control systems and applications will be presented.

We are looking forward to seeing you at the MFHS 2017 conference!

Kind regards,

Prof. Joost Lötters	Prof. Gerald Urban
Conference Co-chair	Conference Co-chair

Sponsors

FLUIGENT
SMART MICROFLUIDICS™

axetris

Hahn Schickard

BioFluidiX

IST
INNOVATIVE SENSOR TECHNOLOGY

KLOÉ

Bronkhorst®
Flow Technology

LioniX
INTERNATIONAL

KROHNE

TNO innovation for life

micronit
microtechnologies

micromachines
an open access journal by MDPI

truedyne

MESA+
INSTITUTE FOR NANOTECHNOLOGY

UNIVERSITY
OF TWENTE.

Conference committee

Chairs

Prof. dr. ir. Joost Lötters
MESA+ Institute for Nanotechnology, University of Twente, Enschede, the Netherlands
Bronkhorst High-Tech BV, Ruurlo, the Netherlands

Prof. dr. Gerald Urban
Institüt für Mikrosystemtechnik (IMTEK), Albert-Ludwigs-Universität
Freiburg, Germany

Technical program committee

Prof. dr. Ellis Meng
Department of Biomedical Engineering, University of Southern California
Los Angeles, United States of America

Prof. dr. Shuichi Shoji
Department of Electronic and Physical Systems, Waseda University
Tokyo, Japan

Prof. dr. Jens Ducrée
School of Physical Sciences, Dublin City University
Dublin, Ireland

Prof. dr. Wouter van der Wijngaart
Micro- and Nanofluidic systems, KTH Royal Institute of Technology
Stockholm, Sweden

Prof. dr. Bernhard Jakoby
Institute for Microelectronics and Microsensors, Johannes Kepler University
Linz, Austria

Em. prof. dr. Nico de Rooij
Microsystems for Space Technologies Laboratory, École polytechnique fédérale de Lausanne
Lausanne, Switzerland

Dr. Peter Koltay
Institüt für Mikrosystemtechnik (IMTEK), Albert-Ludwigs-Universität
Freiburg, Germany

Dr. Andreas Ernst
BioFluidiX GmbH
Freiburg, Germany

Prof. dr. Andreas Manz
Korea Institute for Science and Technology
Saarbrücken, Germany

Dr. ir. Jankees Hogendoorn
KROHNE Nederland B.V.
Dordrecht, the Netherlands

Prof. dr. Paddy French
Electronic Instrumentation Laboratory, Delft University of Technology
Delft, the Netherlands

Dr. ir. Remco Wiegerink
MESA+ Institute for Nanotechnology, University of Twente
Enschede, the Netherlands

Dr. ir. Niels Tas
MESA+ Institute for Nanotechnology, University of Twente
Enschede, the Netherlands

Program

Wednesday, 4th of October

17:00 – 19:00	Registration and welcome reception	Lobby

Thursday, 5th of October

8:00 – 8:45	Registration	Lobby
8:45 – 9:00	Welcome & announcements	Theater
9:00 – 9:30	Invited talk 1: Jan Eite Bullema	Theater
9:30 – 10:50	Session 1: Sensors	Theater
10:50 – 11:20	Coffee break & exhibition	Lobby
11:20 – 12:40	Session 2: Actuators	Theater
12:40 – 13:40	Lunch & exhibition	Lobby
13:40 – 15:00	Session 3: Interfaces & Fluidic Control Systems	Theater
15:00 – 15:30	Coffee break & exhibition	Lobby
15:30 – 16:00	Invited talk 2: Sabeth Verpoorte	Theater
16:00 – 17:45	Poster session & exhibition	Lobby
18:00 – 20:00	Conference dinner	Wilmink
20:00	Evening show	Wilmink

Friday, 6th of October

8:00 – 8:45	Registration	Lobby
8:45 – 9:00	Welcome & announcements	Theater
9:00 – 9:30	Invited talk 3: Cor van Kruijsdijk	Theater
9:30 – 10:50	Session 4: Applications	Theater
10:50 – 11:20	Coffee break & exhibition	Lobby
11:20 – 12:40	Session 5: Late News	Theater
12:40 – 12:50	Closing session & awards ceremony	Lobby
12:50 – 13:30	Lunch & exhibition	Lobby
14:30	Optional lab tour	University

Invited talks

Manufacturing microfluidics with 3D printing

Drs. ing. Jan Eite Bullema, Senior Scientist at TNO Technical Sciences

3D Printing / Additive Manufacturing appears to be an attractive technology to realize fluidic devices. By many still mainly seen as technology for development purposes, as 3D printing makes it relative easy to make small series with design iterations (e.g. different inlet apertures, different channel length, mixer size). In fact 3D printing evolves rapidly as a manufacturing technology. This is especially true for fluidic devices that have a more complex design – like many organ-on-chip devices. Recent developments in 3D printing have made 3D printing more attractive as a manufacturing technology. Dolomite has introduced the Fluidic Factory 3D printer for fast prototyping. The Continuous Liquid Interface Process (CLIP) announced by Carbon in the beginning of 2015, makes VAT polymerization 100 timed faster. Carbon has demonstrated (and patented) production of microfluidic products. At TNO we have developed production equipment that enable low cost production of integrated microfluidics with 3D printing.

With 3D printing technology it becomes possible to manufacture functional 3D fluidic structures, e.g. serpentine mixers, Brownian ratchets, Tesla valves. 3D printing makes it also possible to easily integrate fluidic functionalities, like mixing, valving, metering in one device. Which leads to a reduction of integral device costs. It is expected that especially for complex integrated lab-on-a-chip / organ-on-a-chip devices, 3D printing will become the production technology of choice.

Engineering microfluidic organ-on-a-chip systems

Prof. dr. Sabeth Verpoorte, Professor of Pharmaceutical Analysis, Research Institute of Pharmacy, University of Groningen, The Netherlands

Engineering cellular microenvironments that more accurately reflect the in vivo situation is now recognized as being crucial for the improvement of the in vitro viability and in vivo-like function of cells or tissues. Microfluidic technologies have been increasingly applied since the late 1990's for this purpose, with a growing number of examples of perfused cell and tissue cultures in microfluidic chambers and channels. The well-defined solution flows provided by microfluidics mean enhanced cell growth and function through improved nutrient delivery and waste removal. Additional benefits include the implementation of well-defined temporal and spatial (bio)chemical gradients, and mechanical signals that cells experience in their natural environment. Because the ability to culture cells and tissue under such controlled conditions leads to cellular function that is distinctly more organ-like, the microfluidic systems used are now referred to as "organs-on-a-chip" or "microphysiological systems". Reported organ-on-a-chip systems are as diverse as the biological models they have been designed to study. Most examples are based on cell culture models, which involve seeding cells into a chip with the eventual formation of a 2D or 3D tissue-like structure. The biological approach in these cases could be regarded as "bottom-up". Less common are the "top-down" biological approaches, in which organotypic tissue samples are directly obtained from mammals or human subjects for further study. Regardless of the biological model of interest, all organ-on-a-chip systems must be designed to accommodate cell or tissue culture, which implies precise peripheral control of medium transport to and from the chip. The use of microfluidics to do this rather than a pipetting instrument of some kind opens up the possibility for continuous perfusion of cell or tissue culture, a starting point for the creation of cellular microenvironments that are more representative of the in vivo situation. Moreover, peripheral pumping systems can be configured to change the composition of perfusion media at specifically programmed timepoints throughout the experiment to include compounds expected to induce some form of cellular response. This enables the definition of time-varying dosing experiments of drugs, nutrients or other compounds that reveal real-time effects on cells, something which is far more tedious or even impossible to accomplish in more conventional well plate formats. This presentation will focus on examples from our labs in which we have designed “top-down” and “bottom-up” organ-chips incorporating means to both monitor culture conditions and quantify cell behaviour. Our “bottom-up” example constitutes the culture and investigation of primary human endothelial cells in microfluidic devices. In a simple demonstration of the importance of microenvironment in cell culture, clear differences in cell phenotype are observed when human umbilical vein endothelial cells grown in microchannels and well plates are compared. In a “top-down” example, a microfluidic device was designed for perfusion culture of precision-cut organ slices. Metabolic studies employing precision-cut liver slices and on-line HPLC analysis were successfully demonstrated with this device, as was a multi-organ slice experiment showing regulation of bile acid synthesis in the liver by the intestine.

Porous Media everywhere! Microfluidic experience and opportunities in Shell

Prof. ir. Cor van Kruijsdijk, Sr. Principal Researcher at R&D Physics, Emerging Technologies, Shell R&D, The Netherlands

The use of microfluidic devices in Shell goes back to the 1980’s where we studied the dynamic behaviour of a brine, H_2S, sulphur mixture at subsurface conditions, T=120 °C, p=31 MPa. Here safety was the biggest driver for the choice of microfluidics. Currently we have a focus on chemically enhanced oil recovery where we are studying the fundamental processes of oil displacement by chemically enhanced water. Microfluidic devices are also starting to penetrate other divisions in Shell. Many processes in “New Energies” take place in porous media of one kind or another, batteries, photo-chemical/electrical cells, porous catalytic bed reactors etc. Moreover, microfluidic devices are finding its way in analytical chemistry either for sample preparation and/or direct measurement of fluid properties and composition. A significant part of these processes can be studied using currently available technology. However, some of the catalyst supported gas reactions push past the current operating envelopes of microfluidic devices as they require temperatures upwards of 1000 °C. Moreover, the currently available spectroscopic methods for in-situ measurements are challenged by the small densities of the gas phase.

Session 1: Sensors

Thursday, 5th of October, 9:30 – 10:50
Chairs: Jankees Hogendoorn & Joost Lötters

9:30 – 9:50	**Micro Coriolis mass flow sensor with integrated resistive pressure sensors** Jarno Groenesteijn, Dennis Alveringh, Thomas Schut, Remco Wiegerink, Wouter Sparreboom and Joost Lötters	Page 16
9:50 – 10:10	**Gas concentration and flow speed measurement with a thermal sensor for applications with binary gas mixtures** Christoph Hepp, Florian Krogmann and Gerald Urban	Page 20
10:10 – 10:30	**Micro Coriolis gas density sensor** Wouter Sparreboom, Gijs Ratering, Wim Kruijswijk, Egbert van der Wouden, Jarno Groenesteijn and Joost Lötters	Page 24
10:30 – 10:50	**A miniaturized flame ionization detector applicable in a field device** Jan Foerster, Winfred Kuipers, Christian Koch, Christian Lenz, Steffen Ziesche and Dominik Jurkow	Page 27

Session 2: Actuators

Thursday, 5th of October, 11:20 – 12:40
Chairs: Remco Wiegerink & Peter Koltay

11:20 – 11:40	**Precise Flow-control using photo-actuated hydrogel valves and PID-Controlled LED actuation** Colm Delaney, Peter McCluskey, Simon Coleman, Jeffrey Whyte, Nigel Kent and Dermot Diamond	Page 53
11:40 – 12:00	**Electrostactically in-plane driven silicon micropump for modular configuration** Sebastian Uhlig, Sergiu Langa, Klaus Schimmanz, Holger Conrad, Bert Kaiser, Matthieu Gaudet and Harald Schenk	Page 57
12:00 – 12:20	**Standards and guidelines for microfluidic interconnections, building blocks and verification testing** Henne van Heeren	Page 61
12:20 – 12:40	**Experimental characterization of a generator of non-newtonian droplets based on a micro cross-junction** Behnam Rostami and Gian Luca Morini	Page 63

Session 3: Interfaces & Fluidic Control Systems

Thursday, 5th of October, 13:40 – 15:00
Chairs: Niels Tas & Paddy French

13:40 – 14:00	**A single-use in-line flow sensor for closed-loop controlled precise non-contact liquid dispensing** Sabrina Kartmann, Fritz Koch, Andreas Ernst, Roland Zengerle and Peter Koltay	Page 86
14:00 – 14:20	**Automated detection of droplet shape evolution for hollow AFM cantilever flow calibration** Eleonoor Verlinden, Edin Sarajlic, Frans Vos, Andreas Engel, Urs Staufer and Murali Ghatkesar	Page 90
14:20 – 14:40	**3D-Printing: An attractive tool to realise microfluidic chip holders** Sander van den Driesche, Frank Bunge, Frieder Lucklum and Michael J. Vellekoop	Page 94
14:40 – 15:00	**Prism signal processing: a recursive fir technique applied to the efficient tracking of resonant sensor systems** Manus Henry	Page 98

Session 4: Applications

Friday, 6th of October, 9:30 – 10:50
Chairs: Andreas Ernst & Jankees Hogendoorn

9:30 – 9:50	**3D fractals as SERS substrates for detection of neutorotoxic agents in gas phase** Marta Lafuente, Erwin Berenschot, Roald Tiggelaar, Reyes Mallada, María Pilar Pina, Jesús Santamaría and Niels Tas	Page 124
9:50 – 10:10	**Lab-on-Chip for DNA concentration and separation with a resolution length of 6 bp** Bayan Chami, Marius Socol and Aurelien Bancaud	Page 128
10:10 – 10:30	**Crystallization of Zinc(II) complex containing lysozyme by super water repellent doubly reentrant structure umbrella pillar array** Daiki Tanaka, Wataru Kawakubo, Dong Hyun Yoon, Tetsushi Sekiguchi, Takashiro Akitsu and Shuichi Shoji	Page 132
10:30 – 10:50	**Microfluidics for the assessment of the effectiveness of nanoencapsulated methotrexate against osteosarcoma** Oihane Mitxelena-Iribarren, Yolanda González-Fernández, Edurne Imbuluzqueta, Maite Mujika, Maria Blanco-Prieto and Sergio Arana	Page 136

Session 5: Late News

Friday, 6th of October, 11:20 – 12:40
Chairs: Remco Wiegerink & Paddy French

11:20 – 11:40	**Flow rate independent microfluidic gradient generator** Stefan Höving, Dirk Janasek and Pedro Novo	Page 152
11:40 – 12:00	**Gas density and viscosity measurement with a microcantilever and determination of woobe index, calorific value and total inert gas content of natural gas** Christof Huber, Patrick Reith and Anastasios Badarlis	Page 156
12:00 – 12:20	**Inline sizing of nano particles using ultrasound** Gert-Jan van Groenestijn, Arno Volker, Nicole Meulendijks, Paul van Neer, Guillaume Pierre and Cédric Julien	Page 160
12:20 – 12:40	**A new type of reactor system: aerogel-based optofluidic microreactor with integrated optofluidic waveguides** Yaprak Özbakir, Alexandr Jonáš, Alper Kiraz and Can Erkey	Page 164

Poster session

Thursday, 5th of October, 16:00 – 17:45

Sensors

Poster 1	**Miniaturized gas composition sensor for natural gas and biogas** Arjen Boersma, Jorgen Sweelssen and Huib Blokland	Page 31
Poster 7	**Viscosity determination by the in-line detection of flow time through a cylindrical tube** Fritz Koch, Sabrina Kartmann, Roland Zengerle, Andreas Ernst and Peter Koltay	Page 33
Poster 16	**Design principles and fabrication method for a miniaturized fuel gas combustion reactor** Yiyuan Zhao, Henk-Willem Veltkamp, Meint de Boer, Yaxiang Zeng, Jarno Groenesteijn, Remco Wiegerink and Joost Lötters	Page 37
Poster 25	**Ultraminiature pH ISFET with back side contacts and Ta_2O_5 gate material for use in a guidewire tip** Albert Prak, Hans van den Vlekkert and Marc-Alan Levine	Page 41
Poster 27	**Micro Coriolis mass flow sensor driven by external piezo ceramic** Yaxiang Zeng, Jarno Groenesteijn, Dennis Alveringh, Remco Wiegerink and Joost Lötters	Page 45
Poster 42	**Extending the accredited low flow liquid calibration range** Tom Platenkamp and Joost Lötters	Page 49

Actuators

Interfaces & Fluidic Control Systems

Applications

MICRO CORIOLIS MASS FLOW SENSOR WITH INTEGRATED RESISTIVE PRESSURE SENSORS

J. Groenesteijn[1]*, D. Alveringh*[2]*, T.V.P. Schut*[2]*, R.J. Wiegerink*[2]*, W. Sparreboom*[1] *and J.C. Lötters*[1,2]
[1] Bronkhorst High-Tech BV, Ruurlo, The Netherlands
[2] MESA+ Institute for Nanotechnology, University of Twente, Enschede, The Netherlands

ABSTRACT

We report on novel resistive pressure sensors, integrated on-chip at the inlet- and outlet-channels of a micro Coriolis mass flow sensor. The pressure sensors can be used to measure the pressure drop over the Coriolis sensor which can be used to compensate pressure-dependent behaviour that might occur and it can be used to calculate the dynamic viscosity of the fluid inside the channels.

KEYWORDS

Resistive pressure sensor, micro Coriolis mass flow sensor, multiparameter measurement, viscosity measurement

INTRODUCTION

We report on novel resistive pressure sensors, integrated on one chip with a micro Coriolis mass flow sensor. The two pressure sensors are placed on the inlet- and outlet-channels of the Coriolis mass flow sensor, which not only allows the measurement of the in- and outlet pressure, but also the pressure drop over the flow sensor. By using the quantities measured by the Coriolis sensor (mass flow and density) together with the pressure drop, the dynamic viscosity can be measured in real-time as is shown schematically in Figure 1. The pressure measurement can also be used to compensate pressure-dependent behaviour of the Coriolis sensor. The pressure sensor consists of a Wheatstone bridge of metal tracks meandering over a channel. As a result, the design of the fluidic path of the Coriolis sensor [1] and the fabrication process [2] do not have to be adjusted to add the pressure sensors to the flow sensor.

In the past, many microfluidic sensors have been made using their own unique fabrication process, e.g. Coriolis flow sensors [3, 4] and pressure sensors [5, 6]. However, since these fabrication processes are unique, combining these sensors on the same chip is hard to achieve. In [7], we integrated a capacitive pressure sensor with a micro Coriolis mass flow sensor. However, this pressure sensor suffered from low sensitivity and large drift. Due to crosstalk between the different capacitive read-outs, these pressure sensors and the Coriolis sensor could not be read out simultaneously. The resistive pressure sensors presented here consist of a Wheatstone bridge which is actuated and read out using a lock-in amplifier. As a result, the sensitivity is higher, the drift lower and it can be operated together with the Coriolis sensor.

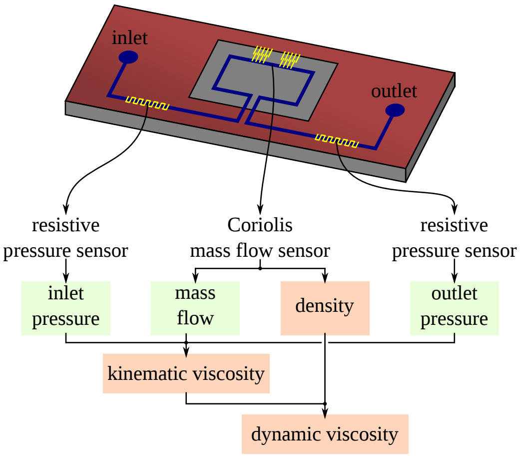

Figure 1: Overview of the integrated multiparameter measurement system. The output of the pressure sensors and the Coriolis sensor can be used to determine the viscosity of the fluid.

THEORY

The design of the pressure sensors is shown schematically in Figure 2 and an SEM image is shown in Figure 3.[8] The resistive pressure sensors consist of a channel with the four resistors of the Wheatstone bridge on top. Each resistor consists of 123 strain gauges placed perpendicular to the direction of the channel and the (unstrained) sections that connect these together. When a pressure is applied inside the channel, the flat top will deform. Two of the resistors are placed in the center of the channel, where the flat top of the channel will elongate the strain gauges due to the deformation of the top and will thus increase in resistance. The two other resistors are placed at the edge of the channel, close to where it is anchored in the silicon bulk. The deformation will cause a compression of the strain gauge and will thus decrease the resistance. The input voltage of the Wheatstone bridge is applied by the

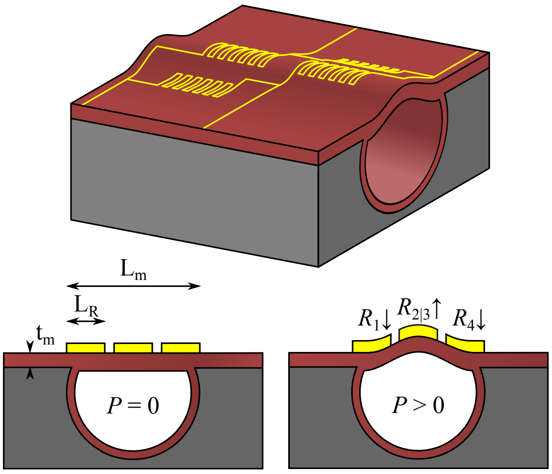

Figure 2: Illustration of the design of the resistive pressure sensor. The flat part at the top of the channel will deform due to an applied pressure. The thin-film resistors on top will then elongate or compress due to this deformation.

function generator in a Stanford Research SR830 lock-in amplifier and the output voltage is measured by the same lock-in amplifier. The output voltage is equal to:

$$V_{\text{out}} = V_{\text{in}} \left(\frac{R_2}{R_1 + R_2} - \frac{R_4}{R_3 + R_4} \right) \tag{1}$$

All resistances are designed to be equal when no pressure is applied and the resistances can be rewritten as:

$$\begin{aligned} R_1 = R_4 = R_0 - \Delta R_{1,4}, \\ R_2 = R_3 = R_0 + \Delta R_{2,3} \end{aligned} \tag{2}$$

When substituting equation (2) into equation (1) and assuming the change in resistance is much smaller than the initial value the output voltage can be calculated using:

$$V_{\text{out}} = V_{\text{in}} \frac{\Delta R_{2,3} + \Delta R_{1,4}}{2R_0} \tag{3}$$

Here R_0 contains both the initial resistance of the strain gauges as the resistance of the parts connecting them. To estimate $\Delta R_{2,3}$ and $\Delta R_{1,4}$, the deformation has been simulated using Comsol Multiphysics. Since the deformation in the length-direction of the channel will be constant, a 2D simulation of the cross-section of the channel will suffice to simulate the deformation of one strain gauge. Separate simulations were performed for the elongating and compressing resistors using a pressure range of 1 to 10 bar. The resulting change in length is shown in Figure 4. The deformation of the two different strain gauges is not equal, indicating that $\Delta R_{2,3} \neq \Delta R_{1,4}$. The deformation is in the order of a few nm on strain gauges of $40\,\mu\text{m}$, indicating a change in resistance less than $0.1\,\%$ of the unstrained value.

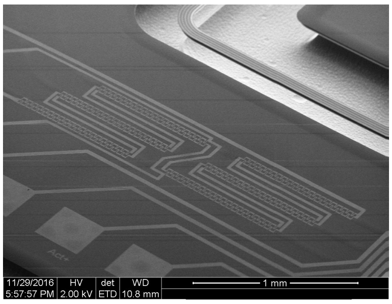

Figure 3: SEM image of the fabricated resistive pressure sensor. To reduce the pressure drop over the in- and outlet channels, three parallel channels are used. A single pressure sensor is placed on all three, measuring the average pressure inside the three channels.

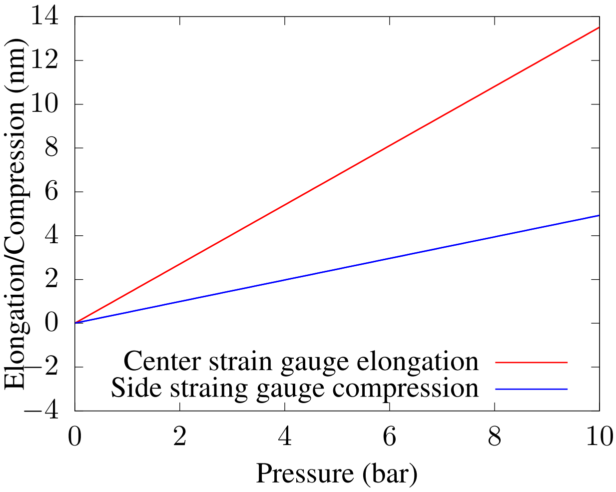

Figure 4: Simulated change in strain gauge length for the elongating and compressing resistors. The initial length of each is $40\,\mu\text{m}$.

EXPERIMENTAL

To characterize the sensors, gauge pressures have been applied in the range of 0 to $1\,\text{bar}$ in steps of $0.1\,\text{bar}$. The results of these measurements are shown in Figure 5. The amplitude of the applied voltage V_{in} is $100\,\text{mV}$ at a frequency of $1.5\,\text{kHz}$. The results show a linear response with a sensitivity of $4\,\mu\text{V}\,\text{bar}^{-1}$ without any noticeable hysteresis. Tests show that the burst pressure is higher than $10\,\text{bar}$. The pressure drop is measured together with the mass flow for water and isopropyl alcohol (IPA) in a flow-range of $0\,\text{g}\,\text{h}^{-1}$ to $12\,\text{g}\,\text{h}^{-1}$ with a pressure at the inlet of 3 and $4\,\text{bar}$. The results of these measuremnets are shown in Figure 6. Future work will include design optimization for the pressure sensor and characterization of the different parameters that can be measured using multiple fluids.

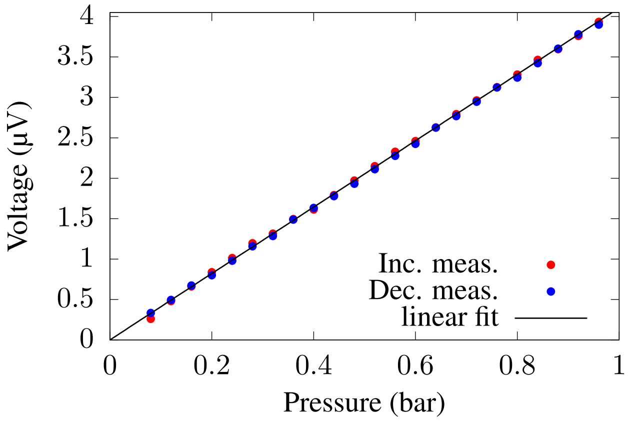

Figure 5: Characterization of the pressure sensor with a pressure applied by a pressure controller in the range of 0 bar *to* 1 bar. *There was no fluid flow during the measurement.*

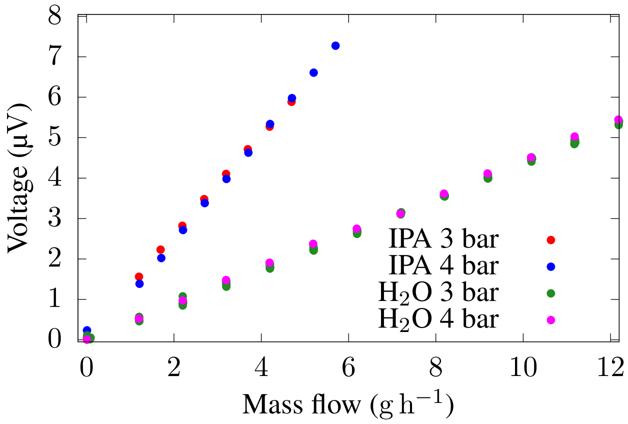

Figure 6: Measurement of the pressure drop over the sensor at varying flow rates of both water and IPA. The measurements are done using an input pressure of 3 and 4 bar.

APPLICATIONS

Compensation

The fabrication process allows to make free hanging channels with a very thin channel wall. This makes a sensor made using these channels very sensitive to properties of the fluid inside the channel. For the pressure sensor, the deformation of the channel due to pressure results in an accurate pressure measurement. However, in the Coriolis mass flow sensor, this deformation changes the stiffness of the channel and will thus result in a pressure dependent resonance frequency of the sensor. Since flow introduces a pressure drop over the length of the vibrating channel, this too adds a pressure dependence. This can be seen in Figures 7 and 8 where the resonance frequency is measured during a flow measurement using IPA and during static measurements using mixtures of water and IPA. When assuming that

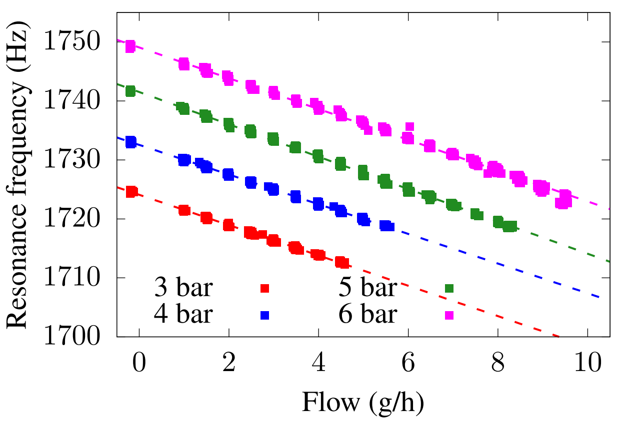

Figure 7: Measured resonance frequency of the Coriolis mass flow sensor for different flow and input pressure. The used fluid is IPA.

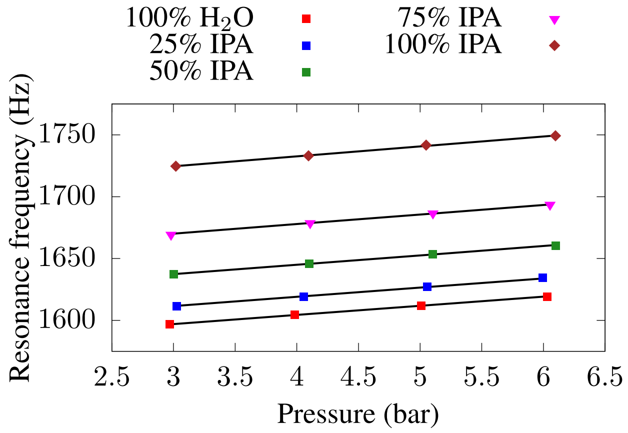

Figure 8: Measured resonance frequency of the Coriolis mass flow sensor for different mixtures of water and IPA at different input pressures. The black lines indicate the calculated frequency using equation (4).

the stiffness of the channel is linearly proportional to the pressure, the resonance frequency can be calculated using:

$$\omega_0 = \sqrt{\frac{k_0 + \alpha \cdot P}{m_{channel} + \rho \cdot V_{channel}}}, \qquad (4)$$

where ω_0 is the resonance frequency, k_0 is the spring constant of the channel without an applied pressure, α is a calibrated value indicating the pressure dependence of the stiffness, P is the pressure in the channel, $m_{channel}$ is the mass of the channel, ρ the density of the liquid and $V_{channel}$ the volume of the liquid inside the channel. Using the results in Figure 8 for pure water and pure IPA, α and k_0 can be calibrated. The resulting modelled resonance frequencies are indicated using black lines.

Viscosity

The pressure drop over a channel, the mass flow through that channel and the density of the fluid in that

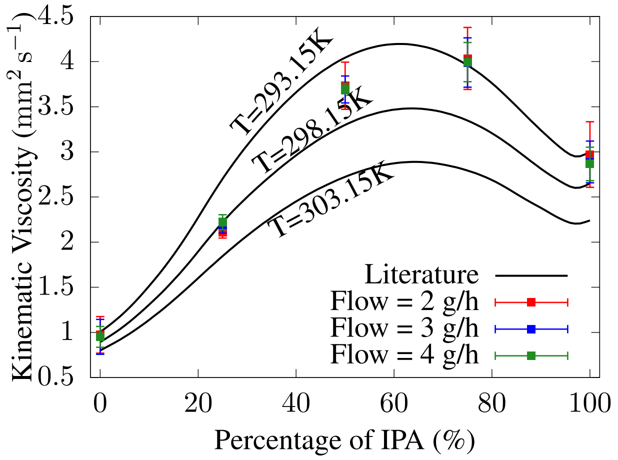

Figure 9: The kinematic viscosity of mixtures of water and IPA. Measurements from [9] are shown as reference values.

channel can be used to find the dynamic viscosity of liquids. To do this, the Hagen-Poiseuille equation has to be rewritten to:

$$\mu = \frac{\pi \Delta P \rho D_h^4}{128 L \Phi_m}, \tag{5}$$

where μ is the dynamic viscosity of the fluid, ΔP is the pressure drop over the channel, ρ is the density, D_h is the hydraulic diameter of the channel, L is the length of the channel and Φ_m is the mass flow.

The Coriolis flow sensor can already be used to measure the density and mass flow, so combined with the pressure sensors, the dynamic viscosity can be determined. Figure 9 shows the results for different mixtures of water and IPA. A calibration using pure water was used to calculate the viscosity using the output of the different sensors. Since the temperature of the fluid in the channel could not be measured during the measurements and the viscosity is heavily dependent on the temperature, the calibration is done at 17 and 21 degrees Celsius. The figure also shows the measured viscosity of the mixtures according to [9].

CONCLUSION

We report on resistive pressure sensors, integrated with a micro Coriolis mass flow sensor. The pressure sensor has a linear response with a sensitivity of $4\,\mu\mathrm{V\,bar}^{-1}$ in the range of 0 to 1 barg. The integrated pressure sensors have been used to compensate the pressure-dependence of the stiffness of the free-hanging channel in the micro Coriolis mass flow sensor, improving its accuracy. By using the measurements of the pressure sensors and the micro Coriolis mass flow sensor, the viscosities of several mixtures of water and IPA have been determined.

REFERENCES

[1] W. Sparreboom, et al., “Compact mass flow meter based on a micro Coriolis flow sensor”, Micromachines, 4(1), pp.22-33, 2013

[2] J. Groenesteijn et al., “A versatile technology platform for microfluidic handling systems, partÂăI: fabrication and functionalization”, Microfluidics and Nanofluidics, 21 (7), pp. 127, 2017

[3] P. Enoksson et al., “A silicon resonant sensor structure for Coriolis mass-flow measurements”, Journal of Microelectromechanical Systems, vol. 6, no. 2, pp. 119-125, Jun 1997

[4] J. Haneveld et al., “Modeling, design, fabrication and characterization of a micro Coriolis mass flow sensor”, Journal of Micromechanics and Microengineering, vol. 20, 2010

[5] W. P. Eaton et al., “Micromachined pressure sensors: review and recent developments”, Smart Materials and Structures, vol. 6, no. 5, p. 530, 1997

[6] Y. Zhang et al., “A high-sensitive ultra-thin MEMS capacitive pressure sensor”, in The 16th International Solid-State Sensors, Actuators and Microsystems Conference (TRANSDUCERS). IEEE, 2011, pp. 112-115

[7] J. C. Lötters et al., “Integrated multi-parameter flow measurement system”, in The IEEE 27th International Conference on Micro Electro Mechanical Systems (MEMS). IEEE, 2014, pp. 975-978

[8] D. Alveringh et al., “Resistive pressure sensors integrated with a Coriolis mass flow sensor”, accepted at The 19th International Solid-State Sensors, Actuators and Microsystems Conference (TRANSDUCERS). IEEE, 2017

[9] F.-M. Pang et al., “Densities and viscosities of aqueous solutions of 1-propanol and 2-propanol at temperatures from 293.15K to 333.15K”, Journal of Molecular Liquids, vol. 136, no. 1, pp. 71-78, 2007.

CONTACT

* J. Groenesteijn, j.groenesteijn@bronkhorst.com

GAS CONCENTRATION AND FLOW SPEED MEASUREMENT WITH A THERMAL SENSOR FOR APPLICATIONS WITH BINARY GAS MIXTURES

C.J. Hepp[1]*, F.T. Krogmann*[1] *and G.A. Urban*[2]
[1]Innovative Sensor Technology IST AG, Ebnat-Kappel, Switzerland
[2]University of Freiburg, Freiburg Institute for Advanced Studies, Freiburg, Germany

ABSTRACT

A sensor and a measuring method for detecting flow speed and simultaneously gas concentration of binary gas mixtures is presented in this contribution. The key features of this sensor are the time-independent excitation modes (constant power and constant temperature) in combination with the sensor design. In constant power mode a flow independent but gas sensitive region is established, wherein the gas content can be analyzed. The flow independent region is obtained due to the width of the membrane. The paper focuses also on possible applications of this measuring method. Options and limitations are discussed.

KEYWORDS

Thermal flow sensor, flow speed, thermal conductivity, gas concentration.

INTRODUCTION

The first micro-machined thermal flow sensor was developed over 40 years ago [1]. These sensors offer several advantages compared to other flow measurement techniques such as a low cost fabrication, an excellent low flow sensitivity and an outstanding long term stability due to the lack of moving parts [2]. Applications of thermal flow sensors are various and these sensors are implemented e.g. in devices for process control or for medical applications.

Thermal flow sensors can be classified in three main categories based on the sensor layout and measuring principle:

- Anemometric
- Calorimetric
- Time-of-flight

Thermal anemometers feature in the simplest form one resistor, which is used simultaneously as joule heater and temperature sensor. The widely used excitation mode for this sensor is the Constant Temperature Anemometer. In this configuration the heater is set to a constant temperature difference towards the ambient temperature. As flow passes the heating element, heat is transferred from the heater in the fluid [3]. Consequently, the temperature of the heater cools – as higher the flow as higher the cooling – and the electronics resets the temperature difference, which requires more electrical power. The output signal of this sensor is the power needed to maintain the temperature difference. Materials used for this type of sensor have a well-defined temperature coefficient of resistance.

The design of calorimetric flow sensors feature a centered heating element and two temperature sensors, one located upstream, the other located downstream. The temperature difference between the up- and downstream temperature sensor is a function of the flow rate. The direction of the flow rate is measured by the sign of this temperature difference [3]. These types of sensors are mainly excited in the constant power mode.

Time-of-flight sensors consist of a heater and a temperature sensor located further downstream. The flow rate is a function of the time, which a heat pulse needs from the heater to the temperature sensor [3].

The output signal of all these types mainly depends on flow rate and regime, the construction of the flow channel and the thermal gas properties. One of the main drawbacks is the dependency towards the thermal gas properties. Therefore the sensor has to be calibrated to the gas of the application or correction factors have to be implemented if other gases occur. Consequently a change in the thermal properties – namely thermal conductivity, specific heat capacity and density – will lead to a change in the sensor's output signal. So far thermal flow sensors cannot be applied in applications, where flow speed and the thermal gas properties vary simultaneously, because an inaccurate flow measurement will be taken. The thermal gas properties will change in applications where the gas type or the gas concentration changes. This drawback can be overcome with a thermal sensor which is measuring flow speed and gas concentration at once. Common applications, where both parameters vary, are for example in biogas plants or in the breath gas analysis, which are in the focus of this paper.

Research in this topic – the measurement of flow rate and thermal gas properties – is carried out since long time. Methods have been developed where the flow measurement principle does not depend on the thermal gas properties. Other research groups used time dependent excitation modes of the heating element [4]. One drawback of time dependent excitation modes is the complex excitation and data acquisition.

Time independent excitation modes have been used so far to measure the gas thermal conductivity in no flow condition and correcting the flow rate afterwards. No flow condition or nearly no flow condition is achieved by special sensor design or by stopping the fluid from time to time. The main drawback is that this thermal system can be very complex.

CONCEPT AND APPLICATIONS

The approach presented in this paper is a thermal sensor for measuring gas concentration and flow rate in binary gas mixtures simultaneously. The design is based on the calorimetric layout with a heater and two temperature sensors located up- and downstream. The material of the heater (platinum) enables the use of two time-independent excitation modes (constant power and constant temperature).

In constant power mode, the gas concentration is obtained by the temperature of the downstream element; based on the theoretical relationship to thermal conductivity [5]. The output signal in this mode depends only on thermal conductivity in a certain flow range due to the layout of the sensor [6]. By knowing the gas concentration, flow rate is extracted from the temperature different between the two temperature sensors in constant temperature mode. The measurement technique is shown in Fig. 3. The gas components of the mixture have to be known in advance to apply this technique.

Applications of this sensor can be in anaerobic distinctions to analyze the gas concentration of methane and flow rate. Thus, the fermentation process can be monitored on-line and optimized. Furthermore, the fuel value of the biogas can be calculated. Another possibility with this sensor is to analyze the breath in terms of flow rate and the carbon dioxide concentration. Thus, diagnostics can be combined in one device and diseases might be recognized earlier. Therewith, new methods of treatment can be developed. The mixtures in these both applications can be seen as a binary gas mixture. Biogas consists mainly of methane and carbon dioxide, other gases occur as well but in low concentrations (below 2 %). Thus, biogas is seen as a binary gas mixture in this paper. In biogas plants the methane content varies between 25 and 75 % due to the fermentation process. Air consists mainly of nitrogen and oxygen other gases have a concentration with less than 1 %. Nitrogen and oxygen have nearly the same value in thermal conductivity. The concentration of carbon dioxide increases of 5% due to the breath and can be even higher for some diseases. The concentration of oxygen lowers in this case; the concentration of nitrogen is constant. Consequently, also in this application the gas mixture and the variation of the content can be seen as a binary mixture. These applications have been successfully proven under laboratory conditions (experiments with binary gas mixtures of CH_4-CO_2 (biogas analysis) and CO_2-N_2 (breath gas analysis)).

SENSOR

The cross section of the developed thermal system is shown in Fig. 1. The assembled sensor in a flow channel is illustrated in Fig. 2. The design of the calorimetric flow sensor features a polyimide membrane wherein the platinum resistance temperature detectors are embedded [6]. This technology has on one hand the advantage to provide enough sensitivity due to the polyimide membrane; on the other hand the switch between the excitation modes is easily possible, because platinum can be heated up and simultaneously its temperature can be measured. The unique feature is the design of the membrane area. The substrate around the heater serves as heat sink, thus, in power mode a nearly constant temperature on the downstream element is obtained towards flow rate, however the signal depends on the gas' thermal conductivity. The flatness of the signal is reached only in power mode because of the decrease in heat conduction and an increase of heat convection towards the downstream element by an increase in flow rate. Contrary to temperature mode, the heat conduction is constant by an increase in flow rate. The fabrication process was described in a previous work [6]. The distance between heater and temperature sensor is 192µm (distance *L* in Fig. 1).

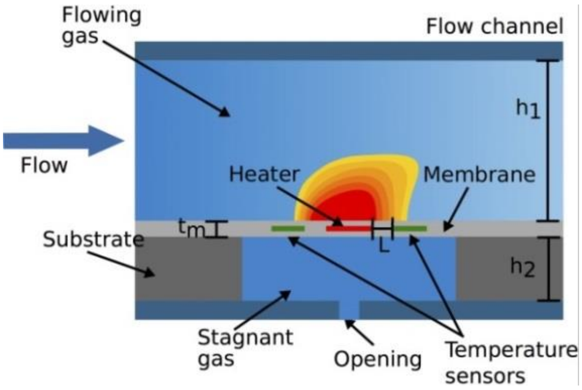

Figure 1. Cross section of the developed thermal system. The sensor features a membrane layer wherein the platinum layer is embedded. Substrate serves as heat sink to establish the flow independent region (see Fig. 5).

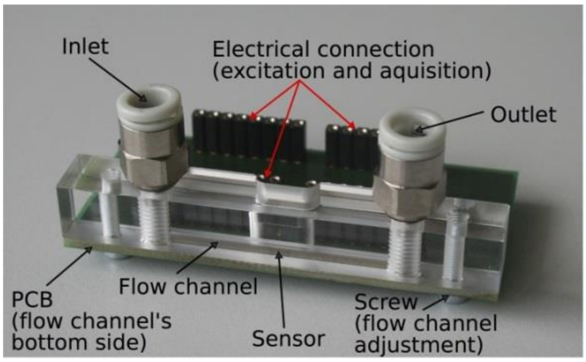

Figure 2. Picture of the assembled thermal system. The flow channel area is 2 mm^2.

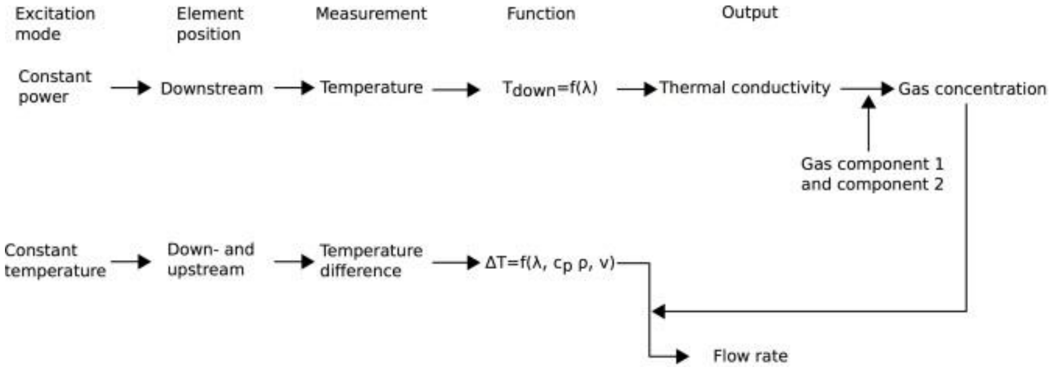

Figure 3. Measurement principle: Gas concentration is measured in constant power mode, afterwards flow speed in constant temperature mode. Power, temperature respectively, on the heater is kept constant independent of flow speed and gas type.

EXPERIMENTAL SETUP

The gas concentration is generated by adjusting the normal volume flow in two Mass flow controllers (MFC). With these controllers, the normal volume flow is adjusted in the flow channel. The binary gas mixtures are obtained by varying the flow rate of these two MFCs. The normal volume flow is changed between 0 and 150 sccm. Thus, a laminar flow profile is expected in the flow channel due to a Reynolds number below 300. The excitation and the acquisition of the sensor’s signals are performed with a LABView program and a DAQ-module form National Instruments. With this setup the power on the heater is controlled to 12 mW in constant power mode, the temperature difference between heater and ambient temperature is 75 K in temperature mode, respectively. The thermal properties of the mixtures have been taken from [8].

EXPERIMENTAL RESULTS

Power mode

The temperature of the downstream element as function of the normal volume flow is shown in Fig. 4 for different gas concentrations of each mixture from 100% methane to 100% carbon dioxide and 100% carbon dioxide to 100% nitrogen. The temperature variation is less than 1% in the flow independent region. The flow independent region is obtained due to the design of the membrane area [5]. The temperature of the flow independent region corresponds to the thermal conductivity of the gas and therewith to the gas concentration of the mixture (Fig. 5 for mixture of CO_2-CH_4); as higher the thermal conductivity of the gas, as higher the temperature of the downstream element. In order to apply this method, the thermal conductivity of the gas components have to differ, as higher the difference as better is the resolution (see Fig. 5).
The relative accuracy of the measuring method is calculated to 3% related to thermal conductivity [5].

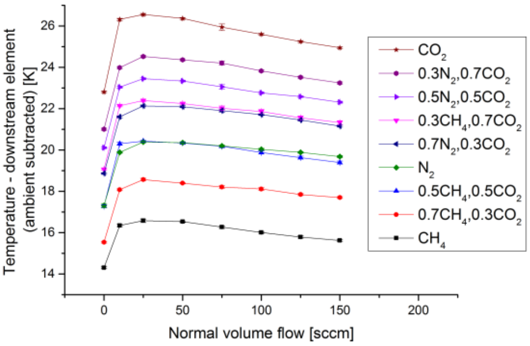

Figure 4. Constant power excitation: Temperature of the downstream element as function of flow speed. The flow independent, but gas sensitive region is obtained due to the sensor design.

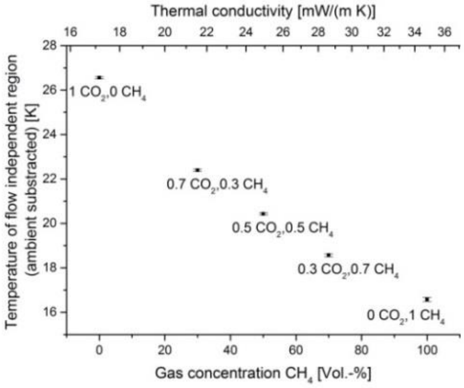

Figure 5. Constant power mode: Output signal as function of thermal conductivity and gas concentration.

Temperature mode

Figure 6 shows the temperature difference as function of flow speed for different gas concentrations of the two mentioned applications. The temperature difference increases continuously by an increase in flow rate. This signal depends on both flow rate and the gas type, concentration respectively. Flow rate can be extracted by knowing the gas concentration. In this mode, the continuous signal is obtained, because the heat transfer by conduction is constant over flow rate and not decreasing as in power mode for each gas.

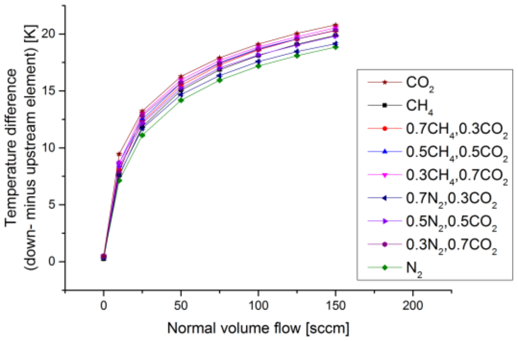

Figure 6. Constant temperature excitation: Temperature difference between up- and downstream element as function of flow speed.

DISCUSSION

The time needed to switch between the two excitation modes is a key parameter in the analysis of the breath gas. The switching time between the two modes is estimated by the response time of the sensor [5]:

$$t_{63\%} = R_{th} * C_{th} \qquad (1)$$

Based on Eq. 1, the response time for the sensor as shown in Fig 1 is calculated to 3ms. One drawback is that this value has not yet been proven experimentally.

Adults breathe 12 to 18 times per minute. This fact leads to a required response time of the sensor of around 3 to 5ms. Thus, the excitation mode can be changed every second breath, leading to a gas concentration value of carbon dioxide and flow rate around four times per minute.

The flow independent region can be varied by changing the distance between heater and temperature sensor *L* [6]. The above mentioned accuracy seems to be low for this application. In order to increase the accuracy in terms of gas concentration the distance *L* has to be decreased. However, the range of the flow independent region also decreases [6].

Breath gas has a relative humidity of 100% r.H. The change in relative humidity can have an influence towards the accuracy. The high over-temperature of the sensor ($\Delta T = 75$ K) can reduce this influence. This estimation shows that this concept can be used for analyzing breath gas.

The response time of the sensor is not important parameter in biogas plants, because the gas concentration does not change suddenly due to the fermentation process. In biogas plants, the robustness towards high humidity is more important. Biogas measured direct after the fermenter has a relative humidity close to 100% r.H. as the other application. Another critical point is the content of H_2S in the ppm-range. High humidity in combination with H_2S can lead to corrosion of the materials. Consequently, the first step before analyzing the biogas content is to remove the humidity in condensation traps and the sensor has to be placed behind it. The calculated accuracy of 5% in terms to the gas concentration seems to be sufficient to monitor the fermentation process.

CONCLUSIONS

For the first time, the detection of multi parameters has been successfully demonstrated for several applications by lab experiments with this measurement concept – time independent excitation modes contrary to AC-excitation. In order to apply this method, flow speed has to be in a specific range. The design of the sensor has to be constructed application specific due to the special requirements of the different applications; one design for all applications is not possible with this measuring method.

The investigation of mixtures with more than three components is a task for future works. This might be possible by analyzing the temperature of the heater in power mode. This enhanced concept provides an additional output signal. Thus, "real" biogas can be analyzed.

REFERENCES

[1] A. van Putten, S. Middelhoek, "Integrated silicon anemometer", Electronic Letters, Vol. 19, No. 21, pp. 425-426, 1974.

[2] A. Cubukcu, E. Zernickel, U. Buerklin, G. Urban, "A 2D Thermal Flow Sensor with sub-mW power consumption", Sensors and Actuators A: Physical, Vol. 163, pp. 449-456, 2010.

[3] J. T. W. Kuo, L. Yu, E. Meng, "Micromachined Thermal Flow Sensors – A Review", Micromachines, Vol. 3, pp. 550-573; 2012.

[4] D. Reyes, K. Kogan, A. Cubukcu, G. Urban, "Simultaneous flow and thermal conductivity measurement of gases utilizing a calorimetric flow sensor", Sensors and Actuators A: Physical, Vol. 203, pp. 225-233, 2013.

[5] C. Hepp, F. Krogmann, G. Urban, "Design and Characterization of a Thermal Sensor Achieving simultaneous Measurement of Thermal Conductivity and Flow Speed", *Proc. of 18th Transducers*, June 21-25, 2015, pp. 1065-1068.

[6] C. Hepp, F. Krogmann, G. Urban, "Flow Rate independent sensing of Thermal Conductivity in a Gas Stream by a Thermal MEMS-Sensor – Simulation and Experiments", Sensors and Actuators A: Physical, Vol. 253, pp. 136-145, 2017.

[7] C. Sosna, T. Walter, W. Lang, "Response time of thermal flow sensors with air as fluid", Sensors and Actuators A: Physical, Vol. 172, pp. 15-20, 2011.

[8] E.A. Mason, S.C. Saxena, "Approximate formula for the thermal conductivity of gas mixtures", Physics of Fluids, Vol. 1, No. 5, pp. 361-369, 1958.

MICRO CORIOLIS GAS DENSITY SENSOR

W. Sparreboom[1], *G. Ratering*[1], *W. Kruijswijk*[1], *E.J. van der Wouden*[1], *J. Groenesteijn*[1],
J.C. Lötters[1,2]
[1] Bronkhorst High-Tech BV, Ruurlo, The Netherlands
[2] MESA$^+$ Institute for Nanotechnology, University of Twente, Enschede, The Netherlands

ABSTRACT

In this paper we report on gas density measurements using a micro Coriolis sensor. The technology to fabricate the sensor is based on surface channel technology.

The measurement tube is freely suspended and has a wall thickness of only 1 micron. This renders the sensor extremely sensitive to changes in medium mass and therefore density.

The average stability of the density measurement is 0.01 kg/m^3. Temperature dependency is 0.02 kg/m^3/°C. Pressure dependency is approximately 2 kg/m^3/bar. Accuracy of several common gases is on average better than 0.2 kg/m^3.

KEYWORDS

Gas, Density, Coriolis sensor

INTRODUCTION

Gas density sensors are interesting for quality control and real time gas composition measurement [1]. Here we report on gas density measurements using a micro Coriolis sensor as reported in [2]. A Scanning Electron Microscopy (SEM) picture of the sensing tube is given in figure 1.

SENSOR DESCRIPTION

Novelty

The sensor has an extremely thin wall of only 1 micron, which renders the sensor extremely sensitive to changes in medium mass and therefore density. The ratio of the mass of the medium inside the tube and the mass of the tube is at least 10-20 times larger than in conventional stainless steel tubes. As compared to current MEMS Coriolis density sensors this ratio is more than 2 times larger than current MEMS Coriolis density sensors [3].

Chip

The sensor chip is based on the technology developed by Dijkstra et al [4]. With this technology channels at the surface of a silicon substrate can be fabricated. In figure 1 a SEM picture is given of the tube. The free hanging tube has an inner diameter of approximately 50 µm and a wall thickness of approximately 1 µm. The tube wall is LPCVD silicon rich silicon nitride. The electrodes are gold.

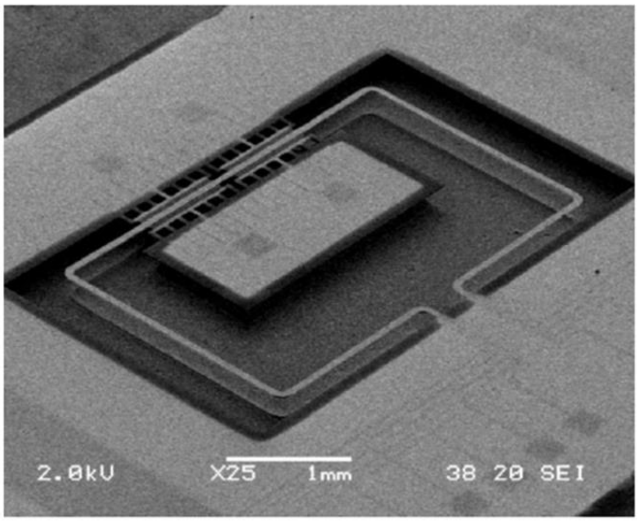

Figure 1: Scanning Electron Microscopy photo of the sensing tube. Sensing structures are shown at the top left of the figure.

Electric and fluidic interface

Actuation of the tube is performed using Lorentz force. The detection part uses electrostatic comb structures [2]. Here displacement of the tube causes a change in capacitance that is transformed into a voltage change. This is detected by a digital signal processor (DSP) via several analog to digital (ADCs) and chip actuation is performed using digital to analog converters (DACs). The combination of the above components and the sensor renders a closed control loop that locks the actuation frequency to the tube resonance frequency. This type of control loop is commonly called a phase locked loop (PLL). The chip is interfaced to a charge amplifier by wirebonding to a printed circuit board (PCB).

The chip is interfaced to the outside world using two 1/16” stainless steel tubes. The seal material between the stainless steel tubes and the chip is Kalrez.

EXPERIMENTAL

Before the density experiments helium (He) pressure and leak tests were performed. The sensor is He tight ($< 2 \times 10^{-9}$ mbar.l/s) up to 20 bar.

To check the stability of the sensor the density of nitrogen gas was measured. This was done in the setup presented in figure 2. The sensor was flushed with nitrogen for 10 minutes. To prevent gas diffusion to and from the sensor valves before and after the sensor were closed and the density was logged.

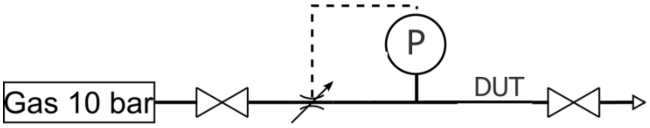

Figure 2: Schematic view of the setup. DUT is defined as device under test. Gas pressure is delivered using a mechanical pressure controller at 10 bara. A pressure meter (P) is used to electronically control the pressure using an electromagnetic valve.

In two separate experiments temperature and pressure dependency of the sensor was measured. The temperature dependency was measured in a climate chamber (Vötch VC4018). The pressure dependency was measured using the setup given in figure 2.

The density measurement was calibrated on nitrogen and water at zero flow, atmospheric pressure and room temperature.

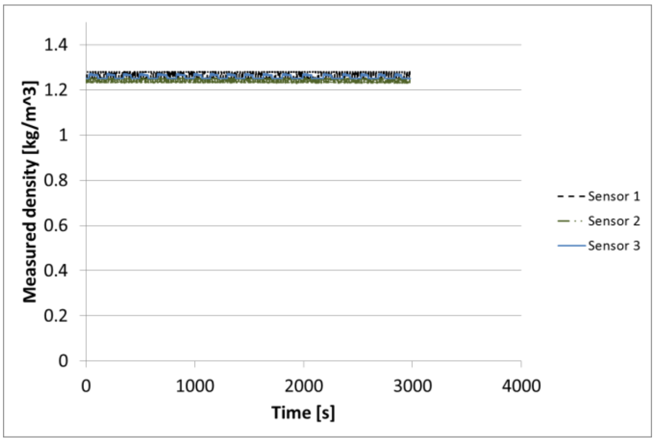

Figure 3. Measured density of nitrogen at room temperature as a function of time.

RESULTS

The result of measurements with three different sensors during 50 minutes is given in figure 3. The stability is approximately 0.01 kg/m^3.

Table 1. Measured density versus reference density

	Reference density [kg/m^3]	measured density [kg/m^3] sensor 1	measure d density [kg/m^3] sensor 2	measure d density [kg/m^3] sensor 3	average deviation [kg/m^3]
N2	1.25	1.25	1.25	1.25	0.00
Ar	1.79	1.76	1.56	1.78	-0.08
CO2	1.98	1.90	1.80	1.91	-0.10
He	0.18	0.20	0.24	0.36	0.09

Temperature dependency is 0.02 kg/m^3/°C. Pressure dependency is approximately 2 kg/m^3/bar. Especially the measured pressure dependency is too high for practical use in gas density measurement. Therefore, pressure sensors will be included to compensate the pressure effect.

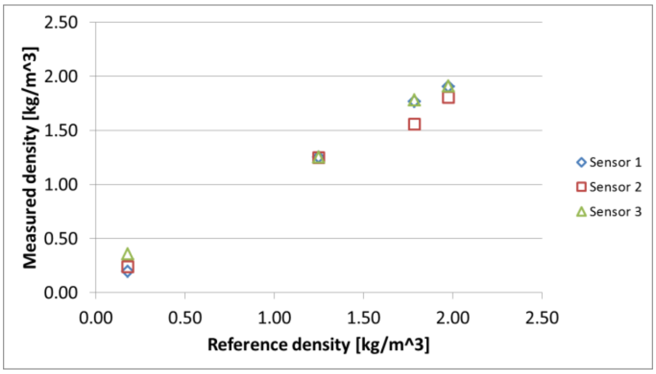

Figure 4. Measured density of helium, nitrogen, argon and carbon dioxide as a function of reference density.

The sensors were tested for several common gases (helium, nitrogen, argon and carbon dioxide). The result of this measurement is shown in figure 4 and 5 and in table 1. Interestingly it shows excellent behavior (i.e. within the measured stability) at nitrogen, however, not with the other gases. This is likely caused by calibration. Since calibration is only done for one gas and one liquid and liquid has an approximately 1000 times higher density than gas, minute errors in this calibration cause considerable errors in density measurement for media other than in this case nitrogen and water.

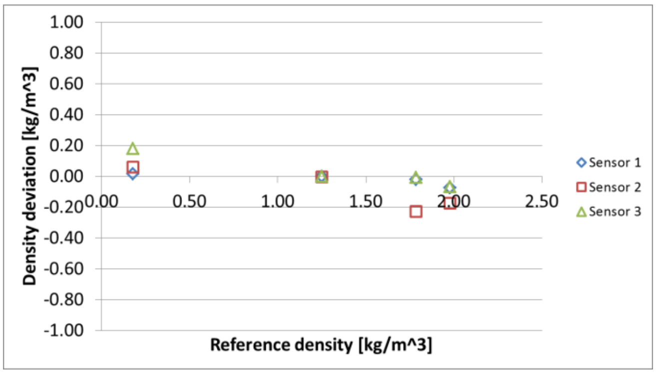

Figure 5. Measured deviation in density of helium, nitrogen, argon and carbon dioxide as a function of reference density.

CONCLUSION

To conclude we presented experiments on gas density measurements using a micro Coriolis sensor. The sensor element is freely suspended and is made of silicon nitride. This makes the sensor chemically resistant to most gases. We tested this chip with several common gases and found predictable behavior. The average stability of the density measurement is 0.01 kg/m^3. Temperature dependency is 0.02 kg/m^3/°C. Pressure dependency is approximately 2 kg/m^3/bar. The current calibration method needs improvement since average errors up to 0.2 kg/m^3 are measured between several common gases.

ACKNOWLEDGEMENTS

This project was funded by Bronkhorst. We thank Sebastiaan Veldkamp for assistance with the electronics. Sander Wiggers for firmware development and Sander Klein Hesselink for the mechanical design.

REFERENCES

[1] E.J. van der Wouden, J. Groenesteijn, R.J. Wiegerink, J.C. Lötters. “Multi Parameter Flow Meter for On-Line Measurement of Gas Mixture Composition”, Micromachines 2015, 6, 452-461

[2] J. Haneveld, T.S.J. Lammerink, M.J. de Boer, R.G.P. Sanders, A Mehendale, J.C. Lötters, M. Dijkstra, R.J. Wiegerink, “Modeling, design, fabrication and characterization of a micro Coriolis mass flow sensor”, Journal of Micromechanics and Microengineering, 2010.

[3] D. Sparks, R. Smith, M. Straayer, J. Cripe, R. Schneider, A. Chimbayo, S. Anasari, N. Najafi. “Measurement of density and chemical concentration using a microfluidic chip”, Lab on a Chip, vol. 3, pp 19-21, 2003

[4] M. Dijkstra, M.J. de Boer, J.W. Berenschot, T.S.J. Lammerink, R.J. Wiegerink, M. Elwenspoek, “A versatile surface channel concept for microfluidic applications”, J. Micromech. Microeng., 17 (2007) 1971-1977.

CONTACT

*W. Sparreboom, w.sparreboom@bronkhorst.com

A MINIATURIZED FLAME IONIZATION DETECTOR APPLICABLE IN A FIELD DEVICE

J. Förster[1], W. Kuipers[2], C. Koch[1], C. Lenz[3], S. Ziesche[3] and D. Jurkow[4]
[1] KROHNE Innovation GmbH, Duisburg, Germany
[2] KROHNE Messtechnik GmbH, Duisburg, Germany
[3] Fraunhofer IKTS, Dresden, Germany
[4] VIA electronics, Hermsdorf, Germany

ABSTRACT

Reliable and very sensitive detection of hydrocarbons can be achieved with a flame ionization detector (FID). Due to the required complex gas infrastructure for the operation of an FID these devices have not been implemented as true field devices yet. Miniaturization by using ceramic multi-layer technology leads to a strong reduction of gas consumption and allows autonomous operation of the FID with gas supply by electrolysis and without external gas infrastructure. Thus, the use of an FID as a field device is now possible for the first time. Characterization of this miniaturized FID reveals a performance comparable to conventional FIDs.

KEYWORDS

Flame Ionization Detector, FID, μFID, Miniaturization, Electrolysis, Field Device, Ceramic Multilayer Technology, LTCC

INTRODUCTION

Reliable and very sensitive detection of hydrocarbons is very important in the context of emission control, environment protection, or the monitoring of areas exposed to explosion hazards. For emission control and environment protection small amounts of hydrocarbons in the order of few ppm must be detected to ensure that emissions comply with effective regulations. Thus, a very sensitive measurement method has to be applied to fulfill these needs. In the case of explosion protection the detection of hydrocarbons must be very reliable. Temperature and humidity as well as different substances in the surrounding area must not lead to false alarms. Therefore, the measurement method has to be insensitive to environmental conditions but selective towards hydrocarbons at the same time.

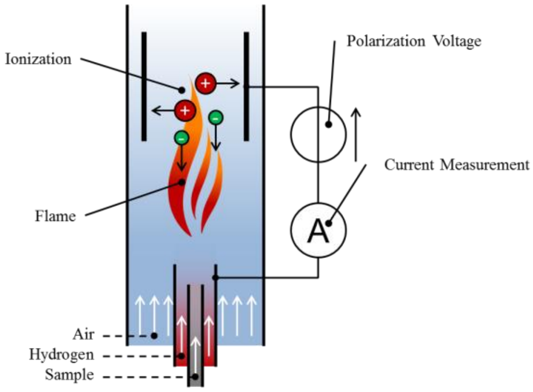

Figure 1: Schematic drawing of a conventional FID.

All of these aforementioned requirements are met by the flame ionization detector (FID). The FID is very sensitive and selective towards hydrocarbons and insensitive to environmental conditions. In an FID hydrogen is burned together with air, as shown in Figure 1. A sample gas is added to this flame. Hydrocarbons contained in the sample gas are ionized by the flame and can then be extracted by an electrical field. The resulting electrical current is proportional to the carbon content of the sample. The FID has a very low detection limit and a high selectivity towards hydrocarbons. Thus, it can reliably detect extremely small amounts of hydrocarbons in the sample (ppm or ppb region) [1].

In the context of emission control, environment protection, and explosion protection FIDs have the best performance of all available technologies. However, the true potential of FIDs is not leveraged completely due to expensive supply with the necessary pure hydrogen and conditioned air for operating. Until now, this required complex gas infrastructure impedes the use of FIDs as field devices. Therefore, this work describes an innovative approach to realize the operation of an FID with internal electrolysis using a special way of miniaturization.

MINIATURIZATION OF THE FID

Electrolysis generates pure hydrogen and oxygen. Both gases shall be used to operate the FID. Thus, the gas consumption of the FID must be reduced and it must be operable on pure oxygen instead of on synthetic or conditioned air. Both requirements are met by miniaturizing the FID realizing an innovative planar counter-current geometry [2], as shown in Figure 2. The usage of pure oxygen at the high temperature of the hydrogen flame and the humidity of the gases due to the electrolysis require a high corrosion resistance of the miniaturized FID. Conventional miniaturized systems based on MEMS-technology are not sufficient in this case. Therefore, ceramic multilayer technology LTCC which is

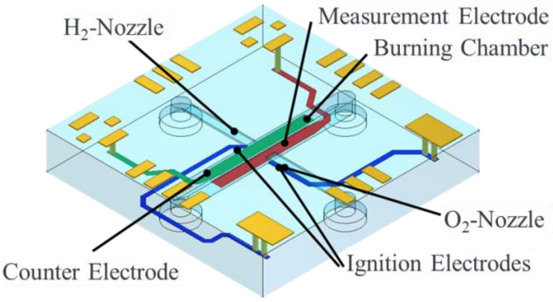

Figure 2: Drawing of the µFID geometry.

extremely robust towards high temperatures and chemicals has been used to manufacture the miniaturized FID (µFID) [3].

The µFID measures 15 mm x 15 mm x 2.5 mm. It has a small counter-current burner geometry in the sub-millimeter regime allowing operation with a small diffusion flame. To study the influence of the burner geometry on the µFID performance different nozzle sizes have been realized. Type A has full-sized nozzles, type B has half-sized nozzles, and type C has asymmetric nozzles. To supply the µFID with gases and to apply all control and measurement signals the µFID has several interfaces. All fluidic connections are placed at the bottom side of the chip and all electric connections are placed at the upper side of the chip. This enables easy integration of the chip into a measurement system. Not shown in Figure 2 is the guard electrode which is placed inside the chip to prevent from measuring a leakage current between counter electrode and measurement electrode.

CHARACTERIZATION OF THE µFID

As mentioned before, the gas consumption of the FID is reduced by the miniaturization. Thus, the first parameter to be characterized is the gas consumption of the µFID. Further important characteristics of the µFID are its operating point, its sensitivity, its noise, and its resulting detection limit.

For all measurements the ceramic chip was fixed on a heated mounting to avoid condensation in the exhausts of the µFID which results in flame extinction and electrical leakage currents [4]. The gas flows were controlled with conventional (mass) flow controllers. The electrical controlling and measurement of the µFID was done with a self-developed measurement setup [4].

Minimum Gas Consumption

To determine the minimum gas consumption of the µFID the flow of the hydrogen as well of the oxygen was reduced while the flame temperature of the µFID was monitored. As reported in [4], monitoring the surface temperature in the center of the chip corresponds best with the flame. These measurements show that the gas consumption of the µFID can be reduced down to 0.48 l/h of hydrogen which is less than half of the hydrogen consumption of conventional FIDs. Furthermore, due to the use of pure oxygen the gas consumption could be reduced from 30 l/h of air down to less than 0.24 l/h of oxygen. These reduced gas flows allow in deed for the use of electrolysis as the gas supply of the µFID.

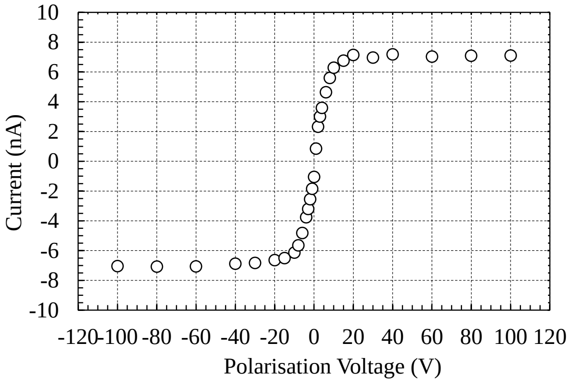

Figure 3: Ion current of the µFID (Type A) as a function of the polarization voltage at a concentration of 9000 ppm Methane in Nitrogen.

Operating Point

The first step for the characterisation of the sensitivity of the µFID was the determination of an adequate operating point, i.e., finding the best relation between polarization voltage and current. Therefore, the polarization voltage was swept from -100 V to +100 V while all other parameters were kept constant. The results of such a measurement are shown in Figure 3. This figure shows, that the current saturates for a polarization voltage of about 40 V. Therefore, for all following measurements the operating point of the µFID was defined at a polarization voltage of 40 V.

Sensitivity

The sensitivity was then characterized by varying the carbon content in the sample gas while all other parameters were kept constant. The result of such a

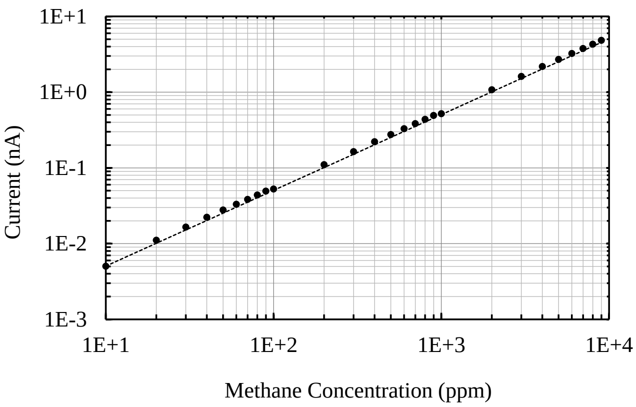

Figure 4: Function of the ion current of µFID type A as a function of the Methane concentration.

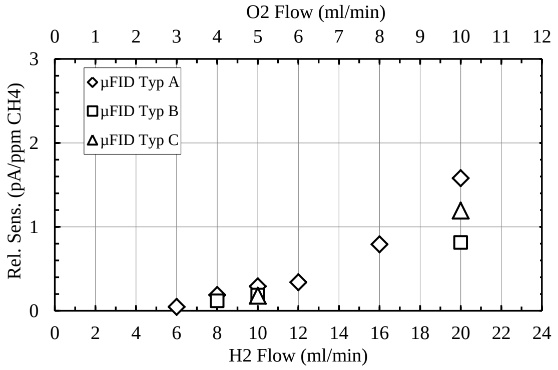

Figure 5: Relative sensitivity of the µFID for several gas flows.

measurement is a linear dependency of the ion current on the carbon concentration as shown in Figure 4. The slope of this linear function is the relative sensitivity S_{rel} of the µFID. It is defined as the resulting current per a specific carbon concentration. As the curve in Figure 4 clearly illustrates, the characteristic line of the µFID is linear over a range of three decades at least. This behaviour is typical for an FID [5].

As can be seen in Figure 5 the relative sensitivity increases with rising gas consumption. This behaviour is present in all three µFID types. In addition, Figure 5 reveals that µFID type A has the highest relative sensitivity of all three variants. This indicates that this type might be the most promising µFID type for the field device application.

Noise

The noise of the µFID is defined as ±3σ [5]. Therefore, the standard deviation of the ion current during time periods of 100 s was calculated. As the signal to noise ratio is most crucial at very low signal levels, the noise estimations have been performed without any hydrocarbon content in the sample gas. The results are shown in Figure 6. These measurements show that the noise is not dependent on the gas consumption. The small variations are due to measurement uncertainty only. This is a huge improvement compared to the first µFID designs reported in [4] where a strong dependency of the noise on the gas consumption was present. Thus, the elimination of the leakage current with the guard electrode proofs to be a very effective way to reduce the noise of the µFID.

Detection Limit

The detection limit represents the smallest concentration of hydrocarbon in the sample gas which can be detected reliably. However, the detection limit is restricted by the noise of the µFID [3]. The detection limit (DL) can be determined from the value of the noise (N) and the relative sensitivity (S_{rel}) [5]. It is given by

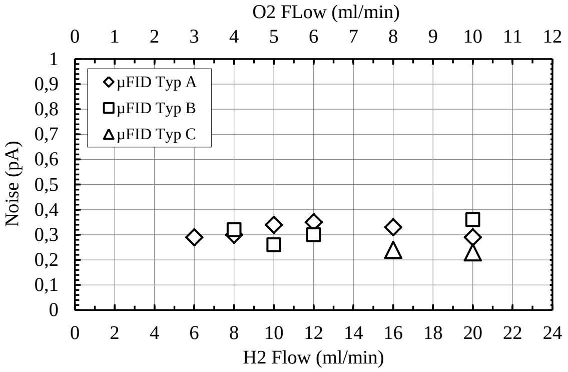

Figure 6: Noise of the µFID as a function of gas consumption.

$$DL = \frac{2*N}{S_{rel}}\,. \qquad (1)$$

The values of the detection limit calculated with eq. (1) from the values of the relative sensitivity and the noise are shown in Figure 7. As the noise is constant and the relative sensitivity increases with rising gas consumption the detection limit decreases with increasing gas consumption. For small gas flows of 8 ml/min hydrogen and 4 ml/min oxygen the detection limit is between 1.5 mg/m^3 and 2.9 mg/m^3 depending on the chip type. However, for higher gas flows around 20 ml/min hydrogen and 10 ml/min oxygen the µFID can detect carbon quantities down to approximately 0.2 mg/m^3.

The values for the detection limit at higher gas flows are comparable to conventional FIDs. As these higher gas flows are in the same range as the gas flows of conventional FIDs, the performance of the µFID is equal to the performance of conventional FIDs. Furthermore, the µFID has the benefit that the gas consumption can be reduced down to less than the half of conventional FIDs while still attaining a low detection limit.

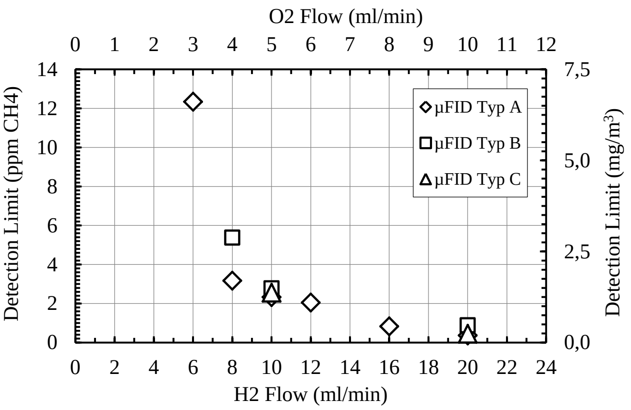

Figure 7: Detection limit of the µFID for several gas flows.

THE µFID AS A FIELD DEVICE

As mentioned before the µFID shall be used as a field device. Therefore, to determine the µFIDs potential to be used as a field device all fluidic components around the µFID chip of which a field device will consist must be taken into account. First, the gas supply will be done by electrolysis. Second, the sample to be analyzed must be injected into the µFID. This is done with the help of a membrane pump.

Both the gas supply by electrolysis as well as the pump generates fluctuations in the fluidic system. This represents a higher noise level of the µFID and might also have an effect on the relative sensitivity of the µFID. Thus, these additional fluctuations will reduce the performance of the overall device. Therefore, the relative sensitivity and the noise of the overall system have been measured to determine the resulting detection limit.

The first measurement already revealed that the fluctuations caused by the electrolysis and the pump have a negative effect on the flame stability of the µFID. Only for gas flows of at least 12 ml/min hydrogen the flame inside the µFID is stable and allows steady operation of the system. Thus, the gas reduction of the overall system is not as big as of the single µFID chip. However, these gas flows are still significantly lower than in conventional FIDs and allow for gas supply by electrolysis.

Further measurements showed that the relative sensitivity is not affected by the fluctuations. However, the noise of the µFID is three-times higher due to the fluctuations. Thus, the detection limit of the system is also three-times higher. Therefore, the system can reliable detect a carbon concentration of approximately 2.4 mg/m^3 at the lowest possible gas flow of 12 ml/min hydrogen and 6 ml/min oxygen. It can also still detect carbon concentrations below 1.0 mg/m^3 at higher gas flows.

The measurements did also reveal that the humidity of the gases generated by electrolysis does not affect the µFID. The behavior of the µFID during the ignition phase did not change when switching from gas bottle supply to the gas supply by electrolysis. Furthermore, even humid sample gas did not change the response of the µFID. Thus, the µFID is also comparable to conventional FIDs in its robustness against humidity.

CONCLUSION

The miniaturization of an FID was successfully performed using the ceramic multilayer technology LTCC. The performance of the resulting µFID chip at common gas flow rates is comparable to conventional FIDs. In addition, the µFID allows stable operation at reduced gas flows while still offering a good detection limit of 1.5 mg/m^3. The overall system based on this µFID still achieves a good detection limit of approximately 2.4 mg/m^3 with small gas flow rates which allow for gas supply by electrolysis. Thus, this µFID paves the way for the introduction of a FID as a field device for the first time.

ACKNOWLEDGMENTS

This work is part of the project “FIDEX – Autonomer Mikroflammenionisationsdetektor für den Explosionsschutz in zivilen Kanalisationsnetzen” and is financially supported by the German *Bundesministerium für Bildung und Forschung BMBF* (#13N13271).

REFERENCES

[1] H. H. Hill, D. G. McMinn “Detectors for Capillary Chromatography”, J. Chemical Analysis, 1992, pp. 7-21.

[2] W. J. Kuipers, J. Müller “Characterization of a microelectromechanical systems-based counter-current flame ionization detector”, J. Chromatography A, 1218, pp. 1891-1898, 2011.

[3] C. Lenz, H. Neubert, S. Ziesche, J. Förster, C. Koch, W. Kuipers, M. Deilmann „Development and Characterization of a Miniaturized Flame Ionization Detector in Ceramic Multilayer Technology for Field Applications”, Proceedings of Eurosensors, 2016.

[4] J. Förster, W. Kuipers, C. Koch, C. Lenz, S. Ziesche, D. Jurkow „Miniatured Flame Ionisation Detector for Explosion Protection in Civil Sewerage Networks”, S-CUBE, Springer, DOI 10.1007/978-3-319-61563-9_14, 2017

[5] W. J. Kuipers, “Design, Fabrication and Characterization of a MEMS-Based Counter-Current Flame Ionization Detector”, Doktor Hut Verlag, München, 2011

CONTACT

J. Förster, j.foerster@krohne.com

MINIATURIZED GAS COMPOSITION SENSOR FOR NATURAL GAS AND BIOGAS

A. Boersma[1], J. Sweelssen[1] and H. Blokland[2]
[1]TNO, De Rondom 1, 5612AP Eindhoven, The Netherlands
[2]TNO, Leeghwaterstraat 44, 2628 CA Delft, The Netherlands

In the coming years, more gas will be imported from different sources all over the world, through pipelines and as Liquid Natural Gas (LNG). Furthermore, the need for a transition towards a sustainable energy supply will result in an increase of the production of biogas. A significant part of the biogas will be fed into the distribution grids for natural gas. In Europe the composition of both LNG and biogas deviate from the traditional sources, such as the on-shore gas fields and North Sea gas.

The currently available gas quality measuring systems (e.g. GC, Wobbe Index analyzer, etc.) cannot fulfill the need for a cost-effective inline measuring method. An example is proposed in the EDGaR project, in which the gas composition is measured using a combination of NDIR, photoacoustics, thermal conductivity and viscometry[1][2]. Although this combined approach can measure the composition very accurately, the size and costs of such a system is too high for widespread implementation. For that reason, TNO together with gas grid operators and Bronkhorst High-Tech started the development of a new type of gas sensor, based on gas sensitive coatings on an electronic platform.

The gas sensitive coatings can be based on polymers, metal oxides or semiconductors that change an electronic property upon absorption of the target gasses. One approach that is widely used is based on the change in resistivity of a metal oxide layer at elevated temperatures. However, this approach cannot be used for in-line measurements in calorific gas, because there is no oxygen present for sensor regeneration.

Therefore, a capacitive platform was chosen, made from an array of interdigitated electrodes (figure 1, figure 2), each of which was coated with a polymer based coating, specifically tuned to one of the target gasses[3][4]. The responsive coatings that were applied on the capacitive comb electrodes were based on fluoro, silicone and imide polymers, some having porous additives for the capture of the gas molecules. The cavity size and porosity was tuned to the chemistry and molecular size of the individual gasses. When gas molecules are captured inside a cavity, the dielectric constant changes, giving rise to changing capacitances, measured by the electronics. The capacitive chips were bonded to a sensing-PCB (figure 3), and installed in the gas exposure vessel (figure 4). The signal processing PCB was kept out of the gas mixtures for practical and security reasons.

The gas sensing device was exposed to the target gases of methane, ethane, propane, nitrogen, carbon dioxide and water vapor, and mixtures of various gases. The concentrations in these mixtures were chosen to approach the concentrations in a typical gas (i.e. ~80 vol% methane, ~3 vol% ethane, ~1 vol% propane). Two examples are given in figures 5 and 6: one coating exposed to methane concentrations between 65 and 87 vol% (at 1 bara and 25 °C), and another coating exposed to ethane concentrations between 0 and 5 vol%.

Combining the response of multiple sensor chips makes it possible to simultaneously obtain the concentrations of the individual components of the target gas mixtures. Subsequently, other gas parameters can be calculated from the composition, such as the calorific value, Wobbe index, and density.

We will present the recent progress with respect to miniaturization of the electrodes and electronics, the development of the responsive coatings and application process, and the result of the testing and characterization of the sensor in gas mixtures. We will show that miniaturization of the sensor system not only enables the integration in gas flows, but also leads to higher accurate measurement results. Furthermore, this miniaturization also opens the possibilities to measure gas compositions in microfluidic devices.

Word Count: 600

REFERENCES

[1] EDGaR, www.edgar-program.com
[2] G. de Graaf, F. Bakker and R.F Wolffenbuttel, Sensor platform for gas composition measurement, Proc. Engin. 25 (2011), 1157-1160.
[3] D. Snelders, A. Boersma, A-J. de Jong, Gas Sensor Array and Method, 2014, WO2016003272
[4] A. Boersma, J. Sweelssen , H. Blokland, Gas composition sensor for natural gas and biogas, Procedia Engineering 168 (2016) 197 – 200

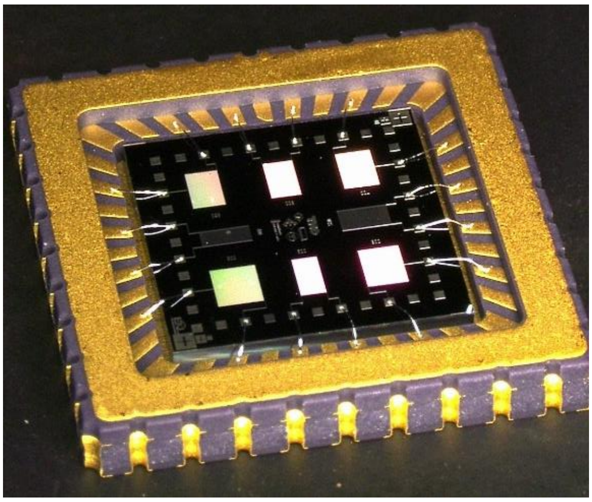

Figure 1: Eight interdigitated electrodes manufactured on a silicon wafer and packaged.

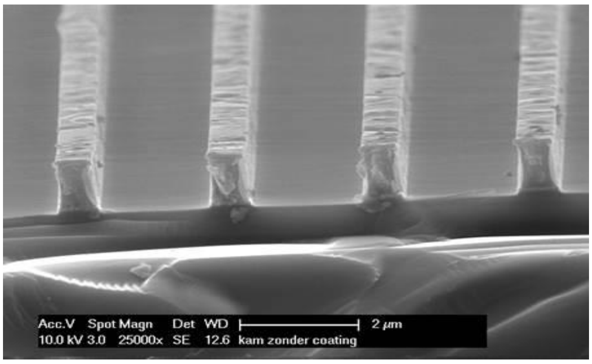

Figure 2: An example of the cross-section of an interdigitated electrode with a spacing of almost 2μm.

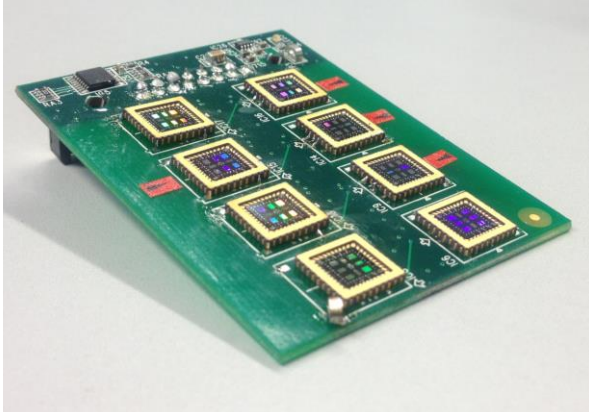

Figure 3: Eight sensor chips installed on the sensing-PCB for simultaneous measurements.

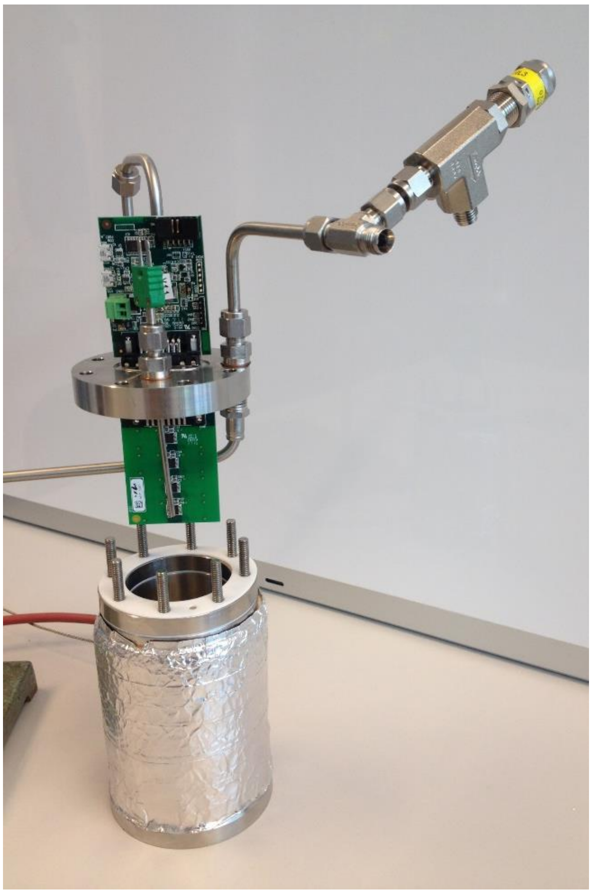

Figure 4: Full sensor (sensing-PCB and processing-PCB) installed in exposure vessel

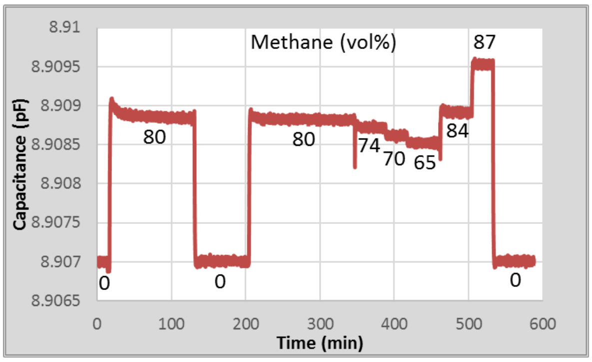

Figure 5. Response of one of the coatings to a change of methane concentration at 1 bara and 25 °C.

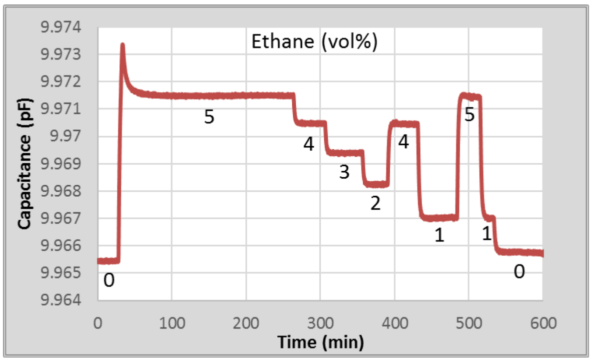

Figure 6. Response of one of the coatings to a change of ethane concentration at 1 bara and 25 °C.

VISCOSITY DETERMINATION BY THE IN-LINE DETECTION OF FLOW TIME THROUGH A CYLINDRICAL TUBE

F. Koch[1]*, S. Kartmann*[1]*, R. Zengerle*[1]*, A. Ernst*[2] *and P. Koltay*[1,2]
[1] University of Freiburg, Laboratory for MEMS Applications, Freiburg, Germany
[2] Biofluidix GmbH, Freiburg, Germany

ABSTRACT

This paper reports on a novel in-line viscosity measurement concept, with several benefits compared to common approaches. The measurement concept is based on the determination of the transition-time of a liquid/gas interface while filling a well-defined capillary. In contrast to previous work [1] this paper determines the transition-time for the first time in a non-contact capacitive way.

The viscosity is determined by recording the time of a travelling liquid/gas front while filling a capacitive flow sensor setup using the differential pressure principle, as presented in [2]. Thereby, the viscosity is calculated from the measured flow rate assuming laminar flow through the sensor channel with known diameter.

The method enables to determine the dynamic viscosity with a mean coefficient of variation (CV) of 8.4% for a measuring range between 1 and 20 mPa s. It showed to be high valuable for fast viscosity calibration of flow sensors based on the differential pressure principle.

INTRODUCTION

The presented viscosity calibration is fully implemented in a capacitive flow sensor presented by the authors earlier [2]. The flow sensor consists of two capacitive pressure sensors on both sides of a capillary, acting as defined fluidic resistance, as shown in figure 1.

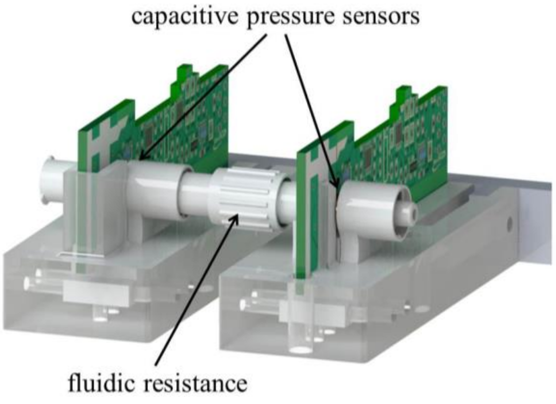

Figure 1: Visualization of the flow sensor setup that consists of two capacitive pressure sensors and a fluidic resistance mounted in between. The read-out electronic for each pressure sensor is implemented on printed circuit boards.

Each pressure sensor measures the hydrodynamic pressure by detecting the radial expansion of an elastic tube, acting as measuring cell. Semispherical gold electrodes are mounted on the printed circuit board (PCB) with the isolation distance *g* and the inner radius *r*. They surround the measuring cell and enable the detection of a flow induced expansion due to a changed amount of dielectric material ε_r resulting in a changed capacitance.

The higher the pressure the more the elastic tube expands and the distance *s* between electrodes and tube decreases, as shown in figure 2. The expansion of the measuring cell can be detected electrically by applying an arbitrary e.g. sinusoidal signal on one of the electrodes and compare it with the detected signal on the other electrode.

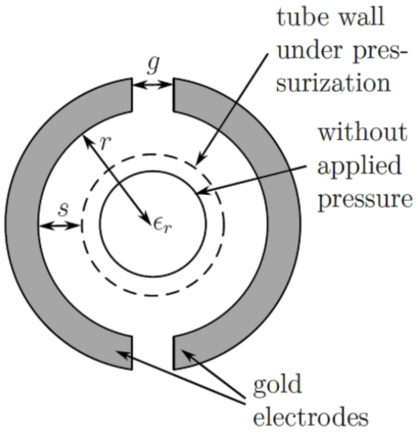

Figure 2: Schematic side view of the elastic expansion of the tube between two spherical gold electrodes with and without external pressure applied. The distance s between electrodes and tube decreases under pressure by which the amount of dielectric material between the electrodes is increased. This measuring principle is used for both capacitive pressure sensors.

The measuring cell is composed of a solid mounting with Luer Lock connections on both sides with an elastic silicone tube in between. It is enclosed by half-shell electrodes fabricated on a PCB with 3.2 mm width. The complete read-out and amplification electronics are implemented on the PCB and the sensing electrodes are realized by side metallization, as shown in figure 3.

The centrical and stable position of the measuring cell with respect to the electrodes can be adjusted by turning regulating screws from the bottom and the sides into the 3D printed housing.

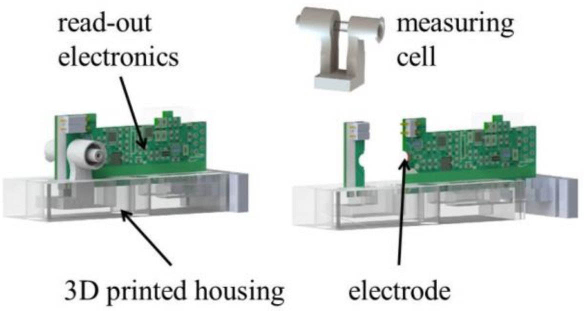

Figure 3: Visualization of a single pressure sensor setup composed of a disposable elastic measuring cell with elastic silicone tube between two Luer Lock connections. The measuring cell can be mounted in a 3D printed housing between two half-shell electrodes realized as side metallizations on a PCB.

The combination of two pressure sensors on both sides of the fluidic resistance enables to calculate with the law of Hagen-Poissuille the volumetric flow, as it was already presented for MEMS flow sensor devices [3]. The fluidic resistance is thereby linearly affected for incompressible and Newtonian liquids by their viscosity. Therefore, the viscosity has to be precisely known to calculate the flow from a given pressure difference. Figure 4 shows the change in differential pressure for flow rates between 0 and 50 µl/s of liquids with different viscosities. A pre-calibration of each fluid is therefore highly desired before every measurement when using this type of flow sensor.

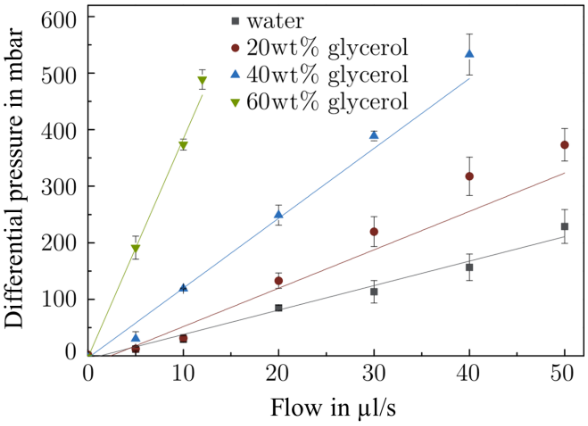

Figure 4: Pressure differences across a fluidic resistance made of a metallic capillary with 100 µm inner diameter and 16.5 mm length as a function of the flow rate and viscosity of the liquid. Aqueous liquids with different glycerol concentrations and viscosities between 1 mPa s and 9.75 mPa s were evaluated. The viscosity of the liquids increases with increasing glycerol concentration. The slope of each curve correlates to the viscosity of the corresponding liquid and must be determined before every flow measurement as calibration curve.

WORKING PRINCIPLE AND REALIZATION

The presented method is based on the principle of a capillary viscometer. It does not measure the flow time of a well-defined volume of liquid, as it is present for example in an Ostwald's viscometer, but considers instead the moving liquid/gas interface while the sensor is filled. This transition-time can be only measured once each time the sensor setup is filled. Therefore, the results cannot be averaged as it is common for other viscosity measuring techniques, e.g. using an oscillating viscometer [4] and the method has a higher methodical error. Still the presented approach is useful, as it can be easily integrated into a differential flow sensor without additional effort.

The two capacitive measuring cells are highly responsive and can therefore determine in high temporal resolution when the liquid/gas front enters each of the two measuring cells while filling the sensor setup. A change of medium from air to liquid inside the measuring cells results not in a radial expansion of the tube as presented before, but in a sudden change of relative permittivity when liquid replaces air. Therefore, this method does not require any kind of external optical measurement of the liquid's movement respectively travel time as it is present for other methods using the same calibration technique [5].

The travelling time through the capillary is mainly influenced by the applied differential pressure, the channel's geometry and the liquid properties. The driving pressure is created for all experiments in the same way, by a liquid reservoir of 20 cm height and an additional pneumatic pressure of 50 mbar. For the fluidic resistance between both pressure sensors a capillary made of stainless steel with an inner diameter of 100 µm and length of 16.5 mm was used.

When measuring the transition-time of the liquid/gas interface, the liquids front must pass a series connection of three fluidic resistances:

- R_{supply}, the fluidic resistance of the supply tubes and the outlet of the liquid reservoir
- R_{mc}, the fluidic resistance of the first measuring cell
- R_{cap}, the fluidic resistance made by the metallic capillary

The resistance of the elastic measuring cell R_{mc} is neglected due to its high diameter and short length compared to the other fluidic elements. The measured transition-time begins at the moment the liquid enters the first measuring cell and ends when it leaves the capillary to flow into the second measuring cell.

The filling of the sensing parts can therefore be separated in two phases:

1. The meniscus enters the measuring cell and fills the measuring cell. The flow rate is limited by a constant fluidic resistance of R_{supply} and can be described by the law of Hagen-Poiseuille.

2. The meniscus has completely filled the measuring cell and fills the capillary, which can be described by a combination of capillary and pressure driven flow approximated by the Washburn equation [6].

1. The fluidic resistance of the first measuring cell is neglected and approximated by an opened end. Therefore, the pressurized reservoir creates in the first phase a constant flow rate, which is independent of the liquid volume inside the measuring cell. This relation is valid until the volume of the measuring cell V_{mc} is completely filled and can be described by the law of Hagen-Poiseuille in equation (2)

$$Q = \frac{V_{\mathrm{mc}}}{t_1} = \frac{\Delta P_{\mathrm{total}}}{R_{\mathrm{supply}}} \tag{2}$$

where Q is the volumetric flow, V_{mc} the volume of the measuring cell which is filled in a defined time t_1, $\Delta P_{\mathrm{total}}$ the total applied pressure and R_{supply} the fluidic resistance of the supply tube. The filling time of the measuring cell can be calculated with the formula for a fluidic resistance created by a circular inelastic capillary by solving equation (2) for t_1 as

$$t_1 = \frac{V_{\mathrm{mc}} \cdot R_{\mathrm{supply}}}{\Delta P_{\mathrm{total}}} = \frac{\pi {r_{\mathrm{mc}}}^2 l_{\mathrm{mc}} \cdot 8 \frac{l_{\mathrm{supply}}}{{r_{\mathrm{supply}}}^4} \eta}{\Delta P_{\mathrm{total}}} \tag{3}$$

With length l_{mc} = 5 mm and radius r_{mc} = 1.25 mm of the measuring cell, its volume yields V_{mc} = 24.5 mm^3. The dimensions of the supply tube are given by l_{supply} = 350 mm and r_{supply} = 0.8 mm. This results in a linear dependency of the filling time t_1 on the liquid's viscosity.

2. After the measuring cell is completely filled the capillary starts to fill and the now increasing fluidic resistance results from two fluidic elements: First, the supply tube creates a constant fluidic resistance, which can be modelled as a tube of same diameter as the capillary, but with an equivalent length $l_{\mathrm{equ}} = 0.35 \cdot l_{\mathrm{cap}}$ to maintain the value of R_{supply}. Second, the fluidic resistance of the capillary, which changes during the meniscus movement through the capillary, has to be considered. This filling process can be described by Washburn's differential equation [6]

$$\frac{dl}{dt} = \frac{\left[P_A + g\rho(h - l_s \sin(\psi)) + \frac{2\sigma}{r}\cos(\theta)\right] \cdot \left[r^2 + 4\varepsilon r\right]}{8 l \eta} \tag{4}$$

with P_A the applied pressure and h the height of the liquid reservoir. For the given experimental conditions the inclination angle of the capillary ψ and the coefficient of slip ε can be set to 0. With these simplifications the equation can be integrated over the total length of the capillary $\mathrm{l}_{\mathrm{cap}}$ and solved for t_2 as follows

$$t_2 = \frac{4\left[(l_{\mathrm{cap}} + l_{\mathrm{equ}})^2 - {l_{\mathrm{equ}}}^2\right]}{\left[\Delta P_{\mathrm{total}} + \frac{2\sigma}{r}\cos(\theta)\right]} \eta \tag{5}$$

The two transition-times t_1 and t_2 have to be added up to yield the total transition-time, which is detected by the measurement setup.

EXPERIMENTAL RESULTS AND DISCUSSION

Six different aqueous liquids were analyzed, which are listed with their rheological properties in table 1. A cone plate rheometer from Anton Paar (Physica MCR 101) was used to determine the viscosity, the density was calculated from literature values [7], [8]. The content of glycerol in deionized (DI) water was changed for the first four liquids and mainly increased the liquid's viscosities from 1.00 up to 9.75 mPa s. The variations in density and surface tension were significantly lower in the range between 1.00 and 1.14 $\mathrm{g\,cm^{-3}}$ and between 67.7 and 72.0 $\mathrm{mN\,m^{-1}}$ respectively.

Due to the high surface tension of the water/glycerol solutions, which could cause high capillary forces and systematic errors in the measurement two more sample liquids, namely fluid F and fluid B as described in [7] with reduced surface tensions were additionally investigated.

Table 1: Overview of the used test liquids and their viscosities and densities.

Test liquids	Viscosity in mPa s	Density in $\mathrm{g\,cm^{-3}}$
Deionized water	1.00	1.00
Water + 20% glycerol	1.83	1.03
Water + 40% glycerol	3.48	1.08
Water + 60% glycerol	9.75	1.14
Fluid F	2.70	1.08
Fluid B	19.10	1.17

Table 2: Overview of test liquids surface tensions and contact angles on cleaned stainless steel surface.

Test liquids	Surface tension in mN/m	Contact angle in °
Deionized water	72.0	61.6 ± 4.6
Water + 20% glycerol	69.5	65.2 ± 3.5
Water + 40% glycerol	69.9	62.1 ± 3.7
Water + 60% glycerol	67.7	58.3 ± 7.0
Fluid F	39.1	54.6 ± 7.6
Fluid B	30.5	33.6 ± 2.1

The capillary action influences the transition-time t_2 and varies with changing surface tensions σ and contact angles θ, as shown in equation (5). This wetting inside the capillary cannot easily be measured due to the non-transparency and high curvature of the capillary. Therefore, the contact angle had to be measured on a test sample of the same material of stainless steel. It was cleaned twice with ethanol and DI water as it was the same procedure before each measurement with the metallic capillaries. The static contact angle was measured with a system from dataphysics (OCA 15 plus) for ten different 3 µl droplets with twice measurements on both sides of the droplet. The surface tensions were taken from literature [7], [8]. All values and standard deviations are shown in table 2.

Transition-times of the liquid/gas interface to pass the capillary tube were measured ten times for all liquids. The resulting mean values and their standard deviations are shown in figure 5 in black squares. The expected transition-times resulting only from the advancing meniscus through the measuring capillary t_2 calculated with equation (5) are shown as red dots and the sum of the transition-times t_1 and t_2 is displayed as in blue triangles.

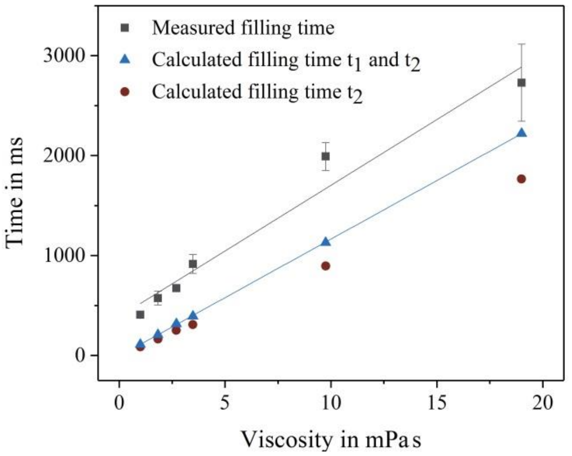

Figure 5: Measured transition-times of aqueous test liquids (black squares) with mean values and standard deviations of ten measurements. The results are compared with the transition-times for filling only the capillary (red dots) calculated by Washburn's equation and the combined transition-times of filling measuring cell and capillary (blue triangles).

The mean CV of all liquids was 8.4% corresponding to an average error of ± 121 ms, mainly increased by the liquid with the highest viscosity and lowest surface tension. A linear fit to the measured data (black line in figure 5) shows an offset of 394 ms from the origin, which could be caused by a systematical delay in the data acquisition. Still, the slope of the line fit is in reasonable agreement with the slope of the calculated filling time t_1 and t_2 (blue line in figure 5). The deviation is about 12% and it could be readily explained by a higher effective resistance in the experimental setup than in the simplified model used for the calculation. The transition zone before the liquid/gas front enters and after it leaves the measuring capillary could for example take additional time or the fluidic resistance contribution of the measuring cells might not be fully negligible.

However, as the offset as well as the proportional deviation can be described by constant correction factors quite well, the sensor should be applicable for viscosity measurements, if such empiric correction is considered for example by calibration.

SUMMARY AND OUTLOOK

The presented method showed for the first time a viscosity measurement technique by determining the transition-time of a liquid/gas interface through a metallic capillary in a non-contact capacitive way. All measurement points for liquids with viscosities between 1.00 and 19.10 mPa s were clearly separated from each other and showed reproducible values of significantly different transition-times, which enables to draw conclusions on their viscosity.

Furthermore, the method requires nearly no additional effort, except for a constant pressure source, if the presented flow sensor according to the differential principle is used. Filling the sensor with liquid is in any case required and a necessary procedure before usage of the flow sensor. The method is therefore not considered mainly as alternative for viscometer measurement, but enables with low effort a fast in-line pre-calibration of the flow sensor for different liquids.

The systematic offset between measured data, model and literature values might be reduced by either implementing a more precise model of the filling dynamics and/or by explicit calibration of the sensor. Further investigations are planned in order to decrease the uncertainty of the method and to investigate density effects with isoviscous liquids.

REFERENCES

[1] C. Trejo-Soto, E. Costa-Miracle and I. Rodriguez-Villarreal, "Capillary filling at the microscale: control of fluid front using geometry" PLoS One 11, 2016.

[2] S. Kartmann, M. Kellermann, R. Zengerle, P. Koltay, A. Ernst, "Simulation study of a novel capacitive pressure sensor concept based on the geometrical deformation of an elastic measuring cell", 2nd MFHS Conference, 2014.

[3] M. Boillat, A. van der Wiel, A. Hoogetwerf and N. de Rooij, "A differential pressure liquid flow sensor for flow regulation and dosing systems" Micro Electro Mechanical Systems, MEMS '95, IEEE, 1995.

[4] K. Hausler, W. Reinhart, P. Schaller, J. Dual, J. Goodbread and M. Sayir, "A newly designed oscillating viscometer for blood viscosity measurements", Biorheology 33, 397–404, 1996.

[5] N. Srivastava, R. Davenport and M. Burns, "Nanoliter Viscometer for Analyzing Blood Plasma and Other Liquid Samples", Anal. Chem., 77, 383-392, 2005.

[6] E. Washburn, "The dynamics of capillary flow", Physical Review 17, 273,1921.

[7] N. Losleben, J. Spinke, S. Adler, N. Oranth and R. Zengerle, "Model fluids representing aqueous in-vitro diagnostic reagents for the development of dispensing systems" Drug Discovery Today, vol. 18, no. 21-22, pp. 1035–1042, 2013.

[8] M. Pagliaro and M. Rossi, "The future of glycerol: New uses of a versatile raw material", RSC green chemistry series. 2nd ed., ASIN 1849730466, 2008.

DESIGN PRINCIPLES AND FABRICATION METHOD FOR A MINIATURIZED FUEL GAS COMBUSTION REACTOR

Y. Zhao[1], H.-W. Veltkamp[1], M.J. de Boer[1], Y. Zeng[1], J. Groenesteijn[2], R.J. Wiegerink[1], and J.C. Lötters[1,2]
[1] MESA+ Institute for Nanotechnology, University of Twente, Enschede, The Netherlands
[2] Bronkhorst High-Tech BV, Ruurlo, The Netherlands

ABSTRACT

Wobbe Index meter is widely used to reflect the energy content and gas quality of a fuel gas mixture. It is highly in demand to downscale from the conventionally large Wobbe Index facility to a miniaturized Wobbe Index meter. Therefore spontaneously combustion of the fuel gas/air mixtures on a MEMS-based combustor can provide in-line temperature monitoring of the combustion produced heat. However, flame can be quenched by the channel walls when the walls are closely spaced. Therefore, it is crucial to design a micro-combustor with good thermal management and strong mechanical stability. MEMS-based Trench-Assisted Surface Channel Technology is designed and developed to realize these large-volume suspended combustor structures.

KEYWORDS

Micro-Combustion; Exothermic Microreactor; Micro-flame Quenching; Trench-Assisted Surface Channel Technology.

INTRODUCTION

Gas exchangeability

The composition of natural gas originating from different countries differs substantially. In the Netherlands, real-time information of the natural gas composition is getting more important since the Dutch gas grid will change with the introduction of biogas, hydrogen and foreign natural gas.What's more, the transition of natural gas payment from per cubic meter to per amount of heat generated also requires precise in-line gas quality monitoring. Gas blends need to be tuned to deliver a constant energy content to the end-users. Wobbe Index is widely used in many countries to reflect the energy content of fuel gases.[1] For any given orifice, all the gas mixtures that have the same Wobbe Index will deliver the same amount of heat and are interchangeable.[2]

Wobbe Index

Wobbe Index is calculated by the Higher Heating Value and the square root of the Specific Gravity of the fuel gas, as shown in equation (1).

$$\text{Wobbe Index} = \frac{\text{Higher Heating Value}}{\sqrt{\text{Specific Gravity}}} \tag{1}$$

Heating values [$\mathrm{MJ\,kg^{-1}}$] of a fuel are used to quantify the maximum amount of heat that can be generated by the fuel combustion with air at the standard conditions (25 °C and 101.3 kPa). The amount of heat release from the fuel combustion will depend on the phase of water in the products. If the product water is in the gas phase, the total heat release value is denoted as the Lower Heating Value (LHV). When the water vapor is condensed to liquid, additional energy equals to the latent heat of water vaporization can be extracted. The value of the total energy release is called the Higher Heating Value (HHV). The value of the LHV and HHV is related by the amount of energy released during the phase change of water between the vapor and liquid, as shown in equation (2):[3]

$$\mathrm{LHV} = \mathrm{HHV} - \frac{N_{\mathrm{H_2O,\,P}} \times M_{\mathrm{H_2O}} \times h_{fg}}{N_{\mathrm{fuel}} \times M_{\mathrm{fuel}}} \tag{2}$$

where $N_{\mathrm{H_2O,\,P}}$ is the number of moles of water in the products and $M_{\mathrm{H_2O,\,P}}$ is the molecular weight of water. Latent heat for water at standard conditions is $h_{fg} = 2.44\ \mathrm{MJ\,kg^{-1}}$. N_{fuel} is the number of moles of fuel burned and M_{fuel} is the molecular mass of the fuel.

Specific Gravity, also called relative density, is defined as the density of the fuel gas divided by the density of dry air of standard composition at the same specified conditions of pressure and temperature.[3]

Higher Heating Value from a constant-volume reactor

For a closed system of the constant-volume reactor, at the standard conditions, the Higher Heating Value of a fuel is calculated as shown in equation (3):[3]

$$\mathrm{HHV} = \frac{-Q^0_{rxn,v} - \left(\sum_i N_{i,\mathrm{P}} - \sum_i N_{i,\mathrm{R}}\right) \times \hat{\mathrm{R}}_u \times \mathrm{T}_0}{N_{\mathrm{fuel}} \times M_{\mathrm{fuel}}} \tag{3}$$

where $N_{i,\mathrm{P}}$ and $N_{i,\mathrm{R}}$ are the number of moles of spieces i in the product and reactant, respectively. $\hat{\mathrm{R}}_u$ is the universal gas constant and T_0 is the standard temperature. N_{fuel} is the number of moles of fuel burned and M_{fuel} is the molecular mass of the fuel. The amount of heat transfer $-Q^0_{rxn,v}$ flows from the combustion system to the environment can be estimated depends on the specific heat exchange mechanism of the reactor, namely convective heat transfer, conductive heat transfer and radiative heat transfer.

DESIGN PRINCIPLES FOR A SMALL-SCALE WOBBE INDEX METER

Miniaturization of Wobbe Index meter

For the central heating systems and fuel gas supplies industries, conventionally available Wobbe Index facilities have large volume of around $1\,\mathrm{m}^3$. Moreover, they cost more than $50,000$€ and consumes large quantities of gas sample to measure the Wobbe Index of the fuel gas. For in-line gas quality monitoring and easy operations in the remote areas, an on-chip Wobbe Index meter[4] shows promising benefits of downscaling both the device size and the energy consumption when comparing to the currently available systems.

Our envisioned integrated Wobbe Index meter consists of a gas density sensor and a small-scaled combustor fabricated by the same MEMS technology. Proof-of-concept for a density sensor has been demonstrated from the micro-Coriolis flow sensor.[5] Here we will discuss the design principles and propose a fabrication technology to realize the small combustor. Future work is planned to design and fabricate a gas density sensor by the same technology.

Our approach to experimentally obtain the HHV value of the fuel gases is by performing complete combustion of the fuel gases on-chip with precise temperature monitoring and in a controlled volume combustion chamber. The combustor chip design consists of mainly three functional parts, namely the mixer, preheater and combustor. Stoichiometric fuel gas and air are first sufficiently mixed in a diffusion-driven mixing channel. Then the well-mixed combustible gas mixture can be preheated to just below the auto-ignition temperature of the fuel gas. Once the complete combustion takes place in the designated combustion chamber, the flame temperature and flame burning velocity can be measured and deduced by the local temperature sensor. Finally, HHV of fuel gases can be further calculated by thermodynamic relations depends on the mechanism of the heat transfer from the hot combustor to the temperature sensor.

However, down-scaling of the combustor sizes introduces new problems, namely the micro-flame quenching phenomena.

Flame propagation

Fuel gas complete combustion with the stoichiometric or excess air is a highly exothermic reaction. The reaction has a self-propagating reaction zone which is also known as flames. The burning velocity and the flame temperature are the two characteristic properties of flames. Flames will propagate through the stationary unburnt gas mixture at a characteristic burning velocity. The velocity of this wave is controlled by both the diffusion of heat and the diffusion of active radicals. In details, a larminar flame propagation in premixed gases has two mechanisms: firstly, the unburnt mixture is conductively heated by the burnt zone and become sufficiently rapid to start self-propagating. Secondly, the active radicals diffuse from the burnt reaction zone to the unburnt mixture and ignite the exothermic reaction. Therefore, both mass and heat diffusion of the active radicals contribute to the propagation of the reaction zone and determines the burning velocity and flame temperature. However, down-scaling of the combustor channel dimensions from macro-sizes to micro-sizes will probably cause flame quenched by the closely-spaced walls.

Down-scaling caused flame quenching

Fuel gas combustion in small-scale channels has been reported to suffer from flame extinction.[6] In the microchannels where the surface-to-volume ratio is so large that the heat loss through the channel wall surfaces to the environment becomes substrantial. Once the heat loss to the surroundings is even larger than the heat generated from the exothermic combustion reaction, the flame or the reaction zone stops propagating in the channel and extinguishes,this is known as the thermal quenching of the micro-flames.[6] Therefore, in order to maintain continuous flame propagation, there exists a threshold where the characteristic channel dimension must be larger than the critical quenching diameter of the fuel gas.[7] Good thermal management of the combustion reactor is crucial to surpress the thermal quenching of the micro-flames. Promising results from the Swiss-Roll combustors[8] have shown that the excess enthalpy or heat recirculation can extend the flame flammability limit to even under the traditionally known critical quenching distance for the fuel gas.

Another down-scaling effect taking place in the small combustion reactors is the radical quenching. When the characteristic channel diameter is not much larger than the mean free path of the reactants molecules, a substantial amount of active radicals would easily diffuse from the homogeneius combustion zone to the surface of the inner walls. These heterogeneous radicals adsorption and recombination at the inner wall surface would cause the flame quenched even when there is little heat loss to the environment.[7] A straightforward solution to minimize the radical quenching is to choose chemically inert channel inner wall materials. Also, temperature of the channel walls plays a major role to control the kinetics of the adsorption, recombination and desorption of the radicals and molecules.

Summary of the combustor design principles

In order to fabricate a small-sized combustor to burn the fuel gas on chip and measure the elevated temperature from the combustion produced heat, it is necessary to maintain a continuous flame propagation without flames extinction induced by thermal quenching or radical quenching. The most important principles for designing a micro-combustor are as follows: Firstly, design a combustion channel with sufficiently large cross-sectional area is the key principle for sustaining a continuous flame propagation. In addition, excess enthalpy can be supplied to the system by heating up the combustor channel walls and preheat the unburnt gas mixtures. Moreover, chemically inert wall material and channel wall temperature tuning is key to reduce radical quenched by the wall. Finally, a reliable and accurate local temperature sensor is essential for in-line monitoring the flame location and burning speed.

TRENCH-ASSISTED SURFACE CHANNEL TECHNOLOGY

We developed a micromachining fabrication process called Trench-Assisted Surface Channel Technology (TASCT) to realize such a micro-combustor with a large internal volume. TASCT is evolved from the concept of the Surface Channel Technology[9][10] developed for the micro-Coriolis chips, where the silicon wafer is isotropically etched through the small-slit pattern to create channels right underneath the surface of the wafer.

These surface channels have the cross-sectional shape of a partially circular channel with a flat top, the channel size and shape are determined by the designed slits pattern. Channels with diameter around 300 µm can still be made by the Surface Channel Technology. However, the mechanical stability are likely to decrease once the channel diameter becomes larger. In order to make channels with larger cross-sectional area, we introduce new features of high aspect-ratio trenches into the Surface Channel Technology concept.

The TASCT process requires a SOI wafer and all the channels are realized in the device layer. The fabricated channels and chambers have a rectangular cross-section, as illustrated in Figure 1 of a SOI wafer with cross-sectional view. The height of the channel side walls is 50 µm, which is defined by the device layer thickness of the SOI wafer. Surface channels of any desired planar shape and dimension can be achieved through the combination of the high aspect-ratio refilled trenches and the Surface Channel technology. SOI wafer is heavily doped and the silicon heaters are defined by the 3 µm wide trenches to heat up the chamber side walls. Platinum heaters and temperature sensors are placed on top of chamber to heat up the chamber roof membrane and sense the temperature variation. To provide thermal isolation, large cavities can be made underneath and to the sides of the combustion chamber. Flexure structures are made of channels across the side cavities and they are not depicted here.

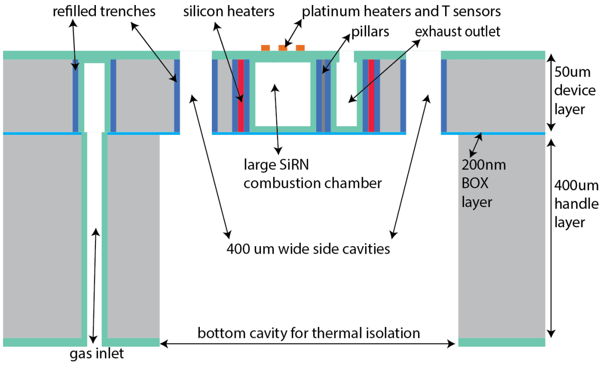

Figure 1: Schematical cross-sectional view of a suspended large-volume combustion chamber using TASCT fabrication process, key features are indicated in the illustration.

A more detailed description of TASCT can be found in the MFHS extended abstract submission from H.-W. Veltkamp with the title ”Fabrication of Large-Volume Rectangular Channels using Trench-Sidewall Technology and A SOI Substrate”.

CONCLUSION AND FUTURE WORK

In conclusion, we discussed the motivation of developing a miniaturized Wobbe Index meter. Flame quenching phenomena in the small channels drive us to discover the principles when designing the micro-combustor suitable to have continuous combustion of the fuel gas. We also developed an innovative fabrication method TASCT to realize a large-volume combustor channel with good thermal management and strong mechanical strength from a SOI wafer. Future work will be continuing the fabrication of a complete Wobbe Index meter with the integration of all the fluidic connections and heat management electronics to perform fuel gas combustion on the chip.

ACKNOWLEDGEMENT

This work is part of the research programme Integrated Wobbe Index Meter with project number 13952, which is (partly) financed by the Dutch Technology Foundation STW, which is part of the Netherlands Organisation for Scientific Research (NWO).

REFERENCES

[1] Union, I. G. (2011). Petroleum B. guidebook to gas interchangeability and gas quality.

[2] Zachariah-Wolff, J. L., Egyedi, T. M., and Hemmes, K. (2007). From natural gas to hydrogen via the Wobbe index: The role of standardized gateways in sustainable infrastructure transitions. International journal of hydrogen energy, 32(9), 1235-1245.

[3] McAllister, S., Chen, J. Y., and Fernandez-Pello, A. C. (2011). Fundamentals of combustion processes. New York: Springer.

[4] Lötters, J. C., Lammerink, T. S., Pap, M. G., Sanders, R. G., de Boer, M. J., Mouris, A. J., and Wiegerink, R. J. (2013, January). Integrated micro Wobbe index meter towards on-chip energy content measurement. In Micro Electro Mechanical Systems (MEMS), 2013 IEEE 26th International Conference on (pp. 965-968). IEEE.

[5] van der Wouden, E., Groenesteijn, J., Wiegerink, R., and Lötters, J. (2015). Multi parameter flow meter for on-line measurement of gas mixture composition. Micromachines, 6(4), 452-461.

[6] Ju, Y., and Xu, B. (2005). Theoretical and experimental studies on mesoscale flame propagation and extinction. Proceedings of the Combustion Institute, 30(2), 2445-2453.

[7] Maruta, K. (2011). Micro and mesoscale combustion. Proceedings of the Combustion Institute, 33(1), 125-150.

[8] Ju, Y., and Choi, C. W. (2003). An analysis of sub-limit flame dynamics using opposite propagating flames in mesoscale channels. Combustion and Flame, 133(4), 483-493.

[9] Groenesteijn, J., de Boer, M. J., Lötters, J. C., and Wiegerink, R. J. (2017). A versatile technology platform for microfluidic handling systems, part I: fabrication and functionalization. Microfluidics and Nanofluidics, 21(7), 127.

[10] Dijkstra, M., De Boer, M. J., Berenschot, J. W., Lammerink, T. S. J., Wiegerink, R. J., and Elwenspoek, M. (2007). A versatile surface channel concept for microfluidic applications. Journal of Micromechanics and Microengineering, 17(10), 1971.

CONTACT

* Yiyuan Zhao, y.zhao-5@utwente.nl

ULTRAMINIATURE PH ISFET WITH BACK SIDE CONTACTS AND TA$_2$O$_5$ GATE MATERIAL FOR USE IN A GUIDEWIRE TIP

A. Prak[1], *H.H. van den Vlekkert*[1] *and M.-A. Levine*[2]
[1] LioniX International, Enschede, the Netherlands
[2] Makaha Medical LLC, Pottstown, PA 19465, USA

ABSTRACT

We fabricated ultraminiature ISFETs with backside contacts and a Ta_2O_5 gate. The chips fits in a catheter tip with an internal diameter of 0.3 mm which will be inserted into the brain vasculature to monitor patients suffering from stroke. To fabricate the ISFET we used through silicon vias based on IceMOS TSV technology, ion implantation and backgrinding, thermal oxidation and Tantalum evaporation and oxidation. The behavior of the vias was as expected. The ISFET were measured on a wafer which has undergone exactly the same processing, except for the vias. The Ta_2O_5 ISFETs have almost Nernstian response and very low drift.

INTRODUCTION

Since the invention of the ISFET (Ion Sensitive Field Effect Transistor) by Bergveld in 1970 [1] a large number of technologies for ISFET fabrication and ISFET applications have been developed. A number of vendors offer ISFETs on the market (e.g. Sentron, Mettler Toledo, Honeywell, Fisher Scientific, Endress + Hauser). Typically, the commercial ISFETs are mounted in a probetip either with or without an integrated reference electrode. ISFETs, being solid state devices, offer advantages over their counterparts, pH glass electrodes, in terms of size, mechanical robustness, chemical resistance and ease of maintenance.

Motivated by the fact that continuous pH monitoring is critical for patients suffering from stroke or severe head injury, we pursue a solution to mount an ISFET in a guidewire tip with an ID (inner diameter) of 300 µm for use in the brain vasculature. A chip of such a small size requires a BSC (back side contact) approach because the packaging of an ISFET with front side contacts would be too space consuming, especially the separation of the part exposed to the sample and the dry, electronic part composing the bondpads.

A number of approaches to fabricate BSC-ISFETs have been published through the years. An overview is given in [2]. Most BSC technologies are based on the anisotropic wet etching of the silicon substrate from the backside to achieve an electrical contact with the bottom of the implanted source and drain regions on the front side. Issues associated with this approach are the process compatibility to a CMOS-grade process, the need to perform lithography on a surface with large topography and the relative large footprint caused by the inclined sidewalls of the anisotropically etched contact holes. These issues also exist in an 'inverted' approach based on bonding and etchback in which the gate is positioned in the etched recess and the electrical contacts are on the front side of the wafer [4,5].

Our requirements of a smaller footprint and a CMOS compatible process forced us to explore the possibilities to realize electrical vias by DRIE (Deep Reactive Ion Etching). DRIE became a mature process when the Bosch process was introduced in the mid-90's by Larmer and Schlip [6]. With the Bosch process, it is possible to realize throughholes in a wafer with almost vertical sidewalls and with a very high aspect ratio by cycling of an etching process based on SF6 and a passivation process based on C_4F_8. To our knowledge, the use of DRIE etching for BSC-ISFETs has been very limited. One example is by Ingebrandt et al. [7]. They realized backside contacts by deep reactive ion etching of circular holes with a diameter of 100-150 µm and doping the sidewalls of the holes by gas phase boron doping from planar diffusion sources. They flip-chip bonded the gold plated back side contacts of the ISFET array on a standard 22 pin DIL package. The chip was extremely delicate because in their process the DRIE stopped on a thin dielectric membrane and the contact holes were not filled.

FABRICATION

To fabricate our n-channel BSC-ISFETs we made use of the IceMOS TSV process. IceMOS (Belfast, Northern Ireland) delivered to us a customized substrate with through wafer interconnects of 35 x 70 μm^2 and a resistivity of 0.005 Ω·cm in a p-doped substrate of 5 – 10 Ω·cm. The interconnects are performed using through wafer DRIE etching, sidewall oxidation, and refill of heavily n-doped polysilicon. The substrate is fully CMOS compatible and stable up to temperatures of 1200 ˚C which allows post-via ISFET fabrication including diffusion of source/drain implantations and formation of the gate oxide. After backgrinding to 200 µm and CMP (Optim Wafer Services, Gréasque, France) we obtained substrates as shown in Fig. 2a. To obtain an electric isolation on the backside of the wafer and to form a barrier for the outdiffusion of Phosphorous from the vias during the subsequent high temperature steps, we deposited an SiO_2 layer by LPCVD using TEOS as a precursor (Fig. 2b). Next, a 100 nm screen oxide is grown and wafers undergo Boron and Phosphorous implantations (IBS, Peynier, France) to define the channel stopper and the source/drain areas (Fig. 2c). To realize the gate, the oxide is etched open and a dry CMOS grade gate oxide is grown (80 nm, 1050 ˚C) followed by evaporation, oxidation and annealing of Ta to obtain an ISFET with Ta_2O_5 as the top gate dielectric (Fig 2d). Ta_2O_5 is a gate dielectric known for its superb properties such as almost Nernstian sensitivity (56-58 mV/pH), wide pH range (pH 2-12) and low drift. Finally, contact holes to the vias (front side as well as back side) and source/drain areas are etched using an RIE process for the Ta_2O_5 layer and a BHF etch for the SiO_2, followed by sputtering and patterning of an aluminum (1% Si) layer for interconnects between the source/drain areas and the vias on the front side and the bondpads on the backside (Fig. 2e). A picture of the ISFET is shown in Fig. 3.

The ISFET chip includes an ESD protection electrode connected to a diode to protect the gate against breakdown as a result of electrostatic charge.

The size of the fabricated chips is 0.23 x 1.00 x 0.20 mm^3 (w x l x t) which results in approx. 20.000 chips on a single 100 mm wafer. As far as we know this is the smallest ISFET chip ever made.

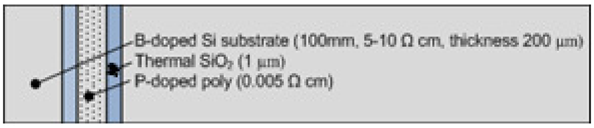

(a) Wafer cross section after realization of interconnects and backgrinding

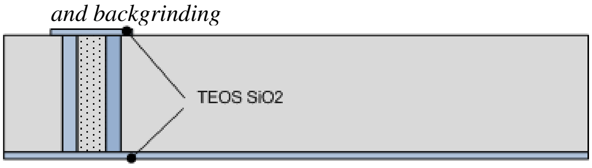

(b) After SiO_2 TEOS deposition (diffusion barrier and isolation)

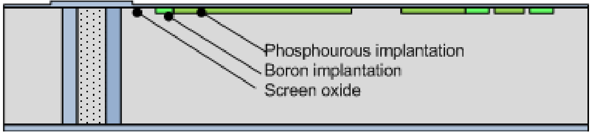

(c) After implantation the source/ drain areas and the channel stopper

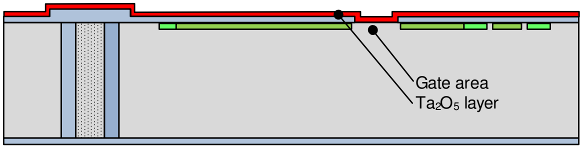

(d) After growing the gate oxide and deposition of Ta_2O_5.

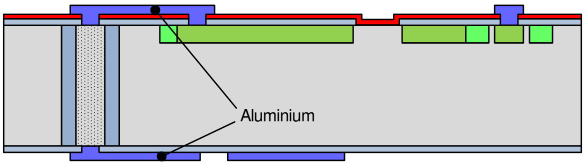

(e) After etching contact holes and aluminum deposition on front side and back side.

Fig. 2. Fabrication process of the BSC-ISFET with Ta_2O_5 gate.

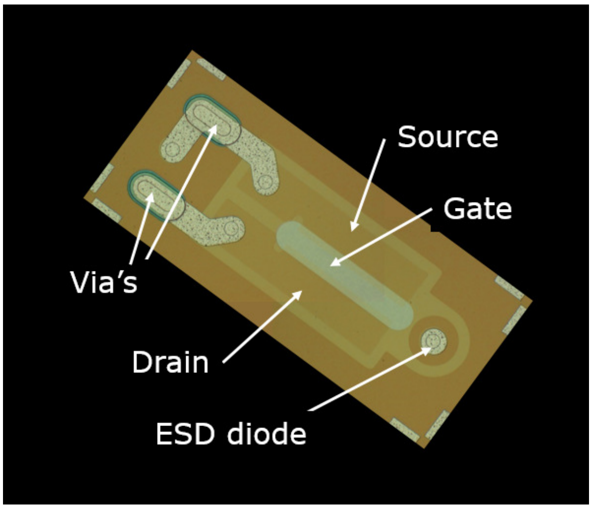

Fig. 2. ISFET chip

RESULTS

Vias

We measured via characteristics such as the via resistance and the isolation of the via from the substrate. Results are shown in Fig. 3.

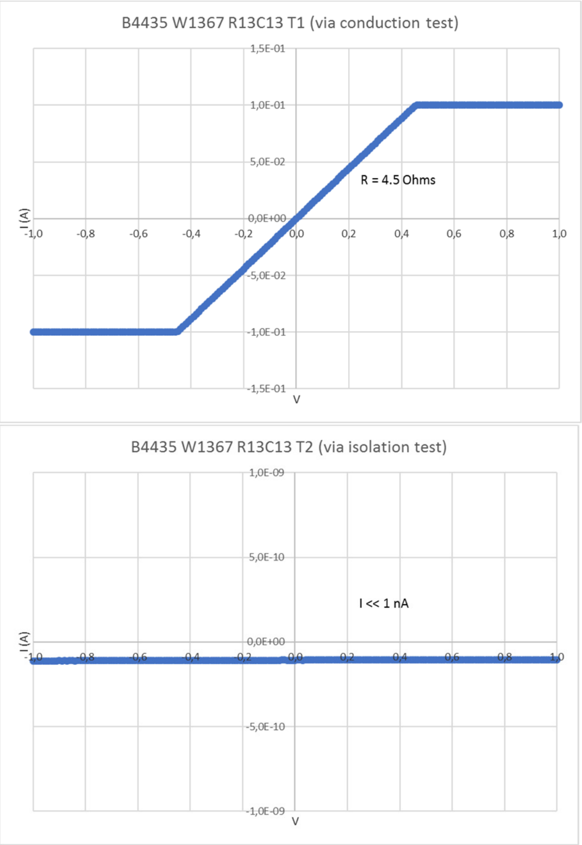

Fig 3. Impedance plots of 2 vias in series (top) and between 2 vias which are not connected, showing that the via resistance is 2,25 Ohms, and the leak current through the liner oxidation < 1 E^{-10} A.

ESD Diode

The diode characteristic of the ESD diode was measured and is shown in fig. 5. The diode closes in the operating range of the ISFET (I leak < 1 nA) and conducts to the substrate at voltages < -0.5 V)

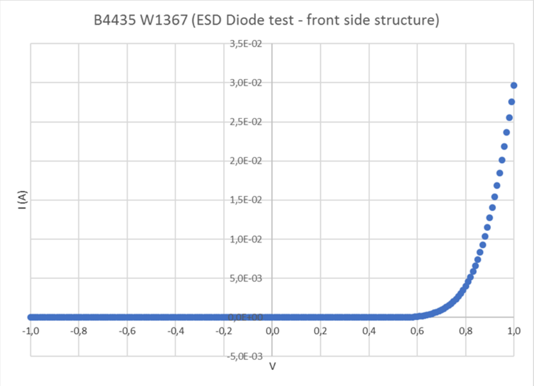

Fig 5. Diode I-V curve of the ESD diode. The leak current in reverse $i_{leak} < 1$ *nA.*

MOSFET

The FETs on the wafer were not working as we expected. After investigating the process and equipment carefully, we found that a cross contamination had occurred in one of the furnaces, resulting in a slight n-doping on the surface of the wafer, including the channel area of the FET which is supposed to be p-doped. In the past we have fabricated identical Ta_2O_5 ISFETs without vias which not suffered from this problem, and therefore we will show the results of those MOSFETS and ISFETs. We expect to obtain the same results from the wafers with vias once the cross-contamination issue has been solved.

Fig 6 shows the Vg-Ids curves of a number of MOSFETs at Vds = 0.5 V. The curves show a very steep response in the threshold region, opening at Vg = 0V and (Ids < 0,1 µA) and having their working point (1 ds = 100 µA) at Vg = 0.5 V.

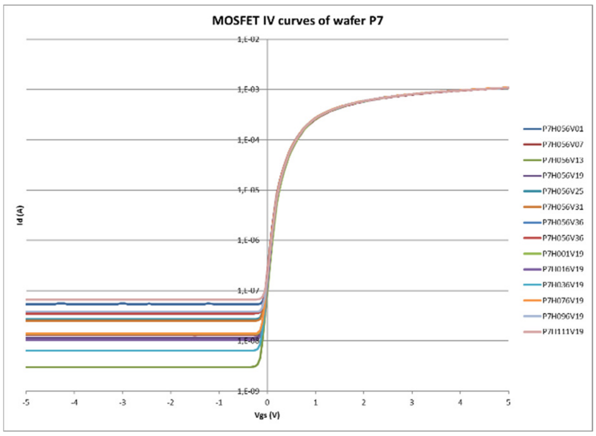

Fig 6. Vg-Ids curves of a number of MOSFETs at Vds = 0.5 V.

ISFET

We measured the most important ISFET characteristics: sensitivity, drift and dVgs/dT as follows:

We mounted 7 ISFETs on a dipstick by means of an epoxy, completely covering the chips and wirebonds, leaving only open the gate area. We measured the ISFET against an Ag / AgCl reference electrode in a temperature controlled bath. The used ISFET Amplifier (type source follower, manufactured by P. Bergveld) was used at operating conditions Vds = 0.5V and Ids= 100 µA. The common Ag/AgCl was kept at ground, and Vgs was used as the readout signal. The Amplifier is capable of controlling 10 channels simultaneously.

The sensitivity was measured by immersing the ISFETs in buffers of pH 4, 7 and 10 and allowing sufficient time for stabilization of the temperature (30 ˚C). We found a sensitivity of almost 59 mV/ pH at 30 ˚C which is close to the maximum set by the Nernst Equation.

The drift was measured by monitoring the gate - source voltage during 72 hours at constant temperature in the dark. We observed a drift of some mV in the first 6 hours, which reduced to less than 1 mV between 6 and 72 hours (fig. 7.

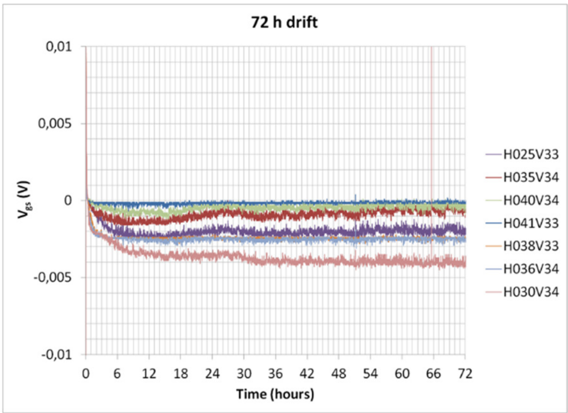

Fig 7. Measured drift rate of 7 ISFETs

At the used setting of Id = 100 µA, the response Vgs depends on temperature. An operating point for which Vgs / dT = 0 results in an ISFET with zero temperature effect on the read-out value, which obviously has many advantages. To find the isothermal operating point we varied Ids from 10 to 100 µA in 5 steps and Vds from 0.1 to 1.0 V (4 steps). For each combination of Id and Vds we measured the response to pH7 at 30 and at 40 ˚C. We found the isothermal operating point at Id = 20 µA being independent of Vds (Fig 8.).

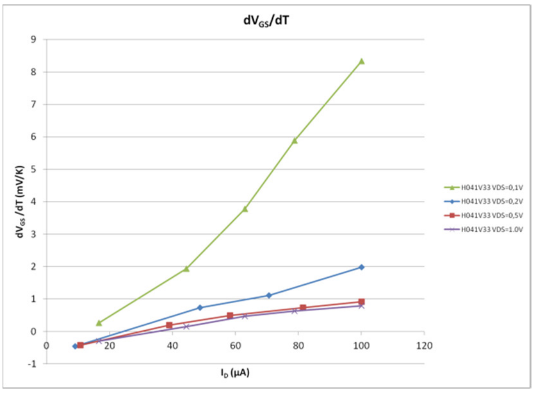

Fig 8. Temperature dependence of the read-out signal Vgs at various values of Id and Vds (--Vds=0.1V; --Vds=0.2V; -- Vds=0.5V;-- Vds=1.0V).

The measured ISFET characteristics are summarized in Table 1.

Table 1. ISFET characteristics

Parameter	**Value**
Sensitivity (pH 4-10, T=30˚C)	58.8 ± 0.2 mV/pH
Offset (pH 7, T=30˚C)	332 ± 50 mV
Drift (0 to 6h)	0.2 ± 0.2 mV
Drift rate (6 to 72h)	< 0.02 mV/h
Isothermal current (dVg/dT =0)	Id = 20 µA

CONCLUSIONS

We fabricated miniature ISFETs with backside contacts to be used in a guidewire tip which will be inserted into the brain vasculature of patients suffering from stroke.

The first process run of these ISFETs was only partially successful because a cross contamination issue in one of the furnaces occurred and caused a shallow doping of the n-type in the p-channel, preventing the ISFETs to work.

Measurements on ISFETs from a similar wafer with an identical ISFET process, but without the vias show very good characteristics: Sensitivity 59 mV /pH at 30 ˚C, drift < 0.02 mV/h after stabilization of 6h and an isothermal operating point at Ids = 20 µA.

REFERENCES

[1] Bergveld P. Development of an Ion-Sensitive Solid-State Device for Neurophysiological Measurements. *IEEE Trans. Biomed. Eng*. 1970

[2] Cane C., Gracia I., Merlos A. Microtechnologies for pH ISFET Chemical Sensors. Microelectron. J. 1997;28(4):389–405.

[3] H.H. Van den Vlekkert, B. Kloeck, D. Prongue, J. Berthoud, B. Hu, N.F. de Rooij, E. Gilli and P.H. de Crousaz, A pH-ISFET and an integrated pH-pressure sensor with back-side contacts, Sensors & Actuators, 14, (1988) 165-176.

[4] H. Yagi and T. Sakai, Rear-gate ISFET with a membrane locking structure using an ultrahigh concentration selective boron diffusion technique, Sensors &Actuators B, 13-14 (1993) 212-216.

[5] A.S. Poghossian, Method of fabrication of ISFETs and CHEMFETs on a SiSiOESi structure, Sensors & Actuators B, 13-14 (1993) 653-654.

[6] F. Lärmer, A. Schlip, A Method of Anisotropically Etching Silicon, Licensed from Robert Bosch GmbH: US Patent No. 5,501,893 (1996).

[7] S. Ingebrandt, C.K. Yeung, W. Staab, T. Zetterer, A. Offenhausser, Backside contacted field effect transistor array for extracellular signal recording, Biosensors and Bioelectronics 18 (2003), 429-435.

MICRO CORIOLIS MASS FLOW SENSOR DRIVEN BY EXTERNAL PIEZO CERAMIC

Y. Zeng[1]*,J. Groenesteijn*[1,2]*,D. Alveringh*[1]*, R.J. Wiegerink*[1] *and J.C. Lötters*[1,2]
[1] MESA+ Institute for Nanotechnology, University of Twente, Enschede, The Netherlands
[2] Bronkhorst High-Tech BV, Ruurlo, The Netherlands

ABSTRACT

We have realized a micro Coriolis mass flow meter driven with an external piezo ceramic. The piezoelectric ceramic is glued on top of sensor chip with a inetrial weight on top of the piezo ceramic. Its ability to measure mass flow is characterized by a laser Doppler vibrometer. Our measurement with water from 0 to 10 ml/h confirms that the sensor response is linear .

KEYWORDS

Micro Coriolis mass flow meter, piezoelectric actuation, Microfluidics, Resonator

INTRODUCTION

Micro fluidic systems have gained interest in lots of fields e.g. medical instrumentations [1], micro reactors [2] and chemical analysis systems [3]. Flow control and flow measurement are critical components for micro fluidic systems.

A Coriolis mass flow meter is a preferred option for flow measurements because of its ability to measure flow rate regardless of fluidic property. Conventional Coriolis flow meters are taking an ever increasing share of the flow meter market. However, there is currently no commercially available Coriolis flow sensor that occupy small space and measure very low flow. Micro Coriolis flow meters in research are driven by either electrostatic force [4] or Lorentz force [5]. However, electrostatic actuation requires high voltage while Lorentz actuation results in Joule heating. Using piezoelectric actuation evades these drawbacks.

THEORY AND DESIGN

A Coriolis mass flow sensor consist of a vibrating flow channel, as shown in Figure 1. In this work, the piezo ceramic actuate the flow channel to vibrate in swing mode as shown by the red arrows in Figure 1. When a mass flow through the channel as indicated by the blue arrow, the induced Coriolis force F_c can be written as:

$$F_c = -2L(\omega \times \phi_m) \qquad (1)$$

where L represent the height of the triangle as indicated in Figure 1. ω is the angular velocity of the swing motion. According to the equation, the direction of the Coriolis force at the left side of the channel is antiparallel to the direction of the swing motion, while direction of Coriolis force at the right side of the channel is parallel to the the direction of the swing motion. The Coriolis force will generate a twist motion that has the same frequency as the swing motion.

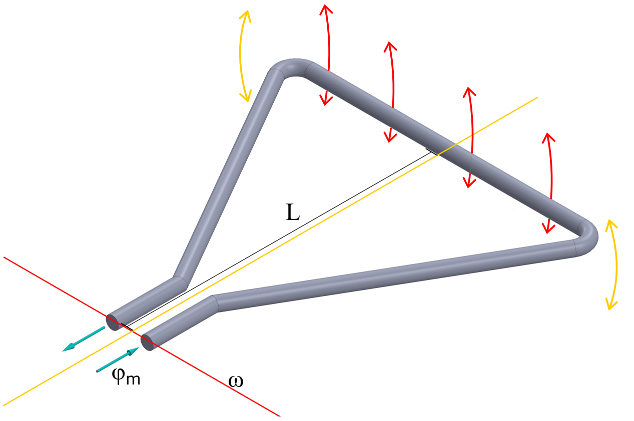

Figure 1: Schematic operating principle of a Coriolis flow meter. The fluidic channel is actuated in the swing mode indicated by the red arrows. The twist mode caused by Coriolis force is indicated by the yellow arrows. The rotation axis of swing and twist motion is showen in rad and yellow line respectively. The blue arrows indicate the liquid flow. The channel is fixed on its two ends.

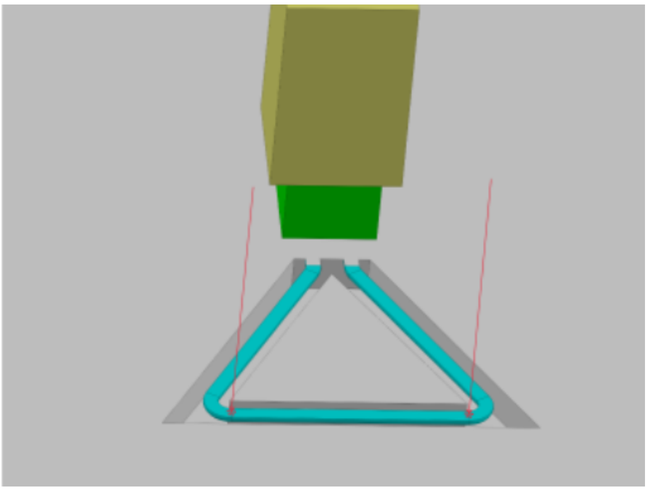

Figure 2: Schematic of the chip with sensor and inetrial weight. The inetrial weight is shown in yellow. The piezo ceramic is shown in green. The microfluidic channel is shown in blue. The red lines indicate the laser from laser Doppler vibrometer when measure the flow versus twist relation

Figure 2 shows the setup of the sensor chip and piezo actuator with inertial (counter) weight on top. Piezo actuator, shown in green, drive the chip. This configuration can excite different resonant modes of the microfluidic channel depending on the frequency of the signal applied to the piezo actuator. This configuration also generate a lot of noise when working. Figure 3 shows a photo of the device.

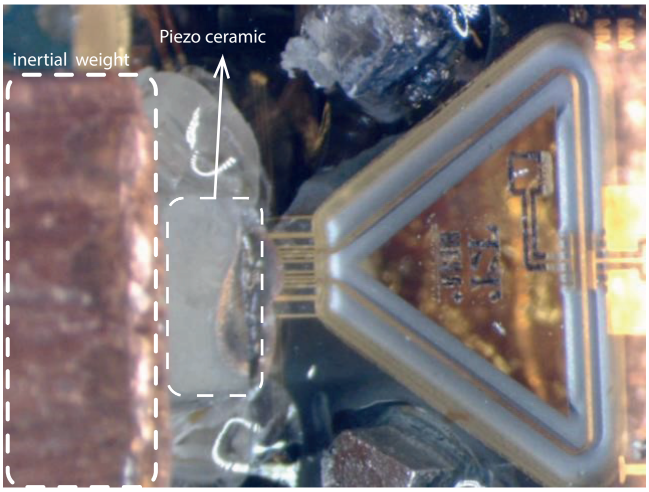

Figure 3: Photograph of chip with piezo actuator and inetrial weight

FABRICATION

The device fabrication process has been reported in [6]. The schematic of the fabrication process is shown in Figure 4. The first process step consist of depositing a 500 nm thick layer of silicon rich silicon nitride (SiRN) on the wafer. Then a layer of chromium is sputtered on top of the SiRN layer. The chromium and SiRN layers are patterned with a slit pattern that defines the channel outline. Then we use isotropic plasma etching to remove silicon through the slits to form microfluidic channel. Then both the the chromium and photo resist are removed. This results in a cross section shown in Figure 4(a). Then a silicon-dioxide layer is deposited using LPCVD. The wafer is then etched from the back side with deep reactive ion etching. These two processes are shown in Figure 4(b) and (c) respectively. After this, silicon dioxide layer is removed and a 1.8 µm SiRN layer is deposited. Then a 10/200nm Cr/Au layer is deposited and patterned. The cross section after this step is shown in Figure 4 (d). The last step is to release the channel. This is done by etching openings in the SiRN and then isotropically etching the exposed silicon. The cross section of the chip after fabrication is shown in Figure 4 (e).

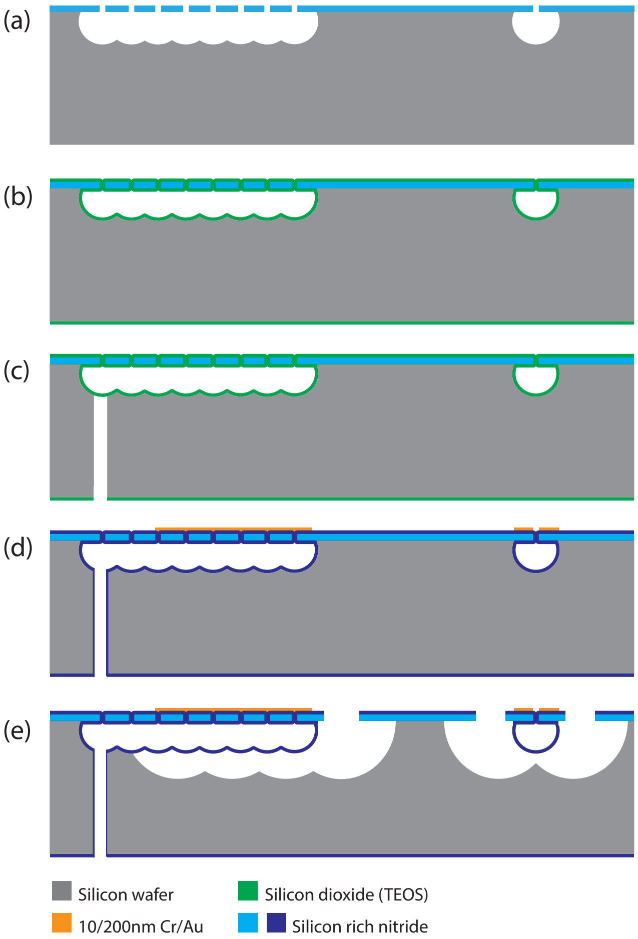

Figure 4: Schematic cross section of the fabrication process. The left side shows a cross-section along the length of a channel while the right side shows a cross-section perpenticular the the channel

After mounting the chip and a fluidic connector on a printed circuit board, a piece of Noliac NAC2001 piezo ceramic was glued on the top of the chip, close to the microfluidic channel, as shown in Figure 2. The piezo ceramic is a piezo stack. Electric connection is made using silver paste. A piece of 5×4×19 mm copper inertial weight was glued on the top of piezo ceramic.

MEASUREMENT SETUP

A Polytec MSA-400 laser Doppler vibrometer was used to characterize the device. All measurements was down when the micro channel is filled with water. A sinusoidal or chirp signal with 4V bias and 2V amplitude was used to drive the piezo ceramic. The bias is applied to avoid shifting of the pooling direction of the piezo ceramic. The referenece beam is placed at a fixed reference point druing normal measurement in order to measure the vibration of micro fluidic channel. In the flow measurement, we use 1390Hz sinusoidal signal to actuate the mode shown in Figure 6. When measuring the twist mode induced by Coriolis force, the measurement and reference beam of the laser Doppler vibrometer is placed as shown in Figure 2. In this setup, only the relative displacement between the two measurement points are detected.

RESULT AND DISCUSSION

Figure 5 and 6 shows two modes we measured using a laser Doppler vibrometer when device was driven with sinusoidal signal. The frequency of signals were 8716Hz and 1390Hz respectively. The piezo ceramic can actuate different modes depending on the frequency of the signal.

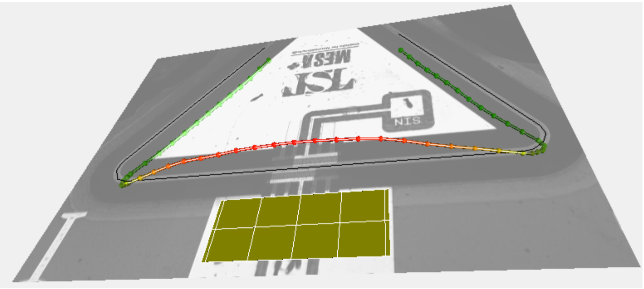

Figure 5: Measured resonance at 8716Hz, the microfluidic channel bend from the middle. there are two static points in resonence process

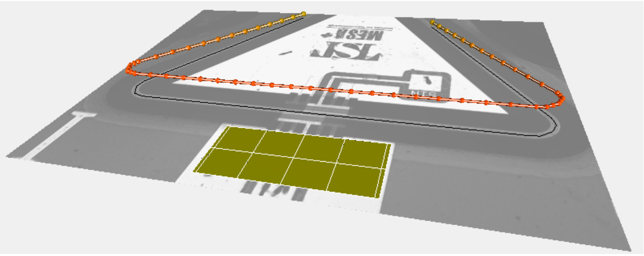

Figure 6: Measured resonance at 1390Hz, there is no static point on channel

Figure 7 show an averaged resonance amplitude between 1000 and 10000 Hz when the chip is driven using chirp signal. First and second highest peak in this figure shows the resonance modes in figure 5 and 6. The mode at 8716Hz has a higher resonance amplitude. This can be explained by the fact that we use an inertial weight to fix the top surface of the piezo ceramic. Thus the frequency of signal influences the force that the piezo ceramic applies on the silicon chip.

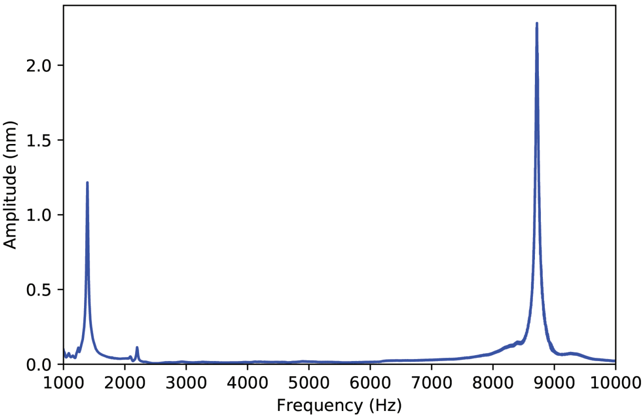

Figure 7: Average spectrum of all the measurement point when the chip is driven using chirp signal

Figure 8 shows a measured twist amplitude as a function of water flow for a range of 0 to 10 mL/h. The resonence amplitude of micro fluidic channel is 2.6 μm. The flow is generated with a syringe pump. A linear relationship between the flow rate and the twist resonence amplitude can be observed.

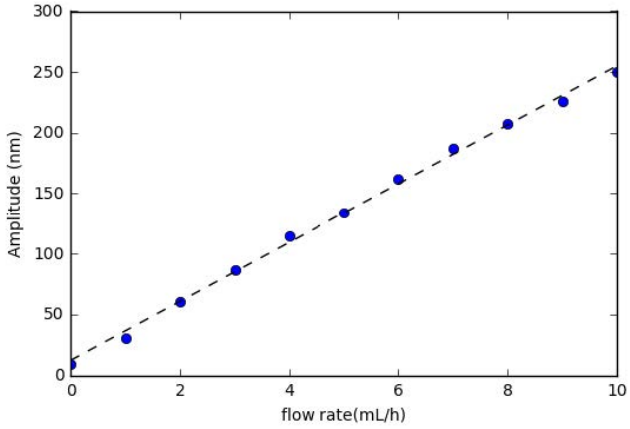

Figure 8: Measured twist amplitude as a function of water flow

CONCLUSIONS AND OUTLOOK

A micro Coriolis flow sensor driven with an external piezo ceramic was presented. The sensor showed a linear response to flow between 0 and 10mL/h. Current device generates a lot of noise when working. Furthermore, the external piezo ceramic and inertial weight will possibly cause difficulties in chip packaging. The next development will focus on integrated piezo actuation and capacitive readout.

REFERENCES

[1] D. Figeys and D. Pinto, "Lab-on-a-Chip: A Revolution in Biological and Medical Sciences.," *Analytical Chemistry*, vol. 72, no. 9, pp. 330 A–335 A, 2000.

[2] K. S. Elvira, X. C. i Solvas, R. C. R. Wootton, and A. J. DeMello, “The past, present and potential for microfluidic reactor technology in chemical synthesis,” *Nature Chemistry*, vol. 5, no. 11, pp. 905–915, 2013.

[3] J. Huang, H.-P. Chou, and M. A. Unger, “Microfluidic chromatography,” 2004.

[4] P. Enoksson, G. Stemme, and E. Stemme, “A silicon resonant sensor structure for coriolis mass-flow measurements,” *Journal of Microelectromechanical Systems*, vol. 6, no. 2, pp. 119–125, 1997.

[5] W. Sparreboom, J. van de Geest, M. Katerberg, F. Postma, J. Haneveld, J. Groenesteijn, T. Lammerink, R. Wiegerink, and J. Lötters, “Compact Mass Flow Meter based on a Micro Coriolis Flow Sensor,” *Micromachines*, vol. 4, pp. 22–33, mar 2013.

[6] J. Haneveld, T. S. J. Lammerink, M. J. de Boer, R. G. P. Sanders, A. Mehendale, J. C. Lötters, M. Dijkstra, and R. J. Wiegerink, “Modeling, design, fabrication and characterization of a micro Coriolis mass flow sensor,” *Journal of Micromechanics and Microengineering*, vol. 20, no. 12, p. 125001, 2010.

EXTENDING THE ACCREDITED LOW FLOW LIQUID CALIBRATION RANGE

T.H. Platenkamp[1], *J.C. Lötters*[1,2]
[1] Bronkhorst®, Ruurlo, The Netherlands
[2] University of Twente, Transducers Science and Technology, Enschede, The Netherlands

ABSTRACT

There is an increasing demand for ISO/IEC 17025:2005 accredited liquid flow calibrations in the range of 1 g/h to 30 kg/h. The accredited Low Flow liquid Calibration Setup [1] (LFCS) at Bronkhorst® covers a flow range of 1 to 200 g/h, leaving a traceability gap in the flow range of 0.2 to 30 kg/h. By extending the calibration setup with two new balances it can perform calibrations from 1 g/h to 30 kg/h, thus covering the traceability gap. Crosschecks between references show good consistency and the setup extension was successfully accredited for ISO/IEC 17025:2005 calibrations. By participating in an intercomparison with National Metrology Institutes (NMI's) the uncertainty of the LFCS extension is traceable to European NMI's.

KEYWORDS

Calibration, gravimetric, micro flow, uncertainty

INTRODUCTION

The importance of ISO/IEC 17025:2005 accredited calibrations cannot be overstated. The ISO/IEC 17025:2005 standard ensures the calibrations and reference equipment is traceable to its primary standard, which represents the fundamental unit. Low flow instruments depend on a traceable uncertainty to perform well in critical applications were knowledge of the exact flow rate is crucial, e.g. critical applications like drug delivery systems and pharmaceutical processes in which the stable delivery and exact amount of drugs plays a key role in successful treatment.

By extending our LFCS to flow rates up to 30 kg/h, we can calibrate flowmeters in a wider flow range that are used in applications were accredited traceability of the flow rate is required. For flow rates above 200 g/h the LFCS is expanded with two balances. Some critical parts needed to be added to the setup in terms of flow generation and evaporation prevention. An uncertainty budget is made to provide the extension with a traceable uncertainty on mass flow.

PRINCIPLE

Both the LFCS for flow rates below 200 g/h and the extension of the setup for flow rates above 200 g/h are based on the gravimetric principle of mass flow measurement, where a balance is used as reference. By differentiating the measured mass (Δm) to measured time (Δt) the resulting output is mass flow ($\dot{m}$), as shown in equation 1 below:

$$\dot{m} = \lim_{\Delta t\to 0}\frac{\Delta m}{\Delta t} = \frac{m_r}{t_r} \qquad (1)$$

where m_r and t_r are respectively the reference mass and reference time. With a RS232 balance interface between balance and data acquisition each collected mass sample on the balance is continuously measured and combined with the correct time sample, resulting in a reference mass flow. The continuous collection of mass samples during a flow measurement is called "dynamic weighing" method [2] and enables the direct comparison between reference- and DUT (Device Under Test) mass flow.

SETUP

The extension of the LFCS consists of a pump, filter, degasser and pressure controller for generation of a pure liquid flow (Figure 2). Upstream from the pure liquid flow generation, the DUT controls a stable flow. Downstream from the DUT the flow rate is compared with one of two reference balances, depending on the flow rate (see Figure 1). Reference 1 is a balance used to measure flow rates between 0.1 kg/h and 2 kg/h. Reference 2 is used to measure flow rates between 1 kg/h and 30 kg/h. The flow range is divided over two balances because of the limitations on readability versus weight capacity of the balance.

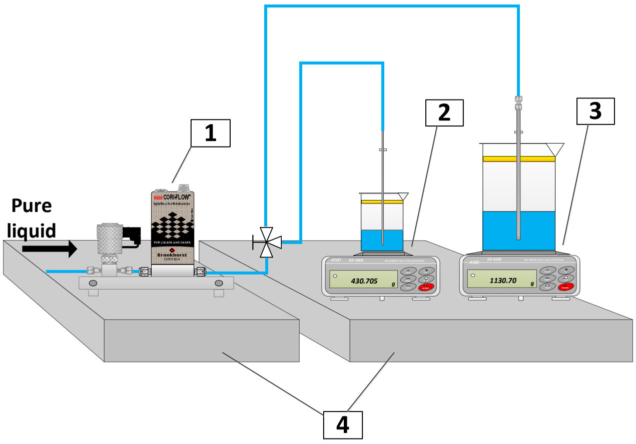

Figure 1. Schematic illustration of the extension setup for comparison between the DUT with control valve(1), balance reference 1(2) and -2(3). Balance and DUT are placed on a granite table(4).

Both the balances and DUT are placed on a granite table with shock absorbing blocks to reduce vibration interference from the environment. The balances are placed in a box to prevent influences of draft and fast temperature changes on the mass flow measurement.

Although the LFCS and its extension are similar, in terms of mass collection and data processing, there is a difference in stable flow generation and evaporation prevention.

Micro pump flow generation

First, in the LFCS (for flow rates <200 g/h) flow is generated by a pressurized liquid tank in an open loop system. In the extension of the setup (for flow rates >200 g/h) pumps are used to generate flow in a closed loop system, making it easier- and faster to handle the amount of water displaced. Figure 2 shows a schematic of the pump driven flow generation. The pump builds up pressure at a constant pump frequency. Downstream from the pump the liquid is filtered and the flow path splits in a flow path for flow measurement and a bypass. The bypass leads back to the water storage tank and acts as a flow stabilizer, by actively controlling the bypass valve to the demanded pressure. Downstream from the pressure sensor the water is pushed through a degasser for flow rates up to 2 kg/h, removing dissolved gas from the liquid.

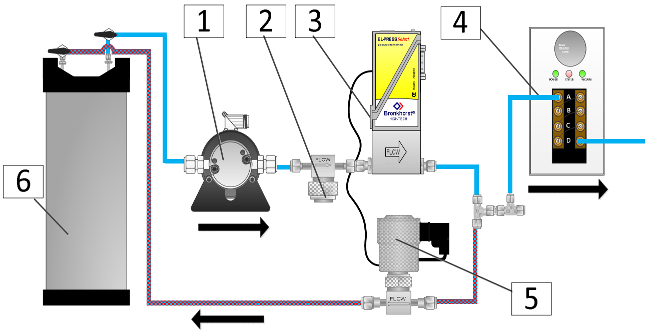

Figure 2. Schematic of pump driven flow generation with pump(1), filter(2), pressure sensor(3), degasser(4), bypass control valve(5) and liquid storage tank(6).

Evaporation prevention

Second, in the LFCS a layer of oil is used on top of the water surface to prevent evaporation of the collected water in the measurement beaker on the balance. Though prevention by a layer of oil on the water surface is suitable for flow rates below 200 g/h, it causes irregularities in the reference mass flow at flow rates above 200 g/h. By using a sealed cover on the measurement beaker (Figure 3) in the setup extension, instead of an oil layer on the water surface, these irregularities are not present. The tube that dispenses the liquid in the measurement beaker runs freely through a small hole in the cover. The use of a sealed cover results in a nearly saturated air between cover and water surface in the measurement beaker, thus reducing and stabilizing the evaporation rate.

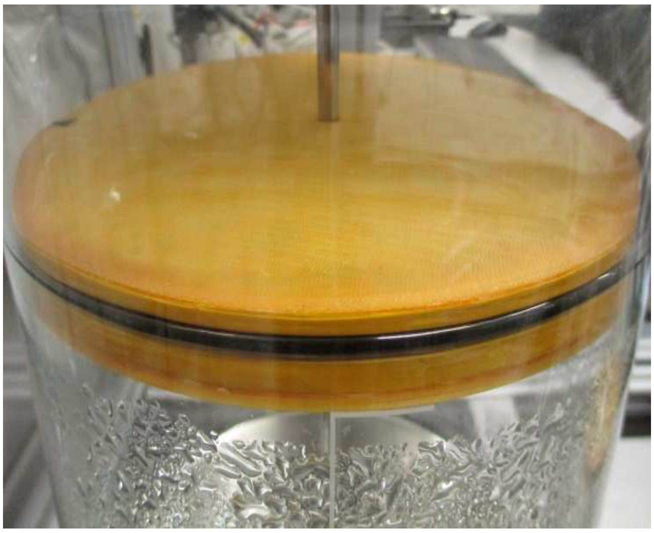

Figure 3. Sealed cover on the measurement beaker to prevent evaporation of the collected water on the balance.

Because the evaporation rate is reduced to a minimum it is considered an uncertainty on the reference flow rate and needs no correction.

UNCERTAINTIES

By extending the LFCS to higher flow rates new parts are added. Some of these new parts add new uncertainties to the uncertainty budget. Components like contact angle force fluctuations and standard Buoyancy corrections change, becoming more dominant in the calculation of the total uncertainty of the extension setup.

Contact angle forces

When water is delivered through the submerged tube in the beaker, the balance measures the mass increase. While the water level in the beaker rises the the water front moves along the tube. While moving along the tube, the contact angle between water and tube depends on the tube properties and other possible environmental effects. Irregularity in the contact angle results in irregular vertical forces [3], thus influencing the measured mass flow on the balance.

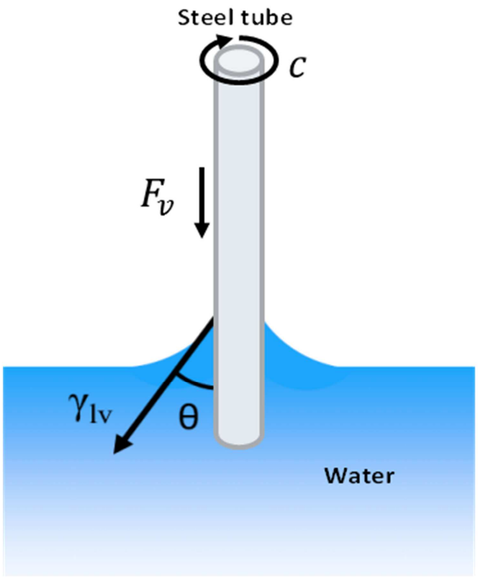

Figure 4. This schematic shows the meniscus between a steel tube and waterinterface. The contact angle (θ) results in a vertical force (F_v).

Figure 4 with equation 2 show that the vertical force (F_v), between water and tube, is dependent on the contact angle (θ), surface tension (γ_{lv}) and circumference (c) of the tube.

$$F_v = \gamma_{lv} c \cos\theta \qquad (2)$$

Nonlinear Buoyancy mass flow correction

The standard Buoyancy correction due to density differences between calibration and measurement [4] on the balance ($\mathrm{m_{cor1}}$) is shown in equation 3 below. Besides the initial mass ($\mathrm{m_r}$), The correction depends on the difference in weighted mass- and air density during calibration ($\rho_{\mathrm{mass\_cal}}$ and $\rho_{\mathrm{air\_cal}}$) and measurement (ρ_{object} and ρ_{air}). During calibration the weighted mass is a calibrated weight. During flow measurement the weighted mass is a beaker with liquid; the object.

$$\mathrm{m_{cor1}} = \frac{\mathrm{m_r}*\left(1-\frac{\rho_{\mathrm{air\_cal}}}{\rho_{\mathrm{mass\_cal}}}\right)}{\left(1-\frac{\rho_{\mathrm{air}}}{\rho_{\mathrm{object}}}\right)} - \mathrm{m_r} \qquad (3)$$

Because the extension of the LFCS uses larger beakers of borosilicate glass the density of the object varies, thus changing the Buoyancy correction as the beaker collects more water. An example of this nonlinear relation between object density and amount of collected water in a 1000 ml beaker is shown in Figure 5.

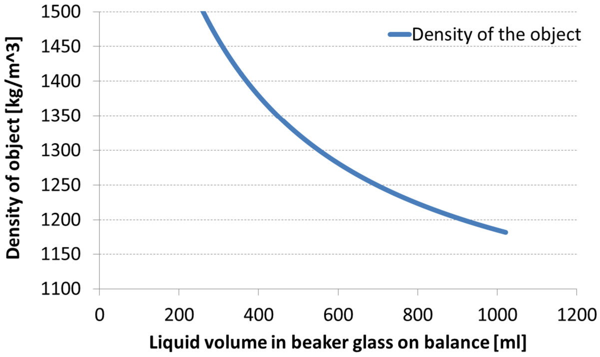

Figure 5. Nonlinear relation between density of the object and the amount of water collected in the beaker. Density of the borosilicate glass is 2230 kg/m^3. Water density at 21 °C and 1 bar(g) is 998.2 kg/m^3.

RESULTS

Crosschecks

Crosschecks between the LFCS and the extension setup confirm good consistency. The crosschecks were performed with a Bronkhorst® ML120- and M13 mini-Cori flowmeter as transfer standards. The ML120 was used to measure the deviation on 100, 150 and 200 g/h points between the LFCS and reference 1 of the extension setup (Figure 1). The M13 was used to measure the deviation on 1000, 1500 and 2000 g/h between reference 1 and -2 in the extension setup of the LFCS.

Table 1 and Figure 6 show that the measured deviation is within the combined uncertainty. To judge whether the results are consistent the E_n value is used. The E_n value should be below 1 in order to confirm consistency between the references.

Table 1. Crosscheck results between references.

Bronkhorst results

REF flow rate (g/h)	Deviation measured by TS (%)	Combined uncertainty (%)	$\mathrm{E_n}$ value (-)
100	-0.04	0.14	0.28
150	-0.05	0.14	0.35
200	-0.02	0.14	0.14
1000	0.01	0.14	0.07
1500	0.02	0.14	0.14
2000	0.01	0.14	0.07

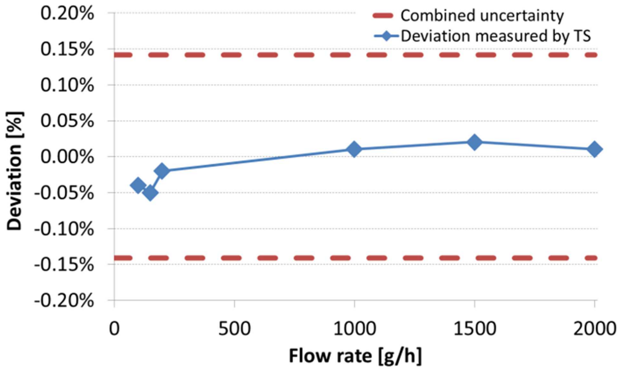

Figure 6. Graphical display of the results presented in Table 1.

Intercomparison

Bronkhorst® participated in an intercomparison on liquid flow rates of 0.5 to 10 kg/h between European NMI's. The intercomparison was coordinated by VSL under EURAMET project 1379, in which liquid micro flow rates from 0.5 kg/h to 10 kg/h are compared between the primary standards of the participants. The participating NMI's are VSL (Netherlands), DTI (Denmark), CMI (Czechia), CETIAT (France), METAS (Switzerland) and LEI (Italy). A M14 mini-Cori from Bronkhorst® was used as the transfer standard in the comparison. Though the results are not yet published at the time of writing, preliminary results show good consistency ($E_n < 1$) between Bronkhorst® and the average of the participating NMI's. When published on https://www.euramet.org/, the results show the traceability of the calibration setup towards the primary standards of European NMI's.

Previous intercomparisons, in which Bronkhorst® participated with the LFCS for liquid flow rates below 200 g/h, already showed good consistency [5][6].

CONCLUSION

The LFCS extension closes the traceability gap for micro flows above 200 g/h. Parts are added to the LFCS extension to provide pure and stable water flows up to 30 kg/h. A new uncertainty budget was made, including the new- and changed uncertainty component contributions to the total uncertainty of the extension setup. By performing crosschecks the extension setup was validated. The results show good consistency. When published, the results of the intercomparison show the traceability towards European NMI's. The LFCS extension setup was ISO/IEC 17025:2005 accredited at the end of July 2017.

REFERENCES

[1] T.H. Platenkamp, W. Sparreboom, G.H.J.M. Ratering, M.R. Katerberg and J.C. Lötters, "Low Flow Liquid Calibration Setup", *Micromachines*, 2015, 6, 473-486, published 22 April 2015.

[2] I.I. Shinder, M.R. Moldover, "Feasibility of an Accurate Dynamic Standard for Water Flow", *Flow Measurement and Instrumentation*, Vol 21, pp 128-133 (2010), published 2010.

[3] P. de Gennes, F. Brochard-Wyart, D. Quéré, "Capillarity and Wetting Phenomena", Springer Science+Business Media, inc., 2004.

[4] S. Davidson, M. Perkin, M. Buckley, "The Measurement of Mass and Weight", *Measurement Good Practice Guide*, No. 71, Crown Copyright 2004, June 2004 National Physical Laboratory.

[5] P. Lucas, "Comparison of primary standards for liquid micro flow rates", *EURAMET project 1291*, April 2015, https://www.euramet.org/ .

[6] P. Lucas, "MeDD – Task 1.1. Comparison – supplement report", *MeDD – Task 1.1. Intercomparison supplement report*", May 2014, http://www.drugmetrology.com/ .

PRECISE FLOW-CONTROL USING PHOTO-ACTUATED HYDROGEL VALVES AND PID-CONTROLLED LED ACTUATION

Colm Delaney[1], *Peter McCluskey*[1], *Simon Coleman*[1], *Jeff Whyte*[2], *Nigel Kent*[1,2] *and Dermot Diamond**[1]
[1] Insight Centre for Data Analytics, National Centre for Sensor Research, Dublin City University, Dublin 9, Ireland
[2] School of Mechanical and Design Engineering, Dublin Institute of Technology, Bolton Street, Dublin, Ireland

ABSTRACT

Herein we demonstrate remarkable control of flow within fluidic channels using photo-actuated hydrogel valves. By polymerizing the valves in situ it has been possible to create highly-reproducible valves. Through the use of an LED platform and a PID algorithm we have generated extremely accurate flow control and created prototype devices to document their potential application within the microfluidics field.

KEYWORDS

Stimuli-responsive, photo-actuators, hydrogel, valve, flow-control, PID

Accurately controlling flow using actuators fully embedded within microfluidic devices has long been a hurdle within our research community. While inroads have been made, through the use of pneumatic valves based on soft-polymers[1], there still exists a paucity of low-cost and precise actuators. In recent years, several groups have turned to photo-responsive polymers as a means for fluid handling. Sumaru *et al.* first showed that hydrogels functionalized with a photoactive spiropyran molecule could be used to act as a photo-controlled valve within a microfluidic channel.[2] Conversion between the hydrophobic spiropyran and hydrophilic protonated-merocyanine forms causes the actuation of the polymer gel between swollen and contracted states.

Our group has made significant progress over recent years in the field of photo-actuated spiropyran materials,[3] firstly through the copolymerization of a proton source and more recently through the use of a photo-actuation platform. This achieved simple open/closed control of fluid flow within a microfluidic device which was subsequently improved by pulsing the light source.[4, 5] The work presented herein is a further advance on control of intermediate states between fully open and closed valves. In particular, through the use of proportional integral derivative (PID) control of power to the illuminating LEDs, we have achieved unprecedented accuracy in controlling flow rate and avoided over/under-shoots upon actuation.[6]

EXPERIMENTAL

The hydrogel valves were photo-polymerised in-situ from a monomeric cocktail which consisted of 200 mg NIPAAm, 8.35 mg MBIS (3 mol% relative to NIPAAm), 7.91 mg SPA-8 (1 mol% relative to NIPAAm), 7.42 mg PBPO (1 mol% relative to NIPAAm) and 6.05 µL AA (5 mol% relative to NIPAAm) dissolved in 500 µL of the polymerisation solvent (2:1 v/v, THF:DI water).

The microfluidic chips were designed using AutoCAD 2014 and were fabricated using clear 2 mm PMMA by rastering with a CO_2 laser ablation system (Epilog Zing Laser Series) at dimensions of 1 mm wide and 250 µm deep. The valve chamber comprised a 1 mm diameter pillar centred within a circle of diameter 2.6 mm which extended from the wall of the channel, as seen in Figure 1. The channels were sealed with a 1 mm PMMA capping layer using previously described solvent bonding processes.[5] Polymerisation and actuation was achieved using blue surface-mounted LEDs (Kingbright HB Blue 450nm, 600 mW/4.5 lm/1.3 cd, 3.5V) at 450 nm wavelength. The valves were polymerised around cylindrical pillars that provided a physical anchor to prevent movement of the valve. The elliptical valve profile was adopted as more symmetrical circular/cylindrical profiles were found to expand into the channels and become lodged in position, permanently blocking the liquid flow. Once the unreacted monomer solution had been removed, the channels were filled with deionised water and left overnight to ensure full hydration of the hydrogel valves. As outlined previously,[5] a constant head of pressure was maintained throughout all the experiments using two reservoirs of different volumes.

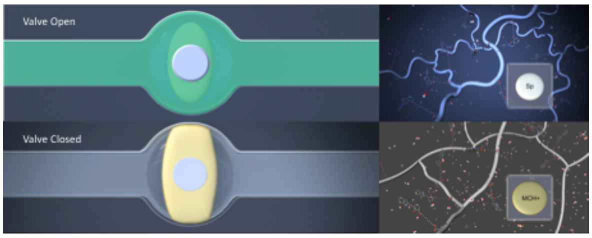

Figure 1: Hydrogel valves within microfluidic fluidic channels under light irradiation (open) and in the fully swollen (closed) states.

By introducing a monomeric cocktail mixture into a 200 µm x 1 mm microfluidic channel, hydrogel valves were photo-polymerised in-situ using 450 nm LEDs from the actuation platform. Once any unreacted monomer was removed, the valves were left to fully hydrate overnight and swell to fill the width of the channel (Figure 1) thereby blocking liquid flow from the attached reservoir. This polymerization technique yielded valves with excellent reproducibility which were fully embedded within the microfluidic chip (Figure 2). The homogeneity of valve production is particularly evident in Figure 2 (b) which shows sequential actuation of four separate valves within a single microfluidic chip. Fast actuation times, with excellent stability (flow rate = 10 µL/min) and highly reproducible behaviour is evident for all four valves. This highlights the capacity of this methodology to incorporate valves within microfluidic manifolds in a controlled and reproducible manner. Even more fascinating, is the highly precise flow control that can be achieved using these photo-actuators.

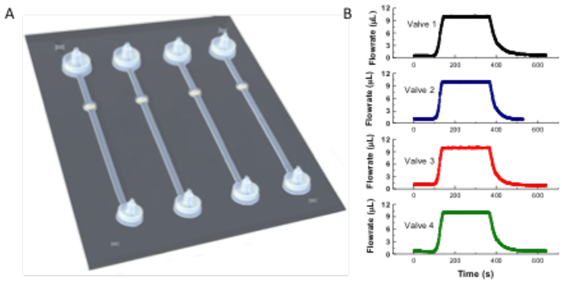

Figure 2: (A) Representation of photo-actuated valves within a microfluidic chip; (B) Actuation profiles (10 µL/min) for 4 valves on a single microfluidic chip.

RESULTS AND DISCUSSION

Precise regulation of the relationship between flowrate and LED power has been achieved by using a flow meter to provide feedback to a PID controller. Through optimization of proportional (K_P) and integral (K_I) variables it has been possible to create a system which accurately detects disparity between the measured and set flowrates and which compensates by varying the light irradiation. An in-house developed user interface (Figure 3) enables the user to input control parameters, such as desired flowrate and maximum LED irradiation. The system then operates autonomously to deliver these flow profiles. An example of such a sequence can be seen in Figure 4. Over a period of 2 hours, the system actuates between three flowrates, with excellent accuracy. Moreover, the stability of the set flow rate over this extended period is particularly remarkable, as outlined in Table 1.

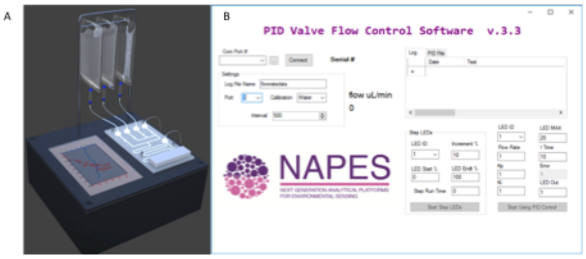

Figure 3. (A) Actuation platform with irradiation LEDs beneath the valve chambers in a microfluidic chip; (B) Graphic User Interface for valve-actuation platform.

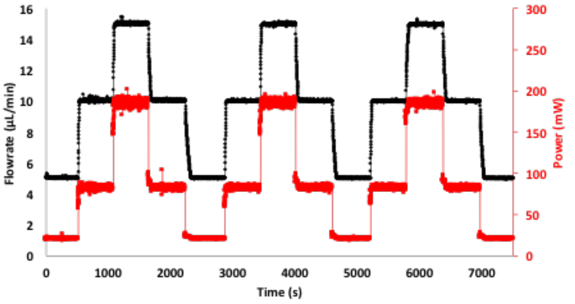

Figure 4. Cycles of (5.0, 10.0, 15.0, 10.0, 5.0 µL/min) shown in black (K_P = 10.0; K_I = 0.1), overlaid with power supplied to the LED to achieve actuation in red.

Our results also suggest there is a high correlation between flow rate and LED power. These values, shown in red in Figure 4, point to the possibility of predicting the flowrate of such a characterized system through the LED power, without the need for an external flow-sensor.

Additionally, simultaneous tracking of flowrate and LED power can serve as a diagnostic of valve performance, thereby opening the possibility for developing complex fluidics incorporating multiple valves.

Table 1. Summary of statistics for data presented in Figure 4. Flow rate units are µL/min; Power units are mW. Averages and standard deviations are for n=100 consecutive points selected randomly from each steady-state flow-rate region.

Set Flow Rate	Average Flow Rate	SD	%RSD	%RE	MOD error	Power
5.0	5.039	0.018	0.351	0.772	0.039	20.598
10.0	10.050	0.048	0.476	0.502	0.050	82.280
15.0	15.048	0.047	0.315	0.317	0.048	185.260
10.0	10.064	0.039	0.391	0.638	0.064	82.197
5.0	5.032	0.018	0.366	0.636	0.032	20.650
10.0	10.045	0.029	0.290	0.449	0.045	82.316
15.0	15.030	0.037	0.246	0.200	0.030	185.506
10.0	10.043	0.034	0.343	0.428	0.043	82.474
5.0	5.021	0.020	0.390	0.425	0.021	20.598
10.0	10.023	0.029	0.287	0.226	0.023	82.602
15.0	14.996	0.034	0.226	-0.027	0.004	184.974
10.0	10.033	0.026	0.259	0.327	0.033	82.226
5.0	5.019	0.016	0.321	0.388	0.019	20.573
	Average =	0.0292	0.3068		0.0316	

To develop on these findings and demonstrate the applicability of our system, a detection platform, based on a Paired Emitter-Detector Diode (PEDD) system was fabricated with a photodiode and two 750 nm LEDs placed at 90 °. The LEDs and photodiode were incorporated into a 3D printed holder which was specifically designed to minimise stray light and ensure the reproducibility of measurements. As before, the LED control platform operated via a 12-bit 16 channel PWM controller (PCA9685) connected to an Arduino Uno microcontroller using the i2c protocol. An output value of 4096, equivalent to an output current of 150 mA, set the LED at 100% intensity. Figure 5 shows a schematic of the four constant current drivers which controlled the LEDs used to actuate four polymer actuators, where each driver was connected to a different output of the PWM controller, thereby allowing individual control of each photo-actuated valve. A UART (serial) connection between the Arduino and the laptop enabled the control software to send the PWM value used to maintain or vary the flow rate.

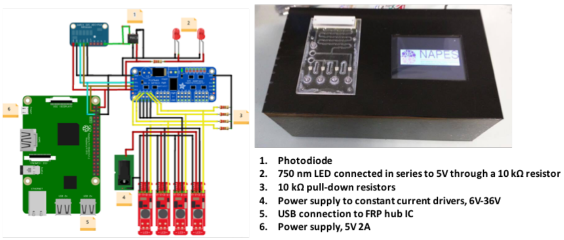

1. Photodiode
2. 750 nm LED connected in series to 5V through a 10 kΩ resistor
3. 10 kΩ pull-down resistors
4. Power supply to constant current drivers, 6V-36V
5. USB connection to FRP hub IC
6. Power supply, 5V 2A

Figure 5: Detection and actuation platform showing the wiring diagram used and the final design including a touchscreen interface.

Full integration of both valve and detection modules then allowed for 1) control of flowrate of reagent, 2) mixing of reagent and sample and 3) detection of absorbance at 750 nm. The final prototype, shown in Figure 6 shows the modular nature of the design which allows for off-chip flowrate determination and complete mixing of reagent and sample. Four photo-actuated valves, shown in yellow, allow for selection between calibration samples of high, low and medium concentrations. The sample continues through the flow-cell where it is then analysed in real time using the PEDD system. These values are then relayed, through the Arduino microprocessor, to a computer where they are saved and processed, as seen in Figure 7.

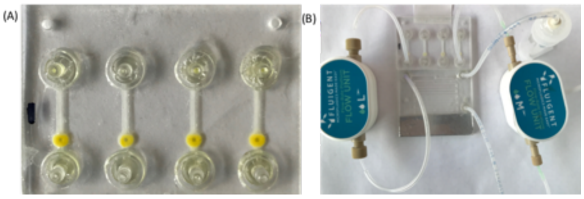

Figure 6: Modular nature of the analytical-detector chip; (A) photo-actuated microvalves polymerized in situ; (B) combined device, showing off-chip flow-rate measurements for both sample and reagent flows.

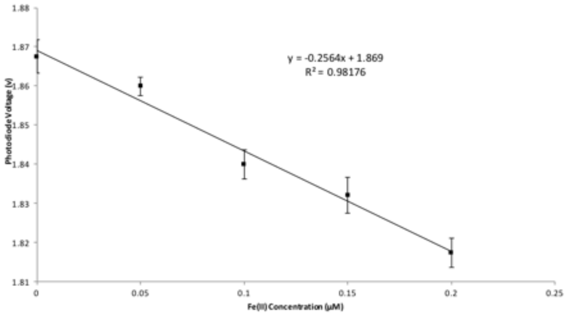

Figure 7: Calibration curve showing on-chip determination of Fe(II) concentration.

CONCLUSION

We have demonstrated flow control through the incorporation of stimuli-responsive materials within microfluidic channels. We subsequently elaborated on this discovery to yield highly-precise flow control through the use of a PID controller. Using an adapted platform, it has also been possible to document potential application of this technology. These results raise new challenges for researchers interested in fabricating and characterising complex microfluidic systems with multiple integrated valves. It is possible that a sub-set of flow sensors could be used to characterise a larger population of valves by switching individual or groups of valves and observing the impact on the output flow-patterns obtained from the valves, and applying machine learning approaches to identify the optimum channel/valve/flow sensor arrangement.

REFERENCES

[1] I.E. Araci, S.R. Quake, Microfluidic very large scale integration (mVLSI) with integrated micromechanical valves, Lab on a Chip, 12(2012) 2803-6.

[2] S. Shinji, S. Kimio, O. Katsuhide, H. Kazuaki, T. Toshiyuki, K. Toshiyuki, Photoresponsive polymer gel microvalves controlled by local light irradiation, Sensors and Actuators A: Physical, 140(2007) 176-84.

[3] W. Francis, A. Dunne, C. Delaney, L. Florea, D. Diamond, Spiropyran based hydrogels actuators — Walking in the light, Sensors and Actuators B: Chemical, 250(2017) 608-16.

[4] J. ter Schiphorst, S. Coleman, J.E. Stumpel, A. Ben Azouz, D. Diamond, A.P.H.J. Schenning, Molecular Design of Light-Responsive Hydrogels, For in Situ Generation of Fast and Reversible Valves for Microfluidic Applications, Chemistry of Materials, 27(2015) 5925-31.

[5] S. Coleman, J. ter Schiphorst, A. Ben Azouz, S. Bakker, A.P.H.J. Schenning, D. Diamond, Tuning microfluidic flow by pulsed light oscillating spiropyran-based polymer hydrogel valves, Sensors and Actuators B: Chemical, 245(2017) 81-6.

[6] C. Delaney, P. McCluskey, S. Coleman, J. Whyte, N. Kent, D. Diamond, Precision control of flow rate in microfluidic channels using photoresponsive soft polymer actuators, Lab on a Chip, 17(2017) 2013-21.

CONTACT

Colm Delaney, colm.delaney@dcu.ie

ELECTROSTACTICALLY IN-PLANE DRIVEN SILICON MICROPUMP FOR MODULAR CONFIGURATION

S. Uhlig[1,2*], *M. Gaudet*[1,2], *S. Langa*[1,2], *K. Schimmanz*[2], *H. Conrad*[1], *B. Kaiser*[1], *H. Schenk*[1,2]
[1] Fraunhofer Institute for Photonic Microsystems, IPMS, Dresden and Cottbus, Germany
[2] Chair of Micro and Nano Systems, Brandenburg University of Technology, BTU, Cottbus, Germany

ABSTRACT

We present an in-plane reciprocating displacement micropump for liquids and gases which is actuated by a new class of electrostatic bending actuators capable of deflecting beyond the electrode gap distance. The so called "Nano Electrostatic Drive" (NED) actuator was introduced by us in 2015 for out-of-plane actuation. The device presented utilizes an in-plane actuation solution. Depending on the requirements of the targeted system, the micropump can be modularly designed to meet the specified differential pressures and flow rates by a serial arrangement of the actuators and parallel arranging pump-base units respectively.

KEYWORDS

MEMS; Micropump; Electrostatic Actuation; Nano e-Drive; In-plane reciprocating displacement micropump

INTRODUCTION

Electrostatic actuation has many advantages in microelectromechanical systems (MEMS), in terms of scalability, fast response time (<µs), simplicity in fabrication and low power consumption. However, the majority of integrated electrostatic drives in microfluidic handling systems such as micropumps [1] and microvalves [2] devices are limited in either deflection or driving voltage, which results in higher power consumption or low stroke volumes. With the novel concept of the "Nano Electrostatic Drive" (NED) driving principle, introduced in 2015 [3], we are able to deflect beyond the limiting gap distance.

In addition, the majority of mechanical reciprocating micropumps [1] work with an out of plane mechanism of a membrane clamped at its perimeter, that needs to be extended to large chip areas in order to increase the stroke volume. Furthermore, a hybrid assembly mechanism of actuator and pump is necessary in many cases. We propose a monolithic fabricated device by CMOS-compatible bulk micromachining processes that can be modularly designed to meet flow rate and differential pressure specifications for pumping liquids and gases.

ACTUATION

The NED-actuators commonly consist of a series of defined shaped electrodes separated by an electrostatic gap and insulating spacers [3]. Upon applying a control voltage V, the electrostatic force cause to curve the actuator. As a simple approach, the NED can be considered as a Bernoulli beam with a constant bending moment M, i.e. constant radius of curvature R along the beam, defined positive as in Fig. 1.

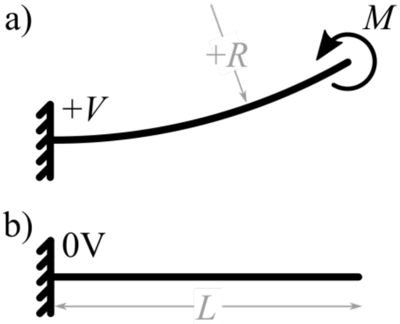

Figure 1: Working principle of clamped-free NED-actuator with length L. (a) Actuated state - circular bending line, with constant bending moment M i.e. const. radius of curvature R. (b) Non-actuated state.

By adding four of these NED-Actuators and rearranging them to a clamped-clamped (c-c) configuration with a length 4*L* = *L'* and use of alternating radius scheme +*R*, -*R*, -*R*, +*R*, the effective bending Moment M_{eff} is 2*M*.

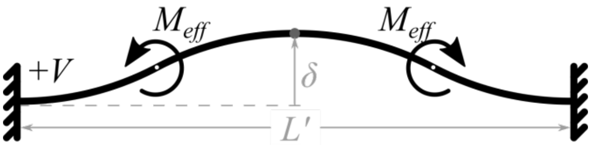

Figure 2: Bending line of four rearranged NED-actuators to c-c configuration, when actuated.

The maximum deflection δ_{max} can be derived for the case of pure bending to:

$$\delta_{max} = \frac{M_{eff}\, L'^2}{32\, EI},$$

where EI is the bending stiffness of the actuator. Thus, the stroke volume ΔV of the NED-actuator is the area passed over by the actuator multiplied by its height h, $\Delta V = \left({}^{L'}/_{2}\ \delta_{max} \right)\ h$.

WORKING PRINCIPLE

The maximum pressure P_{max} that a single NED-actuator in c-c configuration is able to generate can be estimated by its force at middle point at zero displacement $F_{BL}(\delta = 0)$. The so called "blocking force" given by:

$$F_{BL} = 6\frac{M_{eff}}{L'}$$

The blocking force divided by the major area $A_{Act.-Fl.}$ facing the fluid, cf. Fig. 6, yields in a corresponding “blocking” pressure:

$$P_{max} = \frac{F_{BL}}{A_{Act.-Fl.}}$$

The total differential pressure ΔP is generated by the actuator on the two cavities present on its sides. This creates an over-pressure $+P$ in the first cavity and an associated under pressure $-P$ in the second one.

At each position of the active displacement, the actuator delivers a specific pressure following the upper part of the pressure/displacement graph presented in Fig. 3. In the same manner, canceling the applied moment will allow the deformed actuator to release the bending energy, moving back to its original position. This actuation phase is represented in the lowest part of the graph.

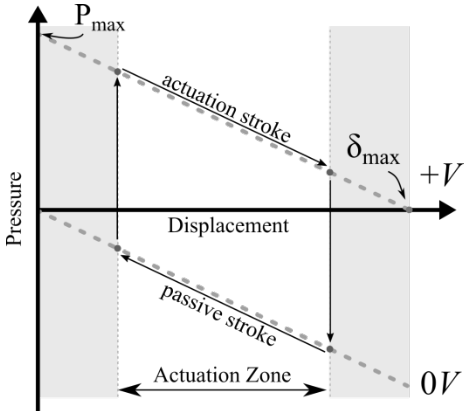

Figure 3: Pressure/displacement graph and concept of NED-actuation scheme in the micropump.

By considering the linear flow/pressure relation given by Poiseuille law [4], which is in agreement with Fig. 3, for a large displacement, the generated pressure tends to zero, resulting in a flow rate also converging to zero. It will consequently take a longer time to move the actuator over its entire amplitude to δ_{max} ,as well as, during the passive intake phase.

To ensure that active supply and passive intake stroke will take nearly the same time it’s intended to actuate in an interval around an operation point that is at the actuators half displacement, i.e. half of the stroke volume.

A simple arrangement of one NED-actuator with two valves permits already to create a rectified flow and represents a micropump.

VALIDATION WITH SIMULATION

In order to validate the concept and the behavior of the NED in-plane micropump we carried out 2-way Fluid-Structure Interaction (FSI) simulations by using ANSYS, Academic Research, R18. Here, the toolboxes transient mechanical and fluent were combined via the system coupling box. Two NED-actuator design points were validated for pumping air and ethyl-alcohol. We simulated closed cavity model of one NED-actuator beam of length *L’* and one passive flap, cf. Fig. 4.

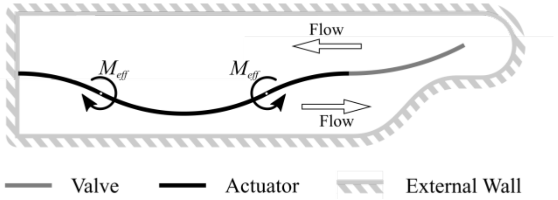

Figure 4: Sketch of 2-way FSI setup used for simulation of micropump behavior.

The actuator itself was modelled as a solid beam with equivalent bending stiffness *EI* of the physical NED-actuator and effective moments M_{eff} applied at ¼ *L’* and ¾ *L’*. The corresponding values are given table 1.

Design	A	B
Medium	Air	Ethyl-Alcohol
EI	8,44 e-09 Nm²	1,05 e-08 Nm²
M_{eff}	3,65 e-07 Nm	2,20 e-07 Nm

Table 1. NED-actuator design point data used for FSI simulation.

Figure 5 shows the generated differential pressure vs. stroke volume graph obtained from the simulation results, as well as, analytical model. Compared to the simplified analytical approach the FSI simulation reflects the expected behavior of the system.

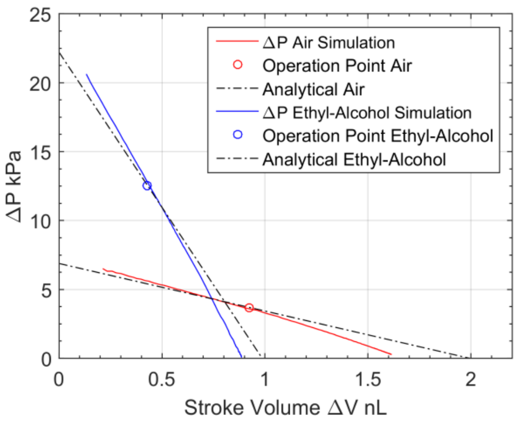

Figure 5: Simulation rand analytical mode results of generated differential pressure vs. stroke volume.

Deviations at the lower end of the curves may arise from nonlinear mechanical effects considered in the structural simulation, as well as, change in the fluidic resistance of the channels due to the actuators deflection, cf. Fig. 4.

The frequency dependent pump rate of the one actuator cavity model is shown, in Fig. 6, for the case of the design of air for 3 different starting positions of the actuation zone, cf. Fig. 3. Here, the maximum flow rate peaks at *0.0125 sccm* for *360 Hz* actuation frequency. For this point the intake and supply stroke need the same time and the actuation interval is symmetric around the operation point.

The consequence of unequal pump phases for selected interval start position of 0.55 δ_{max} and 0.65 δ_{max} is a reduced flow rate. The effect is similar when the outtake stroke begins before the operation point.

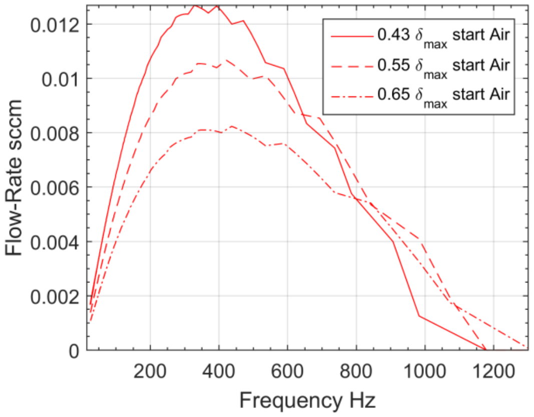

Figure 6: Frequency dependent flow rate generated by closed cavity of one NED-actuator and passive flap-valve.

MICROPUMP DESIGN AND FABRICATION

Two clamped-clamped NED-actuators can be arranged in so called base units shown in. Fig 7, where the actuators face each other and a shift of ½ *L'* length is introduced. The two major actuator sides facing the fluid are separated by a passive flap valve.

One base unit could act already a standalone pump. However, such base entities can further be arranged in parallel configuration. This opens the possibility to easily increase the total stroke volume and therefore to meet application specific flow rate (FR) needs. In order to address certain differential pressures the NED-actuators can be stacked laterally *N*-times. This increases linearly the generated pressure linearly in the pump.

Due to this combination of base pumping entities, the micropump intakes and supplies liquid with each actuation stroke, thus reducing the flow pulsation.

The micropump is composed of a standard wafer bonded on SOI Wafer with orientation (110), cf. Fig. 9. The active device layer has a thickness of 75 µm and contains the driving NED-actuators, as well as, rectification valves and fluidic channels. It is processed by standard bulk-micromaching steps such as deep reactive ion etching (DRIE). The fluidic in- and outlet are located on the top cover while the electrical connections are on the bottom cover (SOI-handle), making a total chip thickness of 900 µm. The entire fabrication process is compatible with CMOS-technologies using only crystalline Silicon, Silicon-dioxide and Aluminumoxid.

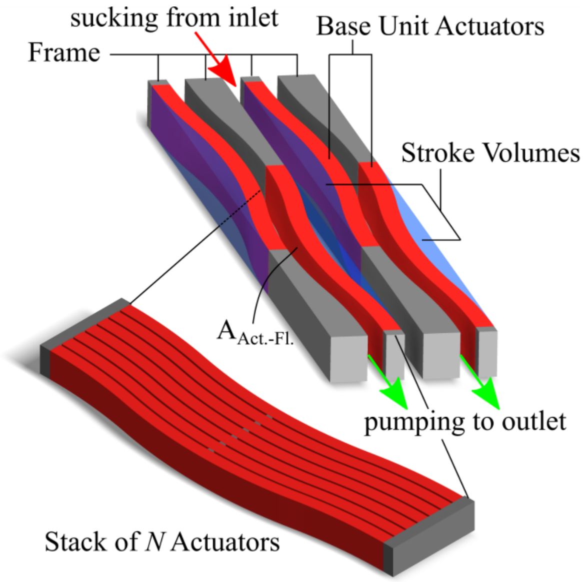

Figure 7: Shown are two parallel base units in actuated state generating a total stoke volume. Supply and intake phase occur simultaneously (above). Possible linear stack of actuators to increase generated pressure difference. (below).

Figure 8 shows an early test design of the in-plane micropump. Shown are inlet feed channels and parallel pumping base units. Visible is only device layer of the SOI-wafer. The inset shows magnified passive valves of 2 base units and beginning of defined shaped electrodes of the electrostatic bending actuators.

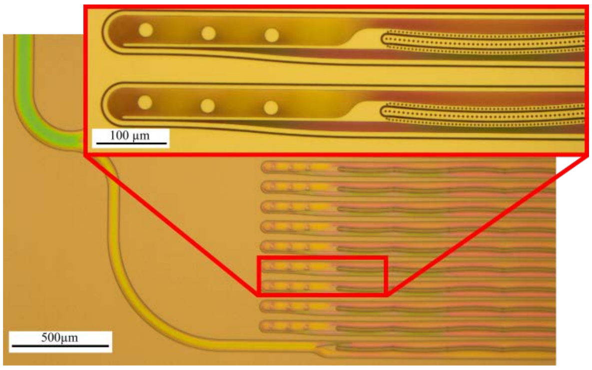

Figure 8: Micrograph of early in-plane micropump test design.

The device layer and, thus, the NED-actuators are fully immersed inside the fluidic medium. Depending on the permittivity of fluid this further enhances the actuation forces [5]. In order to avoid electrical short circuiting the electrodes are additionally encapsulated by a layer of 60 nm Al_2O_3, deposited by atomic layer deposition (ALD).

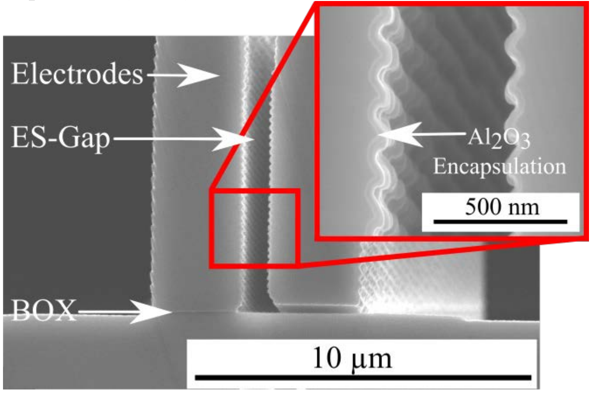

Figure 8: DRIE test etching of electrostatic-gap. (Inset) Encapsulation of NED-electrodes by 60 nm ALD-Al_2O_3. BOX layer is not released.

A slit of currently 1 µm to the top cover wafer (grown thermal oxide) as well as to the handle wafer (SOI – 1 µm buried oxide BOX, cf. Fig. 8) avoids mechanical contact. However, these slits presents a fluidic leak, cf. Fig. 9, that manifest itself as a dead-volume during operation.

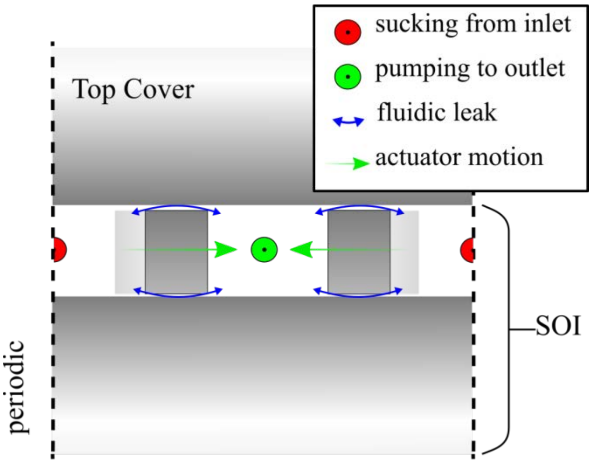

Figure 9: Sketch of 3 layer silicon wafer bonded on SOI wafer. Fluidic transfer is in direction out of image plane (indicated as pointing arrow head circles).

OUTLOOK

We designed two medium specific micropumps dedicated to ethyl-alcohol and air with a modular configuration of 5 parallel base units and 10 actuators per stack.

The maximum flowrate with internal leakage considered is 1400 µL/min at an operating differential pressure ΔP_{op} of 38 kPa for air and 90 µL/min at ΔP_{op} of 120 kPa for the ethyl-alcohol design. General specifications and simulation results are presented in table 2.

This novel approach, permits to laterally stack the driving NED-actuators as well as the pumping units to address applications needs in fields such as lubrication dosage or cooling.

Design	A	B
Medium	Air	Ethyl-Alcohol
Size	4 x 5 x 0,9 mm³	3 x 5 x 0,9 mm³
Actuation voltage	300 V	100 V
No. of base units	5	5
Operation. diff. pressure	38 kPa	120 kPa
Expected FR.	1400 µL/min	90 µL/min

Table 2. Specification and simulation results of current designs.

ACKNOWLEDGEMENTS

This research takes part within the “NED-VAMP” project and is co-financed by the European Fond for Regional Developments (EFRE).

REFERENCES

[1] Laser, D. J.; Santiago, J. G. (2004) A review of micropumps. In J. Micromech. Microeng. Vol. 14

[2] Oh, Kwang W et al. (2006): A review of microvalves. In J. Micromech. Microeng. 16 (5)

[3] Conrad, H. et al. (2015) A small-gap electrostatic micro-actuator for large deflections. Nat. Commun. 6:10078

[4] Bruus, Henrik (2008): Theoretical microfluidics. Oxford: Oxford University Press

[5] Gaudet, M. et al. (2017) Electrostatic bending actuators with a liquid filled nanometer scale gap. IEEE 30th International Conference on Micro Electro Mechanical Systems (MEMS ’17)

*corresponding author, email:
sebastian.uhlig@ipms.fraunhofer.de

STANDARDS AND GUIDELINES FOR MICROFLUIDIC INTERCONNECTIONS, BUILDING BLOCKS AND VERIFICATION TESTING

Henne van Heeren[1]
[1] enablingMNT, Dordrecht, the Netherlands

Introduction

Integrating microfluidic components from different suppliers into systems often needs ad hoc solutions leading to reliability problems. Cleary industry agreements about interconnections and component formats would simplify matters for designers and producers of microfluidic devices. That goes even more for industry wide supported quality standards. Such agreements will make working with microfluidic devices easier and more reliable; i.e. will lead to plug & play microfluidics. A particular problem in the microfluidic industry is the wide variation in technologies and materials used. Therefore, to make the standards widely applicable, they should be formulated in such a way that they are independent of technology and application. A multinational group of microfluidic companies and institutes agreed on such specifications.

Microfluidic interconnections

The first problem discussed was the issues of microfluidic interconnections. These are often made manually. Especially when many connections are needed, this is a costly activity and risking reliability issues. To promote the introduction of easy to use multiport connectors, the positions, sizes and nomenclature of microfluidic ports were defined. (see figure 1) The second important step the group took was defining dimensions of standard microfluidic building blocks to enable easy assembly of the components. It also enables interchanging parts; for instance to use components from different suppliers or to create reconfigurable system. In discussion are now also guidelines about side connectors and microfluidic circuit boards. It is good to mention that all guidelines were only approved after intensive discussions with dozens of companies outside the core group

Towards generic validation testing for microfluidics.

The third step taken was defining a classification off microfluidic devices; seen as an essential step towards industry supported quality specifications. Although at first this classification only addresses pressure and temperature operation ranges (see table 1), they are to be complemented by flow ranges.

The rationales for this part of the discussion are: 1) There are no published generic test protocols based on proven fault modes to assist the development of more reliable microfluidic products. 2) Most of the tools and techniques currently used for failure analysis are leveraged from the IC industry, and are not designed to be used with fluids [1], especially not with liquids. Therefor the microfluidic industry faces the challenge that it needs to define its own testing strategies, methods and reliability models. These testing strategies should be based on the most challenging microfluidic fault modes. Therefore identifying and understanding these fault modes is seen as number one priority for the microfluidic community.

White papers and guidelines

The proposed standards and guidelines are published or will be published as White Papers to ensure wide dissemination. Several of the standards developed so far are currently being transferred to the International Standard Organization (ISO) to become official standards. The guidelines proved to be very easy applicable for designers and within two years after publication of the first guideline, about 15 new products based on these standards are in development. As one of these products already needed further miniaturization, we discussed future (smaller) formats too.

This article will show details of the introduced standards and explain the rationales behind them, illustrated by some examples from products based on these standards.

.Word Count: 582

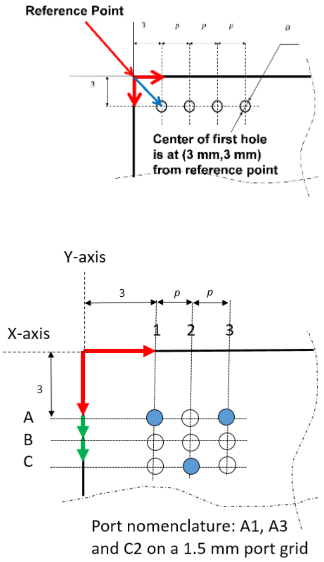

Figure 1: Microfluidic port positions and port nomenclature

Table 1: operational classes for microfluidic devices

Class Type	**Maximum Pressure** (bar)	**Maximum Temperature** (°C)	**Minimum Temperature** (°C)
PT 2/50	2	50	4
PT 2/75	2	75	4
PT 2/100	2	100	4
PT 7/50	7	50	4
PT 7/100	7	100	4
PT 30/50	30	50	4

REFERENCES

[1] Walraven, J.A., Future Challenges for MEMS Failure Analysis, in ITC International Test, Conference. 2003, IEEE. p. 850 - 855

EXPERIMENTAL CHARACTERIZATION OF A GENERATOR OF NON-NEWTONIAN DROPLETS BASED ON A MICRO CROSS-JUNCTION

B. Rostami and G.L. Morini
DIN – Alma Mater Studiorum Università di Bologna, Laboratorio di Microfluidica, Via del Lazzaretto 15/5, Bologna 40131, Italy

ABSTRACT

This paper deals with the experimental characterization of a micro cross-junction for the generation of mono-dispersed micro-droplets of non-Newtonian fluids obtained as solution of water, Tween 20 and Xanthan gum in silicone oil flow. Tween 20 is a surfactant added to the dispersed phase in order to avoid the coalescence of the droplets and to enhance the performance of the device. By means of a series of experimental tests the typical dimensions of the non-Newtonian micro-droplets and their frequency have been correlated to the imposed flow rates of the continuous and dispersed phase at the inlets of the micro cross-junction. The effect of the concentration of xanthan gum in non-Newtonian solution as well as the role played by the presence of the surfactant within the aqueous solution on the mono-dispersed droplets has been studied in detail.

KEYWORDS

Two-Phase Flow, Xanthan Gum, Non-Newtonian flows, Micro Cross-Junction

INTRODUCTION

Nowadays micro-devices are largely used to generate mono-dispersed droplets. Mono-dispersed droplets with low size variation are highly desirable in many technical applications such as DNA and blood analysis, chemical reactions and drug discovery. It has been demonstrated that the main governing and controlling parameters which enable the control of the droplet size generated in a micro cross-junction are the properties of the liquids introduced in the junctions, their inlet flow rates and the geometry of the micro-junction. Despite the importance of non-Newtonian fluids in industrial and pharmaceutical fields, the investigation of their behavior in micro cross-junction during droplet generation can be nowadays considered disregarded. In order to start filling this gap in this work an aqueous solution obtained by using three different concentrations (0.2, 0.3 and 0.5 wt%) of Xanthan gum have been considered as dispersed phase. Tween 20 (2 wt%) has been added to the non-Newtonian solutions to avoid the coalescence of the droplets and to enhance their formation. A wide range of volumetric flow rates at the inlets of the junction, both for the continuous and the dispersed phase, has been imposed in order to be able to detect the different mechanisms linked to the droplet formation as squeezing, dripping and jetting regimes. The non-dimensional droplet diameter has been measured and plotted as a function of flow rate ratio and the Capillary number with the aim to study the effect of the main physical governing parameters on the droplet characteristics.

EXPERIMENTAL SETUP

The experimental apparatus used in this work is shown in figure 1. An inverted microscope (1, *Nikon Eclipse TE2000-U*) with a double system of illumination by means of a Mercury lamp (2a, *Nikon C-SHG1*) from the bottom and a COB LED lamp (2b, *100W, 9000 Lumens*) from the top is the main part of the test rig. An air immersion lens with a numerical aperture NA = 0.25 with magnification M = 10x (3, Nikon, *CFI DS 10X*) is selected to visualize the droplets. A high-speed camera (4, *Olympus I-speed II*) connected to the inverted microscope is used to acquire the droplet images; a LCD monitor (5) and Olympus I-speed II software (6) makes possible a run-time visualization of the flow within the microdevice.

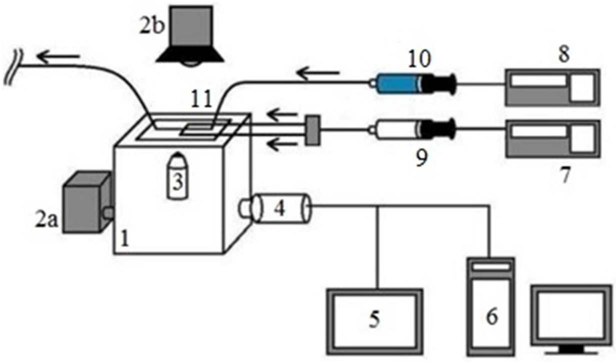

Figure 1. Experimental Setup

The volumetric flow rates of silicone oil (continuous phase) and of Xanthan gum solution (dispersed phase) are controlled by two independent syringe pumps (7, *Cole-Parmer Version Hills* and 8, *Harvard Apparatus PHD4400 Programmable*) and introduced at the three inlets of the junction (11) using two gastight Hamilton syringes (9 and 10). The relative uncertainty of the imposed volumetric flow rate for continuous and dispersed phase is equal to ± 0.5% FS and ± 0.35% FS, respectively.

A glass micro cross-junction has been used as droplet generator (figure 2). The cross-junction is characterized by a cross-section restriction at the junction in which the width of the channel varies from W_w = 390 µm far from the junction to W_j = 195 µm at the junction. The height of the channel (H) is uniform and equal to 190 µm. The continuous phase (Silicone oil by Sigma Aldrich, viscosity 20 cSt, density 0.95 g/ml @ 25 °C) is introduced from the two lateral ports; the dispersed phase is introduced from the remaining port. The main dimensionless parameters involved in the droplet generation with the micro cross-junction are: (i) the flow rate ratio $\alpha = Q_d/Q_c$ and (ii) the Capillary number ($Ca = \mu u/\sigma$), where u (= Q/A) is the fluid velocity.

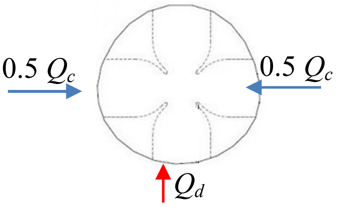

Figure 2. Micro cross-junction and the distribution of the fluids

Tween 20 (Sigma Aldrich, density 1.095 g/ml @ 25 °C) is used as surfactant added to the dispersed phase in small concentration (2 wt%). The density of continuous and dispersed phases has been measured by using a density determination kit (RADWAG AS 220.R2). The viscosity of silicone oil is measured using a Cannon-Fenske Viscometer while a Brookfield DV-II+ viscometer has been used for the non-Newtonian solutions. The aqueous solutions of Xanthan gum exhibit a shear thinning behavior and the power-law model is used for its characterization. Surface tension is measured by means of a force tensiometer (KSV Sigma 700).

The geometrical characteristics of the droplets (diameter, length, position of the edge with respect to the centre of the junction) are calculated based upon the acquired images by using a Matlab code [1].

During the tests, the continuous phase (silicone oil) flow rate (Q_c) varies from 0.3 to 20 ml/h; the range of dispersed phase (Xanthan gum solution) flow rate (Q_d) has been varied from 0.01 to 2.1 ml/h.

RESULTS

Three typical droplet mechanisms have been identified at low continuous flow rates ($0.5 \leq Q_c \leq 2$ ml/h $\approx 0.005 \leq Ca_c \leq 0.026$) while Q_d changes from 0.01 to 2.1 ml/h, as shown in figure 3. By changing the flow rates at the inlets of the micro-junction it becomes possible to obtain droplets generated at the cross-junction (DCJ, figure 3a), droplets formed downstream with respect the junction (DDC, figure 3b) and a stratified flow in which the continuous and the dispersed phases flow in parallel (PF, figure 3c).

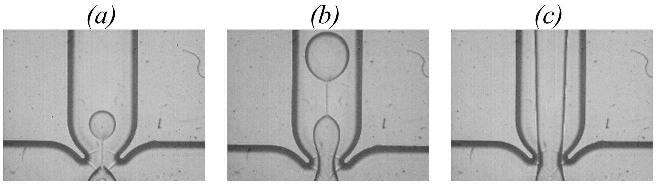

Figure 3. Typical mechanisms of the droplet formation for an aqueous 0.5 wt% Xanthan gum solution when Q_c = 1.5 ml/h and Q_d = 0.015, 0.2 and 1.65 ml/h, respectively.

Three mechanisms for the droplet generation can be obtained by changing the values of α and Ca_c, as shown in figure 4.

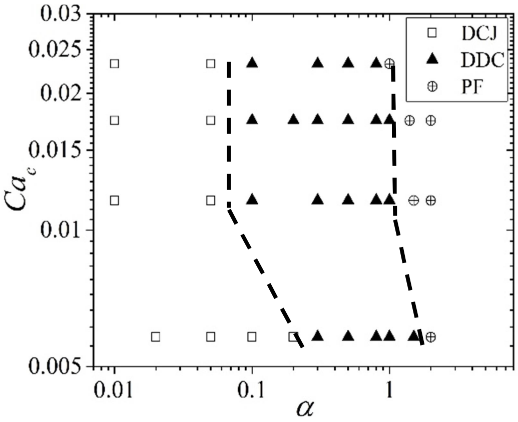

Figure 4. . Flow pattern map as a function of flow rate ratio α and Capillary number linked to the continuous phase (Ca_c) for a 0.3wt% Xanthan gum solution

In presence of non-Newtonian fluids, like the aqueous Xanthan gum solution, a thin micro-thread may be seen before the droplet breakup due to the large viscosity of the dispersed phase. This thread follows the droplet after the breakup as a satellite. The thread is stretched if Q_c increases. Figure 5 shows the non-dimensional droplet diameter D^* as a function of flow rate ratio α. The non-dimensional droplet diameter D^* is defined as:

$$D^* = \sqrt{D_h D_v} \big/ H \tag{1}$$

where D_h and D_v are the droplet horizontal and vertical maximum dimensions, respectively and H is the channel height.

Figure 5 highlights that when the droplet formation is linked to the dripping and jetting mechanisms ($\alpha < 0.1$, i.e. large Q_c and/or low Q_d) the droplet dimension depends weakly on α and the mono-disperse emulsion at the outlet of the micro-junction is characterized by droplets having a diameter close to the height of the channel ($D^* \approx 1$).

On the contrary, when $\alpha > 0.1$, the droplet generation is due to the squeezing mechanism and larger droplet dimensions can be obtained by increasing α ($D^* > 1$).

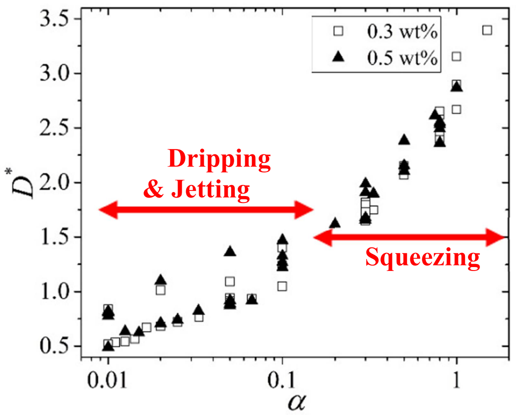

Figure 5. Droplet dimensionless diameter D^* as a function of α for two aqueous solutions having different Xanthan gum concentrations

In squeezing regime the droplet diameter depends weakly on Ca_c; on the contrary, the channel size and Q_d play important roles [2]. Due to the larger values of Q_c and, consequently, to the larger values of shear forces, the impact of Ca_c on D^* is more evident in dripping regime [3, 4].

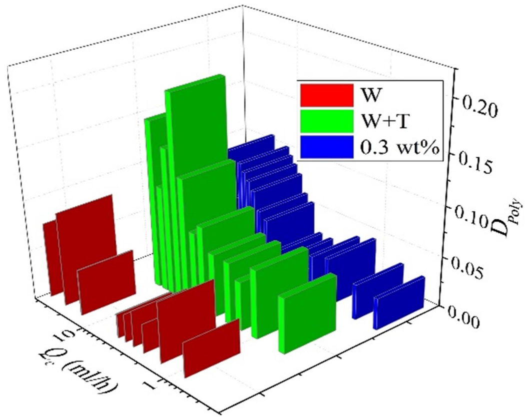

Figure 6. Polydispersity of the droplet diameter for pure water (W), water with Tween 20 (W+T) and the aqueous 0.3 wt% Xanthan gum solution (0.3 wt% Xanthan gum)

The value of the droplet polydispersity (D_{Poly}), defined as the standard deviation of the droplet size distribution at the outlet of the junction divided by the mean droplet size, has been calculated by varying the flow rate of the continuous phase for a fixed flow rate of the dispersed phase Q_d (=0.1 ml/h). Lower polydispersity values are desirable because, in this case, at the outlet of the droplet generator a mono-dispersed emulsion of droplets having small differences in terms of dimensions can be obtained.

Figure 6 presents the polydispersity of the droplet diameter as a function of Q_c, obtained by using as dispersed phase pure water (W), water with surfactant (W+T) and an aqueous solution of Xanthan gum (0.3 wt%). By observing figure 6 it is evident that in many cases it is possible to obtain a value of D_{Poly} less than 0.1 (10%) even if no surfactant is added to the dispersed flow (i.e. pure water). This result confirms that the micro cross-junction is an efficient droplet generator able to guarantee a production of homogeneous micro-droplets in terms of diameter.

Finally, the effect of Q_c and Q_d on the droplet frequency f, defined as the inverse of the time interval between two consecutive droplets, has been investigated. In figure 7 the droplet frequency obtained by using an aqueous Xanthan gum 0.3 wt% solution as dispersed phase is plotted as a function of Q_d for fixed values of Q_c. When Q_d is increased, the droplet formation time decreases and the frequency increases. The same occurs when Q_c is increased for a fixed Q_d because an increase in Q_c increases the shear force which determines a faster droplet breakup.

In addition, when Q_d increases in correspondence of large values of Q_c the droplet frequency becomes more variable, as highlighted by the error bars of figure 7. A maximum droplet frequency around 100 Hz can be obtained by increasing both Q_d and Q_c**.** However, in this case the frequency is not stable, as underlined by the large error bars represented in figure 7. In order to obtain a stable behavior of the droplets at the outlet of the junction in terms of frequency, the experimental data suggest to limit the use of this device for $Q_c < 2$ ml/h; in this case the maximum droplet frequency is about 10 Hz for Q_d around 1 ml/h.

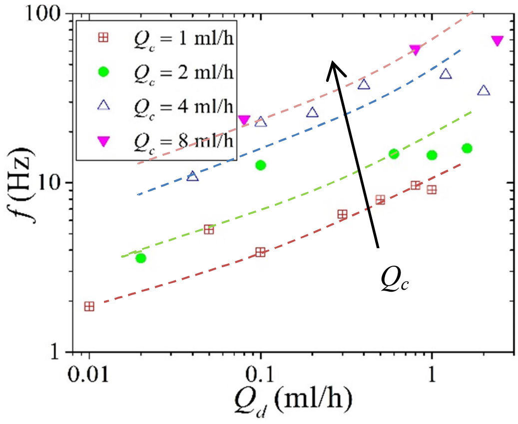

Figure 7. Effect of Q_d and Q_c on the droplet frequency for an aqueous Xanthan gum 0.3 wt% solution

In order to check the effect of the properties of the non-Newtonian fluid on the droplet frequency, two different concentrations of Xanthan gum have been used. Higher concentrations of Xanthan gum mean higher fluid viscosity and this generally leads to lower droplet frequency because the number of droplets generated per second tends to decrease if the viscosity of the dispersed phase is larger. In figure 8 the droplet frequency obtained for two aqueous Xanthan gum solutions and for water with surfactant (2 wt% of Tween 20) is plotted as a function Q_c for a fixed value of Q_d (=0.1 ml/h). A lower viscosity of the dispersed phase contributes to decrease the droplet formation time. The data shown in figure 8 underline that there is not a significant difference between the frequencies of the droplets obtained for the two Xanthan gum solutions even if the viscosity tends to increase with the adopted Xanthan gum concentration.

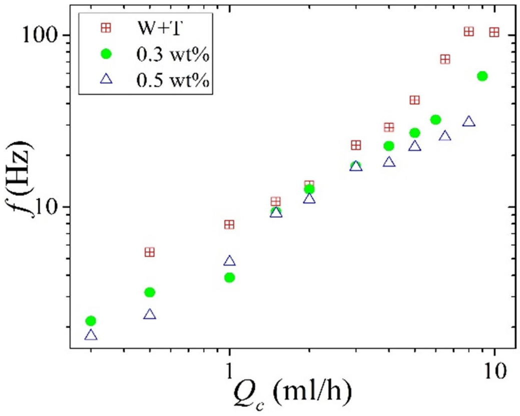

Figure 8. Droplet frequency for water with surfactant (W+T), and aqueous 0.3 wt% and 0.5 wt% Xanthan gum solution as a function of Q_c *and a fixed value of* $Q_d = 0.1$ *ml/h*

The observation of the dynamics of the droplet generation is useful in order to understand the reason of the increase of the instability of the droplet frequency for large values of Q_c (or low values of Q_d).

Droplet formation time can be divided in two periods: the growing period and the breakup period. At low values of Q_d (or very high values of Q_c) the duration of the growing period is increased because the dispersed fluid crosses an instable phase in which it is not able to start the droplet growing (hesitancy stage). The duration of this stage can vary test by test and this fact explains the large error bars shown in figure 7 in correspondence of large values of Q_c.

In order to obtain a stable behavior of the micro droplet generator it becomes mandatory to avoid to operate in presence of a hesitancy stage during the droplet growing. The experimental results underline that the droplet generator is able to produce stable mono-disperse homogeneous droplets with a fixed frequency only by operating at $Q_c < 2$ ml/h and $Q_d > 0.1$ ml/h. Xanthan gum reduces the frequency variation under 10% if compared with water and surfactant.

CONCLUSIONS

In this work the generation of a mono-dispersed emulsion of non-Newtonian droplets of aqueous Xanthan gum solutions in a continuous flow of silicone oil is studied experimentally by using transparent micro cross-junction. Different droplet breakup mechanisms (squeezing, dripping and jetting) can be activated by varying the imposed flow rate at the inlets and/or the Capillary number. The effect of Q_c and Q_d on the non-dimensional diameter of the droplets has been investigated by comparing two non–Newtonian solutions having a different Xanthan gum concentration (0.3 wt% and 0.5 wt%) with water in which a surfactant (2 wt% of Tween 20) has been added. The results show that the cross-junction is generally able to generate homogeneous mono-dispersed droplets with a polydispersity lower than 5%. Non-Newtonian solutions are characterized by a larger polydispersity. In terms of droplet frequency, the larger values of viscosity, characteristic of the Xanthan gum solutions with respect to water with surfactant, tend to reduce significantly the droplet frequency. For the micro cross-junction tested in this work the optimal operational conditions when Xanthan gum solutions are used as dispersed phase are defined as follow: $Q_c < 2$ ml/h and $Q_d > 0.1$ ml/h.

Under these conditions, the microdroplet generator is able to produce droplets having a non-dimensional diameter between 1 and 1.5 with a polydispersity lower than 5% and a stable droplet frequency of around 10 Hz.

REFERENCES

[1] B. Pulvirenti, B. Rostami, G. Puccetti, G. L. Morini, “Determination of droplet contours in liquid-liquid flows within microchannels”, Journal of Physics: Conference Series, Vol. 655, 012028, 2015.

[2] M. N. Kashid, A. Renken, L. Kiwi-Minsker, “CFD modelling of liquid-liquid multiphase microstructured reactor: Slug flow generation”, Chemical Engineering Research and Design, Vol. 88, pp. 362-368, 2010.

[3] X. B. Li, F. C. Li, J. C. Yang, H. Kinoshita, M. Oishi, M. Oshima, “Study on the mechanism of droplet formation in T-junction microchannel”, Chemical Engineering Science, Vol. 69, pp. 340- 351, 2012.

[4] M. De Menech, P. Garstecki, F. Jousse, H. A. Stone, “Transition from squeezing to dripping in a microfluidic T-shaped junction”, Journal of Fluid Mechanics, Vol. 595, pp. 141-161, 2008.

CONTACT

* B. Rostami, behnam.rostami2@unibo.it

FAST ACTUATOR BASED ON SHORT-TIME WATER ELECTROLYSIS

I.V. Uvarov[1], *M.V. Lokhanin*[2], *A.V. Postnikov*[1] *and V.B. Svetovoy*[1,3]
[1] Yaroslavl Branch of the Institute of Physics and Technology RAS, Yaroslavl, Russia
[2] Department of Physics, P.G. Demidov Yaroslavl State University, Yaroslavl, Russia
[3] Zernike Institute for Advanced Materials, University of Groningen, Groningen, The Netherlands

ABSTRACT

An actuator based on water electrolysis with a fast change of voltage polarity is presented. It allows a significant increase of the operation frequency due to fast termination of the gas generated by the electrochemical process. The actuator consists of a working chamber with metallic electrodes and supplying channels. The chamber is formed in a layer of SU-8 and covered by a flexible polydimethylsiloxane membrane, which deforms as the pressure in the chamber increases. Cyclic operation of the device is demonstrated at a frequency of 200 Hz that is four orders of magnitude faster than for existing electrochemical microactuators.

KEYWORDS

Actuator, electrolysis, bubbles, microsystems

INTRODUCTION

Membrane actuator is a wide spread component of microfluidic systems. It is a key part of pumps [1], valves [2], lenses, mirrors [3] and other devices. Different mechanisms driving the membrane are in use such as pneumatic, piezoelectric, and electromagnetic to mention a few [4]. Since the actuator is usually integrated with other microfluidic components, its structure should be as simple as possible. Electrochemical actuation is very attractive because it allows a simple design and provides a strong response. It is based on the electrochemical gas production with the following termination of the gas. The main disadvantage is a long response time due to slow recombination of the gas inside of the working chamber [1]. Recently a short-time electrolysis using alternating polarity voltage pulses was demonstrated, which allows fast generation and termination of the gas [5]. Here we describe design and performance of the electrochemical membrane actuator working on the new actuation principle.

MATERIALS AND METHODS

Design of the actuator is schematically shown in Fig. 1. The device has a working chamber with metallic electrodes inside it, channels for filling the system with the electrolyte, and holes for connection with microfluidic tubes. The diameter of the chamber is 500 µm and the height is 8 µm. An oxidized silicon substrate is used as the bottom wall, the side walls are made of cured SU-8 resist, and the upper wall is the flexible polydimethylsiloxane (PDMS) membrane with a thickness of 30 µm. The material of electrodes is 500 nm thick Al layer covered by a 500 nm thick Ti layer. The electrolyte is a molar solution of Na_2SO_4 in distilled water. A photo of the actuator with close-up view of the chamber is shown in Fig. 2. In this work we use circular electrodes. They provide more homogeneous current density distribution in comparison with the interdigitated fingers used previously [6].

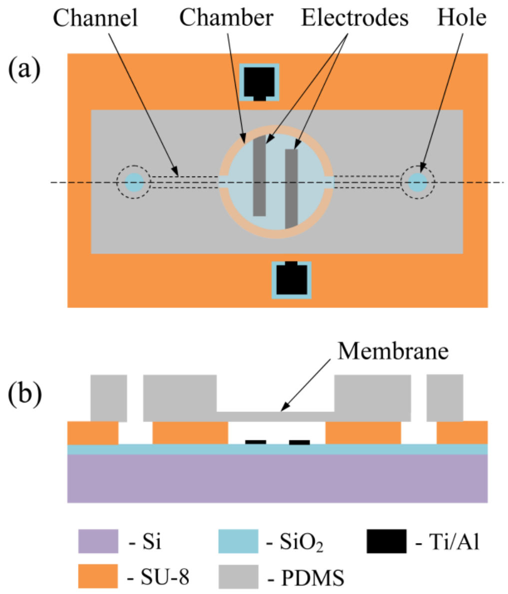

Figure 1: Design of the actuator: top view (a) and the cross-section (b).

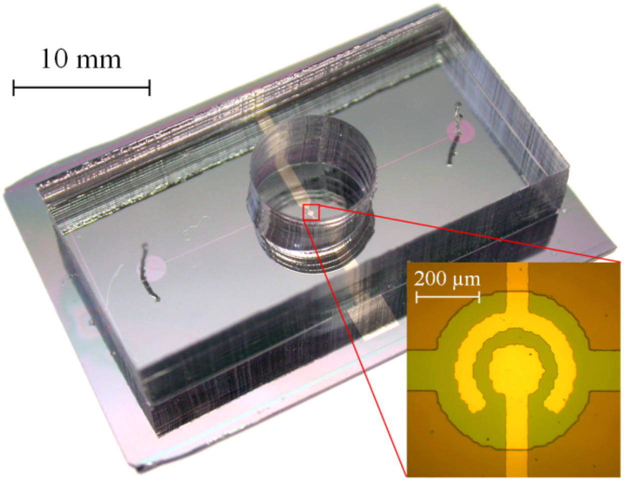

Figure 2: Ready to use actuator. The inset shows a zoomed view of the working chamber.

The actuator operates in the following way. A series of short (~1 µs) voltage pulses of alternating polarity is applied to the working electrode while the other one is grounded. These pulses produce hydrogen and oxygen due to water electrolysis but all the gas is collected in nanobubbles [5]. The pressure increases in the chamber and pushes the membrane up. When the pulses are switched off, the gas in nanobubbles recombines into water in 1 ms or so releasing the pressure and the membrane returns to its initial state. Unlike the conventional operation mode when a single polarity voltage pulse is applied to the electrodes, in the alternating polarity mode hydrogen and oxygen molecules are not spatially separated and form not only H_2 and O_2 bubbles, but also bubbles containing mixtures of H_2 and O_2 [5]. The latter disappear in the reaction, which is ignited in nanobubbles spontaneously. The mechanism of the reaction is still not completely clear but the reaction happens with the assistance of the gas-liquid interface [5]. Short recombination time allows a significant reduction of the actuation cycle.

The main steps of the fabrication process are shown in Fig. 3. The process includes three stages. At the first stage a silicon substrate containing the electrodes, the chamber and channels is prepared. The wafer is thermally oxidized in wet oxygen so that a dielectric layer of a thickness of 0.9 µm is formed (Fig. 3a). Next, the electrodes are fabricated (Fig. 3b). A 10 nm thick adhesive Ti layer, 500 nm thick Al layer, and 500 nm thick Ti layer are deposited by magnetron sputtering followed by the UV photolithography and the wet etching of Ti/Al/Ti layers. Further, the walls of the chamber and channels are formed in 8 µm thick layer of the photoresist SU-8 3005 (Fig. 3c). The post-exposure baking of SU-8 is done at a temperature no higher than 95 °C in order to preserve the residual epoxy groups on the SU-8 surface [7].

At the second stage a PDMS structure holding the membrane is fabricated. The silicon wafer is treated in hydrofluoric acid solution for 10 s to make its surface hydrophobic. Then a PDMS layer with a thickness of 30 µm is applied to the wafer by spin-coating of liquid compound (Sylgard 184, 10:1 mixture) and curing at the temperature of 100 °C during 35 min (Fig. 3d). Next, 4 mm thick PDMS structure with a through hole of 8 mm in diameter is formed separately and bonded to the thin PDMS layer using oxygen plasma treatment (Fig. 3e). Further, the structure is detached from the wafer with the through hole being closed by a membrane. After that the inlet and outlet holes with a diameter of 0.5 mm are made in the structure by a biopsy puncher (Fig. 3f).

At the final stage the PDMS structure and the silicon substrate are assembled together using irreversible bonding of PDMS to SU-8 (Fig. 3g). The bonding is based on the chemical reaction between PDMS and SU-8 by generating amino groups on PDMS surface with nitrogen plasma treatment and allowing the amino groups to react with the residual epoxy groups on SU-8 surface at elevated temperatures [7]. The PDMS structure is exposed to N_2 plasma with the pressure of 0.5 mbar and 700 W power during 1 s. Exposed surface is brought into contact with the SU-8 surface. The assembled parts are treated at 100 °C for 30 min to drive the chemical reaction. After cooling the samples are ready for filling with the electrolyte and testing.

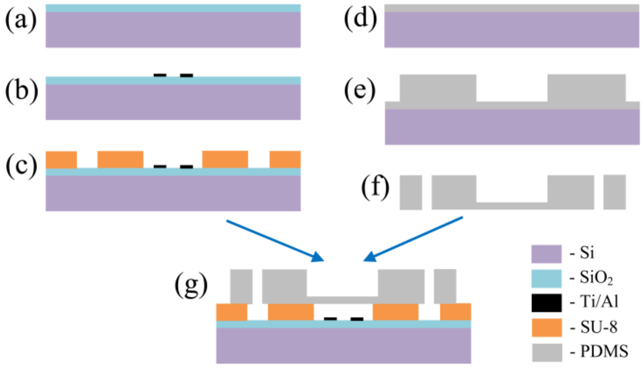

Figure 3: Fabrication procedure.

Performance of the actuator is measured using a homemade interferometer with orthogonal signals. Laser beam (wavelength $\lambda = 0.63$ µm) is focused on the center of the membrane by 10x objective lens. To increase the reflectivity of the membrane 20 nm thick Al layer is deposited onto its surface. The driving voltage is provided by a waveform generator Tektronix AFG1022 and amplified ten times using a homemade amplifier. The voltage, current flowing through the electrodes, and the output signals of the interferometer are recorded by a PicoScope 5000.

RESULTS AND DISCUSSION

To drive the actuator a series of $N = 40000$ rectangular voltage pulses of alternating polarity with a duration of $t_0 = 1$ µs (frequency of pulses $f = 500$ kHz) is applied to the electrodes. Duration of the series is $t_s = Nt_0 = 40$ ms. Deflection of the membrane with time at a different amplitude of pulses U is shown in Fig. 4. During the first 5-10 ms the membrane moves upward at a constant speed but then the process slows down. Increase in the voltage amplitude U leads to a higher deflection. The deflection of 7 µm is achieved at $U = 12$ V. When the amplitude increases up to 13 V an explosion of a microbubble happens inside of the chamber that sharply pushes the membrane (red line in Fig. 4). The bubble can not be observed directly during the test because the membrane is optically opaque. Nevertheless, the explosion is accompanied by a typical drop of the current in the system [6, 8]. The observed part of the membrane has the speed of about 4 mm/s. The deflection of the membrane exceeds 20 µm that is nearly 3 times higher than the deflection without formation of the microbubble.

Exploding microbubbles were observed previously in an open system [8] and in the closed chamber [6]. A series of the voltage pulses provides a high concentration of the H_2 and O_2 nanobubbles inside of the chamber. When the concentration is high enough, nanobubbles merge into a microscopic bubble. This bubble contains a stoichiometric mixture of gases and the combustion reaction is ignited in the bubble spontaneously producing a significant pressure jump that pushes the membrane. The explosions can significantly increase the force and stroke of the actuator. However, here we are concentrated on the actuation regime without explosions.

Dependence of the maximum membrane deflection per cycle on the pulse amplitude is shown in Fig. 5. The data for different number of pulses N in a series are also presented. For each N the value of U is limited by the explosion of the bubble. The longer the series, the lower the amplitude of pulses needed to obtain a given deflection. The highest deflection of 8.3 µm is reached at $U = 13.4$ V and $N = 20000$.

The longest series of pulses used in the experiment has a duration of $t_s = 40$ ms. When the pulses are switched off, the membrane returns to its initial state in about $t_r = 40$ ms (see Fig. 3, $U = 11$-13 V). Thus, the duration of the operating cycle t_c does not exceed 100 ms, and the actuator can work at a frequency f_c of about 10 Hz. The cycle duration for existing electrochemical actuators is several minutes [1, 9], which corresponds to a frequency of 0.01 Hz. Thus, a short-time electrolysis produced by the alternating polarity voltage pulses demonstrates the increase of the operating frequency by three orders of magnitude.

Periodical operation at $f_c = 10$ Hz is shown in Fig. 6a. The membrane oscillates with the amplitude $d = 4.7$ µm. The volume of liquid pumped per cycle by a micropump (for example, peristaltic) based on this actuator can be estimated as $V_0 \approx 0.5\pi R^2 d = 0.5$ nl, where $R = 250$ µm is the radius of the working chamber. The flow rate of such a pump would be $Q = 60 f_c V_0 = 0.3$ µl/min.

Nevertheless, the actuator can work even faster. The complete return of the membrane to the initial state is not necessary. It can stay deformed during operation and oscillate around a certain equilibrium position. Fig. 6b demonstrates cyclic work at the frequency $f_c = 200$ Hz. In this case short series of pulses ($N = 1000$) is applied to the device. Relatively high amplitude $U = 22$ V is needed to maintain sufficient deflection of the membrane. Low oscillation amplitude $d = 1.3$ µm is compensated by high operation frequency. Flow rate of the pump would be $Q = 1.7$ µl/min. It is comparable with the value provided by modern microactuators, although they have much larger chamber volume (> 10 µl [1, 9]) than the presented device (1.6 nl). Small chamber volume is beneficial for drug delivery systems where the precise dosing is necessary [10].

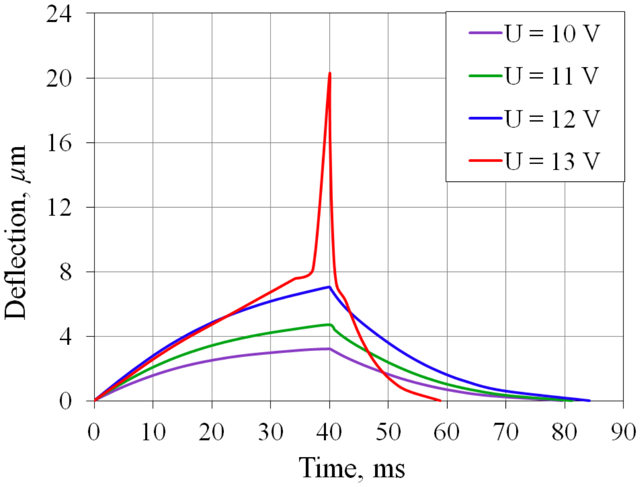

Figure 4: Deflection of the membrane with time for the series of N = 40000 pulses. At U = 13 V the membrane is sharply pushed up by the explosion of the microbubble in the chamber.

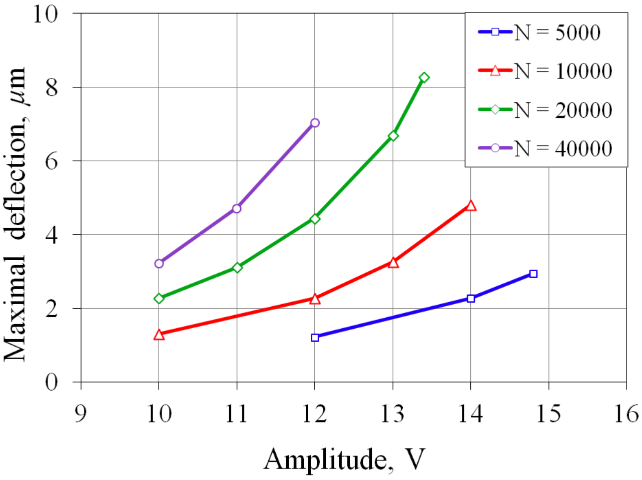

Figure 5: Dependence of the maximal membrane deflection per cycle on the amplitude of pulses.

A problem revealed by the tests is a gradual degradation of the electrodes. A layer of titanium oxide grows on their surface with operation time and reduces the Faraday current. As a result higher voltage is required to keep the current sufficiently large. Due to titanium oxidation the consumed power cannot be reduced below 0.25 W. Additional work has to be done to find an appropriate material for the electrodes and reduce the power consumption.

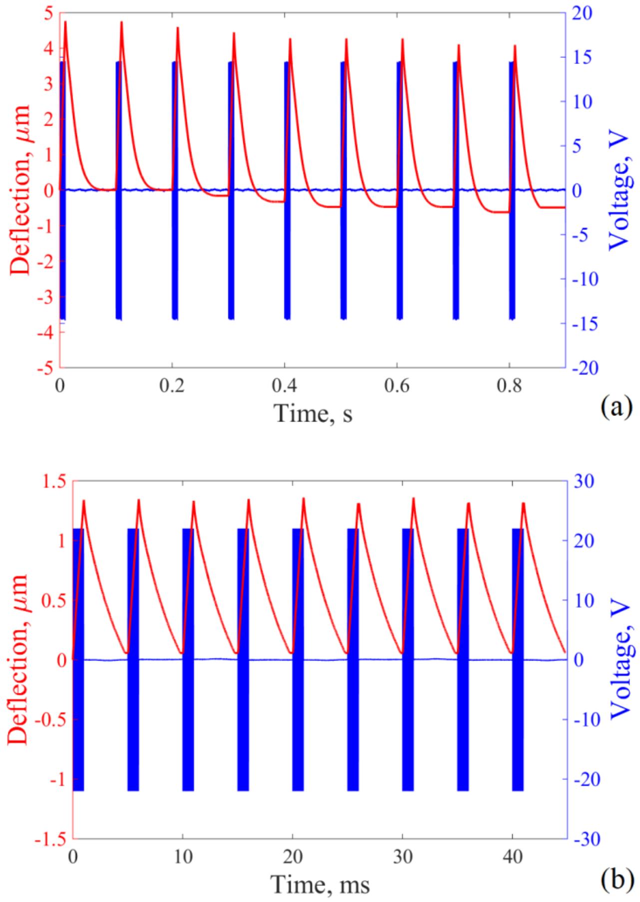

Figure 6: Cyclic operation of the actuator. (a) Series of pulses are applied at the frequency f_c = 10 Hz. N = 10000, U = 14 V. (b) f_c = 200 Hz, N =1000, U = 22 V.

CONCLUSIONS

An electrochemical membrane actuator was presented. It was designed to demonstrate a new actuation principle based on water electrolysis with a fast change of voltage polarity. The device consisted of the oxidized silicon substrate with metallic electrodes, working chamber covered by PDMS membrane, and channels for liquid. Performance of the actuator was investigated, deflection of the membrane was measured using a homemade interferometer. Recently proposed alternating polarity mode allowed to achieve sufficiently short actuation cycle due to very short time for the gas termination in comparison with conventional electrochemical actuators. Cyclic operation at frequency as high as 200 Hz was demonstrated. Micropump based on the actuator could give a flow rate of the order of 1 µl/min and provide pumping of liquid by portions of less than 1 nl.

ACKNOWLEDGMENTS

We thank H.S. Rho for help with the fabrication of PDMS membranes. This work is supported by the Russian Science Foundation, Grant No.15-19-20003.

REFERENCES

[1] Y. Yi, U. Buttner, A.A.A. Carreno, D. Conchouso, I.G. Foulds, “A Pulsed Mode Electrolytic Drug Delivery Device”, J. Micromech. Microeng., Vol. 25, 105011, 2015.

[2] D.E. Lee, S. Soper, W. Wang, “Design and Fabrication of an Electrochemically Actuated Microvalve”, Microsyst. Technol., Vol. 14, pp. 1751-1756, 2008.

[3] A. Werber, H. Zappe, “Tunable Pneumatic Microoptics”, J. Microelectromech. Syst., Vol. 17, pp. 1218-1227, 2008.

[4] A.K. Au, H. Lai, B.R. Utela, A. Folch, “Microvalves and Micropumps for BioMEMS”, Micromachines, Vol. 2, pp. 179-220, 2011.

[5] V. Svetovoy, A. Postnikov, I. Uvarov, R. Sanders, G. Krijnen, “Overcoming the Fundamental Limit: Combustion of a Hydrogen-oxygen Mixture in Micro- and Nano-bubbles”, Energies, Vol. 9, 94, 2016.

[6] I.V. Uvarov, S.S. Lemekhov, A.E. Melenev, V.B. Svetovoy, “Exploding Microbubbles Driving a Simple Electrochemical Micropump”, J. Micromech. Microeng., Vol. 27, 105009, 2017.

[7] Z. Zhang, P. Zhao, G. Xiao, B.R. Watts, C. Xu, “Sealing SU-8 Microfluidic Channels Using PDMS”, Biomicrofluidics, Vol. 5, 046503, 2011.

[8] A.V. Postnikov, I.V. Uvarov, M.V. Lokhanin, V.B. Svetovoy, “Highly Energetic Phenomena in Water Electrolysis”, Sci. Rep., Vol. 6, 39381, 2016.

[9] H. Gensler, R. Sheybani, P.-Y. Li, R.L. Mann, E. Meng, “An Implantable MEMS Micropump System for Drug Delivery in Small Animals”, Biomed. Microdevices, Vol. 14, pp. 483-496, 2012.

[10] M.S. Giri Nandagopal, R. Antony, S. Rangabhashiyam, N. Sreekumar, N. Selvaraju, “Overview of Microneedle System: a Third Generation Transdermal Drug Delivery Approach”, Microsyst. Technol., Vol. 20, pp. 1249-1272, 2014.

CONTACT

* I.V. Uvarov, i.v.uvarov@bk.ru

MEMS BASED ROTARY VALVE

G.A.J. Besselink[1], F. Schreuder[1], F. Falke[1], V. Berweiler[2], H.F. Knapp[3], S.F. Graf[3], A. Prak[1],
T.T. Veenstra[1] and R.G. Heideman[1]
[1] Lionix International BV, Enschede, The Netherlands
[2] EPFL, Lausanne, Switzerland
[3] CSEM, Alpnach, Switzerland

ABSTRACT

MEMS based rotary valve

This work describes the fabrication of a MEMS based rotary valve and its integration with a micro sensor. The sensor was used for the monitoring of the refractive index of the valve outlet stream in order to test valve functionality. The MEMS based valve approach shows advantageous properties such as compactness, a high configurability by design, and small internal volumes. Results are shown of a favorable injection of sample from a sample loop with a marked reduction of plug dispersion.

KEYWORDS

MEMS, valve, rotary valve, injection valve, liquid handling, sample loop, refractive index, sensor.

INTRODUCTION

Valving is a very important functionality in (microfluidic) biosensor systems especially when the sensor has to be regenerated and multiple liquids, including the sample, have to be used in a timely and ordered fashion. Several different types of microvalves have been described in the literature [1] from which the pneumatic- and the pinch-type microvalves are well-known. The rotary valve, on the other hand, is a type of valve that is very commonly used in analytical laboratory equipment due to attributes such as robustness of operation, fastness of fluid switching and a limited internal volume. Disadvantages of these valves are the high costs and the bulky size of the set-up (including motors and connections). The current work describes a hybrid fabrication approach [2] for delivering a MEMS based rotary valve, which in principle can replace a whole set of standard multiport rotary valves. Furthermore, a further system integration step was carried out by combining the MEMS based rotary valve with an optofluidic micro sensor chip. This way, an assembly was realized that is compact, configurable by design and has a low internal volume. This approach was developed within one of our previous EU projects (BIOFOS) that aimed to realize a demonstrator for early detection of food contamination. Goal of the liquid handling development work within BIOFOS was to automate all liquid handling steps that belonged to the BIOFOS bioassay protocol (injection and/or dilution of sample, incubation, washing, regeneration and preconditioning). The current paper describes the valve design, its way of operation and some basic functional testing.

MATERIALS AND METHODS

Rotary valve

The MEMS based rotary valve consists of a liquid handling chip (‘stator’) and a Teflon rotor part (‘rotator’). The liquid handling chip was made from borosilicate glass and fabricated by application of several photolithography steps in combination with processing steps such as wet etching, powder blasting, gold layer deposition, and fusion bonding. The basic layout of the liquid handling chip (Figure 1) comprises several microfluidic channels (320 μm x 60 μm (width x depth)) that have outlets at the bottom side (Figures 1 and 2: holes in blue) for connection to the outer world (Figure 2) and outlets at the top side (Figure 1: holes in orange) that are opened/closed by the proper positioning of the Teflon rotor. In the center, a through hole (in grey) was made in order to accommodate the rotary axis. Additionally, gold leads and electrodes (Figure 1: in orange/yellow) were microfabricated in order to implement five separate conductivity sensors that in principle can be used for checking the filling state of individual channels.

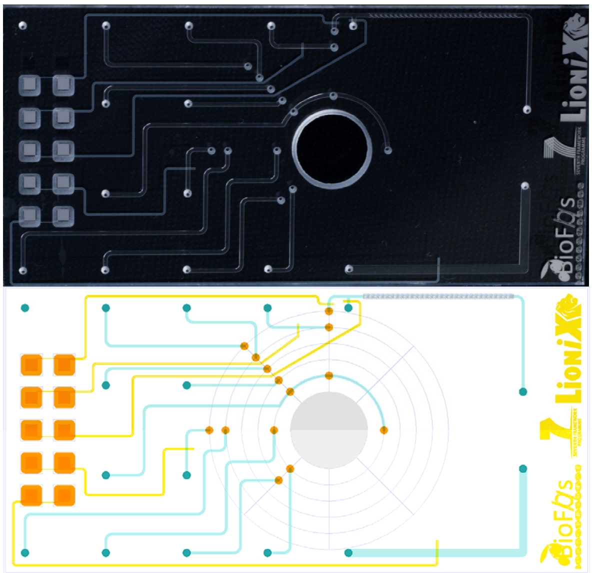

Figure 1: Top: Photomicrograph of the liquid handling chip (dimensions: 19x45 mm, thickness: 1.4 mm). Bottom: Drawing of the chip design.

Flow was supported by two peristaltic pumps (P1 and P2), which could be done in an automated way by using a liquid handling script. P1 and P2 support flow through the available flow path as the pump tubings are connected to specific outlets at the bottom of the liquid handling chip (P1/P2, IN/OUT in Figure 2). In the original BIOFOS bioassay protocol, delivery of buffer fluids is mainly supported by P1; delivery of the sample loop content is done by the action of P2. Loading of the sample loop was done manually by using a disposable syringe.

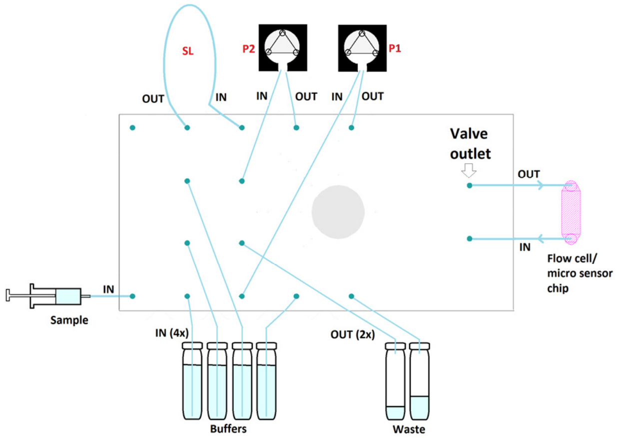

Figure 2: Schematic representation of the configuration of the bottom outlets of the liquid handling chip regarding their connection to the outer world. Flow was supported by two peristaltic pumps (P1 and P2) while the loading of the sample loop (SL) was done by means of a syringe.

The microfabricated Teflon rotor part (Figure 3) is designed to be mounted on top of the liquid handling chip (at an applied torque of about 0.5 Nm). The surface of the Teflon part is in intimate contact with the glass chip and contains slots that, depending on the position of the rotor, enable establishment of a flow path between specific fluidic outlets on the top side of the liquid handling chip. The rotational position of the rotor is controlled by a stepper motor (Figure 4) and can be adjusted in 8 steps.

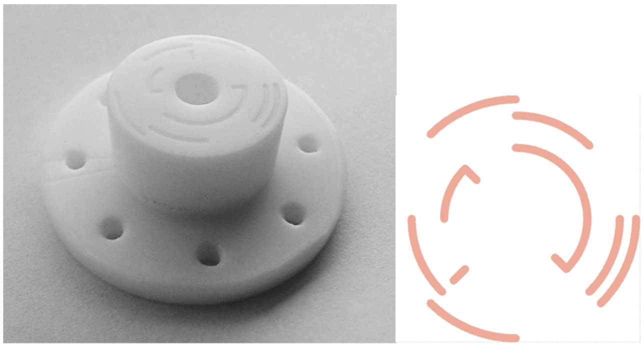

Figure 3: Left: Photograph of the Teflon rotor. Right: Design of the slots on the surface (slot dimensions: 0.6 mm x 0.3 mm (width x depth)).

Assembly with micro sensor

As part of the final assembly, the outlet of the rotary valve was closely connected to a flow cell on a separate sensor chip (schematically indicated as 'Flow cell/micro sensor chip' in Figure 2) for the monitoring of the refractive index of the valve outlet stream [3]. This way, the functionality of the valve could be tested. The assembly of the MEMS based rotary valve together with the sensor chip holder is shown in Figure 4.

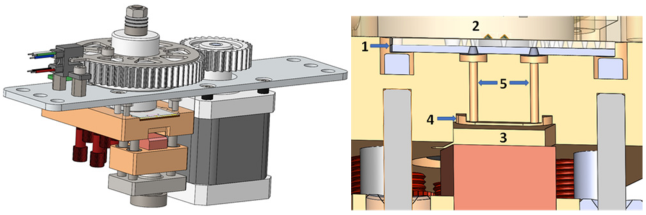

Figure 4: Left: CAD drawing of the rotary valve/ sensor chip assembly. Right: Cross-sectional view, 1: liquid handling chip, 2: Teflon rotor, 3: space in holder for sensor chip, 4: flow cell, and 5: inlet/outlet channel for the fluidic connection between the rotary cell and the sensor chip.

RESULTS

Operating pressure

In order to measure the operating pressure in the fluidic system, the rotary valve assembly was filled with water and a pressure sensor was attached to an inlet by means of a T junction. System pressure appeared to be directly dependent on the flow rate, reaching a value of ≈2.5 Bar at a flow rate of 1 ml/min (Figure 5). In a preliminary check, leak tightness of the rotary valve was proven at system pressures of 2500 mBar and higher. Maximal flow rate applied during our experiments was 180 µl/min (corresponding with a system pressure of about 500 mBar), which makes this a safe flow regime with regard to leakage.

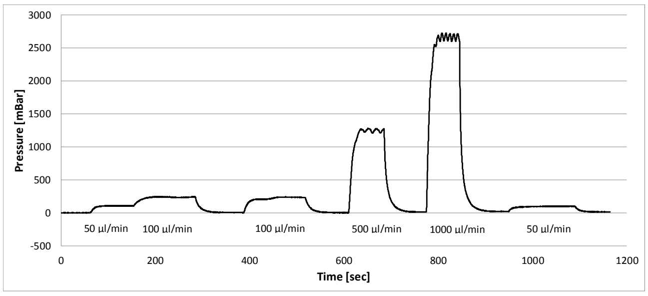

Figure 5: System pressure measured on the rotary valve assembly at different volumetric flow rates.

Switching valve performance

Functional testing was done with water and different sucrose solutions in order to enable distinction of the different liquid streams by refractive index sensing. The refractive index of the valve outlet stream was monitored by the closely attached micro sensor. Selection of the one or the other liquid requires the rotation of the Teflon rotor part toward a certain position as schematically shown in Figure 6. The switching valve performance was tested by stepping between three different model liquids (0, 2.9 and 8.5 % (w/w) sucrose in water) from different vial sources and their connections to the respective outlets (Bind.Buf, Wash.Buf and Reg.Buf).

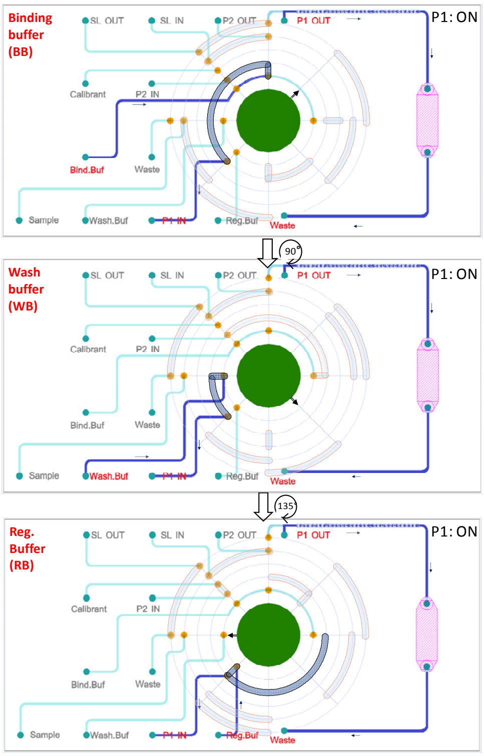

Figure 6: Schematic drawing for explaining the principle of the switching valve operation. Channels in dark blue indicate the flow path that is active while the outlet names in red are the relevant active connects. The rotational position of the rotor valve is indicated by means of an arrow (←).

The results revealed a distinct stepping behavior and the reaching of stable plateau levels as shown in Figure 7. Furthermore, very similar and reproducible results were found when testing three separate rotary valve/sensor chip assemblies that were fabricated according to the same procedure.

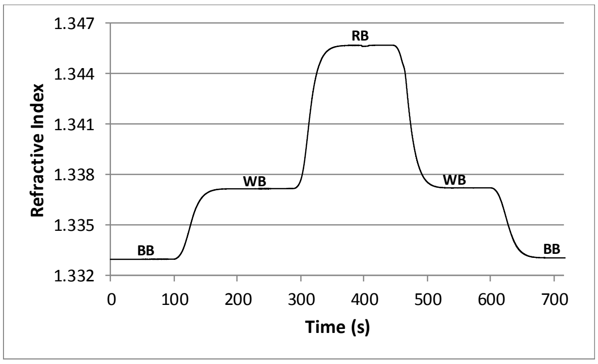

Figure 7: Refractive index monitoring on the valve outlet stream during liquid switching.

Injection valve performance

An injection valve is a specific type of switching valve, which is extended with a sample loop. The purpose of an injection valve is to introduce a specified volume of sample into a carrier stream toward a separation or detection system while maintaining a continuous flow. The principle of the injection valve operation is schematically shown in Figure 8.

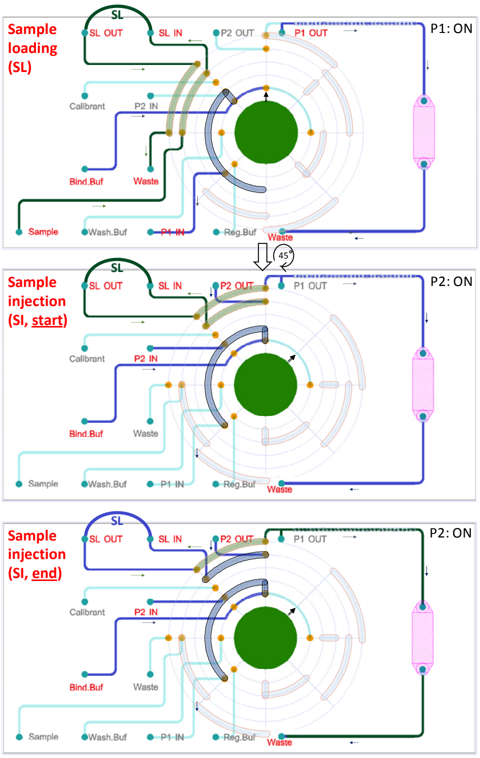

Figure 8: Schematic drawing for explaining the principle of the injection valve operation. Channels in blue (buffer) and green (sample) indicate the active flow paths while the outlet names in red are the relevant active connects. Rotational position of the rotor is indicated by (←).

Introduction of sample in the sensor chip was very rapid as indicated by the very steep and nearly stepwise change in signal level when switching from water to a solution of sucrose in water (solid line in Figure 9). This stepwise introduction of sample is related to the small internal volume of the rotary valve/sensor chip assembly (a total of about 4 µl between the sample loop outlet and the refractive index micro sensor). Sample injection was also done by using a conventional injection valve directly connected to P1 OUT using narrow-bore feed tubing (internal volume: 5.3 µl). Injection with the conventional injection valve resulted in a sample plug that was less confined at the front end (Figure 9: dashed line). The time that was needed for reaching the higher plateau in signal level was <10 seconds for the micromachined rotary valve and about 80 seconds for the conventional valve (Figure 9). In order to have an internal check for the actually delivered injection volume, differential flow was applied during sample injection namely a doubling of flow rate (from 30 to 60 µl/min) after the first 200 µl injection volume. This change in flow rate can be recognized in the graph as a kink (indicated by an arrow in Figure 9) occurring at the rear end of the sample plug. It is obvious that, also with the MEMS based rotary valve, significantly more elution volume (>200 µl) was needed compared to the 100 µl internal volume of the sample loop, which is related to the high extent of plug dispersion at the rear end. Cause of this enhanced dispersion at the rear end is the radial diffusion of the highly diffusive sucrose (diffusion coefficient $\approx 5.2\text{x}10^{-10}$ m^2/s), which becomes increasingly dominant at a longer plug passage time.

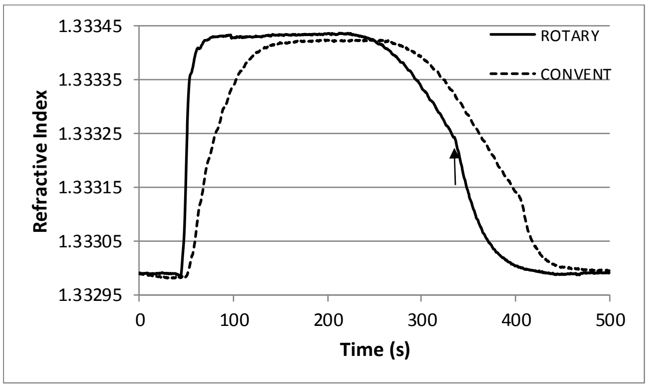

Figure 9: Refractive index measured on the valve outlet stream during sample injection of sucrose (0.3 % (w/w) in water). Sample loop volume was 100 µl. At the point indicated by the arrow, the flow rate was changed from 30 µl/min to 60 µl/min.

Duration of the plateau phase in the case of the MEMS based and conventional rotary valve systems was about 170 s and 130 s, respectively. The shorter duration of the plateau phase for the conventional system can be explained by the higher extent of dispersion at the plug front end. Dispersion at the plug rear end was nearly similar for the both systems.

Partial loop injection

One way to limit the extent of plug dispersion at the rear end is to apply partial loop injection, i.e., to inject a volume that is smaller than the internal volume of the sample loop. This keeps contact time between the rear end of the injected sample plug and the carrier stream limited and involves injection of mainly the front end part of the sample plug. Figure 10 shows an example of the well-defined plug that was found when executing partial loop injection. As a result, original sample concentration was preserved over more than 95% of the sample passage time.

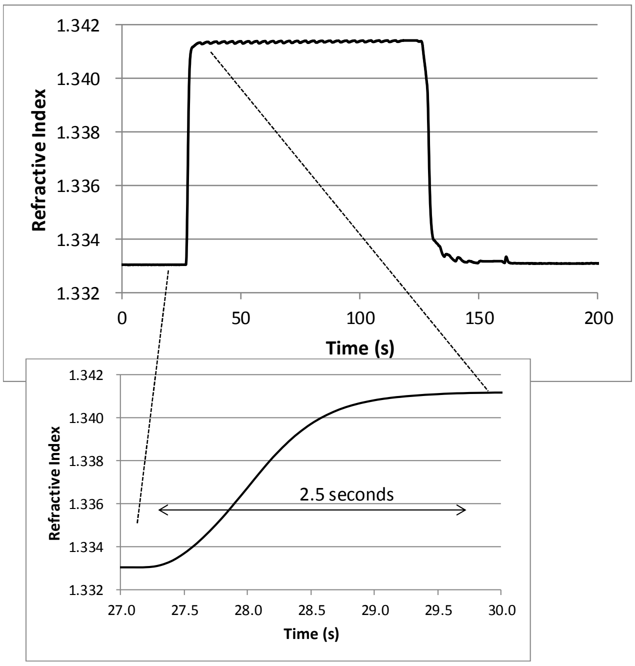

Figure 10: Refractive index measured on the valve outlet stream during partial (≈50%) loop injection of sucrose (5.8 % (w/w)).

CONCLUSIONS

An advanced system integration has been described for fabrication of a MEMS based rotary valve and its combination with a sensor chip. This assembly is compact, configurable by design and has a low internal volume. Results are shown of a reliable fluid switching and a favorable sample loop injection with a marked reduction of plug dispersion.

REFERENCES

[1] A. Au, H. Lai, B. Utela, A. Folch, “Microvalves and Micropumps for BioMEMS”, Micromachines, Vol. 2, pp. 179-220, 2011.

[2] A. Prak, H. Leeuwis, R. Heideman, A. Leinse, G. Borst, “Integration of Optical Waveguides and Microfluidics in a Miniaturized Antibody Micro-Array System for Life Detection in the NASA/ESA ExoMars Mission”, Proc. of SPIE 2011, February 17, 2011, 79280L-1.

[3] G. Besselink, R. Heideman, E. Schreuder, L. Wevers, F. Falke, H. van den Vlekkert, “Performance of Arrayed Microring Resonator Sensors with the TriPleX Platform”, J. Biosens. Bioelectron., 7:2, 2016.

CONTACT

*G.A.J. Besselink, G.A.J.Besselink@lionix-int.com

ACKNOWLEDGEMENT

This work was supported by the EU-funded FP7 project ICT-BIOFOS (Contract No. 611528): www.ict-biofos.eu.

INNOVATIVE TECHNOLOGY FOR INTUITIVE FLUID FLOW CONTROL WITH PRESSURE ACTUATION ON A COMPACT DEVICE

*Clémence Vergne[1], Lionel Matthys[1], *Thibaut Thupnot[1]*
[1] Fluigent SA, Villejuif, FRANCE

ABSTRACT

This abstract presents research data on a new technology to regulate the pressure of fluid reservoirs for microfluidic setups such as lab-on-a-chip platforms or droplet generators. This technology relies on a unique combination of valves that are controlled by a dedicated algorithm which is much more advanced than simple PID routines. Indeed, the smart control of the different sorts of valves allows at the same time to reduce the reaching time, keeping a very high flow stability, reducing drastically the air consumption and the electrical consumption. This technology was integrated in the new Flow EZ™ product from the Fluigent new product series LineUP™.

KEYWORDS

Microfluidics, flow control, pressure actuation

INTRODUCTION

Conventional flow control systems, such as syringe and peristaltic pumps, are poorly adapted to the control of flows in microchannels. Our approach is based on a pressurization of reservoirs filled with fluids to be injected in the microsystem. The regulated pressure generates pulse-free and very stable flows through the microchannels, with short settling time. Coping with any external disturbance to deliver the best flow response, this technology is perfectly suited for droplet manipulation and microfluidic cell biology experiments.

Although pressure-driven flow proposes high performances in term of flow-rate settling time and stability, a pressure pump is used in microfluidic lab and needs to be designed on purpose. LineUP™ series fits in this term microfluidic lab bench needs. Setups evolve every day and the ability of adding injection lines directly by the customer requires expandable system. A microfluidic set-up is also very different from a lab to another with different number of pumps, need of valving systems, flow-rate ranges and so on. Modularity seems to be a good way of answering to all requirements and this is how we designed the LineUP™ series. Scientists involved in microfluidic researches have been changing from physicists and engineers to biologists and chemists. Nowadays, microfluidic is becoming more a tool with incredible advantages than a subject of study as it were in the 90’s. In order to let these scientists focus on their science, the microfluidic handling systems must be very easy to use. Software development has been a priority for Fluigent since our customers control our devices through it. We present here brand new software with all required functionalities: data logging, up to 16 injection line overview and control, modular graphic interface adapting its window disposition to the connected hardware.

For a long time, researchers have been limited by their microfluidic pumps’ performance. Historically, syringe pumps and peristaltic pumps have been adapted to microfluidic format but their technology leads to unsteady flows and long settling times at this scale. Short settling times lead to fast setting-up of an experiment and can be very useful when controlling single objects such as cells or droplets. Stability of flows is generally one of the most critical parameter for a microfluidic pump. Indeed, smooth flow leads to high droplet monodispersity or to good biological repeatability results.

We present here LineUP™ Flow EZ™ system, the next generation liquid handling device for microfluidic experiment with a smart modular design and the best specification on the market, along with Fluigent A-i-O Software providing a new user experience suited for microfluidic labs and scientists.

Flow EZ™ module

The working principle of a pressure controller is to pressurize the sample reservoirs in order to control the pressure drop between the inlets and the outlets of the microfluidic system (see Figure 1). It takes a constant pressure as an inlet and delivers a required pressure at its outlet. This regulated (outlet) pressure pressurizes the reservoir, driving the liquid up through the tubing and into the microfluidic setup. Controlling the outlet pressure allows the user to control the rate at which fluid is injected into the microfluidic setup.

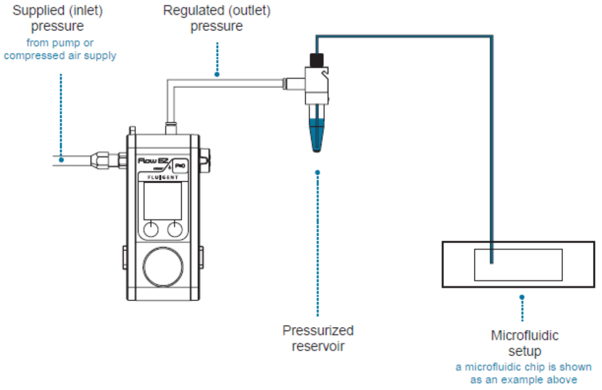

Figure 1:Working principle of microfluidic pressure pump

Generally speaking, pressure is not the value the experimenter wants to control and monitor. Indeed, depending on the hydrodynamic resistance of the fluidic system (basically the microfluidic chip and the tubing around it) a given pressure in the reservoir will lead to different flow-rates. The Flow EZ™ can connect a flow sensor (Flow Unit, Fluigent) for flow-rate control (see figure 2).

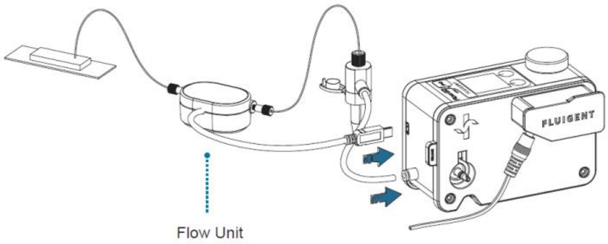

Figure 2: Connection of the flow sensor to the Flow EZ™.

Embedded functionalities

The local control of pressure and flow-rate has been a request from customers. The Flow EZ™ has an OLED display (see Figure 3) and few buttons for basic local features. All has been designed for an easy and intuitive start even for users not used to pressure regulators.

1 click: Set pressure to 0
Click again: go back to previous pressure
Long click: put it stand by

The functionality is written on the display

Turn dial: adjust the pressure/menu navigation
1 Click: Control off, select pressure value
Click again: Apply pressure
Click while in Menu: enter/OK

Figure 3: Close-up on the OLED screen and few features easily accessed.

The user can directly dial a pressure order in a very intuitive way, keeping his eyes on the microscope lens for example. An acceleration function induces big pressure increments when the dial is turned fast and very small increments when dialing slowly.

The embedded user interface has two main screens: the control window and a menu (See figure 4).

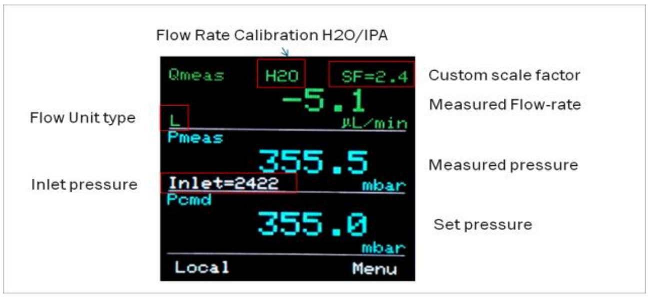

Figure 4: Control window of the Flow EZ™.

Among the features, the user can change flow rate and pressure units, apply a custom scale factor to the flow-rate monitoring when using particular fluids and calibrate the system.

Disposition in a lab bench

Generally speaking, a lab bench is not a spacious and clean surface; this sentence does not need any reference. A microfluidic pump can be invasive when several injection lines are involved. The philosophy of Line UP™ series is to feet to any lab bench. The system has been designed for operating in different positions (See figure 5)

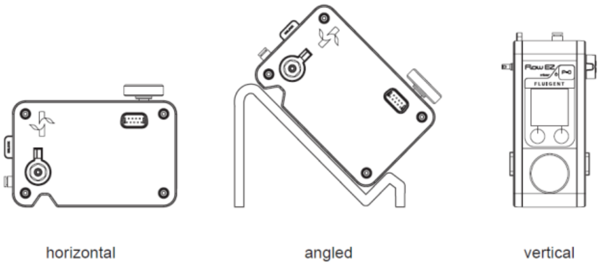

Figure 5: The Flow EZ can be used in different positions.

Wires and tubing are sometimes a mess and we decided to include a channel for managing inlet pressure tubing and power supply wire. We also raised the modules in order to give the possibility to pass outlet pressure tubing and the Flow Unit wires under the module (See figure 6).

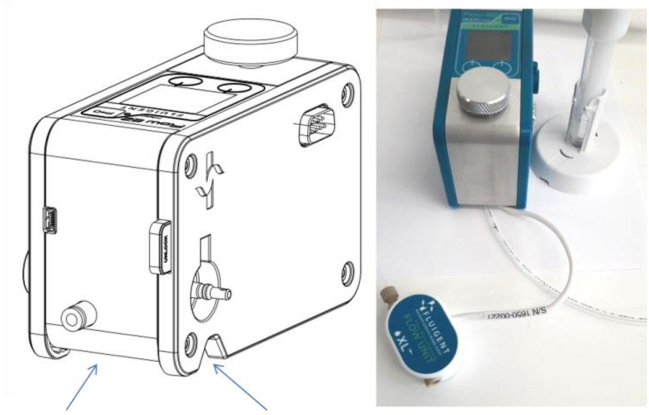

Figure 6: Wire and tubing management under the Flow EZ module.

Technology and performance

The resolution of the generated flow-rate depends on the resolution of pressure sensor in the pressure pump. For instance, the first technology Fluigent has developed, called FASTAB™, offers a resolution of 0.03% of the full scale (pressure sensor resolution) as well as a stability of 0.1% of the measured value. In term of responsiveness, the typical response and settling times of this technology is relatively fast and is a function of the technology of the pressure controller and the configuration of the microfluidic setup. For instance, based on the FASTAB™ technology, the MFCS™ series has a response time down to 40ms and a settling time down to 100ms for small reservoirs (< 15 mL).

The expansion of microfluidics in a large diversity of fields and the entering of microfluidics into industrial processes has highlighted the need to pressurize volumes that are more and more important. For that reason, we have developed a new technology that is based on a unique combination of valves and pressure sensors, controlled by a dedicated algorithm which is much more advanced than simple PID routines. Indeed, the smart control of the different sorts of valves allows at the same time to reduce the reaching time, keeping a very high flow stability. This technology allows to reduce drastically the settling time for reservoir which volume is higher than 15 mL.

The first results of this implementation are shown on figure 7, where the settling times for pressure or flow rate orders from 0µL/min to 1.5µL/min, and from 1.5µL/min to 0µL/min are compared to the response of a high precision syringe pump. The entire set-up was made of 50cm-long tubing with 50µm ID filled with distilled water. Settling times as low as 20ms can be easily be reached as compared to several minutes for the syringe pumps.

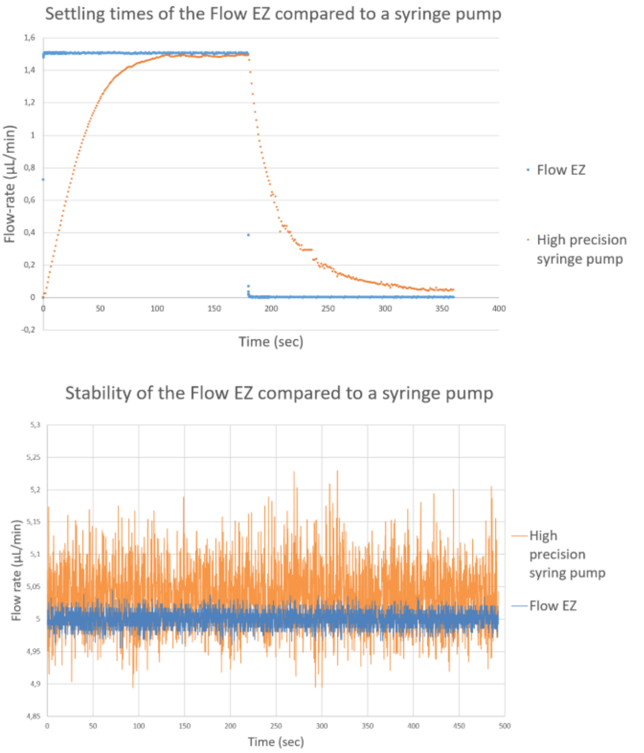
Settling times of the Flow EZ compared to a syringe pump

Stability of the Flow EZ compared to a syringe pump

Figure 7: Settling times for orders from 0µL/min to 1.5µL/min and from 1.5µL/min to 0µL/min. Stability measurements for 5 µL/min flow rates.

As there are no mechanical parts involved in the regulation of the pressure inside the reservoirs, the pulseless flow is comparable to Fluigent former technology. The results of this technology are also shown on figure 7, where the stability of the flow at 5µL/min is compared to the stability of a high precision syringe pump. A stability as low as 0.1% can be reached as compared to high precision syringe pumps.

Another field in which microfluidics is more and more useful is cellular biology. The biggest concern of cell biologist is to ensure the “good shape” of the cells all along the experiment, it means avoiding any mechanical constraint or noisy shear stress. For that reason, the technology has been developed on a modular way that allows to choose between two control modes. One is called the fast mode, which is the one by default. It is optimized for a very rapid pressurization of big volumes, adapted for experiments where long transient regimes result in a loss of costly reagents for instance. A second mode, called the smooth mode, has been optimized to settle the right pressure twenty times slower than the previous one to avoids all types of shear stress on cells. It was made really to tune the setup to fit the most with what matters for the user.

Then finally and focusing on the future of microfluidics, the air and electrical consumption have been reduced thinking of the future integration of our technology in more portative and autonomous systems.

Expendability concept

The LineUP™ Series is a modular microfluidic flow control system, allowing a user to stack different module in a line (figure 8). Today, two modules are proposed: The Link module allows a stack to be connected to a PC for controlling and monitoring. The Flow EZ™ is a pressure regulator.

Figure 8: LineUP™ system. A: Link module. B: Flow EZ™ module.

The user can stack up to 8 Flow EZ™ modules in a line by oneself and in a hot plug and play way, meaning that the system does not need to be rebooted when a new unit is connected. The expandability of the system requires communication, power supply and inlet pressure to be transmitted from one unit to the downstream modules (See figure 9). From a pressure side of view, this feature needs smart connectors: opened when connected and closed when disconnected.

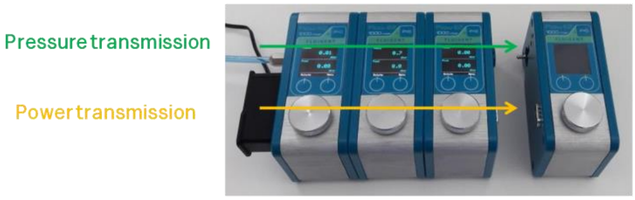

Figure 9: Expandability concept of the LineUP™ series.

Fluigent A-i-O Software

The ability to control the pressure orders directly from the Flow EZ™ module comes with the option to control the order from a dedicated software as well: the Fluigent All-in-One software. The connection between the pressure regulator and the computer is made through a USB cable to the Link module.

In addition to the live monitoring and control of the pressure and the flow-rates (if flow sensors are connected to the Flow EZ™), the software offers a 20ms sampling rate for data recording. Work has been made to highly customize the user interface, with resizable panels for instance, to keep the use of the software as intuitive as the direct control on the Flow EZ™. A caption of the interface is shown in Figure 10.

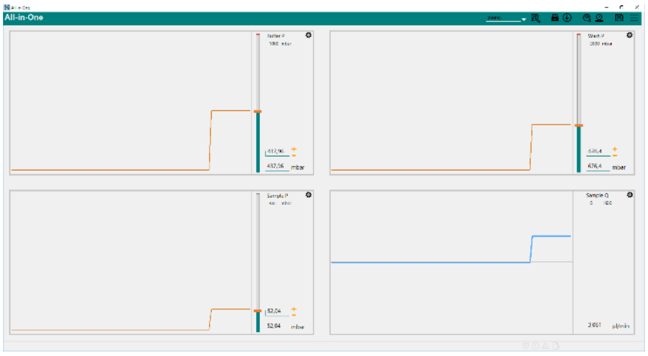

Figure 10: Caption of the A-i-O software panel with 3 pressure channels (orange) and 1 flow-rate measurement (blue) display.

Graphs can be displayed in absolute values or in relative values (in percentage of the full scale) for a complete visualization.
An integrated help has been integrated as well to guide users in need of advice on the modules and the features of the software.

CONCLUSION

We developed a complete solution for a very versatile use of our products. The technology kept all the advantages of the pressure actuation and improved the drawbacks of the former technology. Each pressure block can be easily used on its own, can be easily used with other modules within a line. All modules can be easily controlled directly with the intuitive dial, or remotely from the software.

CONTACT

*Thibaut Thupnot, Thibaut.thupnot@fluigent.com

Demonstration of Active Microfluidic Valves Fabricated in Cyclic Olefin Copolymer

B. Hoogenberg [1], M. Skolimowski[1], D. Jonker[1,2], and M. Blom[1]*
[1] Micronit Microtechnologies BV, Enschede, The Netherlands
[2] Saxion University of Applied sciences, Enschede, The Netherlands

ABSTRACT

We report active microfluidic valves fabricated in cyclic olefin copolymer (COC). The monolithic valve device is assembled without use of adhesives. The longevity tests and valves characteristic are presented. The future application of COC microvalves includes Lab-on-a-Chip and Organ-on-a-Chip systems, where use of materials other than silicone rubbers is required.

KEYWORDS

Active microfluidic valves, cyclic olefin copolymer, COC, fluid handling

INTRODUCTION

Active valving

The control of fluid movement or circulation is a key functionality in both Lab-on-a-Chip and Organ-on-a-Chip systems. Active microfluidic valves are subject of many research papers in recent years. The most widespread solutions are based on an actuation of a flexible membrane, usually made of poly(dimethylsiloxane) (PDMS). These valves were first proposed by Unger *et al.* [1] and are commonly referred to as “Quake’s valve”. The most prominent drawback of valves based on PDMS is the material used for fabrication. Although the high flexibility of PDMS makes it a suitable material for membrane fabrication, other properties, like incompatibility with most of non-aqueous solutions and tendency to absorb a wide range of organic compounds, limits its applications. In this work, we describe a solution based on monolithic valve fabrication in Cyclic Olefin Copolymer (COC), that solves those issues and is suitable for a much wider application range.

METHODS

Design

The normally-closed active valve consists of a fluidic side and a pneumatic side, which are separated by an elastomeric COC membrane. On the fluidic side, an obstruction can prevent flow when being closed. On the obstruction, the membrane is not bonded to the substrate, thus allowing fluid to flow from the inlet to the outlet. The pneumatic chamber is used to exert pressure on the membrane, which tightly presses the membrane on the obstruction and thereby closes the valve. Increased pressure on the fluid deflects the membrane, thereby further opening the valve and decreasing the fluidic resistance.

The valves used in the experiments reported in this paper have a diameter of 2000 µm diameter and are 100 µm deep on both peumatic and liquid sides. The pneumatic side consists of a circular cavity with the above mentioned dimensions while the fluidic side consists of two opposing cavities with an 800 µm-wide obstruction, here referred to as the *valve seat*, separating those. The obstruction covers the whole diameter of the valve. The cavities are connected with inlet and outlet channels. The two channels are in-line with each other. The pneumatic connection channel, reaching the pneumatic cavity, enters cavity perpendicular to the fluidic channels.

Fabrication

Two COC substrates (TOPAS 8007) were patterned using micromilling (m10 PRO, DATRON). Submillimeter tools were used to create the cavities designed for the fluidic- and pneumatic side. In addition, drilling operations created the connection vias that will later be used to connect the chip to the microfluidic setup. A 100 µm thick COC elastomer (TOPAS E140) was patterned using a CNC cutting plotter. After patterning, all layers were thoroughly cleaned using a DI and IPA.

The valve obstruction surface was treated to prevent permanent bonding of the flexible membrane. Then, the stack was combined and bonded using direct fusion bonding techniques.

Experiment setup

The valve chips were connected using a Fluidic Connect Pro (Micronit Microtechnologies), ferrules (Micronit Microtechnologies, 1/16” ID), and PTFE tubing (1/16” OD, 1mm ID). A pressure controller (MFCS, Fluigent) was used to apply the pneumatic pressure directly to the chip and fluidic pressures indirectly via a fluidic reservoir. The resulting flow was measured using a fluid flow sensor (XS, S and L Flowunit, Fluigent) based on thermal mass flow, which was placed between the fluidic reservoir and the valve. The chip’s fluidic outlet was connected to a waste reservoir at atmospheric pressure.

Software (MAESFLO, Fluigent) was used to synchronize the applied pressures and measure the resulting flow simultaneously. Using an automation script (AutoIt), the MAESFLO was programmed to test a large range of working pressures. The fluidic pressure ranges from 400 mbar to 1200 mbar with increments of 200 mbar. The pneumatic pressure was applied up to 2000 mbar with 10 mbar increments at a 50 Hz frequency. The pressures were swept and at the same time the flowrates were logged using the flow sensors.

The measurement cycle starts with an increase in fluidic pressure, thereby pushing fluid through the valve. The elastomeric membrane may be in touch with the valve seat, thus preventing flow. The test was designed in such way that the pressure required to open the valve and generate flow through was measured the first time the valve was operated. It is in that sense a ‘destructive’ measurement that can only be performed once per new valve.

Next, all pressures were set to zero for stabilization. The fluidic pressure was then set to the first value (400 mbar) and the pneumatic pressure is incrementally increased up to 2000 mbar. This sweeping was repeated up to 1200 mbar fluidic pressure. For visualization purposes the fluids were stained with a fluorescent dye and movies were captured during valve actuation.
The actual pressure value rather than the set pressure was used for data analysis. Certain characteristics are extracted from the data. The flowrate without an applied pneumatic pressure was used to calculate the open-state fluidic resistance. A pneumatic closing point was determined as the point where the valve starts reacting to pneumatic pressure. Here, we place this point at the pressure where the flow reached 95% of the initial flow. The response steepness is determined from 95% to 5% of the initial flow. This is thus the steepness observed in a flow-pressure plot.

Measurements of low flowrates (valve leakage rates) were performed within a long-running experiment, where the valve was kept closed for multiple hours. By interchanging the outlet tubing to capillary tubing with a 400 µm inner diameter, the sensor readout and an optical readout were combined. Here, manually measuring the displacement over many hours can be used to calculate volume back to leakage rates.

Cyclic testing of the valves was performed up to 200 000 times. Here, a solenoid valve (FESTO) was used to apply and release the pneumatic pressure on the valve. The pressure was cycled between 1500 mbar and -500 mbar. In practical applications, a vacuum is never applied on the pneumatic side. Here, it is used to simulate the pressure exerted by the fluid.

The maximum holding pressure tests were performed by connecting the pneumatic side to an HPLC pump and increase the pressure. After a pressure increase the flow either returned to zero or remained stable. In the latter case, it is concluded that the valve is destroyed.

RESULTS

Valve opening behaviour

It was observed that the valves open at an average pressure of 13 mbar. The maximum required fluidic pressure to initiate flow was 50 mbar.

Valve closing behaviour

An example of the resulting fluidic response to pressures is presented in Figure 1. The overpressure is the pneumatic pressure minus the fluidic pressure, thus all graphs start at the negative of the fluidic pressure. For all fluidic pressures, there is a small plateau where the flow first does not increase. Then, roughly at 200 mbar pneumatic pressure, the flowrate starts to decline. Moreover, the steepness of these curves is comparable for the different fluidic pressures is comparable. For this valve, the flowrate approaches zero when the overpressure is in the range of -100 mbar to 100 mbar.

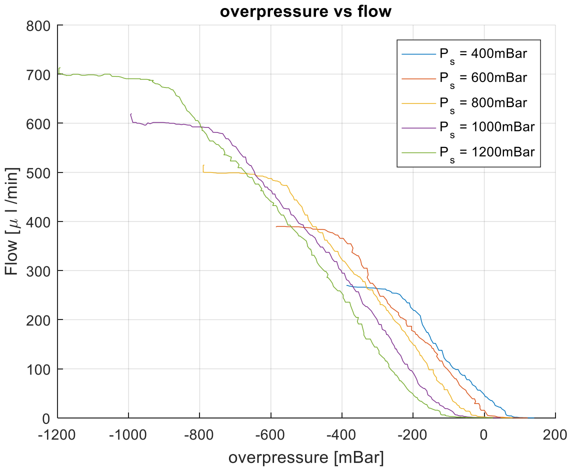

Figure 1, The (over) pressure versus flow graph for one of the valves. Here, the overpressure is the applied pneumatic pressure minus the fluidic pressure. It can be observed that the valve already has a large reduction in flowrate well below the overpressure equals zero.

For further numerical analysis the resulting pressure-flow response was quantified using the definitions previously discussed in the experiment setup section. An example can be found in Figure 2. For each valve, the maximum open-state flow was determined. Using the pressure difference between 95% and 5% of this flow is used to determine the valve’s response range. The last point is where the lower detection limit of the flow sensor is reached.

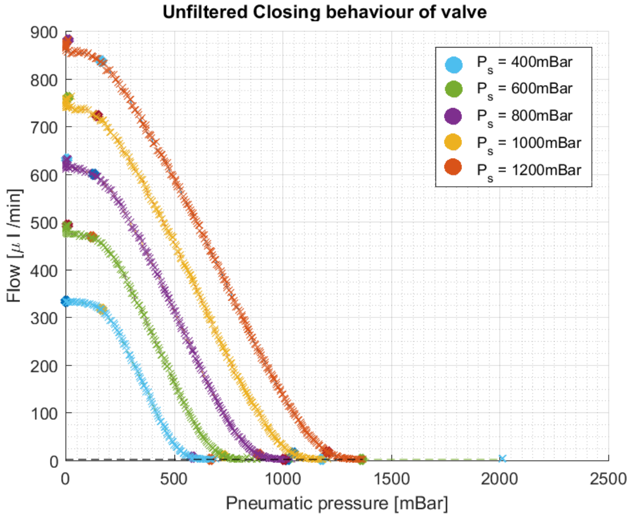

Figure 2, Unfiltered valve closing behaviour with the flow (µl/min) on the y-axis and the pneumatic pressure (mbar) on the x-axis. Several dots are placed on each line. From left to right, these represent: the open-state maximum flow, 95% of the initial flow, 5% of the initial flow and sensor lower limit. These points are used for further analysis.

The pressure at which the valve starts to close (95% flow) is 135 ± 125 mbar. The value at which the response is observed does not shift much with the different fluidic pressure. However, the response pressure was highest for the extreme values (147 mbar pneumatic pressure at 400 mbar and 1200 mbar fluidic pressure) while being minimum around the centre or the range (119 mbar at 800 mbar fluidic pressure).

*Table 1, typical COC valve characteristics. * 99% confidence interval, ** upper boundary 99% confidence interval*

Hydraulic pressure (mbar)	400	600	800	1000	1200
Open-state Resistance (*10^{12} Pa.s/m³)*	<1.61	<1.29	<1.19	<1.15	<1.11
Recommended overpressure (mbar)**	1176	1093	1003	1042	1071
Closed-state leakage (µl/min) **	<0.03	<0.03	<0.03	<0.03	<0.03
Burst pressure (bar)			>12.5		

The value at which the flow is reduced to 5% does increase with the fluidic pressure. For 400 mbar, 863 mbar pneumatic pressure is required on average. For 1200 mbar, this is 1554 mbar. In effect, the range of pressures at which the most evident valve response is observed increases from 147-863 mbar for 400 mbar fluidic pressure to 147-1554 mbar at 1200 mbar fluidic pressure.

The measured overpressure to reduce the flow to the detection limit was 401 mbar. This value is highest for the lower flowrate (463 mbar overpressure at 400 mbar fluidic pressure) while being lowest for the highest fluidic pressure (354 mbar overpressure to close 1200 mbar). Using the mean and standard deviation, a recommended overpressure is formulated. This states the overpressure at which the valve would be closed at 99% certainty. These values can be found in Table 1.

Valve leakage

In addition to the sensor measurements, analysis of leakage was performed. The resulting average leakage is 0.66 nl/min, measured over periods from 6 to 16 hours.

Valve durability testing

The valves that were tested before and after 200 000 actuations show comparable flow and leakage behaviour though at different pressures. The realized leakage is comparable, however, the average overpressure to achieve this increased from 234 mbar to 521 mbar. The standard deviation around these values did not significantly increase. The value at which the valves start to close (95% flow) also did not significantly change.

This increase in pressure is minimal at low fluidic pressures. It is highest (approx. 3 fold) for the high fluidic pressures. This could indicate that a loss of stiffness in the membrane could have most significant effect at higher operating pressures.

Valve bursting

The pressures at which leakage was observed are much higher than the values used during the other experiments. Using the mean and standard deviation, the valves are not expected to burst below 12.5 bar. This is calculated with a 99% confidence interval.

CONCLUSIONS

In this work we presented functional microfluidic valves fabricated in a monolithic COC chip, yielding a practical fluid handling solution. This development brings new opportunities for implementation, considering the material's superior chemical resistance, optical clarity, biocompatibility and low moisture absorption. Furthermore, the on-chip integration of valves reduces dead volume and allows for handling without using other materials than COC for fabrication.

REFERENCES

[1] M. A. Unger, H.-P. Chou, T. Thorsen, A. Scherer and S. R. Quake, “Monolithic Microfabricated Valves and Pumps by Multilayer Soft Lithography”, Science New Series, 288 (5463): 113-116

CONTACT

*B. Hoogenberg, basjan.hoogenberg@micronit.com

AUTOMATED MICROFLUIDIC PRODUCITON OF MONODIPSERSE PLGA MICROPARTICLES

M. de Vargas Serrano[1]*, K. Giannasi*[1] *and W. van Hoeve*[1]

[1] Tide Microfluidics B.V., Capitool 41, 7521 PL, Enschede, The Netherlands

ABSTRACT

The MicroSphere Creator has shown excellent results in producing PLGA particles. Particles produced showed uniformity of production with coefficients of variation (CV) less than 0.2 for sizes ranges between 1.8µm and 2.8µm. This was over prolonged production periods between 2 to 20 hours. All these factors indicate that the Microfluidic technology of the MicroSphere Creator is capable of replacing standard batch processing techniques for the production of highly specialised pharmaceutical products.

KEYWORDS

Microfluidics, tabletop manufacturing, microparticles, microdroplets, microbubbles.

INTRODUCTION

Controlled creation of polymer based particles finds application in the pharmaceutical industry for the loading of targeted drugs and nanoparticles. They play a crucial role in next generation personalised medicines, with high controllability and accurate sizes ensuring accurate doses and limiting wastage of expensive reagents [1]. To meet these needs uniform particles are required. These are produced using a variety of polymeric inactive materials including poly (Ɛ-caprolactone) (PCL), poly (lactide acid) (PLA), and poly (lactic-co-glycolic acid) (PLGA), all of which are FDA recognised drug carriers. These particles can be easily loaded with the drug required to create slow release and personalised delivery. A key part of this technique is controlled dosing, which remains an issue if the produced PLGA particle have a wide size distribution. A solution to this issue is the use of microfluidics to create monodisperse particles.

METHOD

Highly controlled microfluidic production of PLGA particles was carried out using the MicroSphere Creator. The PLGA droplets are created from an continuous phase of 2%m/m Poly (Vinyl Alcohol) (PVA) in de-ionised water as carrier to the disperse phase of 1%m/m Poly(lactic-co-glycolic acid) (PLGA) in Dimethyl Carbonate (DMC). The DMC is miscible in the continuous phase, meaning DMC diffusion out the droplets leaving the accurately formed PLGA particles. This is due to the high solubility of DMC in water, which makes it an ideal candidate to replace Dichloromethane (DCM) as a PLGA solvent for pharmaceutical compounding [2]. As the solubility of DMC in water is an order of magnitude greater than that of DCM. Additionally DMC has an order of magnitude reduction in toxicity compared to DCM.

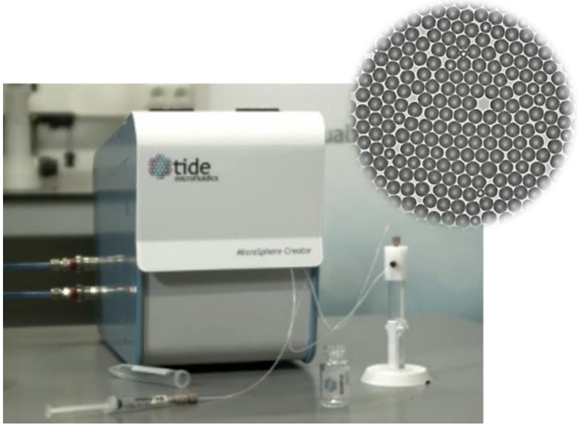

Figure 1: The MicroSphere Creator and a sample of produced monodisperse microparticles

The MicroSphere Creator is shown in Fig 1, along with an example of microparticles produced, is the CE-marked research apparatus of Tide Microfluidics. The system utilises proprietary microfluidic technology to enable uniquely high production rates for the creation of microdroplets of microbubbles. The MicroSphere Creator is ideally suited for the research and development stage microparticle production. It works by using proprietary technology to bring these two fluid components together in a controlled manner

Table 1. Production run settings and results

Run	Production settings		Production results		
	Liquid pressure (mbar)	Gas pressure (mbar)	Production duration (hours:mins)	Final particle mean diameter (µm)	CV
1	1000	650	2:55	2.8	0.2
2	2000	1000	3:11	1.8	0.2
3	600	400	3:40 and 20:00	2.5	0.2

allowing the production of the droplets under high frequency conditions. This means fluid formulations can easily be changed and control parameters of the production are easily adjusted to optimise production. Furthermore the microfluidic production is managed and monitored using the real-time quality control of the MicroSphere Creator. Meaning divergence from set production parameters will result in an automatic stop of the production process.

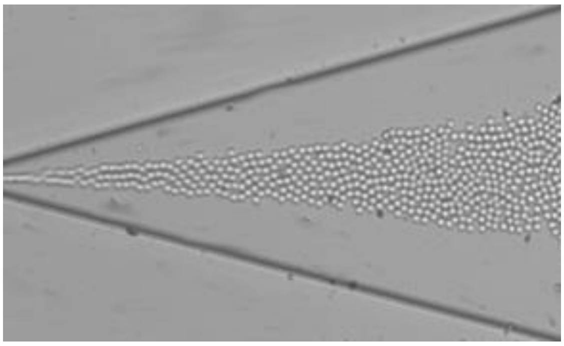

Figure 2: Real-time production image of PLGA particles during Run 3

Production was carried out in a stable laboratory environment under safe working conditions with a laminar flow cabinet used to ensure product quality. Production runs were more than two hours long to investigate stability and reliability of production. Investigations were focused on the production of droplets with sizes 16µm and with a low coefficient of variation (<0.2). These sizes of droplets were expected to create particles of <3.5µm as is predicted by the work of Perez *et. Al* 2015 [3]

RESULTS

The set parameters of the MicroSphere Creator gave reproducible result over long production periods. PLGA particles were of a uniform size in variety of size ranges and produced in high enough volumes using several set working parameters. These working conditions and the resulting sizes and size variation, as well as an indication of production duration can be seen in table 1.

Results indicate that prolonged production of over 20 hours can create stable microparticles that are suitable as drug carriers. Even during these prolonged production runs the unique advantages of pressure controlled microfluidic production can guarantee the monodispersity of the particles produced as can be seen in Figs 2 and 3. Here the results of production run 3 are highlighted with an image of the production in process Fig 2. This production run was analysed for monodispersity as shown in Fig 3, where these produced monodisperse microparticles are shown under 40x magnification in the insert of Fig 3.

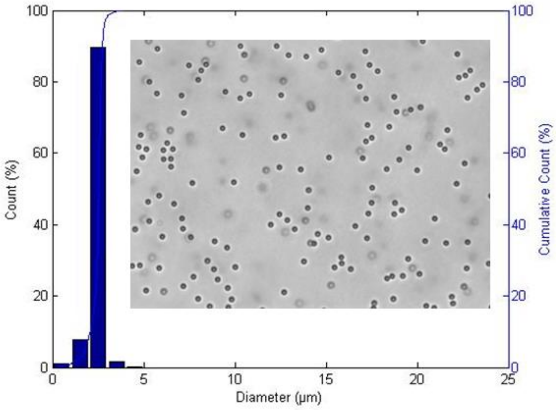

Figure 3: Microparticle size distribution analysis and cumulative distribution analysis, with inset showing produced particles under 40X magnification

CONCLUSION

In general we see a highly monodisperse population of PLGA-based microdroplets can be produced using the MicroSphere creator. Resulting in microparticles created through the rapid pervaporation process of DMC. This is shown to be a stable and controllable technique, providing a low toxic alternative to the current standard DCM solvent. In fact it even enables fast processing and solidification of PLGA particles for increased production for pharmaceutical applications. While also showing a stability of production for 20 hours that is comparable to the shorter production runs for the sample particles.

REFERENCES

[1] M. Björnmalm, Y. Yan and F. Caruso, “Engineering and evaluating drug delivery particles in microfluidic devices,” J. Controlled Release, 190, 2014, pp.139–149.

[2] H. G. Kim, K. M. Kim, Y. H. Kim, S. H. Lee, and G. M. Kim, “Preparation of monodisperse ENX-loaded PLGA microspheres using a microfluidic flow-focusing device,” J. Biobased Mater. Bioenergy, 7, 2013, pp. 108–114.

[3] A. Perez, R. Hernández, D. Velasco, D. Voicu, C. Mijangos, “Poly (lactic-co-glycolic acid) particles prepared by microfluidics and conventional methods. Modulated particle size and rheology,” J. Colloid Interface Sci., 441, 2015, pp. 90–97.

CONTACT

* M. de Vargas Serrano,
m.devargas@tidemicrofluidics.com

A SINGLE-USE IN-LINE FLOW SENSOR FOR CLOSED-LOOP CONTROLLED PRECISE NON-CONTACT LIQUID DISPENSING

S. Kartmann[1]*, F. Koch*[1]*, A. Ernst* [2]*, R. Zengerle*[1] *and P.Koltay*[1,2]
[1] Laboratory for MEMS Applications, IMTEK, University of Freiburg, Freiburg, Germany
[2] BioFluidix GmbH, Freiburg, Germany

ABSTRACT

This paper reports on a closed-loop controlled non-contact liquid dispensing system. The system employs a control algorithm to automatically adjust the dispensed volume, and it consists of a single-use in-line flow sensor and a disposable electromagnetic dispensing valve. By measuring the flow rate in real time, the system can control the opening time of the valve and is thus able to automatically compensate for potential environmental influences such as pressure or temperature fluctuations. Furthermore, the system has the advantage that all fluid-carrying components are easily exchangeable, low-cost disposables. Thus, cost intensive cleaning steps can be avoided. The precision of the system was studied experimentally for volumes in the range of 2.1 µL to 4.9 µL. The resulting coefficient of variation (CV) was below 2%.

KEYWORDS

Flow sensor, dispensing valve, disposable, closed-loop controlled, liquid dispensing system

INTRODUCTION

Whether they are handling microliters of patient samples such as blood or serum or nanoliters of expensive reagents, liquid-handling systems are the heart of laboratory automation. They deliver samples or reagents to cuvettes or multiwell plates for applications such as diagnostics, drug screening, high-throughput applications, clinical research, or other laboratory applications.

The trend over the past several years has been the fabrication of systems that can transfer smaller volumes to plates with an increasing amount of wells from 96 up to 1536 [1]. This trend is now decreasing a bit, as the increasingly high equipment investments are usually no longer justified by the reduced reagent consumption. Adapting a process from a 96 well plate to a 384 is feasible, but if you go even lower down to 1536 wells, the whole process chain and the necessary equipment must be replaced, which leads to high capital investments [2]. Therefore, in addition of reducing the volumes further, improving reliability, hygienic safety and interoperability of liquid handling systems has become increasingly important.

Areas of application such as in vitro diagnostics, drug discovery, medical technology or food industry are the main users of small quantities of liquid. These fields have demanding requirements in terms of dispensing precision and its independence from environmental influences, as well as prevention of cross-contamination. Therefore, it is often necessary to realize the liquid-carrying components as single-use disposable components in order to avoid cleaning processes, as well as minimize the risk of cross-contamination. Thus, there is an increasing demand towards integrating sensors that monitor or even control dispensing and dosing process online.

DESCRIPTION OF THE SYSTEM

The precision of the dispensing system is provided by a single-use flow sensor based on the differential pressure principle [4]. The used dispenser in this case is a pressure/time controlled fully disposable electromagnetic valve presented earlier [3]. The control of the dispensed volume is based on the real-time measurement of the prevailing flow rate in the system during a liquid discharge as shown in figure 1.

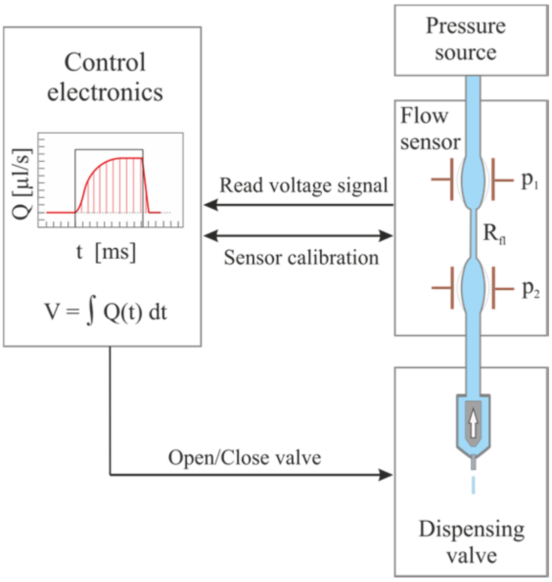

Figure 1: Schematic of the closed-loop control: The flow sensor according to the differential pressure principle is continuously measuring the flow. The sensor is connected to a control electronics that calculates the integral flow during dispensing and closes the valve when the target volume is reached.

First the sensor calibration curves for the individual pressure sensor (p_1, p_2) were determined. Therefore, the system is filled with DI water and the valve is closed. A reference pressure sensor is placed between the pressure source and the single-use sensor. The pressure is ramped up and down 3 times in steps of 25 mbar from 1 to 600 mbar and a pressure calibration curve is determined from the mean value of the measurements. The result is shown in table 1.

Table 1: Experimental determination of the sensor calibration curves for the two pressure sensors p_1 and p_2, where U_1 and U_2 are the measured voltage in mV.

Sensor	**Sensor calibration curve**
P_1	$p_1(U_1) = 0.022 * (-5699 + \sqrt{8.67 * 10^7 + 46000 * U_1})$
P_2	$p_2(U_2) = 0.06 * (-126 + 1.73\sqrt{8.21 * 10^6 + 27500 * U_2})$

When the dispensing valve opens, the differential pressure $\Delta p(t) = p_1(t) - p_2(t)$ over the fluidic resistance will be measured as function of time. This characteristic pressure drop depends on a variety of parameters such as the geometry of the fluidic resistance, the response time of the pressure sensors, the geometry of the nozzle of the dispensing system, the compliance of tubings, etc. Instead of a theoretical calculation of the time course of the pressure drop in the considered system, we decided to measure the characteristics once for an actuation time of 50 ms and an actuation pressure of 300 mbar (see figure 2, black symbols) and take this as reference.

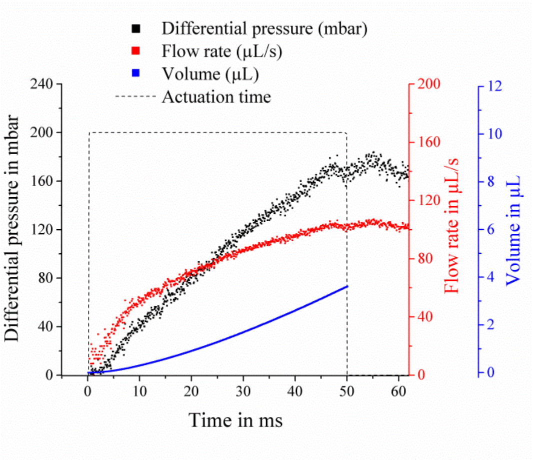

Figure 2: Measured differential pressure based on the sensor calibration curves of Table 1. Here, the valve was actuated for 50 ms with an actuation current of 1 A. Next, the flow rate and the corresponding volume are calculated.

In order to calculate the flow rate, differential type flow meters make use of the Bernoulli equation [5]:

$$p_1 + \frac{1}{2}\rho v_1^2 = p_2 + \frac{1}{2}\rho v_2^2 + losses \quad \textbf{(1)}$$

$$Q_v = A_1 v_1^2 = A_2 v_2^2 \quad \textbf{(2)}$$

In the present case, we neglect the viscous losses caused by the fluidic resistance. By measuring the time variation of the differential pressure in the system one can calculate the volume flowrate Q_v at any point in time by using the following equation, if the density and the geometric dimensions are known:

$$Q_v(t) = \sqrt{\frac{2\Delta p(t)}{\rho(\frac{1}{A_1^2} - \frac{1}{A_2^2})}} \quad \textbf{(3)}$$

Where $\Delta p(t)$ is the differential pressure, A_1 is the inner cross-section area of the measuring cell of the pressure sensor, A_2 is the inner cross-section area of the fluidic resistance and ρ is the density of water. The result of this calculation is depicted in red in figure 2.

Integration over the measured volume flow rate $Q_v(t)$ and comparison with the target volume V_{target} defines a condition for determining the time for closing the valve t_{off}.

$$V_{target} = \int_{t_{on}}^{t_{off}} Q_v(t)dt \quad \textbf{(4)}$$

In practice, the closing time t_{off} for the valve is determined by the closed-loop algorithm like depicted in figure 3.

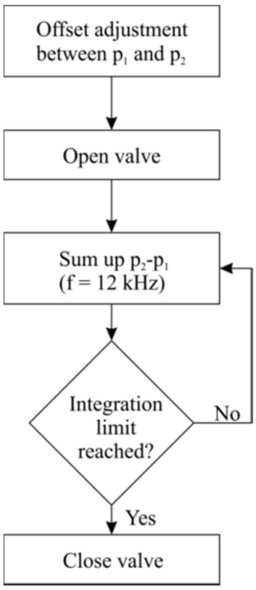

Figure 3: Implementation of the closed-loop algorithm on the microcontroller. The sampling frequency in this case was 12 kHz.

The algorithm performs an offset adjustment in the initial state (p = 0 bar). The offset is determined by averaging over 10 samples of the difference between pressure sensor 1 (p_1) and pressure sensor 2 (p_2) and is then stored as a reference value for the offset adjustment on the microcontroller.

Next, the pressure is regulated to the desired actuation pressure (p = 300 mbar). If the control electronics sends an opening signal to the valve, a certain flow rate will be establish in the system depending on the applied actuation pressure and fluidic resistance of dispensing system. This step initializes the loop-control shown in figure 4. On the microcontroller level, the time-continuous integration of equation (4) can be approximated by a time-discrete summation like follows:

$$\boldsymbol{V_{target} \approx \sum_{i=0}^{N} Q_v^i \, \Delta t_i \approx a\Delta t \sum_{i=0}^{N} \sqrt{\Delta p_i}}$$

Whereby a is a constant derived from the sensor calibration or by using equation (3) and the values $\sqrt{\Delta \mathrm{p_i}}$ are the measured discrete pressure differences (f = 12 kHz). The relation between the target volume V_{target} and the pressure sum $\sum \sqrt{\Delta \mathrm{p_i}}$ is depicted in figure 4.

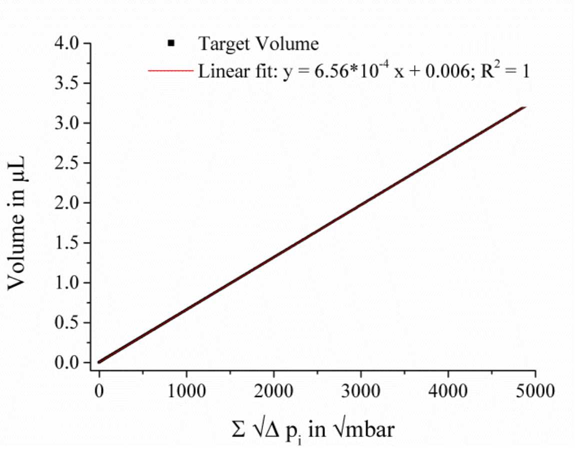

Figure 4: Relation between the pressure sum and the corresponding integral volume derived from the measurement depicted in figure 2.

The addition of pressure values continuous until a previously set pressure sum is reached which corresponds to a desired target volume V_{target}. Then the valve is closed immediately (I = 0 A).

EXPERIMENTAL SETUP

The experimental setup is shown in figure 5. The actuation pressure is applied to the system by a proportional pressure regulator (VPPM, Festo AG & Co. KG , Germany). The single-use flow sensor [4] consists of two pressure sensors connected via a fluidic resistance with an inner diameter of 150 µm and a length of 16.5 mm. The electromagnetic valve [3] is connected in-line to the flow sensor and can be driven by the control electronics (ValveControl V1.9, BioFluidix GmbH, Germany).

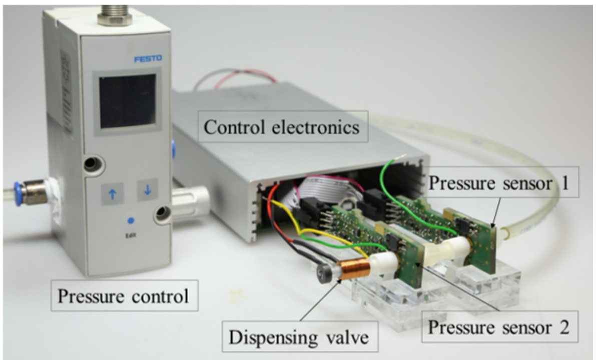

Figure 5: Measurement setup consisting of a proportional pressure regulator acting as pressure source (VPPM, Festo AG & Co. KG , Germany), a disposable dispensing valve [3], a single-use flow sensor [4] and the control electronics (BioFluidix GmbH, Freiburg, Germany).

EXPERIMENTAL RESULTS

In order to evaluate the dispensed volume in dependency of the targeted volume and the set pressure sum, the whole dispensing set-up is placed above a balance. For each run with a given pressure sum, 24 dispenses were performed and the delivered volume was measured using the gravimetric regression method (GRM) [6].

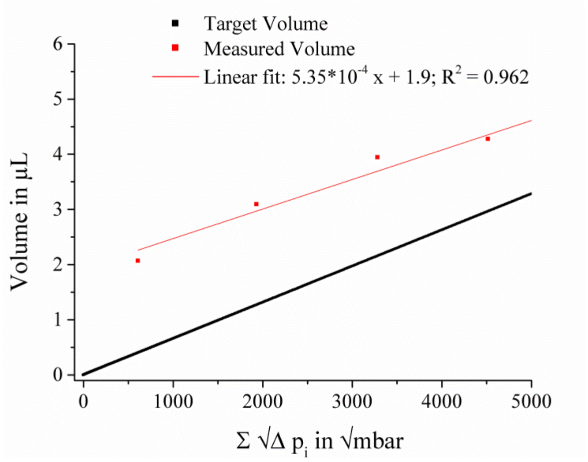

Figure 6: The loop-controlled dispensing performance shows a linear relation between the pressure sum $\sum \sqrt{\boldsymbol{\Delta p_i}}$ and the dispensed mean volume. Each data point represents the mean volume of one run of 24 individual measurements.

The actuating pressure was set to 300 mbar. The opening time is controlled by the closed-loop algorithm like described before. The results are shown in figure 6 and table 2.

Table 2: Experimental evaluation of the precision of the closed-loop algorithm. The current of the dispensing valve was set to 1A and the actuating pressure was set to 300 mbar. The opening time is controlled by the closed-loop algorithm like shown in figure 3. Each run consists of N=24 dispenses. The volume was measured by the gravimetric regression method (GRM) [5].

Target Volume	**N**	**Resulting hold time**	**Measured volume**	**CV**
0.34 µL	24	9-10 ms	2.1 µL	1.7%
1.2 µL	24	13-14 ms	3.1 µL	2.0%
2.1 µL	24	17-18 ms	3.9 µL	0.6%
2.9 µL	24	21-22 ms	4.2 µL	0.6%
3.6 µL	24	27-28 ms	4.9 µL	0.7%

The loop-controlled dispensing performance shows a linear relation between the pressure sum $\sum\sqrt{\Delta \boldsymbol{p}_{\boldsymbol{i}}}$ and the measured mean volume. Both the target volume curve (cf. figure 4) within the control-loop as well as the measured volumes for a given target value have the same profile. However, the measured volume is obviously significantly higher. The offset of the measured curve is in average 1.9 µL.

This offset can be partially explained by the inertia of the dispensing valve. In particular, mechanical inertia of the plunger, fluidic inductivity of the liquid and the electrical inductivity of the coil are responsible for this. Thus, after the current is turned off, the liquid flow does not stop immediately (see also figure 2). In order to further proof this hypothesis, we monitored the closing behavior of the plunger with a high speed camera. After the current is turned off, it takes about 4.8 ms until the valve is completely closed. This extended opening time would correspond to an additional dispensed volume of about 0.8 µL in the present case. This offset could be eliminated by considering the closing time as additional offset factor in equation (4) and the corresponding control algorithm as shown in figure 3. The remaining offset could be probably explained by the fact that, in the first step, the viscous losses due to the fluidic resistance in equation (1) are neglected. Thus, the target volume curve as shown in figure 4 overestimates the volume delivered at a certain value of the pressure sum, which makes the algorithm close the valve too early. This part of the offset might be compensated by calibrating the flow sensor with a reference flow sensor instead of using Bernoulli's equation to determine the relation between differential pressure and flow (c.f. equation (3)). Implementing both corrections will be part of future work.

SUMMARY AND OUTLOOK

The combination of a single-use flow sensor, a dispensing valve and control electronics enables the realization of a cost-effective, loop-controlled dosing system for industrial and medical applications with CVs below 2%.

Though, a good reproducibility and a high precision of the system could be demonstrated in this work, more investigations, optimization and experimental validation have to be carried out. First, the offset has to be compensated by the appropriate means described before. Then other influence parameters, like ambient temperature, aging effects and the influence of different dielectric constants and different pressure conditions have to be investigated before the demanding requirements of industrial and medical applications can be fully met by the described intelligent liquid handling system approach.

REFERENCES

[1] M. J. Felton, "Liquid handling: Dispensing reliability", ANALYTICAL CHEMISTRY, pp. 397-399, 2003.

[2] J. Comley, "Automated Low Volume Dispensing Trends", Informatics & Automation from Technology Networks.

[3] S. Kartmann, P. Koltay, R. Zengerle, A. Ernst, "A Disposable Dispensing Valve for Non-Contact Microliter Applications in a 96-Well Plate Format", Micromachines, Vol. 6, pp. 423-436, 2015.

[4] S. Kartmann, P. Koltay, R. Zengerle, A. Ernst, "Single-use flow sensor based on the differential pressure principle employing the radial expansion of a low-cost silicone tube", Transducers '17 Conference, 2017.

[5] P. Chattopadhyay, "Flowmeters & Flow Measurement", 2006.

[6] D. Liang, C. Steinert, SB Bammesberger, L. Tanguy, A. Ernst, R. Zengerle, P. Koltay, "Novel gravimetric measurement technique for quantitative volume calibration in the sub-microliter range", Measurement Science Technology, vol. 24, 2013.

CONTACT

* S. Kartmann, sabrina.kartmann@imtek.de

AUTOMATED DETECTION OF DROPLET SHAPE EVOLUTION FOR HOLLOW AFM CANTILEVER FLOW CALIBRATION

E.J. Verlinden[1*], *E. Sarajlic*[2], *F.M. Vos*[3], *A. Engel*[4], *U. Staufer*[1] *and M.K. Ghatkesar*[1*]
[1] Department of Precision and Microsystems Engineering, Delft University of Technology, Delft, The Netherlands
[2] SmartTip B.V., Enschede, The Netherlands
[3] Quantitative Imaging Group, Delft University of Technology, Delft, The Netherlands
[4] Department. of Bionanoscience, Delft University of Technology, Delft, The Netherlands

ABSTRACT

A hollow atomic force microscope (AFM) cantilever offers the nanomechanical sensing functionality of an AFM cantilever and has the ability to manipulate pico- to attoliter fluid volumes. In order to use hollow AFM cantilevers for precise fluid manipulations, a calibration procedure is needed that can evaluate the influence of various physical effects on the liquid handling over time. In this work, an image processing method to analyze droplet shape evolution is presented. A water droplet, dispensed from the tip aperture and surrounded by an oil medium, was studied to obtain fluid transport properties.

KEYWORDS

Hollow AFM cantilevers, Image processing, Calibration

INTRODUCTION

Micro/nanoscale chemistry and biology demand tools that can manipulate small liquid volumes. A hollow atomic force microscope (AFM) cantilever offers the nanomechanical sensing functionality of an AFM cantilever and has the ability to manipulate pico (10^{-12}) to atto (10^{-18}) liter fluid volumes[1],[2]. As the interaction force of the cantilever with another surface can be controlled, the device is well suited to manipulate single particles, such as cells or colloids.

Hollow AFM cantilevers have been used for a variety of single cell-based applications: adhesion characterization, cellular surgery and spatial manipulations of cells[3]. Particularly for cellular surgery, it is important to have fine control over the volumes that are manipulated. It has been demonstrated for HeLa cells that liquid injections up to 20% of the cell volume did not reduce cell viability[4]. Since the cell volumes of commonly used mammalian cell lines range from 2 to 7 pL[5], femtoliter volume range control over the manipulated liquid is required.

Furthermore, hollow AFM cantilevers are suitable for characterizing colloidal interactions. Colloidal particles can be temporarily attached to the cantilever by applying underpressure. This enables the examination of single-colloid-substrate interactions[6] and colloid-colloid interactions[7], which is referred to as exchangeable colloidal probe spectroscopy. A potential colloidal application could be to create immiscible phase emulsions with the hollow AFM cantilever, where the droplet/colloidal size and growth rate can be tuned. This would enable several studies on colloidal interface properties (surface tension, particle adsorption at the interface). However, good control over the hollow AFM fluidic system is required to tune custom colloidal solutions.

Hollow AFM cantilevers are operated by applying an overpressure or underpressure on the fluid reservoir, which leads to dispensing or aspirating of fluid, respectively. An analytical microfluidic flow model based on the hydraulic resistance analogy for hollow AFM cantilevers is given as: $Q = \Delta P / R$, with Q representing the flowrate, ΔP the applied pressure on the system and R the hydraulic resistance[8]. However, this model only considers the effects of channel geometry and viscosity of the manipulated fluid. Several time- and size dependent effects on the fluidic system are neglected. Therefore, a calibration procedure is needed to monitor physical contributions not present in the available model. Presented is an image processing method combined with an experimental approach for analyzing fluid transport through the hollow AFM cantilever aperture by studying droplet shape evolution.

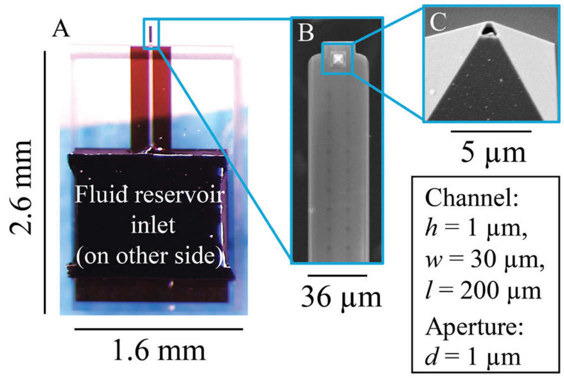

Figure 1: A) a hollow AFM cantilever has an on-chip fluid reservoir (inlet on the backside of the chip, not seen), B) a microfluidic channel inside the cantilever and C) an aperture in the pyramidal tip wall, through which fluid can be pipetted. Image A) is a bright-field optical microscope image, while B-C) are scanning electron micrographs.

MATERIALS AND METHODS

Fluidic system

The hollow AFM cantilevers were made from silicon-rich silicon nitride by a process similar to the method described by Schön et al.[9]. A cantilever chip (stiffness ≈ 2 N/m) consists of the following components: an on-chip fluidic reservoir, a microfluidic channel and an aperture at the cantilever tip (fig. 1). The cantilever chip was glued to a 3D-printed fluidic interfacing part (HTM140, EnvisionTEC); which connected the on-chip reservoir to a pressure controlled fluidic system (OB1, Elveflow®).

Experimental approach

Water was dispensed through the aperture, while the cantilever was placed into immersion oil (Sigma-Aldrich, visc. =150 cSt, dens. = 0.9 g/cm^3). The position of the cantilever chip was controlled by a robotic arm (miBot^{TM}, Imina). The cantilever surface was functionalized with a hydrophobic self-assembled monolayer of trichloro(octyl)silanes (Sigma-Aldrich). The fluid manipulations were monitored in real time by an inverted optical microscope (fig. 2) and recorded on video. The time frames of the pressure controller and the recorded movie were synchronized with a flash of an LED light. Before a pressure change was applied, the pressure control system sent out 300 ms long LED flashes. The LED was placed close to the microscope objective, such that light flashes were observed in the recorded movie.

Image processing

Each experiment was video recorded (framerate = 9 fps) and afterwards individual frames were analyzed. An automated image processing sequence was implemented in Python^{TM}, using the image processing libraries OpenCV and Scikit-Image. For every movie frame a droplet shape was identified and its dimensions were extracted.

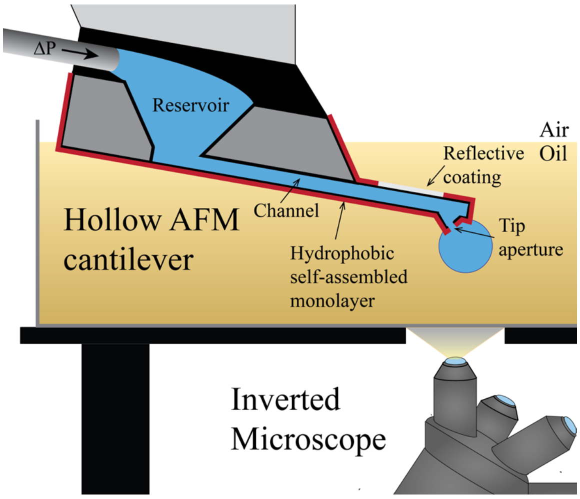

Figure 2: A schematic of the experimental set-up. A water-filled hollow AFM cantilever, connected to pressurized fluidic tubing, was immersed inside an oil medium.

RESULTS AND DISCUSSION

To quantify the relationship between the applied pressure on the reservoir and the dispensed volume, water was dispensed while the hollow AFM cantilever was immersed into oil. The advantages of oil as an external medium were the exclusion of evaporation and diffusion contributions to the flow. The hydrophobic coating minimized the spreading of water on the outer cantilever surface, after the fluid exited the aperture. This enabled the imaging of spherical droplets coming out of the cantilever. The immiscibility and difference in the refractive index between oil and water provided sufficient contrast at the interface for bright field imaging. Therefore, additional fluorescent labeling was not needed.

Experiments were conducted to observe the effect of applied overpressure on the growth behavior of droplets with a certain initial volume. As the droplets were still attached to the cantilever and were in contact with the fluidic aperture, liquid could be exchanged between the droplet and the fluidic reservoir. Figure 3 shows that two different droplets of comparable starting volumes can exhibit either a volume increase or a decrease when the applied overpressure is varied (underpressure is not used). This observed behavior can be explained by the internal pressure of the droplet (Laplace pressure[10]). The Laplace pressure needs to be compensated by an applied overpressure in order to prevent droplets from shrinking. The experiment therefore underlines the importance of investigating different combinations of initial droplet volumes and applied pressures, in order to properly calibrate the fluidic system. Thus, the

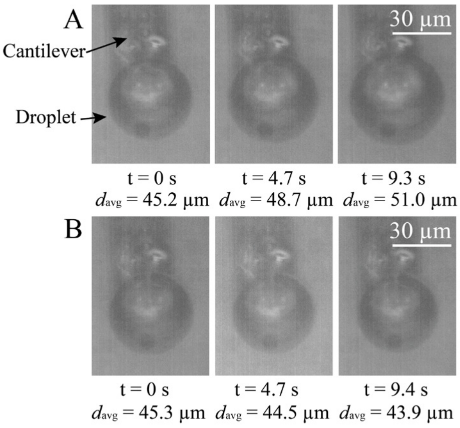

Figure 3: Video frames of water droplets hanging onto the hollow AFM cantilever, while immersed in oil. A)A droplet of an average volume of 48.3 pL grows over a time of 9.3 s while an overpressure of 20 mbar is applied. B) A droplet of comparable volume (V = 48.7 pL) shrinks over a time of 9.4 s while an overpressure of 10 mbar is applied.

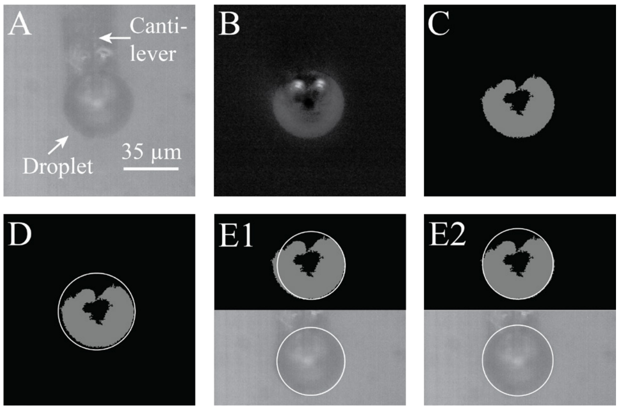

Figure 4: Image processing sequence applied to a video frame of a hollow AFM cantilever dispensing water into oil. A) Bottom view of the cantilever and the attached droplet. B) The resulting frame after background subtraction and bilateral filtering. C) Binary object obtained by Otsu thresholding. D) The size was estimated by fitting a minimally-sized circle around the object. A Hough circle transform was used to identify E1) the small and E2) the large axis of the droplet shape. The detected circles are imposed on the binary(E-top) and the raw image(E-bottom).

amount of experimental data generated would require excessive manual processing. Additionally, the varying imaging noise in the dataset demanded a customized automatic image processing method. Figure 3 shows that the cantilever is visible on the image, both directly and indirectly through the droplet. Since the droplet size varies throughout the videos, the image of the cantilever through the droplet changes, leading to different noisy reflection patterns. Therefore, a parametric investigation of noise reduction over the entire dataset was required, and a customized image processing algorithm was implemented in Pyton^{TM}.

The automated image processing sequence was built to detect the droplet shape evolution with pixel resolution (pixel width = 60 nm) during a recorded experiment (fig. 4A). The algorithm to process every video frame comprised:

(1) subtracting a background image (i.e. a frame acquired prior to the start of the experiment) from the frame to be analyzed;
(2) bilateral filtering to reduce noise in the droplet shape (fig. 4B);
(3) Otsu thresholding to segment the droplet from the image, which resulted in a binary image (fig. 4C);
(4) fitting a circle around the entire binary object to estimate the droplet size (fig. 4D);
(5) performing a Hough circle transform to fit two axes to the droplet shape, a small (fig. 4E1) and a large (fig. 4E2) radius , since the droplet slightly deviated from a perfect circle.

The developed image processing algorithms were tested on the experimental data; videos of droplets of different starting volumes, which were created by applying various pressures over time. The resulting initial volumes were estimated and found to be between 10 to 130 pL. Subsequently, a fixed pressure of 20 mbar was applied to every droplet, while it remained attached to the tip aperture. Since the initial droplet size affects the Laplace pressure of the droplet, we expect to observe a time-dependent flowrate at the same applied pressure for larger droplets compared to smaller droplets. The hydrostatic pressure exerted by the oil medium on the droplet can be neglected for this experiment, as it was calculated to be at least two orders smaller than the applied overpressure.

Figure 5 shows the droplet radii that were detected using the image processing method (dots) for an experiment in which a pressure of 20 mbar was applied on a droplet with a starting volume of 34 pL. To verify the results of the image processing, reference radii (triangles) were fitted manually to 5 frames from the movie. The automatically detected radii for the large and small axis of the droplet corresponded well with the manually detected radii.

The image processing method was then used for the remaining movies of the experiment: droplet volumes ranging from 10 to 130 pL on which a pressure of 20 mbar was applied for 10 s. After the two droplet radii were extracted, an average radius was calculated. This average radius was then used to calculate the droplet volume by assuming an ideal spherical shape. The results are shown in Figure 6. Overall, the larger droplet volumes give rise to larger flowrates, which was expected. Although comparable droplet sizes gave similar profiles in most cases, there

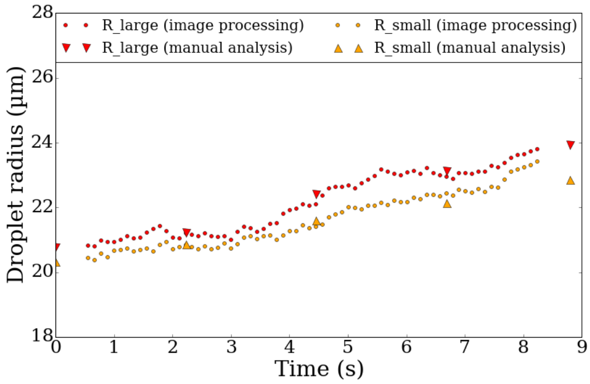

Figure 5: Analysis of a droplet shape evolution, while the droplet was dispensed into oil at an applied overpressure of 20 mbar. The estimated droplet volume at the start of the video was 34 pL. The obtained radii (indicated by circles) were averaged over 5 forward and 5 backward frames for further noise reduction. Two droplet axes were detected, a small and a large droplet axis, since the droplet shape deviated slightly from circularity. The triangles depict manual measurements of droplet radii at 5 different frames.

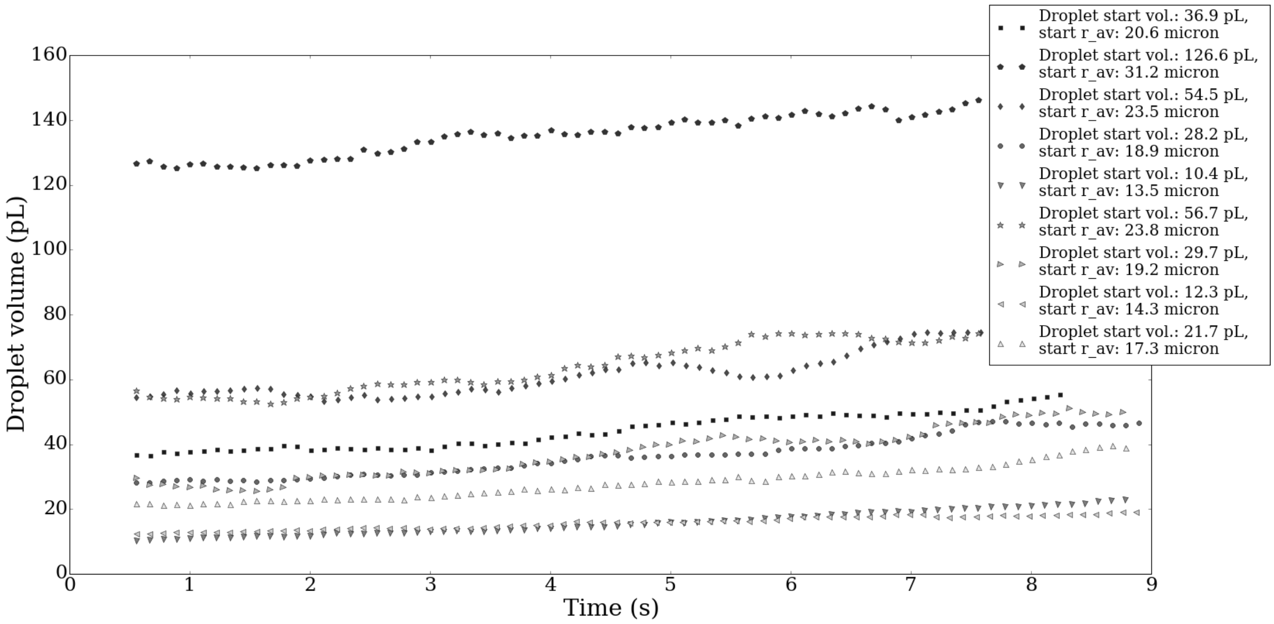

Figure 6: Analysis of droplet shape evolutions at an applied overpressure of 20 mbar. The droplet volumes were obtained by assuming a perfect spherical shape, using the averaged radius of the detected large and small droplet radius. The volumes were then averaged over 5 forward and 5 backward frames for further noise reduction.

are two conditions for which the profiles exhibit large local flowrate fluctuations. A possible explanation for these abrupt fluctuations is the increased noise in the images, which decreased the accuracy of the Hough circle fit. Increased noise can be expected for droplets that exhibit high volume changes over the experimental time frame. The microscope focus was only adjusted before the movie was taken, so a large increase in droplet size can lead to droplets going out of focus; giving rise to blurred and noisy images.

CONCLUSION & OUTLOOK

We have developed and validated an image processing method to analyze time-dependent fluid transport through hollow cantilevers using immiscible liquids. The image processing algorithm was used to analyze a set of experiments in which droplets of different starting volumes were pressurized for 10 s at 20 mbar. Our next efforts will be directed towards developing a model to describe the fluid flow observed in these experiments and calibrate the flow transport using the presented method and data.

ACKNOWLEDGEMENTS

This work is supported by NWO domain Applied and Engineering Sciences (project 13711), Nanosurf AG and SmartTip B.V. We thank Cytosurge AG.

REFERENCES

[1] A. Meister et al. “Nanoscale dispensing in liquid environment of streptavidin on a biotin-functionalized surface using hollow atomic force microscopy probes,” *Microelectron. Eng.*, vol. 86, no. 4–6, pp. 1481–1484, 2009.

[2] M. K. Ghatkesar, H. H. P. Garza, and U. Staufer, “Hollow AFM cantilever pipette,” *Microelectron. Eng.*, vol. 124, pp. 22–25, Jul. 2014.

[3] O. Guillaume-Gentil et al., “Force-controlled manipulation of single cells: from AFM to FluidFM.,” *Trends Biotechnol.*, vol. 32, no. 7, pp. 381–8, 2014.

[4] O. Guillaume-Gentil et al., “Force-controlled fluidic injection into single cell nuclei.,” *Small*, vol. 9, no. 11, pp. 1904–1907, Jun. 2013.

[5] D. Hevia et al., “Cell volume and geometric parameters determination in living cells using confocal microscopy and 3D reconstruction,” *Protoc. Exch.*, pp. 1–15, 2011.

[6] P. Dörig et al., “Exchangeable colloidal AFM probes for the quantification of irreversible and long-term interactions,” *Biophys. J.*, vol. 105, no. 2, pp. 463–472, 2013.

[7] N. Helfricht et al., “Colloidal Properties of Recombinant Spider Silk Protein Particles,” 2016.

[8] R. R. Gruter, J. Voros, and T. Zambelli, “FluidFM as a lithography tool in liquid: spatially controlled deposition of fluorescent nanoparticles,” *Nanoscale*, vol. 5, no. 3, pp. 1097–1104, 2013.

[9] P. Schön et al., “AFM cantilever with in situ renewable mercury microelectrode,” *Anal. Chem.*, vol. 85, no. 19, pp. 8937–8942, 2013.

[10] H. Bruus, *Theoretical Microfluidics*. 2008.

CONTACT

* e.j.verlinden@tudelft.nl, M.K.Ghatkesar@tudelft.nl

3D-PRINTING: AN ATTRACTIVE TOOL TO REALISE MICROFLUIDIC CHIP HOLDERS

S. van den Driesche, F. Bunge, F. Lucklum, and M. J. Vellekoop
University of Bremen, Institute for Microsensors, -actuators and -systems (IMSAS),
Microsystems Center Bremen (MCB),
Bremen, Germany

ABSTRACT

In this contribution, we present 3D-printing as an attractive tool for easy-to-realise and easy-to-use microfluidic chip holders. Stereolithography, an additive manufacturing technique with sub-millimetre resolution, was used to fabricate 3D-holders. Several designed and assembled microfluidic chip holders are presented. The fluidic connection between the chip and holder are realised by O-rings, partly integrated into the 3D-printed structure. A closed channel geometry including several curves and a conical-shaped structure assures the connection between the holder and tubing. The electric connection of bonding pads located on microfluidic chips was realised by spring-probes fitted within the printed holder. Because there is no gluing or wire bonding necessary it is easy to change the chip in the measurement setup. The fixed spring probes and O-rings are aligned automatically due to its fixed position within the holder. Biocompatibility issues can be prevented by coating the 3D-printed structures with Parylene. The given examples show that 3D-printing is an attractive tool to construct microfluidic chip holders.

KEYWORDS

Microfluidic chip-holder, 3D-printing, stereo-lithography, fluidic and electric connections.

INTRODUCTION

The challenge to connect microfluidic devices to the outer world by tubes and wires is an underestimated issue. The variety in microfluidic chip dimensions, channel geometries, number of fluidic inlets and outlets, electrode number and bonding pad sizes, and optical measurement windows make it quite impossible to design a universal chip holder. Almost every designed chip requires a newly specialised holder. There is the possibility to glue bonded-port connectors directly on the chip [1]. However, the footprint of such connectors are relatively large, might not be fitting in the measurement setup, and they incur considerable expenses for single-use components.

A method is needed to quickly build and easily redesign holders for different microfluidic chips.

Injection moulding and micro-milling are possible techniques to fabricate customised microfluidic chip holders [2]. An example of a chip holder manufactured by micro-milling is depicted in Figure 1.

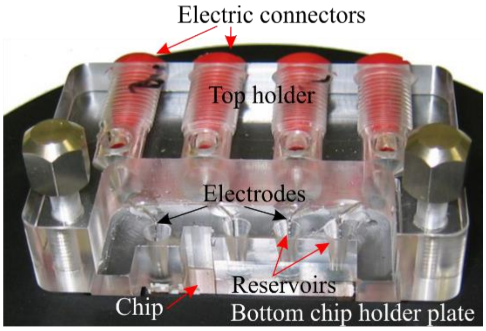

Figure 1: A micro-milled chip holder with liquid reservoirs, electrodes, and electric connections.

The advantage of 3D-printing compared to injection moulding and micro-milling is that complex geometric structures such as curved and closed sub-millimetre channels and specialised connector ports can be printed directly within the holder. Furthermore, there is no need for specialised expensive equipment or moulds.

In this work we present several designed and assembled microfluidic chip holders, including fluidic and electric connections, to show the attractiveness of 3D-printing.

STEREOLITHOGRAPHY

The design of 3D-printed holders can easily be created and adapted in CAD software such as Inventor (Autodesk). The finished design is exported in STL (Standard Tessellation Language, or Stereo-Lithography) format at high resolution for pre-processing with the printer software. Pre-processing the designs includes checking for and fixing any errors to create a completely valid STL file, orienting the part on the build platform, and adding support structures for overhangs as necessary. Finally, the 3D-printer software slices the STL file and supports into individual layers.

There are many different additive fabrication technologies, each with strengths and weaknesses [3]. For parts with features on the sub-millimetre scale, we have decided on using stereolithography technology, which features the highest lateral resolution and surface smoothness. Microstereolithography with projection via a DLP (Digital Light Processing) micromirror array reliably yields feature sizes (channels, holes, walls) down to 100 µm [4]. For larger parts and experimental setups we also employ fused filament fabrication.

In this work a high-resolution microstereolithography DLP printer (Perfactory Micro HiRes, EnvisionTEC Inc., USA), was used to fabricate the chip holders. A high-resolution, high-temperature, low viscosity acrylic polymer resin (HTM140 M, EnvisionTEC Inc. [5]) is used as printing material. Prior to printing, the stirred resin is filtered into the carefully cleaned printer bath for optimal printing conditions. The process is set to a lateral (x/y) resolution of 31 µm and a slicing thickness (z) of 25 µm. The exposure time is typically set to 3000 ms per slice. The maximum build size is 40 x 30 x 100 mm^3.

After printing, all parts are carefully removed from the build platform and ultrasonically rinsed in isopropanol multiple times until no resin residue is left. Then, the realised part is dried with nitrogen or air and the supports are removed. Finally, all parts are cured in a UV flood chamber for at least 5 minutes from each side. Additional steps may include polishing and other surface finish techniques. Total processing time is primarily dependent on the height of the print, typically ranging from a few hours to half a day, which highlights the rapid prototyping characteristics of this approach.

RESULTS AND DISCUSSION

A typical 3D-printed chip holder is depicted in Figure 2. The chip is sandwiched between a top and a bottom holder fitted by M3-screws. The top holder contains liquid reservoirs that are connected to the microfluidic chip by O-rings. The optical window, the area in the centre of the chip, is accessible for optical measurements of biological samples.

Figure 3 shows a holder with fluidic and electric connections. The holder design allows the easy exchange of the chip. None of the connections between the chip and holder are glued.

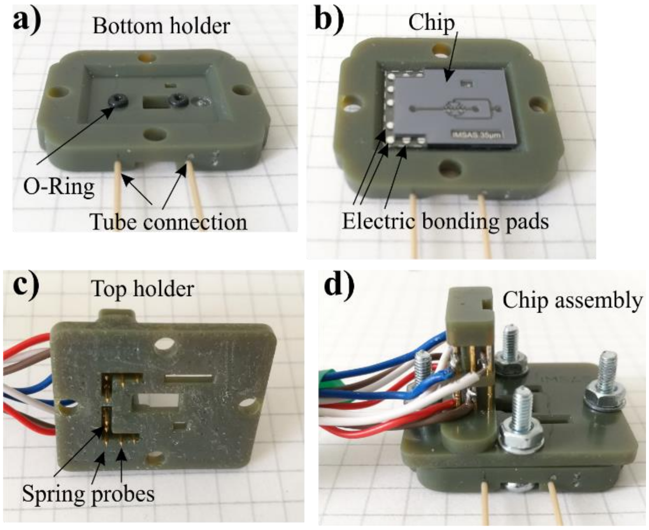

Figure 3: A microfluidic chip holder (~3 x 2.5 cm^2) including fluidic and electric connections. ***a)*** *The bottom holder part contains donut shaped recesses where O-rings connecting the chip to the channel structure within the printed holder, fits.* ***b)*** *A chip fitted in the bottom holder.* ***c)*** *The top holder including spring probes to connect the bonding pads of the chip.* ***d)*** *A photo of the assembled chip and holder.*

The fluidic inlet and outlet connections between the microfluidic chip and 3D printed holder are sealed by O-rings. By creating a half donut-shaped recess in the 3D-printed holder, the O-ring positions are secured, which simplifies the assembly of chip and holder.

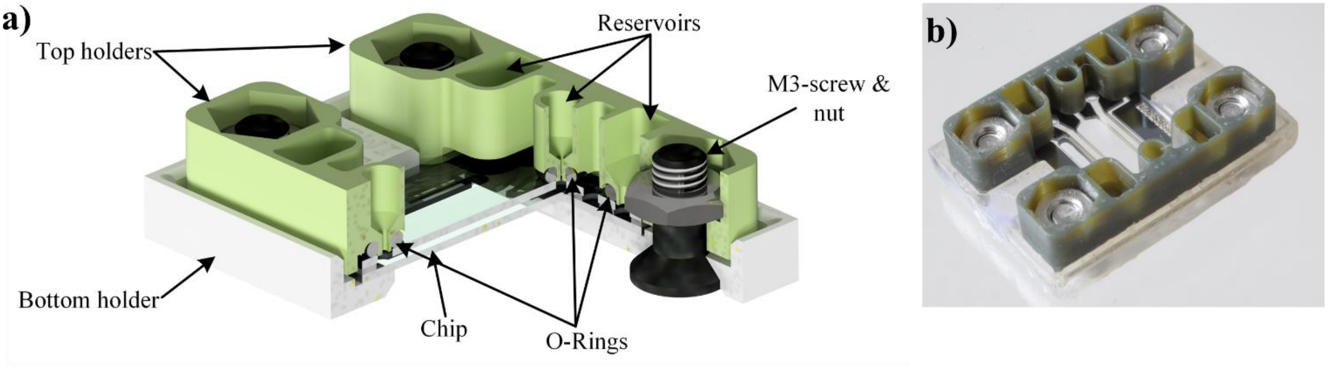

Figure 2: A typical assembly of a microfluidic chip and holder (~3 x 2 cm^2). The chip is sandwiched between two 3D-printed parts, which are fixed by M3 screws. Liquid reservoirs, connected with O-rings to the chip, are integrated in the top holder. ***a)*** *A schematic, and* ***b)*** *a photo of the device.*

The electric bonding pads of the chip are connected by spring probes fitted in the holder (Figure 3c,d and 5). Because these probes are positioned at fixed, predefined locations, they are automatically aligned to the bonding pads during chip and holder assembly. A 3D-printed part with a thickness of approximately 2.5 mm is strong enough to support a microfluidic chip.

The fluid connections to the holder are realised by fixing PEEK tubing with an inner and outer diameter of 250 µm and 800 µm, respectively, directly into the holder (Figure 4). A channel structure with a diameter of 0.7 mm starting at the O-ring recess is directed within the holder to the tube connection, fitting the PEEK tubing. This connection is assured by mechanically clamping the tubing in a conical shaped geometry integrated in the channel.

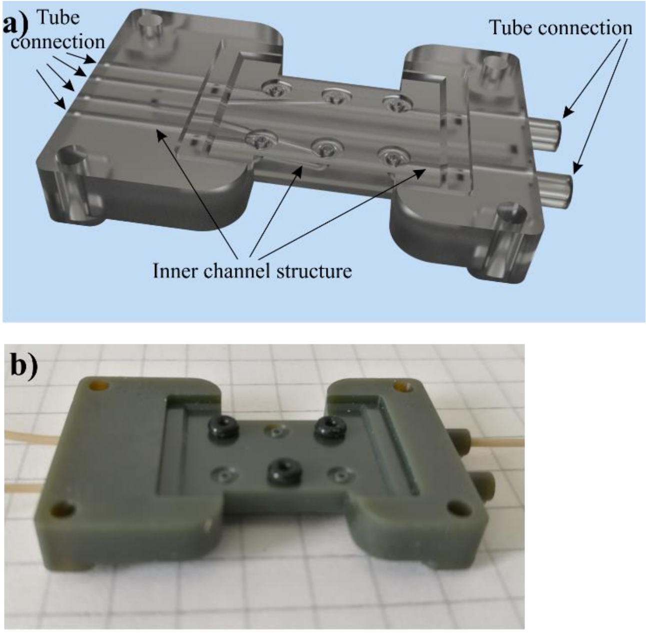

Figure 4: A microfluidic chip holder (~3.5 x 2 cm^2) containing an integrated channel structure to connect the fluidic inlets and outlet of a chip to a tubing. ***a)*** *A 3D rendered image visualising the inner channel geometry.* ***b)*** *A photo of the holder and O-rings placed in their recess.*

An alternative method to design the fluid connection is depicted in Figure 5. Here, tube connections for Labsmith one-piece fittings [2] are integrated in the holder by fixing 2-56 UNC metal nuts. The other end of the tube is connected to a syringe by a Luer-lock connector.

In Figure 6 a microfluidic chip and holder are depicted for optical measurements of biological cells. The measurement chambers of the chip are fully accessible from the top and bottom allowing comprehensive optical cell investigations.

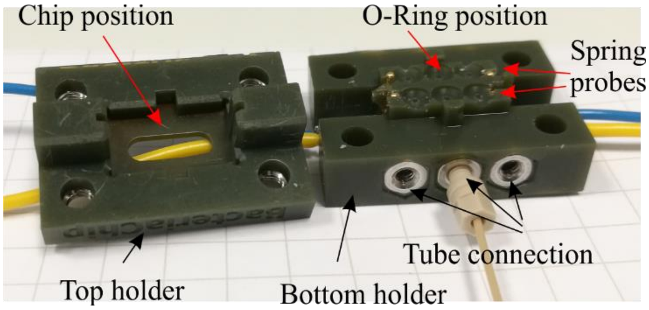

Figure 5: A photo of a microfluidic chip holder (~2.5 x 2 cm^2) with fluidic and electric connections. The fluidic outer connection is realised by placing metal nuts at the end of a channel structure.

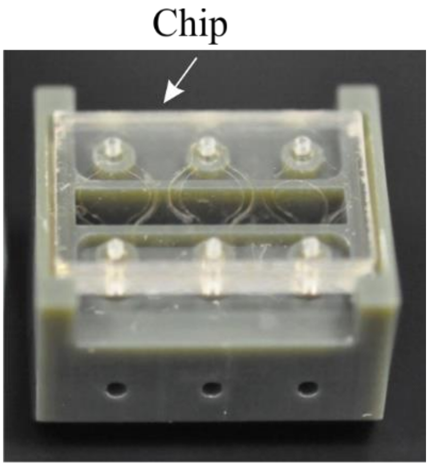

Figure 6: A calcium-fluoride infrared transparent microfluidic chip containing three 3.5 mm diameter optical measurement chambers. The fluidic connections in the holder are made by conical shaped channels. The small dimensions of the holder are optimised for the optical monitoring of biological cells in an infrared measurement setup.

Biocompatibility of 3D-printed holders

We have observed a strong influence in cellular behaviour of mammalian cells and bacteria exposed to 3D-printed structures realised from liquid resins [6]. The resins commonly used for 3D-printing contain UV sensitive photo-initiators, which exhibit a more or less pronounced cytotoxic effect. When measurements are conducted with sensitive biological cells, an efficient and attractive method to prevent such cytotoxic effects is by coating the 3D-printed structures with Parylene [7].

In Figure 7 measurement result are depicted of MDCK cells grown in a multi-well plate for 24 hours exposed to 3D-printed parts with and without Parylene-C coating. The Parylene-C coating strongly inhibits the cytotoxic effect of the resin. The MDCK cells behaviour in Figure 7c is similar compared to the negative control depicted in Figure 7a, while the cells exposed to uncoated parts die.

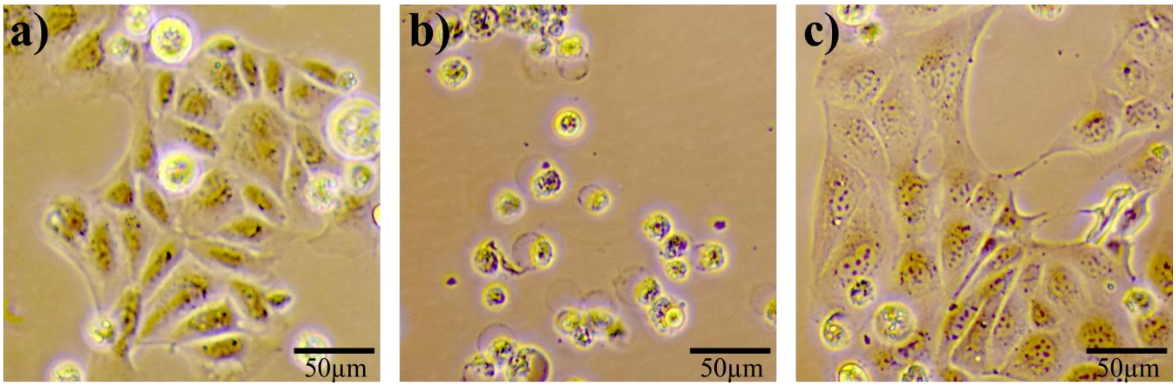

Figure 7: Cytotoxicity test. MDCK cells exposed to 3D-printed structures with and without parylene coating. MDCK cells were grown for 24 hours in culture medium (GMEM and 10% fetal bovine serum supplemented with penicillin and streptomycin). ***a)*** *Negative control. MDCK cells attached to the bottom of a well plate.* ***b)*** *MDCK cells exposed to a 3D-printed part made from HTM140 resin. The cells did not attach to the well plate.* ***c)*** *MDCK cells exposed to a 3D-printed part coated with a 10µm parylene C layer. The cell attached to the bottom of the well.*

CONCLUSIONS

The given examples show that 3D-printing is an attractive tool to realise microfluidic chip holders. The flexibility of 3D-printing allows quick redesign and fabrication of chip holders and adaptation for other chip geometries. Easy chip and holder assembly and disassembly is ensured by applying O-rings, integrated 3D channels and ports for fluidic connections as well as incorporating spring probes in the holder for electric contact to pads on the chip.

REFERENCES

[1] Labsmith One-piece fitting, . http://products.labsmith.com/one-piece-fitting (accessed September 8, 2017).

[2] D.J. Guckenberger, T.E. de Groot, A.M.D. Wan, D.J. Beebe, E.W.K. Young, Micromilling: a method for ultra-rapid prototyping of plastic microfluidic devices, Lab Chip. 15 (2015) 2364–2378. doi:10.1039/C5LC00234F.

[3] M. Vaezi, H. Seitz, S. Yang, A review on 3D micro-additive manufacturing technologies, Int. J. Adv. Manuf. Technol. 67 (2013) 1721–1754. doi:10.1007/s00170-012-4605-2.

[4] C. Sun, N. Fang, D.M. Wu, X. Zhang, Projection micro-stereolithography using digital micro-mirror dynamic mask, Sensors Actuators A Phys. 121 (2005) 113–120. doi:10.1016/j.sna.2004.12.011.

[5] EnvisionTec HTM140 resin, . https://envisiontec.com/wp-content/uploads/2016/09/MK-MTS-HTM140Industrial-V01-FN-EN.pdf (accessed September 8, 2017).

[6] F. Bunge, S. van den Driesche, M.J. Vellekoop, Microfluidic Platform for the Long-Term On-Chip Cultivation of Mammalian Cells for Lab-On-A-Chip Applications, Sensors. 17 (2017) 1603. doi:10.3390/s17071603.

[7] M. Akhtar, S. van den Driesche, A. Bödecker, M.J. Vellekoop, Long-term storage of droplets on a chip by Parylene AF4 coating of channels, Sensors Actuators B Chem. (2017) (in press). doi:10.1016/j.snb.2017.08.032.

CONTACT

* S. van den Driesche, sdriesche@uni-bremen.de

3^{RD} INTERNATIONAL CONFERENCE ON MICROFLUIDIC HANDLING SYSTEMS

PRISM SIGNAL PROCESSING: A RECURSIVE FIR TECHNIQUE APPLIED TO THE EFFICIENT TRACKING OF RESONANT SENSOR SYSTEMS

M.P. Henry[1]

[1] Department of Engineering Science, University of Oxford, Parks Road OX1 3PJ, UK.

ABSTRACT

A new technique called Prism signal processing has been developed which offers an FIR response, including a linear phase characteristic, while being a fully recursive calculation. The Prism signal processing block accepts a time series input and generate either one output or two orthogonal outputs, where the computational requirement is low and independent of data window length. A Coriolis flow metering example is used to illustrate that Prism signal processing is suited to a wide range of resonant sensor systems, and can be used to provide a step change in measurement update rates compared with conventional FIR techniques.

KEYWORDS

FIR filtering, recursive filtering, resonant systems, Coriolis mass flow metering, automotive fuel injection monitoring.

INTRODUCTION

A longstanding research issue for interfaces to sensors such as Coriolis mass flow meters [1] is the development of efficient signal processing techniques for tracking sinusoidal signals. This is particularly important for microfluidic devices where resonant frequencies may be high and where batch times can be short, requiring high measurement update rates. For robust industrial systems, FIR techniques (for example in filtering and/or sinusoidal tracking) are widely preferred over IIR techniques, due to their numerical stability and linear phase characteristics. However, FIR calculations are typically non-recursive, and hence computationally expensive, thus restricting measurement update rates, particularly in intrinsically safe (i.e. low power) devices. A new technique called Prism signal processing has been developed which offers an FIR response and a linear phase characteristic while being a fully recursive calculation.

THE PRISM

Given a noise-free sinusoidal signal $s(t)$:

$$s(t) = A\sin(2\pi ft + \phi), \qquad (1)$$

where t is time, A is the amplitude, f is the frequency in Hertz and ϕ is the phase offset at time t=0, we consider integrals of the following form:

$$I^h_{[s|c][s|c]} = \qquad (2)$$

$$m^2 \int_{-\frac{1}{m}}^{0} [\sin|\cos](2\pi hmt + q) \left(\int_{t-\frac{1}{m}}^{t} [\sin|\cos](2\pi hmt + q) \cdot s(t)dt \right) dt$$

The subscript notation [s | c] indicates the selection of one alternative between s and c. The superscript h is the harmonic number, a positive integer, usually small. m is the characteristic frequency, where, in any digital implementation, its period must be a whole number of sample durations. q is an arbitrary initial phase of the modulation function. Analytically, groups from this integral family can be combined to form simple results. Specifically:

$$G^h_s = I^h_{ss} + I^h_{cc} = A\,\mathrm{sinc}^2(r)\frac{r^2}{r^2 - h^2}\sin(\phi - 2\pi r) \qquad (3)$$

$$G^h_c = I^h_{cs} + I^h_{sc} = A\,\mathrm{sinc}^2(r)\frac{hr}{r^2 - h^2}\cos(\phi - 2\pi r) \qquad (4)$$

Here r is the frequency ratio of the input sinusoid, defined as:

$$r = f / m, \qquad (5)$$

so that $r = 0$ when $f = 0$ Hz and $r = 1$ when $f = m$ Hz.

While the numerical evaluation of double integrals is expensive, these particular groups can be evaluated recursively as follows. Equations (3) and (4) remain true irrespective of the initial phase q of the modulation function in (2). Accordingly, it is possible to evaluate each integral in a ‘sliding window’ arrangement whereby only the oldest product value (data x modulation function) is removed and the newest value computed and included in the updated integral value. Using this approach, it is possible to evaluate G^h_s and G^h_c efficiently, so that the computational cost is low and independent of the window length in samples.

Figure 1 illustrates the structure of the Prism, implemented as two layers of integration blocks. It accepts an input signal $s(t)$ and generates up to two outputs G^h_s and/or G^h_c. The symbol on the right may be used to represent the Prism in diagrams of more complex signal processing arrangements. It will be noted that the two outputs of the Prism (3) and (4) are orthogonal, facilitating the calculation of frequency,

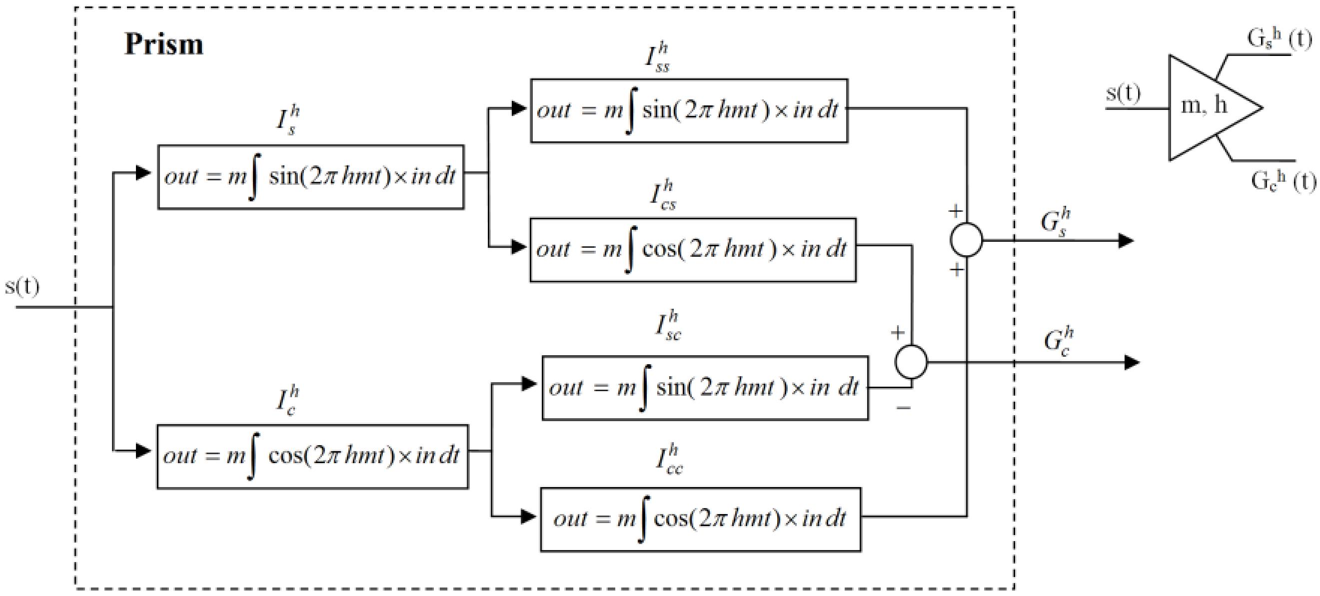

Figure 1: Prism Implementation and Symbol.

phase and/or amplitude information of the underlying signal. Figure 2 shows how the gains of G_s^h and G_c^h vary with frequency for $h = 1$. Notches occur at every multiple of m Hz, including DC. Note also that there is no conventional 'pass band' where the gain is constant. The linear phase and varying gain characteristics of the Prism outputs facilitate a variety of techniques such as low pass, bandpass and notch filtering. Several trackers have been developed to calculate the frequency, amplitude and/or phase of a sinusoidal signal. For example, the Recursive Signal Tracker (RST) has a tracking performance close to the Cramer-Rao Lower Bound [1] despite its low computational load. A conference paper [2] outlines some Prism signal processing techniques, and their use for tracking frequency components in ultrasonic pulses for a pressure sensor validation application.

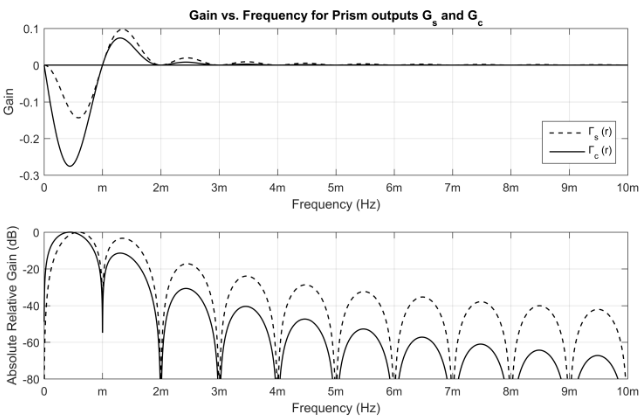

Figure 2: gains of Prism outputs G_s^h and G_c^h for h = 1.

FUEL INJECTION MONITORING

Prism signal processing has been used to develop an application of Coriolis mass flow metering for tracking fuel injection in a laboratory diesel engine. Here, fuel pulses as short as 1 ms are injected into a test cylinder at pressures of up to 100 MPa in a noisy mechanical environment (Figure 3). Working with a conventional commercial flowtube (Rheonik RHM 015, rated to 110 MPa), a new prototype transmitter has been built based around the Zynq-7000 chip [3], in which one of the two ARM Cortex-A9 processors is dedicated to measurement calculation, and where sensor data is sampled and flow measurement values are generated, at 48 kHz. This measurement update rate represents a significant advance on previous 'fast' Coriolis meter transmitters (e.g. 1.5 kHz [4]).

Figure 3: Experimental set up: high pressure diesel fuel line, Coriolis flowtube, injector, cylinder.

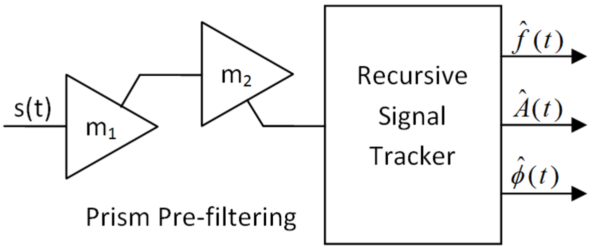

Figure 4. Signal processing scheme for one sensor chamnel of a Coriolis meter, including notch filtering and a Recursive Signal Tracker.

A Prism-based signal processing scheme for the Coriolis meter (Figure 4) includes a tracker for each sensor signal and notch filtering to remove undesired modes of oscillation excited by external mechanical noise. The flow measurement is derived from the difference in the instantaneous phases measured on the two sensor signals. This system is able to detect 1ms fuel pulses distinctly at engine speeds of up to 4000 RPM. Figure 5 shows the effectiveness of notching out the undesired frequency components by comparing the phase difference measurements obtained on the same raw sensor data set with and without the notch filtering.

Figure 6 shows the same flow pulse train in detail, with the noisy data removed. While each pulse is detected distinctly, there remain significant further challenges to overcome in order to obtain precise and accurate flow measurements. A limiting factor on the current system is the relatively low flowtube oscillation frequency (around 150 Hz). This leads to a ‘smearing’ of each 1ms flow pulse over an extended period of time (typically 16 ms). It is expected that the use of higher frequency flowtubes (say towards 1 kHz) would result in better measurement tracking of the fuel injection pulses. A consortium of interested parties is currently preparing a research project to develop new laboratory instrumentation for the automotive industry based on this approach.

As the Coriolis example illustrates, Prism signal processing is suited to a wide range of resonant sensor systems, and can be used to provide a step change in measurement update rates compared with conventional FIR techniques for a given computational budget.

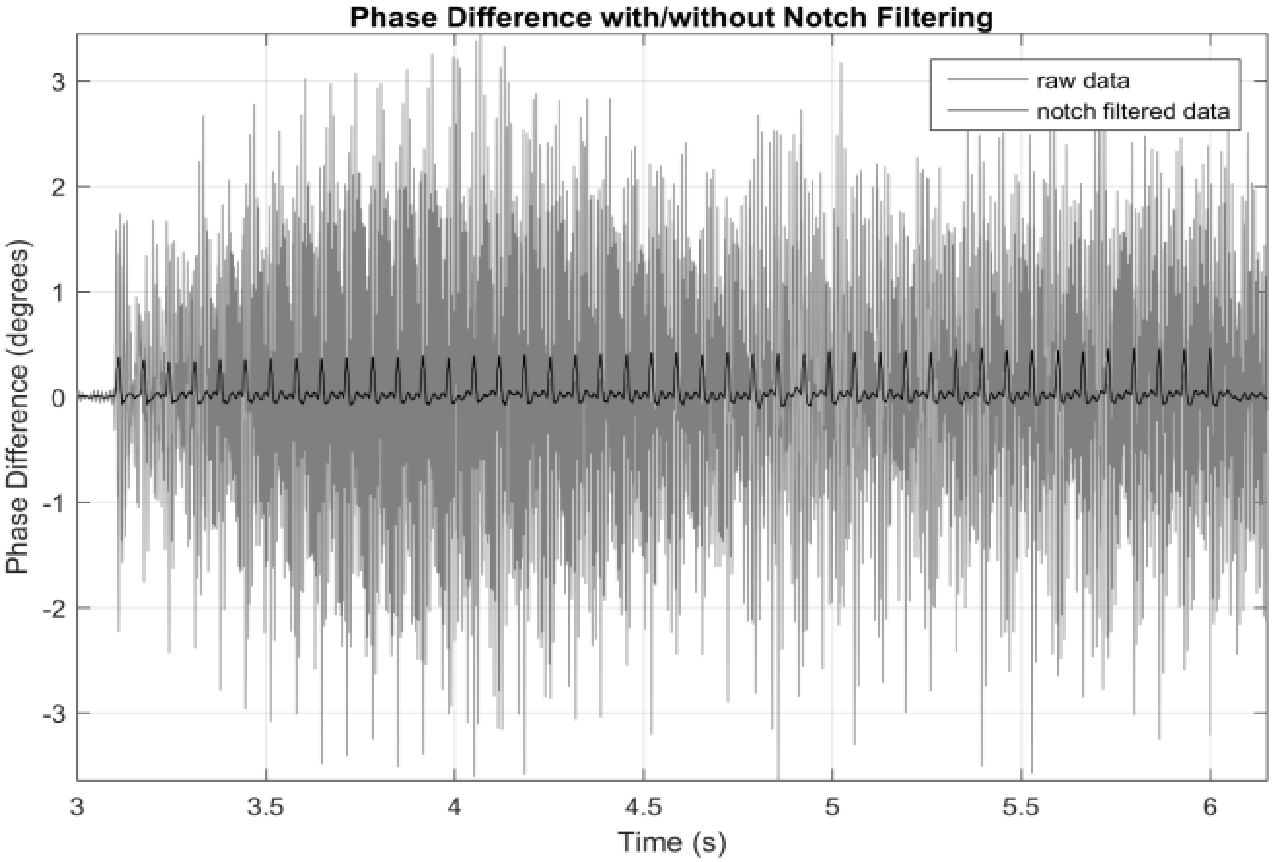

Figure 5. Phase difference measurement from a prototype Coriolis mass flow meter in response to a sequence of 1 ms fuel pulses: wth and without Prism-based notch filtering.

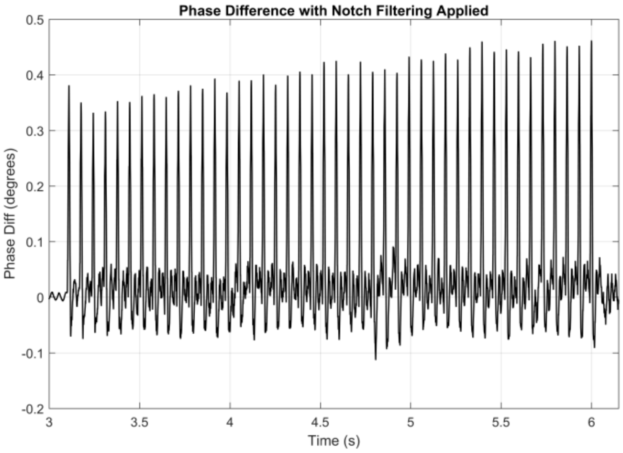

Figure 6. Phase difference measurement (detail).

CONCLUSIONS

Prism signal processing is a new FIR filtering technique which, by providing a recursive calculation with orthogonal outputs, facilitates rapid and flexible signal processing. Note also that as the filter ‘coefficients’ of the Prism are linearly spaced sine and cosine values, Prism reconfiguration (for example to adjust the frequency range over which it operates) is straightforward, and as a general rule of thumb, any device capable of running a Prism should be able to design one. This offers a significant advantage over conventional FIR filtering, where filter design is computationally expensive and almost invariably an offline task.

The Prism is suited to a wide range of applications, particularly those entailing signals with one or more discrete frequency components, even where these frequencies vary with time. For a given computational budget, Prism signal processing may afford a substantial increase in measurement update rate: in the Coriolis example, the update rate increased by a factor of over 100 times compared with conventional commercial devices. These capabilities match the signal processing requirements for high frequency resonant devices used in microfluidic applications.

A patent on Prism signal processing techniques has been filed by Oxford University [5]. We would welcome interest from potential partners in the microfluidic community to develop new applications.

REFERENCES

[1] J. Ruoff, W. Gauchel, and H. Kück, “Advances in Signal Acquisition and Signal Processing of Coriolis Flow Meters,” Procedia Eng., vol. 87, pp. 1585–1588, 2014.

[2] Henry, MP, Bushuev, O, Ibryaeva, O. “Prism Signal Monitoring for Sensor Condition Monitoring”. IEEE International Conference on Industrial Electronics, Edinburgh, UK, June 2017. DOI: 10.1109/ISIE.2017.8001451

[3] Xilinx, https://www.xilinx.com/products/silicon-devices/soc/zynq-7000.html

[4] Clark C, Zamora M, Cheesewright R, Henry M. “The dynamic performance of a new ultra-fast response Coriolis flow meter”. Flow Measurement and Instrumentation 2006;17:391–8.

[5] Henry, MP. “Method and system for tracking sinusoidal wave parameters from a received signal that includes noise.” GB Patent Application GB1619086.0, 11 November 2016.

CONTACT

* M.P. Henry, manus.henry@eng.ox.ac.uk

CORIOLIS MASS FLOW AND DENSITY SENSOR ACTUATION USING A PHASE-LOCKED LOOP

D. Alveringh[1], *T.V.P. Schut*[1], *R.J. Wiegerink*[1], *and J.C. Lötters*[1,2]
[1] MESA+ Institute for Nanotechnology, University of Twente, Enschede, The Netherlands
[2] Bronkhorst High-Tech BV, Ruurlo, The Netherlands

ABSTRACT

This paper reports on novel feedback based actuation electronics that use the voltage from the induction track of a Coriolis mass flow sensor as input signal for a phase-locked loop. The phase-locked loop consists of a phase detector that measures the difference between the actuation voltage and the induction voltage from the Coriolis mass flow sensor. A voltage controlled oscillator is directly tuned by this phase mismatch and synthesizes an harmonic signal for actuation. Therefore, the frequency of the signal synthesized by the phase-locked loop will gradually be adjusted to the resonance frequency of the Coriolis mass flow sensor, making it more robust to disturbances. Besides, waveform shape and amplitude can be easily altered. First experimental results show that the phase-locked loop controls the frequency as a function of density for different fluids. Stability is tested for nitrogen and shows a standard deviation of 0.148 18 Hz for 20 ks.

KEYWORDS

Coriolis mass flow sensor, density sensor, phase locked loop, actuation, resonance.

INTRODUCTION

A first of its kind Coriolis mass flow sensor based on surface channel technology has been realized by Haneveld et al. [1] This Coriolis mass flow sensor is actuated in twist mode by supplying it with a varying electrical signal, inducing Lorentz forces as a result of an externally applied magnetic field. A fluid flow forces the Coriolis mass flow sensor to move in swing mode too; this effect is used to sense the mass flow. Figure 1 shows an illustration of both the twist mode due to actuation and the swing mode due to the Coriolos force. The mechanical resonance frequency of the actuated structure depends on the modal stiffness and on the modal mass. Latter depends on the mass of the channel and the mass of the fluid inside. This means that the Coriolis mass flow sensor can also be used as a density sensor, as long as the resonance frequency can be detected.

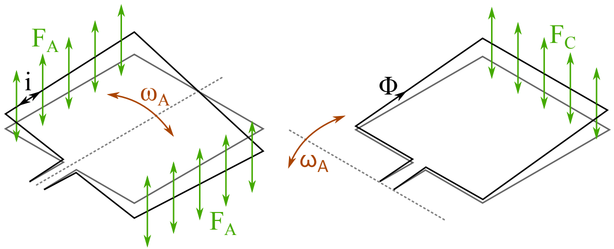

twist mode
(due to actuation)

swing mode
(due to Coriolis force)

Figure 1: The Coriolis mass flow sensor is actuated in twist mode using Lorentz actuation. When a fluid flows through the channel, a swing mode is induced. The ratio between the two modes is a measure for the mass flow. The resonance frequency of the structure is dependent on the density of the fluid.

In the first generation of actuation electronics, the frequency is tuned to the resonance frequency by hand. Since the frequency changes with the density of the fluid inside the channels, an electronic feedback system has been designed that uses the output signal from the Coriolis mass flow sensor to tune the oscillator to the resonance frequency (second generation). In the third generation of this Coriolis mass flow sensor actuation electronics, the induction voltage of an extra metal track on the Coriolis mass flow sensor is amplified and used for actuation [2]. In spite of the convenience and performance improvements with these actuation circuits, there are still multiple drawbacks on these technologies.

- A mechanical disturbance, e.g. vibration, of the Coriolis mass flow sensor will influence the actuation directly.
- A fluidic disturbance, e.g. air bubble, instantly changes the actuation frequency for a short time.
- The analog circuit amplifies the signal rather than synthesizes it, i.e. the signal is not harmonic.

Synthesizing the actuation signal in a controlled way would help overcome these drawbacks. This is done for high frequencies for telecommunication applications with a phase-locked loop [3]. Phase-locked loops are also used for controlled actuation of servo motors [4]. This paper describes the first results of actuation of a Coriolis mass flow sensor using a phase-locked loop.

THEORY

A basic phase-locked loop consists of three components as is illustrated in Figure 2. First, a phase detector finds the phase difference between the output signal $S_\mathrm{o}(t)$ and the input signal $S_\mathrm{i}(t)$. The input signal can be modeled as an harmonic signal with ω_i the frequency and ϕ_i the phase:

$$S_\mathrm{i}(t) = \mathrm{S}_\mathrm{a,i} \cdot \sin(\omega_\mathrm{i} t + \phi_\mathrm{i}), \tag{1}$$

The detected phase difference is then:

$$\phi_\mathrm{e} = \phi_\mathrm{i} - \phi_\mathrm{o}, \tag{2}$$

and could be seen as the error that the phase-locked loop needs to solve. The second component is a low-pass filter. It filters a possible ripple on the phase difference caused by the phase detector and disturbances from the input signal. The last component is a voltage controlled oscillator. This oscillator synthesizes a periodic signal with a frequency dependent on the input. The voltage controlled oscillator always provides an output signal at a frequency, also when no input is given. This is called the quiescent frequency. The output frequency ω_o of the signal is:

$$\omega_\mathrm{o} = \omega_0 + \mathrm{K} \cdot \phi_\mathrm{e}, \tag{3}$$

with ω_0 the quiescent frequency and K the sensitivity of the voltage controlled oscillator. The output signal is therefore equal to:

$$S_\mathrm{o}(t) = \mathrm{S}_\mathrm{a,o} \cdot \sin((\omega_0 + \mathrm{K} \cdot \phi_\mathrm{e})t + \phi_\mathrm{o}). \tag{4}$$

Note that the frequency of the output signal is corrected based on the phase difference between output and input signal. This means that not only the output frequency will approach the input frequency, but the phases will be synchronized as well.

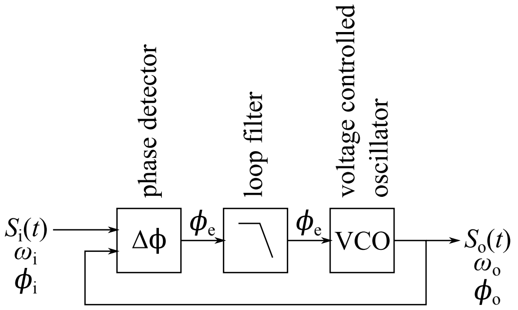

Figure 2: Basic phase-locked loop consisting of a phase detector, a low-pass filter and a voltage controlled oscillator. The phase detector measures the difference between the output and input signal. The voltage controlled oscillator is directly tuned by this phase mismatch and synthesizes an harmonic signal that is synchronized with the input signal.

DESIGN

The chip (Figure 4) is adhesively mounted on a printed circuit board. Fluid inlet and outlet are connected at the backside of the board where a constant mass flow of fluid is applied (Figure 3).

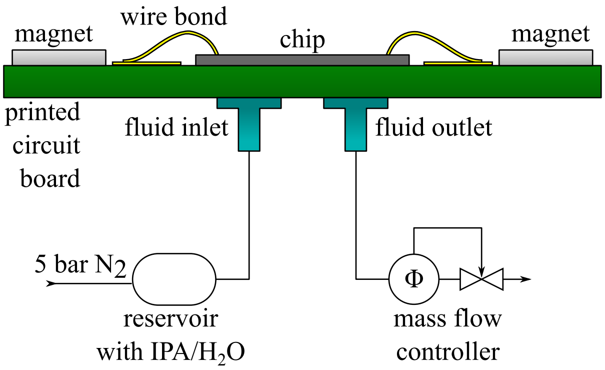

Figure 3: Illustration of the chip assembly on a printed circuit board and its interface to the fluidic measurement setup.

The tested Coriolis mass flow sensor has multiple metal tracks on the channel as can be seen in the scanning electron microscopy close-up in Figure 4. One metal track is used to apply the actuation current, another is used to detect the induced voltage due to actuation. The induction track is connected to a differential amplifier with high input impedance.

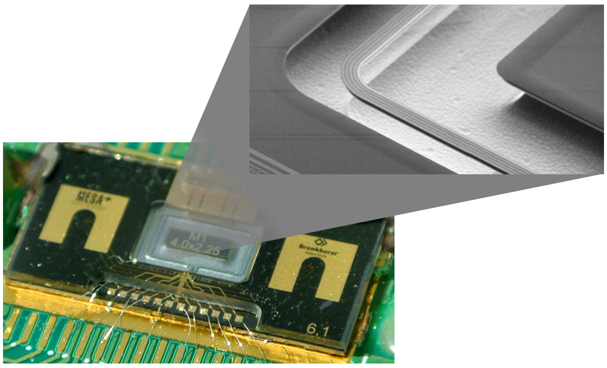

Figure 4: Photograph of the chip with close-up of the suspended channel with multiple metal tracks of the Coriolis mass flow sensor.

The phase-locked loop is realized using a Cypress Semiconductor PSoC 5 development kit and is based on the work of De Lima Fernandes [5]. This development kit has a programmable system on chip with digital and analog electronic components. Figure 5 shows an overview of the phase-locked loop implementation in the programmable system on chip.

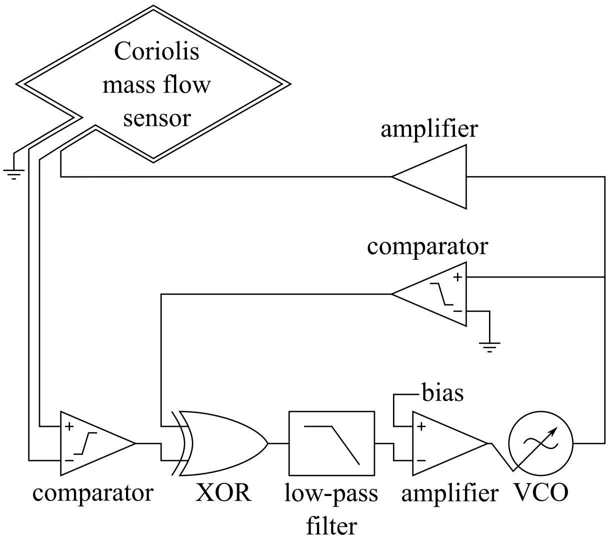

Figure 5: Implementation of the phase-locked loop with the connections to the Coriolis mass flow sensor in a programmable system on chip.

An embedded analog comparator converts the signal to a square wave to make it compatible with digital electronics. An XOR-gate compares the square wave with the synthesized output of the phase-locked loop. This stage performs the phase detection: the XOR-gate gives a pulse at every sample when the square wave from the induction track is not equal to the synthesized actuation voltage. After a full period, the XOR-gate gives a signal with more high values at its output when the phases are more different. The output of the XOR-gate is connected to a low-pass filter, which provides an analog signal that is a measure for the phase mismatch. This first order low-pass filter is implemented using an embedded operational amplifier with an external capacitor and resistor, tuned for a cut off frequency of approximately 1 Hz.

The input of the voltage controlled oscillator is connected to a bias voltage generator to set the quiescent frequency. The bias voltage generator is realized using an embedded operational amplifier. The voltage controlled oscillator with output voltage $V_{\mathrm{vco,o}}$ is implemented as an embedded current source i_{vco} that charges an external capacitor C:

$$V_{\mathrm{vco,o}} = \frac{1}{\mathrm{C}} \int \mathrm{i}_{\mathrm{vco}} \mathrm{d}t = \frac{\mathrm{i}_{\mathrm{vco}} t}{\mathrm{C}}. \tag{5}$$

An embedded comparator connects the capacitor to ground when the threshold, equal to the input of the voltage controlled oscillator $V_{\mathrm{vco,i}}$, is reached:

$$V_{\mathrm{vco,o}} = V_{\mathrm{vco,i}}, \tag{6}$$

and so:

$$V_{\mathrm{vco,i}} = \frac{\mathrm{i}_{\mathrm{vco}} t}{\mathrm{C}} \rightarrow \frac{\omega_0}{2\pi} = \frac{1}{t} = \frac{V_{\mathrm{vco,i}}}{\mathrm{C}\ \mathrm{i}_{\mathrm{vco}}}. \tag{7}$$

An embedded flip-flop is used to force the duty cycle of the output signal to be 50 %. An embedded signal synthesizer is used to synthesize a sine wave for the actuation voltage of the Coriolis mass flow sensor. Figure 6 shows a photograph of the full electronic setup.

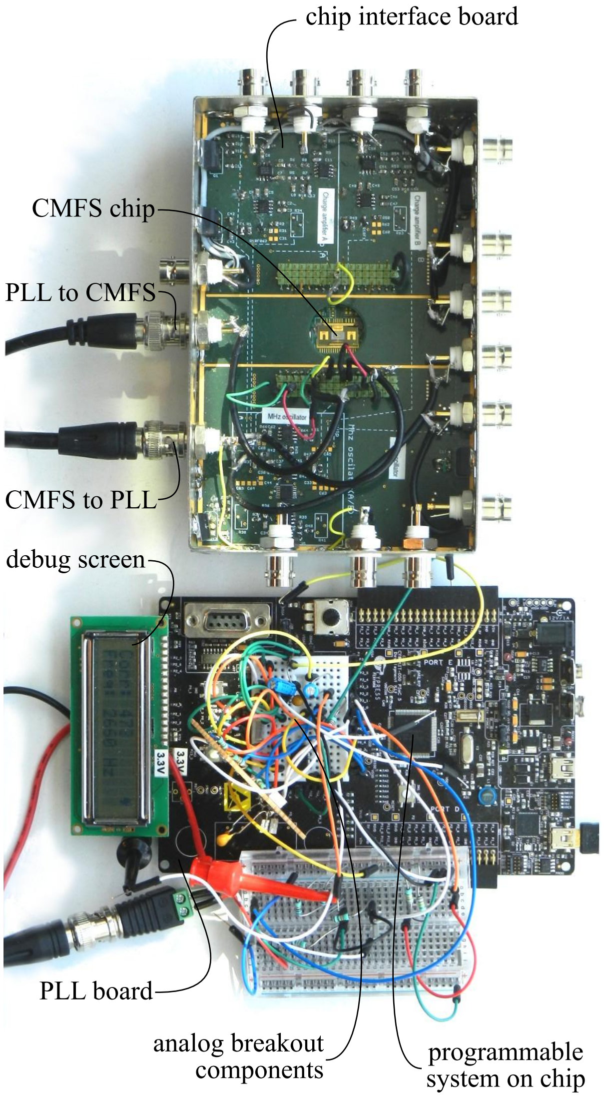

Figure 6: Photograph of the electronic phase-locked loop implementation. The Coriolis mass flow sensor (CMFS) is located in the center on the chip interface board. The phase-locked loop (PLL) is realized on the PLL board in the programmable system on chip and

MEASUREMENTS

To test the phase-locked loop for Coriolis mass flow sensor actuation, multiple fluids are applied to the sensor and the frequencies are recorded using a Keysight 34461A multimeter. The experiments are conducted with nitrogen, water, isopropyl alcohol and a mix of isopropyl alcohol and water (equal volume). The results are plotted in Figure 7 and show that the actuation circuit adjusts the frequency to the resonance frequency of the Coriolis mass flow sensor.

The stability is investigated by finding the mean and standard deviation of 5001 measurements in approximately 20 ks for nitrogen. The mean is 2672.546 Hz and the standard deviation is 0.148 18 Hz, calculated from the data in Figure 8.

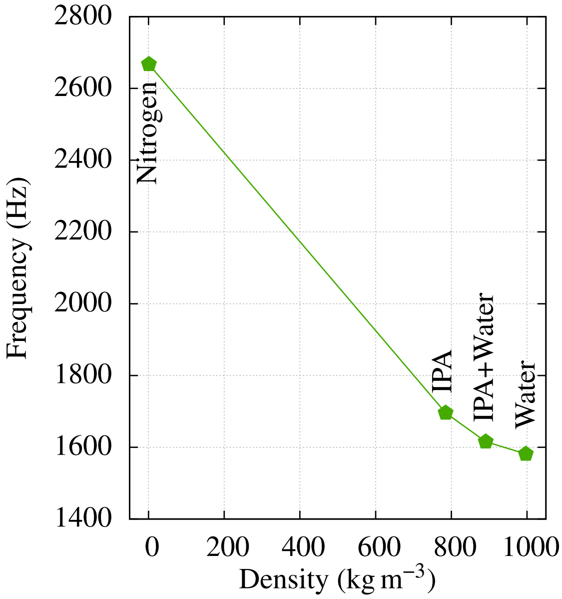

Figure 7: Measured resonance frequencies for four different substances.

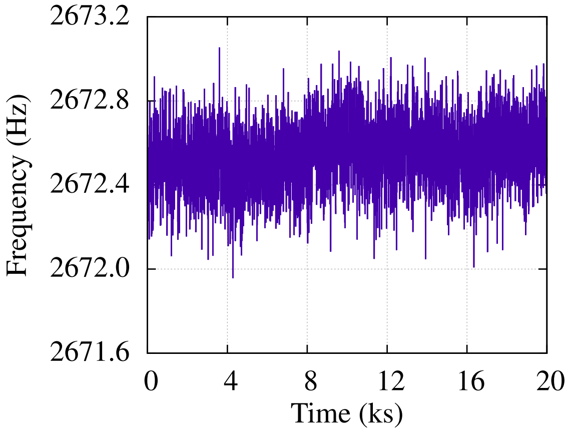

Figure 8: Stability measurement of 5001 samples (20 ks) for nitrogen with constant pressure and mass flow.

CONCLUSION

A phase-locked loop is realized to actuate a Coriolis mass flow sensor at its resonance frequency. First experimental results show that the phase-locked loop controls the frequency for nitrogen, water, isopropyl alcohol and a mixture of water and isopropyl alcohol. In contrast with other actuation methods, it can be fine tuned to make the actuation of the Coriolis mass flow sensor be more robust against disturbances or lower the response time. Besides, waveform shape and amplitude can be easily altered.

Future work will focus on quantitative analysis through measurements of the performance of the PLL compared to the conventional actuation circuits.

ACKNOWLEDGEMENTS

The authors gratefully acknowledge support by the Eurostars Programme through the TIPICAL project (E!8264) and technical support by R.G.P. Sanders and J. Groenesteijn.

REFERENCES

[1] J. Haneveld *et al.*, “Modeling, design, fabrication and characterization of a micro Coriolis mass flow sensor,” *Journal of Micromechanics and Microengineering*, vol. 20, no. 12, p. 125001, 2010.

[2] J. Groenesteijn, “Microfluidic platform for Coriolis-based sensor and actuator systems,” Ph.D. dissertation, University of Twente, Enschede, January 2016.

[3] G.-C. Hsieh *et al.*, “Phase-locked loop techniques. a survey,” *IEEE Transactions on industrial electronics*, vol. 43, no. 6, pp. 609–615, 1996.

[4] G. Volpe, “A phase-locked loop control system for a synchronous motor,” *IEEE Transactions on Automatic Control*, vol. 15, no. 1, pp. 88–95, 1970.

[5] A. De Lima Fernandes, “Demystifying the PLL,” 2013.

CONTACT

* D. Alveringh, d.alveringh@utwente.nl

UNIVERSAL MODULAR FLUIDIC AND ELECTRONIC INTERFACING PLATFORM FOR MICROFLUIDIC DEVICES

D. Alveringh[1]*, R.G.P. Sanders*[1]*, J. Groenesteijn*[1,2]*, T.S.J. Lammerink*[1]*,*
R.J. Wiegerink[1]*, and J.C. Lötters*[1,2]
[1] MESA+ Institute for Nanotechnology, University of Twente, Enschede, The Netherlands
[2] Bronkhorst High-Tech BV, Ruurlo, The Netherlands

ABSTRACT

A universal modular fluidic and electronic interfacing platform for microfluid devices has been designed, built and tested. The platform supports interfacing chips with up to 8 fluidic and 72 electrical connections. The current module set consists of a high frequency oscillator module, a charge amplifier module, a resonator actuator module and a weather station module. These modules can be used to characterize e.g. pressure sensors, density sensors and Coriolis mass flow sensors. For latter device, the platform with these modules performs approximately 2.5 times better in lower noise than the conventional setup. Besides, chip packaging is two to three times less labor intensive.

KEYWORDS

Microfluidics, chip interfacing, sensor characterization, micro sensors, micro actuators, flow sensors, pressure sensors, density sensors.

INTRODUCTION

One challenge in microfluidic sensor and actuator characterization concerns the readout and fluidic interfacing. Usually, a custom packaging method needs to be designed and fabricated for each chip design. For research purposes, sample quantities are limited, therefore packaging is usually done by hand.

The Coriolis mass flow sensor from Haneveld et al. [1] for example, has a fluid path and two capacitive readout structures with capacitance changes in the femto farad range. A specific printed circuit board is designed for this chip, as is illustrated in Figure 1a. Magnets for the Lorentz force actuation are adhesively mounted in trenches at both sides (Figure 1b). The chip is adhesively mounted on the copper surface in the center (Figure 1c). Then, the chip is wirebonded to the printed circuit board (Figure 1d) and pin headers are soldered for electrical connections to the measurement equipment (Figure 1e). Finally, fluidic connectors (Swagelok®1/16") are adhesively mounted on the backside of the printed circuit board. This assembled result can now be electrically and fluidically interfaced, however:

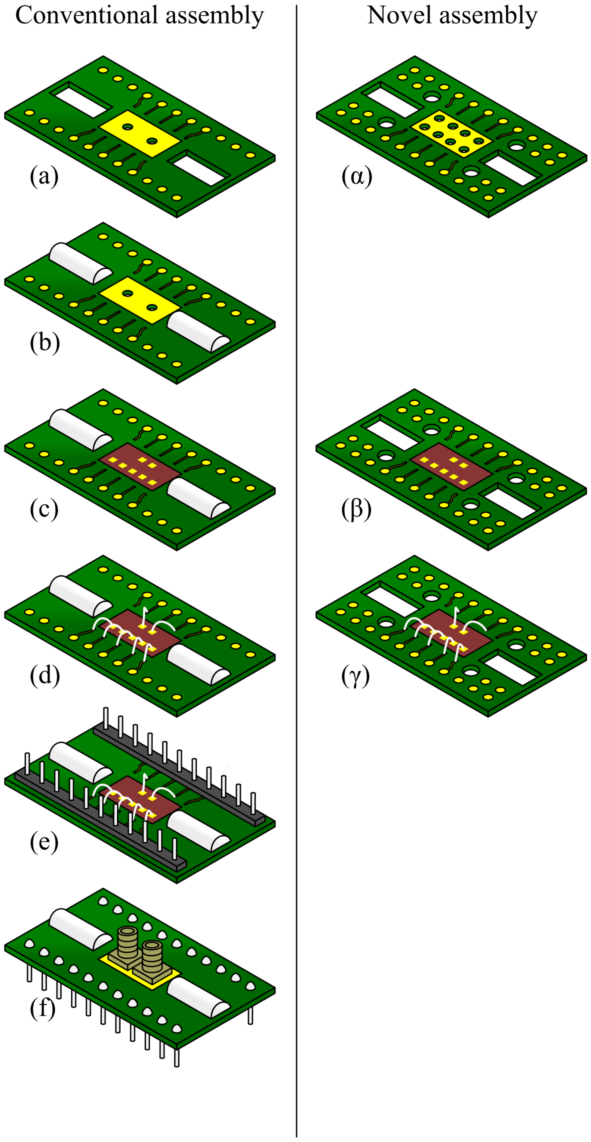

Figure 1: Conventional and novel assembly method for the interfacing of microfluidic chips. The conventional assembly consists of adhesively mounting magnets (b), adhesively mounting the chip on the PCB (c), wirebonding the chip to the PCB (d), soldering pin headers (e) and adhesively mounting fluidic connectors (f). The novel assembly consists of adhesively mounting the chip (β) and wirebonding the chip to the PCB (γ).

- the assembly has been very specific, labor-

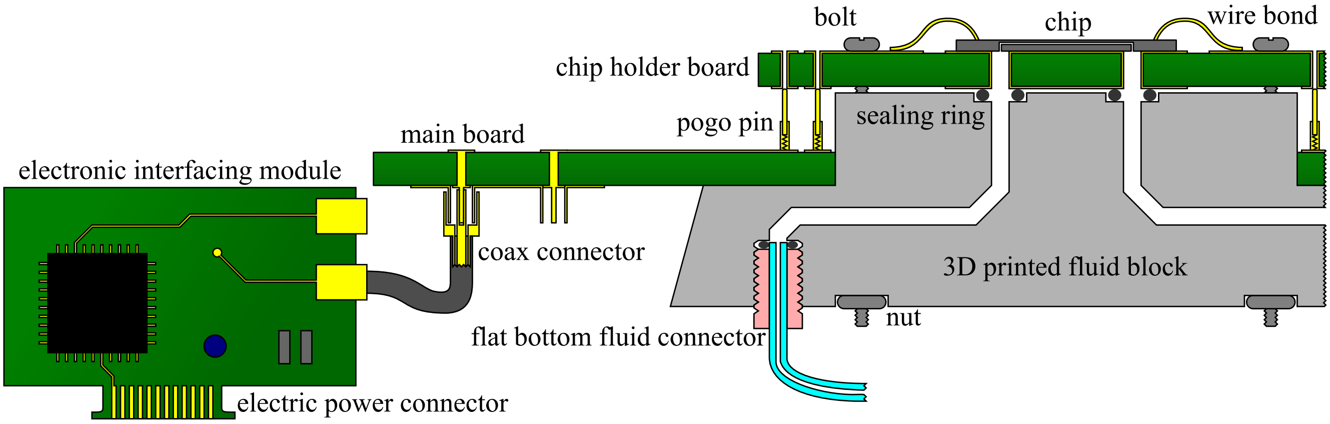

Figure 2: Illustration of all components of the interfacing platform. The chip is mounted on a chip holder board. This board is fluidically connected with a 3D printed fluid block to tubing with flat bottom connectors. The chip holder board is connected electrically via pogo pins to the main board. Coax cables connect the main board to electronic interfacing modules.

intensive and riskful work;

- other microfluidic devices might have different dimensions or need more electric or fluidic connections, the method is not universal.

The complexity of the electronic and fluidic interface is even higher with chips that contain multiple sensors and/or actuators [2, 3, 4, 5]. To gain efficiency, robustness and simplicity, a universal interfacing platform has been designed and built.

INTERFACING PLATFORM

Figure 2 shows an overview of the platform. Every part of the platform will be briefly described below in this section. The electronic interfacing module set will be described in the next section.

Chip holder board

The chip holder board (illustrated in Figure 1α) has been inspired by the conventional packaging method, but has multiple improvements. It features:

- 8 fluid connections;
- 72 electric connections;
- 72 grounding connections for shielding.

The assembly only consists of adhesively mounting the chip on the chip holder board (Figure 1β) and wirebonding (Figure 1γ). There is no need for the assembly of magnets or soldering the pin headers, since this is implemented in the main board design.

Main board

The chip holder board can be clamped on the main board with four screws. The electrical connections are realized with pogo pin connectors. For each signal pin, there is a ground pin diagonally alternated in the 2 × 10 and 2 × 4 connectors to improve shielding. The main board has 16 junction gate field-effect transistors (JFET) directly connected to 16 of the 72 signal pins. These transistors can be used as close-to-the-chip amplifiers for capacitive measurements.

Connections to the main board, from e.g. modules that will be explained later, can be made using micro-miniature coaxial (MMCX) connectors. Figure 3 shows the frontside with the chip holder board being placed on the main board.

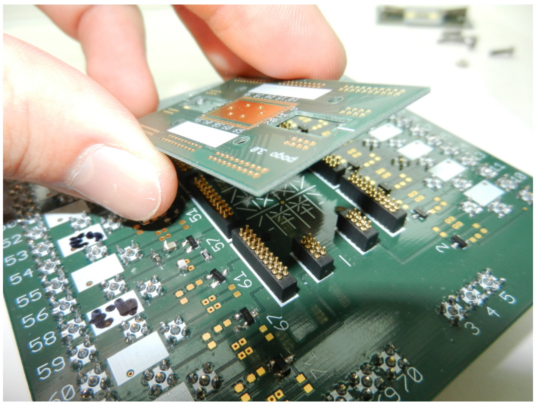

Figure 3: Frontside of the main board with a chip holder board being mounted.

Fluidic connector

Figure 4 shows the fluidic connector on the main board. This polymer 3D-printed fluidic connector allows for up to 8 fluidic connections to the chip holder board. The fluidic contact is made using o-rings placed in grooves in the fluidic connector.

Power board

The power board has 8 Peripheral Component Inter-

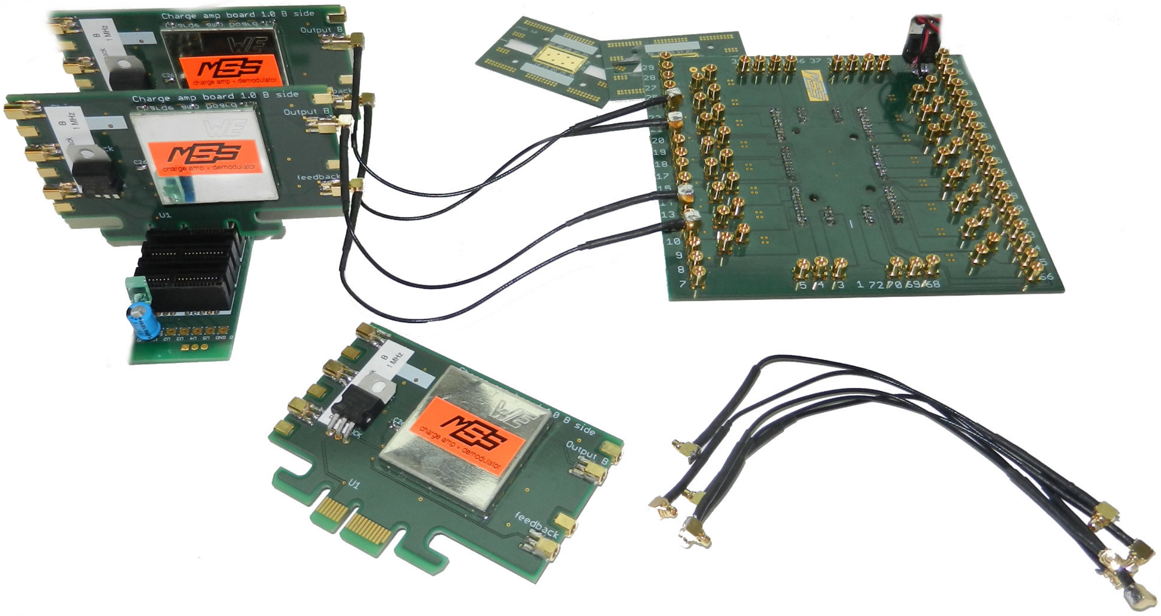

Figure 5: Photograph of the main board with multiple modules.

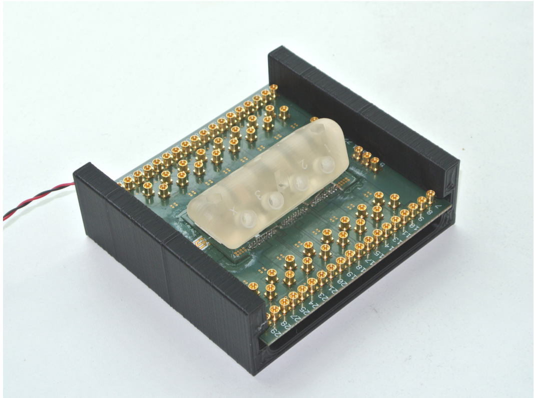

Figure 4: Backside of the main board with the fluid block and the connectors to the modules.

connect Express (PCIe) connectors to hold the modules and supply power to them. The pinout is not consistent with the PCIe standard; the connectors itself are just used because of its capability to clamp and connect to a PCB directly. Multiple voltages can be applied to the modules via the PCIe connectors, but the default supplied voltage is 10 V. Every module has its own voltage regulator to provide a reliable power source for the electronics. Multiple pins of the PCIe connectors are interconnected to provide a possible bus implementation in the future.

ELECTRONIC INTERFACING MODULES

These modules can be connected using coaxial cables via MMCX connectors to the main board. The set consists at the time of writing of a high frequency oscillator module, a charge amplifier module, a resonator actuator module and a weater station module.

High frequency oscillator

This module has two high frequency (mega Hertz range) oscillators. Each oscillator provides a different frequency and has besides the default 5 V square wave output a tuneable amplitude output and an inversed output. The oscillators can be used to provide a carrier signal for e.g. capacitive readout structures. The variable amplitude output can for instance be used for actuation mode cancellation in the capacitive Coriolis mass flow sensor read-out as shown in [6].

Charge amplifier

This module has two charge amplifiers for capacitive readout. Each module also has a demodulation circuits, but the charge amplifier can be used solely as well. The demodulation circuits can be synchronized with the high frequency oscillators, which is convenient for the detection of alternating capacitances (e.g. capacitive Coriolis mass flow sensors [1]).

Resonator actuator

This module consists of a mechanical resonator actuator. The actuator is able to inductively detect the resonance frequency, amplify this signal and actuate the resonator at its resonance frequency. This could, for example, be used for Coriolis mass flow sensors and density sensors [7].

Weather station

This module consists of a temperature, pressure and humidity sensor. This module has a digital Universal Serial Bus (USB) output.

Future modules

One planned module has a high voltage amplifier for piezo actuation. Another planned module has a Wheatstone bridge readout circuit. This module will consist of a voltage supply and voltage meter and could be used for the characterization of thermal flow sensors and resistive pressure sensors.

PERFORMANCE

A Coriolis mass flow sensor has been completely interfaced with all existing modules. The performance of the platform has been tested by measuring the phase shift output of a Coriolis mass flow sensor without flow. The standard deviation has been calculated from the results as a measure for stability. This is done for both the novel platform and the conventional electronics. The phase detection is done using two Stanford Research Systems SR830 lock-in amplifiers. The integration time of the phase detection is varied between 10 ms and 10 s. In Figure 6, it can be seen that the novel platform has a noise level of approximately 2.5 times lower.

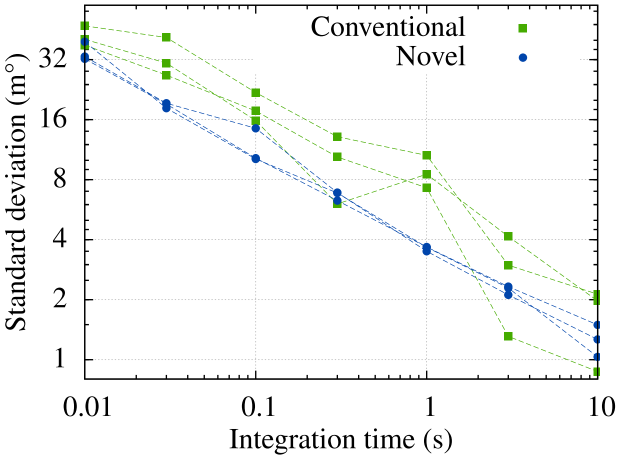

Figure 6: Stability measurement results of the conventional and the novel electronics for lock-in integration times of 10 ms to 10 s.

CONCLUSION

The proposed platform provides a time-efficient way to assemble, interface and characterize microfluidic devices. The high number of electric and fluidic connections combined with the modularity of the electronics enables the characterization of many different types of sensors and/or actuators.

Future work will focus on the design of more interface modules, e.g. a high voltage amplifier for piezo actuation purposes and a readout circuit for Wheatstone bridges.

ACKNOWLEDGEMENTS

This research was supported by the Eurostars Programme through the TIPICAL project (E!8264).

REFERENCES

[1] J. Haneveld *et al.*, “Modeling, design, fabrication and characterization of a micro Coriolis mass flow sensor,” *Journal of Micromechanics and Microengineering*, vol. 20, no. 12, p. 125001, 2010.

[2] J. C. Lötters *et al.*, “Integrated multi-parameter flow measurement system,” in *Proceedings of the 27th IEEE International Conference on Micro Electro Mechanical Systems (MEMS 2014)*. IEEE, 2014, pp. 975–978.

[3] J. Groenesteijn *et al.*, “Single-chip mass flow controller with integrated coriolis flow sensor and proportional control valve,” in *Proceedings of the 29th IEEE International Conference on Micro Electro Mechanical Systems (MEMS 2016)*. IEEE, 2016, pp. 788–791.

[4] D. Alveringh *et al.*, “Integrated pressure sensing using capacitive Coriolis mass flow sensors,” *Journal of Microelectromechanical Systems*, vol. 26, no. 3, pp. 653–661, 2017.

[5] D. Alveringh *et al.*, “Resistive pressure sensors integrated with a Coriolis mass flow sensor,” in *Proceedings of the 19th International Conference on Solid-State Sensors, Actuators and Microsystems (TRANSDUCERS 2019)*. IEEE, 2017, pp. 1167–1170.

[6] D. Alveringh *et al.*, “Improved capacitive detection method for Coriolis mass flow sensors enabling range/sensitivity tuning,” *Microelectronic engineering*, vol. 159, pp. 1–5, 2016.

[7] J. Groenesteijn *et al.*, “A compact micro coriolis mass flow sensor with flow bypass for a monopropellant micro propulsion system,” in *Proceedings of the 2nd Conference on MicroFluidic Handling Systems, MFHS 2014*. Albert-Ludwigs-Universität Freiburg, 2014, pp. 21–24.

CONTACT

* D. Alveringh, d.alveringh@utwente.nl

AN AUTONOMOUS MICROBIOREACTOR BASED ON A FUNCTIONAL LID IN 96-WELL MICROPLATE FORMAT

C-H. Tsai[1]*, S. Zimmermann*[1]*, M. Roggenbuck*[1]*, R. Zengerle*[1,2] *and P. Koltay*[1,3]

[1]Laboratory for MEMS Applications, IMTEK - Department of Microsystems Engineering, University of Freiburg, Germany

[2]Hahn-Schickard Freiburg, Germany and

[3]BioFluidix GmbH, Freiburg, Germany

ABSTRACT

In the biopharmaceutical industry, cell line development (CLD) for the production of therapeutic proteins primarily pursues a high production yield and product quality [1]. A typical process flow of cell line screening is from the selection of suitable cell lines in micro titer plate (MTP) to large bioreactors. However, the whole process may take up to one year. A well-developed, miniaturized and highly-parallel microbioreactor could reduce the processing time as well as the amount of cells and media consumption to make the evaluation more efficient.

In this work, we have developed an integrated microbioreactor (MBR) based on a disposable functional lid (FL) and a standard micro titer plate (MTP), which only requires one pressure source for parallel and reciprocal mixing of cells cultured in suspension in the MTP as an enabling feature for miniaturized cell culture in pharmaceutical CLD. The mixing principle of the FL does not only allow for working with significantly smaller culture volumes (30 - 200µl) on demand for at least one week, but also reduces the requirements of external processing stations.

KEYWORDS

functional lid, microbioreactors, cell line development

INTRODUCTION

The development processes within biotechnology, especially in the fields of cell line development, stem cell development, screening and cultivation applications, primarily require a high production yield, high throughput and high product or data quality. To meet these standards, a stable cell culture environment is required for a large number of experimental cell cultures from the beginning of the process to generate stable single-cell clones respectively reliable data. Cell lines are mainly used in the biopharmaceutical industry for the production of therapeutic proteins (monoclonal antibodies, etc.). One important feature in CLD is mixing of the cells by agitation to maintain a homogenous suspension culture which could be realized by placing MTPs on a shaker [2]. However, cultures in MTPs suffer from the disadvantages that essential parameters for cell survival like pH [3] or dissolved oxygen (DO) [4] cannot be controlled during culture, nor does a shaker provide the same mixing behavior as larger bioreactors applied in the downstream processing and upscaling. In addition, the obtained data is often limited to endpoint measurements. These disadvantages can be overcome by reduced microfluidic microbioreactors [5]. A thorough evaluation of process parameters such as oxygen level or pH value in a controlled reactor significantly increases the likelihood of selecting the best clones and minimizes the risks of scale up. Therefore, a FL based MBR (working volume < 100 µl) with high mixing efficiency, a high degree of automation and parallelization, and high flexibility regarding the later integration of sensors, like presented here, could help to significantly miniaturize and accelerate CLD.

METHOD

The homogeneity of the culture is mostly achieved by stirring or shaking the devices [6]. However, these approaches require relatively complex or large-base devices for the stirring or shaking process and for the control and selection of the process parameters.

We developed a novel microfluidic platform based on a functional lid (FL), which compatible with standard 96-well MTP. The innovation of the FL lies in the mixing principle, which is realized by reciprocal mixing with the aid of the FL applied on top of a 96-well microtiter plate. This mixing principle also allows for working with significantly smaller culture volumes. The 96-fluidic connections (FCs) between the FL and the wells of MTP, allow for mixing, exchange and processing of gases. As shown in Figure 1 (a), we manufactured each FC as lid containing 96 post in the 96-well array format each of them containing a tiny channel in the middle. Figure 1 (b) shows how the FCs are further extended into wells of the MTP wells by attaching pipette tips to the posts. Laser cutting is used to fabricate holes on a standard MTP lid as carrier for the pipette tips to maintain the position of tips extending into the wells. A pressure source is connected to the FCs through manifold for reciprocal operation. The tiny pipeline is dominating the flow resistance in each FC, therefore, it makes the reciprocal gas/fluidic flow through all FCs to be homogenous, provided that the fabrication error between the channels is negligible. Figure 1 (c) shows the system view of a FL extending the FCs into a MTP. Only one pneumatic port is fabricated on the top of the FL, and 96 pipette tips are used to extend 96 FCs of FL into the standard 96 MTP through a MTP lid with 96 fabricated holes.

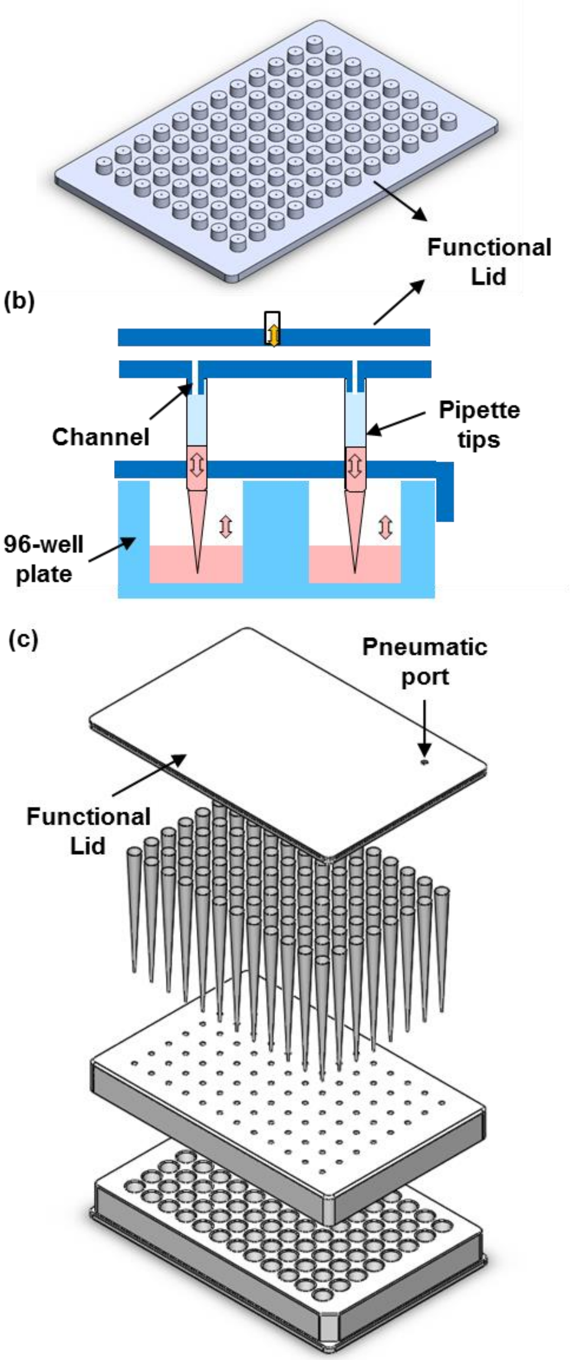

Figure 1: (a) The schematic view of the Functional Lid (FL) with 96 fluidic connections (FCs) (b) The working principle of a FL integrated with pipette tips and a standard micro titer plate (MTP). (c) The system view of a FL extending the FCs into a MTP.

EXPERIMENTAL RESULT

The following experimental results have been derived to verify the concept. We fabricated three different FLs with different geometries, prototype A, B, and C, shown in figure 2 (a). All the FLs are with 16 FCs with different sizes of the pipelines (A: 500 µm in diameter and 4 mm height; B, C: 3 mm in diameter and 4 mm height). For Prototype A and B, we use pipette tips to further extend the FCs into wells. Figure 2 (b) shows the result where the FLs are designed to reciprocate with 50 µl out of 100 µl DI water. Prototype A exhibited only 1-2 µl difference between the individual FCs, and prototype B and C exhibited bigger variation as we expected. The results show that the tiny channels in the FCs distribute the reciprocating flow generated through the single external connection homogenously.

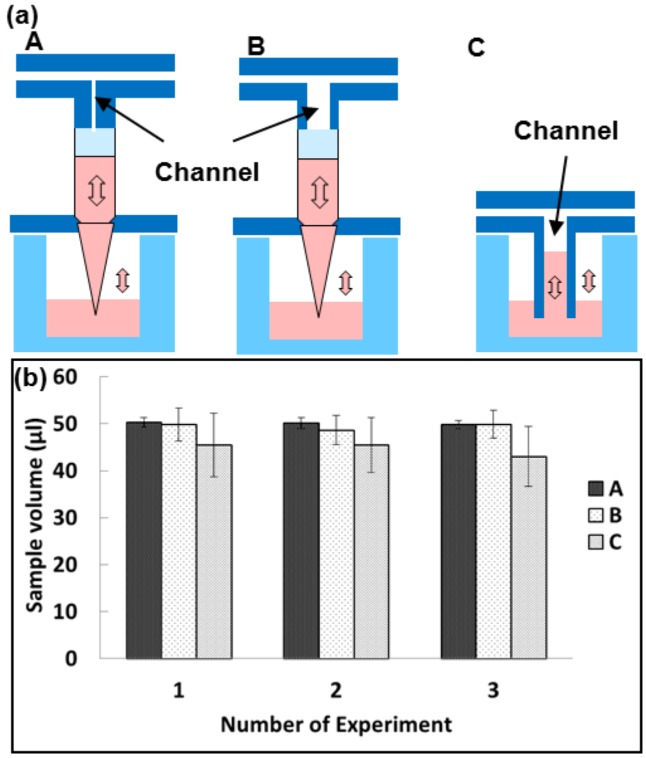

Figure 2: (a) The schematic side view of prototype A, B, and C of the F. (b) The reciprocal volume measurement of prototype A, B, and C. The error bars indicate the statistical variance of the 96 individual FCs within one FL.

We successfully drove the FL by three types of pressure sources: 1. a piezo pump, 2. a peristaltic pump, and 3. a digital hydraulic drive, which was modified from our previous research [7]. Table 1 shows the properties of the different pressure sources. The piezo pump is the smallest as well as cheapest and it can be driven by a battery. The peristaltic pump is more stable regarding the flow rate performance, but also more bulky and expensive. The digital hydraulic drive has the advantage that in can be operated in a wide pressure range.

We further used prototype A to reciprocate 30 µl, 50 µl, and 70 µl out of 100 µl DI water. Figure 3 shows the result, proving the FL is able to reciprocate the medium on demand.

	Piezo	Peristaltic	Reciprocating
Power	Battery	24V DC	5-12V DC
Pressure	60 kpa	100 kpa	180 kpa
Size(mm)	30*15*4	50*40*80	50*18*10
Cost	15 euro	90 euro	50 euro

Table 1: The property comparison of a piezo pump (mp6, Bartels, Germany), a peristaltic pump (TP S-50, THÖLEN, Germany), and a digital pressure source [6]

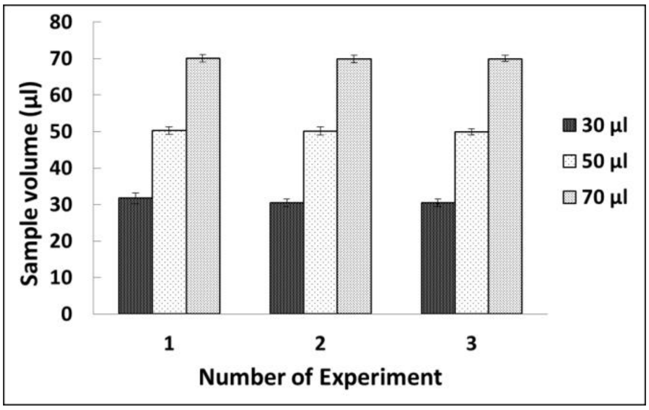

Figure 3: The reciprocal volume measurement of prototype A to reciprocate 30 µl, 50 µl, and 70 µl out of 100 µl DI water.

Figure 4 shows the mixing efficiency of the FL: we introduced 200 µl DI water and 10 µl dyed water into the well of a MTP. One well was operated with a FL to reciprocate 180 µl out of 210 µl DI water, which only required one round of reciprocal operation for fully mixing (~ 30 s) as shown in Figure 4 (a). The other well was left without active mixing, and took an hour for diffusive mixing, as shown in Figure 4 (b).

Figure 5 shows a long-term experimental result: we have reciprocated 70 µl out of 200 µl DI water for one week by a 96-FCs FL operating on all wells of a 96-well MTP simultaneously.

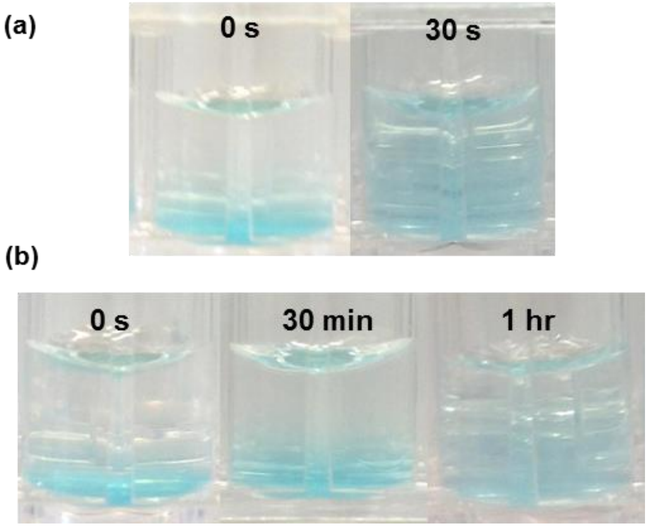

Figure 4: The mixing efficiency testing of a 96-well MTP (a) operated with a FL for reciprocal mixing, and (b) without active mixing (mixing by diffusion only).

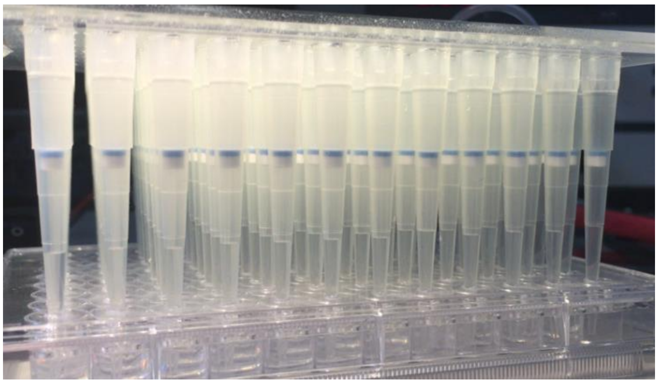

Figure 5: Photo of a FL with 96 pipette tips extending into a standard 96-well MTP for reciprocal mixing. The assembly was operate for one week, without any noticeable change or degradation of the performance of the reciprocal pumping.

SUMMARY AND OUTLOOK

We successfully developed a novel microbioreactor based on a functional lid (FL) microfluidic platform. This FL microfluidic platform is able to achieve mixing by reciprocation in all wells of standard 96 well micro titer plate homogenously. The variation of the reciprocated volume between the individual wells is less than 3 µl. The FL could reciprocate different volumes of DI water on demand from 30 µl to 200 µl by adjusting the working period of the micro pump used for pneumatic actuation, and it can work continuously for at least one week. Other than the traditional way to shake the whole MTP, this FL microfluidic platform offers a different mixing method which is probably more stable and efficient so that the system could integrate with sensors that are attached to the bottom of the MTP easier. Therefore, such microbioreactors hold great potential to distinguish the quality of cell lines in an early stage, which could shorten the research and development period of pharmaceutical production.

In future research, we will develop an autonomous processing device, which is placed on the top of the FL, including a battery driven embedded system as an integrated control unit (e.g. microcontroller, FPGA, embedded Linux, etc.) and should thus be able to provide the driving pressure to the FL according to the previously defined control sequence to reciprocate the cell medium without any external devices and tubing connections. Other functions, which can be implemented by means of sensors mounted below the MTP might include the temperature control, the pH value, the DO value and the CO_2 concentration. The demonstrate long term objective is to demonstrate a completely autonomous microbioreactor with the size of a standard MTP that is self-contained and takes care of mixing and monitoring of the cell cultures fully autonomously. The electronic part is planned to be reusable, and the FL which comes into contact with the sample is considered to be a disposable, single use item. The system could receive processing commands via a touch display on the top or by wireless communication. The measurement and status data can be transferred wirelessly to the laboratory information management system. By using conventional MTPs as test carriers and cell culture vessels, the compatibility with conventional laboratory devices and processes is maintained. The whole system will be designed to be able to use battery supply and to be put into a standard cell incubator for long term cell culture.

ACKNOWLEDGEMENTS

We gratefully acknowledge financial support from the Studienstiftung des deutschen Volks.

REFERENCES

[1] T. Lai, Y. Yang,, & S.K. Ng "Advances in mammalian cell line development technologies for recombinant protein production", *6*(5), pp. 579-603, 2013.

[2] F. Li, N. Vijayasankaran, A. Shen, R. Kiss, A. Amanullah, "Cell culture processes for monoclonal antibody production", mAbs, vol. 2, pp. 466-479, 2013.

[3] G. John, D. Goelling, I. Klimant, H. Schneider, E. Heinzle, "PH-Sensing 96-well microtitre plates for the characterization of acid production by dairy starter cultures", Journal of Dairy Research, vol. 70, pp. 327-333, 2003.

[4] G. T. John, I. Klimant, C. Wittmann, E. Heinzle, "Integrated optical sensing of dissolved oxygen in microtiter plates: A novel tool for microbial cultivation", Biotechnol. Bioeng., vol. 81, pp. 829–836, 2003.

[5] J. I. Betts and F. Baganz, "Miniature bioreactors: current practices and future opportunities", Microbial Cell Factories, vol. 5, 2006

[6] P. Fernandes and J.M.S. Cabral, "Microlitre/millilitre shaken bioreactors in fermentative and biotransformation processes – a review", Biocatalysis And Biotransformation, vol. 24, 2006.

[7] C.H. Tsai, XY. Wu, S. Zimmermann, R. Zengerle, and P. Koltay "Digital hydraulic drive for microfluidic large-scale integration system based on shape memory alloy actuators", Transducers '17, 2017

CONTACT

* Cheng-Han Tsai, Cheng-Han.Tsai@imtek.de

FABRICATION OF LARGE-VOLUME RECTANGULAR CHANNELS USING TRENCH-SIDEWALL TECHNOLOGY AND A SOI SUBSTRATE

H.-W. Veltkamp[1,*]*, Y. Zhao*[1]*, M.J. de Boer*[1]*, J. Groenesteijn*[1]*, R.J. Wiegerink*[1] *and J.C. Lötters*[1,2]
[1] Micro Sensors and Systems, MESA+ Institute for Nanotechnology, University of Twente, Enschede,
The Netherlands
[2] Bronkhorst High-Tech BV, Ruurlo, The Netherlands

ABSTRACT

In this paper we propose an extension of surface channel technology (SCT) which is based on trench side wall technologies from the micro-electronics industry and silicon-on-insulator (SOI) wafers. In this CMOS compatible trench-assisted surface channel technology (TASCT) process, refilled trenches define the outline of the microfluidic channels and chambers in the lateral plane and serve as etch stops during channel etching. This ensures well-defined channel shapes and the possibility to incorporate in-channel pillar structures in order to fabricate large-volume rectangular microfluidic channels, which can be integrated with smaller cross-sectional channels. When a highly-doped device layer is chosen, the possibility arises to add side wall heater structures next to the microfluidic channels as well.

KEYWORDS

Trench-assisted surface channel technology, trench side wall technology, large-volume microfluidics, trench refilling

INTRODUCTION

Conventional SCT[1–3] was initially designed to create a micro mass-flow controller based on the Coriolis effect[4]. The fabricated channels are semi-circular since the channel etch is only limited by the etch mask on top, and the channel side wall only consists of low-stress silicon-rich silicon nitride (SiRN). With the proposed TASCT process, the channels will be rectangular because of refilled trenches, which serve as an etch stop during the isotropic channel etch. This will give a higher accuracy on the control of the final channel shape when compared to conventional SCT. Schematics of both a SCT channel and a TASCT channel are shown in figure 1a and figure 1b, respectively.

(a) *(b)*

Figure 1: Schematics of a SCT channel (a) and a TASCT channel (b). Please note that the figure is not on scale. Colours are indicating ■ Silicon, 🟩 First layer of low-stress SiRN, 🟪 Second layer of low-stress SiRN, 🟦 Burried oxide layer.

These trenches allow in-channel pillar fabrication, which opens the way to fabricate large-volume rectangular surface channels in the lateral dimension of a single silicon-on-insulator (SOI) substrate. This makes TASCT a very controlled technique to make interconnected surface channels of different shapes. When this approach is combined with the suspended channel technology from the SCT and a highly-doped SOI substrate, it is also possible to fabricate free-hanging, mechanical stable and thermally isolated channels with side wall heating elements, which can serve as large rectangular combustion reaction chambers usable for microscale combustion experiments, as is introduced in the paper submitted to this same conference by Y. Zhao *et al.*, entitled *Design principles and fabrication method for a miniaturized fuel gas combustion reactor*. The described TASCT process will be used in the near-future to realize an improved design on the recently developed Wobbe Index meter[5]. This paper describes the proposed steps of the TASCT process.

TASCT FABRICATION PROCESS

The TASCT process that is proposed to be used as way to fabricate rectangular large-volume microfluidic channels and chambers can be divided into five main parts. The first step is the creation of etch stops, and therewith the channel outline, by etching of high-aspect ratio trenches in a SOI substrate with a notching-free Bosch process, followed by subsequent refilling of those etched trenches with low-stress (SiRN). Then, the microfluidic channels and reaction chambers will be etched by first etching slit patterns into the SiRN layer in between the trenches. Through these slits, the underlying Si will be etched away, where the SiRN inside the trenches serve as an etch stop. The next step is the formation of the inner wall of the channels and chambers, which also includes the closure of the slits. This will be done via another deposition run of low-stress SiRN. Then, electrical contact pads will be made onto the Si and a metal will be deposited. This metal will serve as electrical circuits, connecting the Si side wall heaters to the outside world, as heater structures, and as temperature sensors. Then, as final step, the surrounding Si will be etched away with a two-step etch process.

The proposed TASCT process combines notching-free high aspect ratio trench-etching in a highly-doped SOI substrate with strategies from the micro-electronics industry, i.e. trench side wall technology[6], with trench refilling technology[7] and SCT[1].

Each part of the TASCT process will be discussed separately. Each subsection will be accompanied by cross-sectional schematics (not on scale) of a channel structure with a pillar inside. The full colour legend is shown in figure 2.

⬛ Silicon
🟦 Thermal silicon oxide
🟦 Burried oxide layer
🟧 Parylene-C
🟩 1st layer low-stress silicon-rich silicon nitride
🟨 Metallic layers (Cr or Ta and Pt)
🟪 2nd layer low-stress silicon-rich silicon nitride

Figure 2: Legend of the used colours in the cross-sectional images in this paper.

Etch stop and channel outline

The fabrication of the etch stops and the channel outline is the first step in the realisation of TASCT channels, and is visualized in figure 3. A highly-doped SOI substrate with a device layer of 50 µm, a BOX layer of 200 nm, and a handle layer of 450 µm will be oxidized via wet thermal oxidation at 1150 °C in a Tempress Systems furnace. This SiO_2 layer will serve as a hard mask during the trench etching. For that, it will be patterned with 3 µm wide trenches via conventional I-line photo-lithography and SiO_2 reactive ion etching (RIE) in a PlasmaTherm-790 plasma etcher. The high aspect ratio trenches of 3 µm wide will be etched completely down to the BOX layer with a notching-free Bosch process with a low frequency (LF) end-step using an Oxford Instruments PlasmaPro 100 Estrelas deep reactive ion etching (DRIE) plasma system.

Then, a layer of 2 µm parylene-C will be deposited conformally via chemical vapour deposition (CVD) in a PDS 2010 system of Specialty Coating Systems. This layer will serve as BOX layer protection during subsequent hard mask stripping[10]. The surface parylene-C will be etched back using an O_2 plasma in a barrel etcher[8]. Here, we will take advantage of the fact that etching on the surface has a higher rate than etching inside the trenches, i.e. the etch rate is limited by the aspect ratio of the trench. Subsequently, the SiO_2 hard mask will be stripped in buffered HF (7:1 NH_4F:HF) and the remaining parylene-C will be stripped away in a piranha solution (3:1 H_2SO_4:H_2O_2) at 90 °C.

The trenches will be refilled with low-stress (50 MPa) SiRN via low pressure chemical vapour deposition (LPCVD) in a Tempress Systems furnace with a $SiH_2Cl_2/NH_3/N_2$ flow[7]. These refilled trenches will act as etch stops during the channel etch later on.

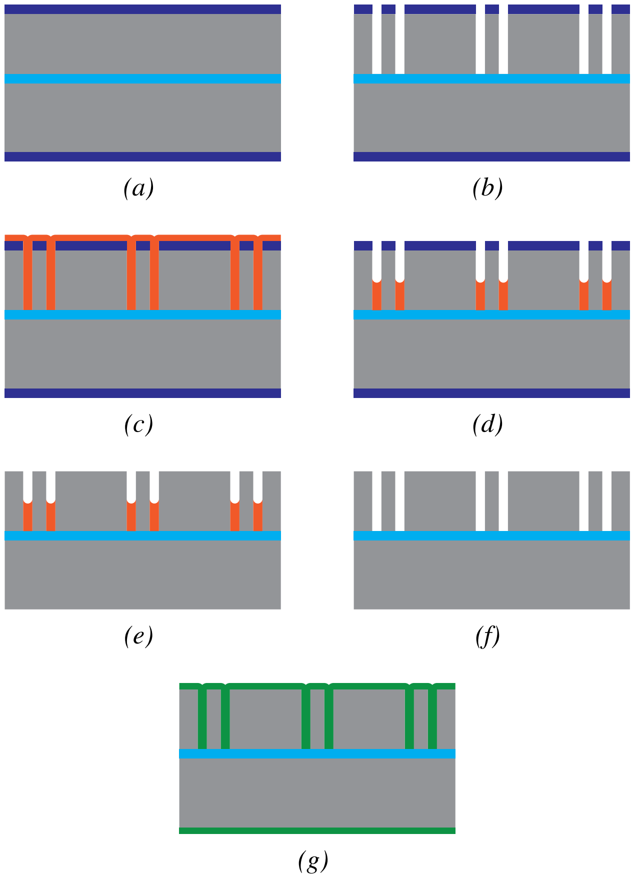

Figure 3: Schematics of the etch stop and channel outline formation in the TASCT process, with the steps (a) thermal oxidation of a SOI wafer, (b) RIE of SiO_2 and notching-free DRIE of Si, (c) CVD of parylene-C, (d) etching of parylene-C in an O_2 plasma, (e) stripping of the SiO_2 hard mask in buffered HF, (f) stripping of the remaining parylene-C in piranha, (g) trench refill with LPCVD of low-stress SiRN.

Channel and chamber etch

Schematics of the microfluidic channel and chamber etch are shown in figure 4. First, a layer of Cr will be sputtered with an home-build sputter machine on top of the low-stress SiRN layer. A slit pattern will be patterned in between two adjacent trenches, which are forming the channel side walls, via I-line photo-lithography and etched with RIE in an Alcatel Adixen AMS100 RIE etcher. These patterned Cr and SiRN layers will be used as etch mask during the isotropic channel etch, like in the conventional SCT process[1,2]. The Cr will act as an etch mask during SiRN and Si etch, preventing the increase of the slit width in the SiRN.

The Si inside the microfluidic channels and chamber structures will be etched away through the slits with a SF_6 plasma in the Oxford Instruments PlasmaPro 100 Estrelas.

After the channel and chamber etch, the Cr layer will be stripped away in wet Cr etchant.

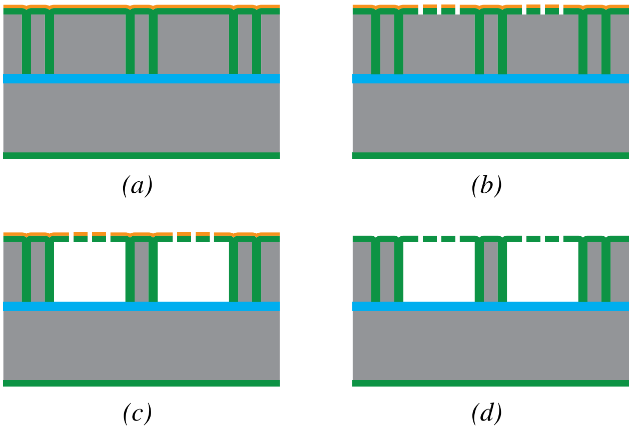
(a)
(b)
(c)
(d)

Figure 4: Schematics of the channel and chamber etch, with the steps (a) Sputtering of a Cr layer, (b) RIE of Cr and SiRN in order to create the slit mask, (c) Isotropic channel and chamber etch with SF_6, (d) Stripping of the Cr layer.

Channel wall formation and closure

After etching away the Si, the inner channel and chamber walls will be formed via another LPCVD run of low-stress SiRN, which will be conformally grown to a thickness slightly more than half the slit width (total layer thickness: ±1.5 times the slit width). This way, a full closure of all the slits will be ensured, thus completely closing the channel. A schematic of the channel closure is shown in figure 5. The use of LPCVD to close the channels is the same as in the conventional SCT process[1–3].

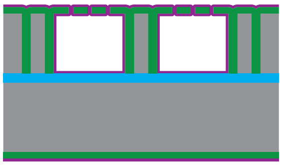

Figure 5: Channel and chamber wall formation via LPCVD of low-stress SiRN, which also ensures full closure of the slits.

Electrical connects and metal deposition

In order to create electrical contacts to the Si side wall heater structures, the two SiRN layers will be patterned via I-line photo-lithography and RIE in the Alcatel Adixen AMS100 plasma etcher. Then, the metallic layers (Pt and an adhesion layer), which serve as both the interfacing between the Si side wall heaters and the macro world, and resistive heaters and temperature sensors will be sputtered.

The adhesion between Pt and the substrate can only withstand elevated temperatures of above 500 °C when a proper adhesion layer is used. From previous work, for example the work by Tiggelaar *et al.*, it is learned that Ti will not survive elevated temperatures and causes delamination, hole formation and agglomeration of the Pt[9]. Therefore, an adhesion layer of Ta will be used, which is known to withstand higher temperatures[9]. First, a thin 5 nm Ta layer will be sputtered in a home-build sputter device, directly followed by a 400 nm Pt layer. The metallic layers will be patterned via ion beam etching in an Oxford Instruments Ionfab 300plus.

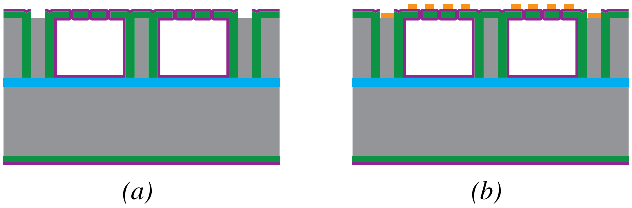
(a)
(b)

Figure 6: Electrical interfacing, with (a) Opening up electrical pads on the Si side wall heater structures, (b) Sputtering of metallic electrical connects, resistive heater and temperature sensing structures.

Channel release

As final step, the channels and chambers will be released in order to create a suspended system, which is thermally isolated from the bulk Si. This release will be done in two steps. First, a directional etch will be performed with the Bosch process, after which an isotropic etch with SF_6 plasma will be used to remove the remaining Si in all directions, creating cavities of sufficient size. Both steps will be performed in the Oxford Instruments PlasmaPro 100 Estrelas. The hole etched with the Bosch process will reduce the etch time of the isotropic etch, and therefore limits the exposure time of SiRN to SF_6. The final channel is schematically shown in figure 7.

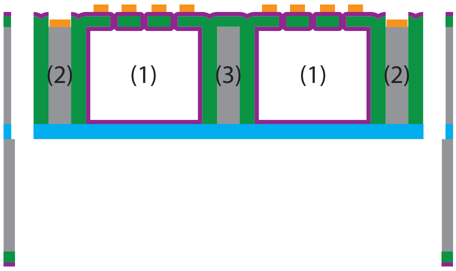

Figure 7: Channel release etch via a combined directional process (Bosch) and isotropic process (SF_6 plasma). In the image, (1) is indicating the channel, (2) is indicating the Si side wall heating structures, and (3) indicates an in-channel pillar.

CONCLUSION

The proposed new trench-assisted surface channel technology fabrication technique combines different well-established micromachining techniques from different industries, like microelectronics and microfluidics, to form a new and elegant approach to surface channel formation. The combination of trench and trench-related technologies with the previously described surface channel technology[1–3] makes that TASCT has potentially more design freedom than SCT and it has the potential to create well-defined large volume channels with a better accuracy than with the SCT technology.

ACKNOWLEDGEMENTS

This work is part of the research programme Integrated Wobbe Index Meter with project number 13952 which is (partly) financed by the Netherlands Organisation for Scientific Research (NWO).

REFERENCES

[1] M. Dijkstra, M.J. de Boer, J.W. Berenschot, T.S.J. Lammerink, R.J. Wiegerink, M. Elwenspoek, *"A versatile surface channel concept for microfluidic applications"*, J. Micromech. Microeng., 17(10), pp. 1971–1977, 2007.

[2] J. Groenesteijn, M.J. de Boer, J.C. Lötters, R.J. Wiegerink, *"A versatile technology platform for microfluidic handling systems, part I: fabrication and functionalization"*, Microfluid. Nanofluid., 21(7), pp. 127(1–12), 2017.

[3] J. Groenesteijn, M.J. de Boer, J.C. Lötters, R.J. Wiegerink, *"A versatile technology platform for microfluidic handling systems, part II: channel design and technology"*, Microfluid. Nanofluid., 21(7), pp. 126(1–14), 2017.

[4] J. Haneveld, T.S.J. Lammerink, M.J. de Boer, R.G.P. Sanders, A. Mehendale, J.C. Lötters, M. Dijkstra, R.J. Wiegerink, *"Modeling, design, fabrication and characterization of a micro Coriolis mass flow sensor"*, J. Micromech. Microeng., 20(12), pp. 125001(1–10), 2010.

[5] J.C. Lötters, T.S.J. Lammerink, M.G. Pap, R.G.P. Sanders, M.J. de Boer, A.J. Mouris, R.J. Wiegerink, *"Integrated micro Wobbe Index meter towards on-chip energy content measurement"*, IEEE 26th International Conference on Micro Electro Mechanical Systems (MEMS), 2013, pp. 965–968.

[6] R.D. Rung, H. Momose, Y. Nagakubo, *"Deep trench isolated CMOS devices"*, 28th International Electron Devices Meeting, 1982, pp. 237–240.

[7] B.R. de Jong, H.V. Jansen, M.J. de Boer, G.J.M. Krijnen, *"Tailored etch-profiles of high aspect ratio trenches to prevent voids after refill with LPCVD SiRN"*, 16th MicroMechanics Europe (MNE) Workshop, 2005, pp. 4–6.

[8] E. Meng, P. Li, and Y. Tai, *"Plasma removal of Parylene-C"*, J. Micromech. Microeng., 18(4), pp. 045004(1–13), 2008.

[9] R.M. Tiggelaar, R.G.P. Sanders, A.W. Groenland, J.G.E. Gardeniers, *"Stability of thin platinum films implemented in high-temperature microdevices"*, Sensors and Actuators A: Physical, 152(1), pp. 39–47, 2009.

[10] H.-W. Veltkamp, Y. Zhao, M.J. de Boer, R.J. Wiegerink, J.C. Ltters, *"Selective SiO_2 etching in three dimensional structures using parylene-C as mask"*, 43th Micro- and Nano-Engineering (MNE) Conference, 2017, p. 380.

CONTACT

* H.-W. Veltkamp, MSc: h.veltkamp@utwente.nl

SYSTEMATIC CLASSIFICATION OF MICROMIXERS

T. Kretzschmar[1]*, M. Baßler* [1] *and K. S. Drese*[2]
[1] Fraunhofer ICT-IMM, Mainz, Germany
[2] University of Applied Sciences Coburg, Coburg, Germany

ABSTRACT

This work is a systematic classification of passive micromixers according to their performance. The basis is the introduction of an efficiency measure which relates both mixing quality and pressure drop. This measure is then applied to data from several experimental characterizations.

It is found that micromixers can be classified into two groups: inertial micromixers with a strong increase in performance above a critical flow rate and mixers based on lamination with a continuous change of the efficiency with growing Reynolds number. This classification is achieved by analysis of the mixing performance rather than describing the mixing principle.

KEYWORDS

Micromixer, mixing efficiency, IEM micromixing model, mixing time

INTRODUCTION

General introduction

Mixing processes are a vital part in microfluidic systems, since many of them include chemical reactions for analysis. The small length scales in microfluidics enhances the surface to volume ratio and thus changes the dominating forces. This leads to a change in flow behavior, most notably that flows in microchannels are typically laminar [1]. Mixing on the macroscale is typically achieved by making the flow turbulent, except for highly viscous media such as polymer blends. This is usually not an option for micromixers as the pressure drops would be prohibitively high. At the same time, the channels are still too large for mixing by diffusion alone, as typical diffusion times lie in the range of minutes [2]. This has led to the development of new mixing structures based on the formation of lamellae and/or vortices or secondary flows. These structures can achieve mixing times in the range of milliseconds to microseconds.

The new potentials and applications have led to the development of a wide range of micromixers with different mixing principles. This makes it difficult to select the appropriate mixer for an application, emphasizing the need for an overview over micromixer performance and a suitable classification.

State of the Art

There are several reviews concerning micromixers available [3-5]. Micromixers are typically categorized as either active or passive. While passive micromixers achieve mixing by manipulating the fluid flow with their internal structure, active micromixers include an additional actuation mechanism that improves the mixing process. This paper focuses on four types of passive micromixers which are less difficult to fabricate as well as easier to implement.

Passive micromixers are commonly classified according to their mixing principle:

- Multilamination/interdigital mixers divide the two fluids to be mixed in series of small parallel channels, thus reducing the scale over which diffusion has to act. The channel is focused to further reduce the size of the fluid lamellae
- Split and recombine micromixers (SAR) try to mimic the Baker transformation by splitting and later rejoining the fluid, thus halving the lamellae size/doubling the amount of lamellae with each mixing element
- T micromixers consist of two inlet channels being joined in an orthogonal mixing channel. At higher flow rates, the impact of the two fluids from the inlet channels results in the formation of vortices, improving the mixing process
- Dean micromixers are essentially curved channels. The curvature leads to centrifugal forces and thus to the formation of a secondary flow. This can lead to a thinning of the fluid lamellae and thus shorter mixing times.

While this classification allows categorizing micromixers, it does not reflect their mixing performance and behavior. Since different measures are used to characterize the mixing behavior, it is difficult to compare the mixer types.

A rough guideline for the application of micromixers is given by Nguyen [3], who divides the mixers further according to the Reynolds numbers (flow rates) in which they are typically applied. Falk and Commenge [2] have analyzed data from several experimental characterizations using the Villermaux-Dushman reaction. They showed a general trend of the mixing behavior, but suggested a universal behavior rather than subdiviation in performance classes.

MOTIVATION

The goal of this work is a systematic classification of passive micromixers according to their characteristic behavior. The basis is the introduction of an efficiency measure which incorporates both mixing quality and pressure drop. This measure is then applied to data from several experimental characterizations, covering the performance of T, Dean, split and recombine as well as multilamination micromixers.

EFFICIENCY MEASURE

The efficiency measure is derived from the efficiency introduced by Ottino and Ranz [6]. It was developed as part of the lamellar mixing model. Mixing processes involve the formation of thin lamellae due to stirring, which reduces the length scale over which diffusion has to equalize the concentrations. Ottino and Ranz assume that on a small local scale, the mixing process can be described by a one-dimensional system given by a stack of striations which are thinned due to shear orthogonal to the lamellae and whose concentration changes due to diffusion. Only shear stresses perpendicular to the stack reduce the size of the lamellae and thus improve mixing. Thus, Ottino and Ranz defined the efficiency as the ratio of the shear rate participating in mixing and the total shear rate, given by the energy dissipation:

$$\eta = \frac{\dot{\gamma}}{\sqrt{2\,\varepsilon/\nu}} \qquad (1)$$

where η is the efficiency, $\dot{\gamma}$ the shear rate contributing to mixing, ε the energy dissipation and ν the kinematic viscosity. The energy dissipation and thus the total shear rate can be estimated from the pressure drop of the micromixer [2]:

$$\varepsilon = \frac{Q\,\Delta P}{\rho V} \qquad (2)$$

where Q is the volume flow rate, ΔP the pressure drop, ρ the density of the fluid and V the total volume of the mixer. The energy dissipation can also be expressed as the Batchelor time scale:

$$t_b = \sqrt{\nu/\varepsilon} \qquad (3)$$

While the total shear rate can simply be determined, $\dot{\gamma}$ cannot be measured directly. However, several idealized models show that there is a connection between mixing times and the effective shear rate.

For laminar flow, Baldyga and Bourne defined a micromixing time for diffusion and shear [2]:

$$t_m = \frac{1}{2\dot{\gamma}} \operatorname{arcsinh}\left(\frac{0.76\dot{\gamma}\delta_0^2}{D}\right) \qquad (4)$$

with the diffusion coefficient D and the initial striation thickness δ_0. Due to the weak influence of the arcus sinus hyperbolicus, the mixing time is almost antiproportional to the shear rate. A similar dependency was found by Baldyga and Bourne for turbulent flow [7]. Thus, the mixing efficiency can generally be described as:

$$\eta = C\,\frac{t_b}{t_m} \qquad (5)$$

where the constant C depends on the corresponding model. Similar dependencies were also found by Raynal [8] and Regenfuss [9]. In this work, only the ratio t_b/t_m will be used as an efficiency measure:

$$\eta' = \frac{t_b}{t_m} \qquad (6)$$

The experimental methods to determine mixing times are presented in the next section.

CHARACTERIZATION METHODS

Optical characterization

In optical characterizations, a microscope setup is used to determine the concentration profile of a fluorescent or colored liquid to determine the mixing performance [10]. A simple approach is to use a transparent liquid and a dye and determine the light absorption over the channel cross section. Since the light absorption corresponds with the concentration of the dye, the concentration profile can be determined and used to calculate a measure such as the concentration variance over the cross section.

A disadvantage of this method is that the concentration is averaged over the depth of the channel. This means that the concentration might appear homogeneous, while actually several unmixed layers exist. A solution is to use chemical reactions that yield colored dyes. Thus, the light absorption only changes when the fluids are actually mixed.

A mixing time or mixing length can be defined as the time or point where the variance or a similar measure falls below a certain value.

Competitive reactions

The optical methods have the obvious drawback that they are not applicable to mixers made from intransparent materials. This can be overcome with a characterization using competitive reactions.

The general idea is that two reactions are competing for one educt used in stoichiometric defect [11]. One of the reactions is almost instantaneous, whereas the second reaction is ideally as fast as the mixing process or slower. For perfect mixing, the educt would be used up by the first reaction only. The second reaction can only take place if there are local overconcentrations of the educt, which is a sign of an insufficient mixing process. Thus the yield of the second reaction is a measure of the mixing performance. Typically, two types of reaction systems are used: the competitive-consecutive and the competitive-parallel reaction system:

Table 1: Competitive Reaction Systems

Competitive-consecutive reaction system	Competitive-parallel reaction system
$A + B \rightarrow R$ $R + B \rightarrow S$	$A + B \rightarrow R$ $C + B \rightarrow S$

Using the yield as the mixing measure has the drawback that the yield is dependent on the used concentration set. A concentration-independent measure is desirable. This can be achieved by using a micromixing model which allows correlating the yield to a characteristic, concentration-independent micromixing time.

ANALYSIS

In this work, the interaction by exchange with the mean micromixing model [2] is used to convert yields into concentration independent mixing times. The model describes the mixing process as two separate volumes that exchange species with a characteristic time t_m . This mass transfer is included in the differential equations for the reaction kinetics. With known reaction kinetics and by assuming different mixing times, these equations can be solved to calculate reaction yields. The resulting diagram can then be used to correlate experimental yields with mixing times. A flow chart of the procedure is shown in figure 1.

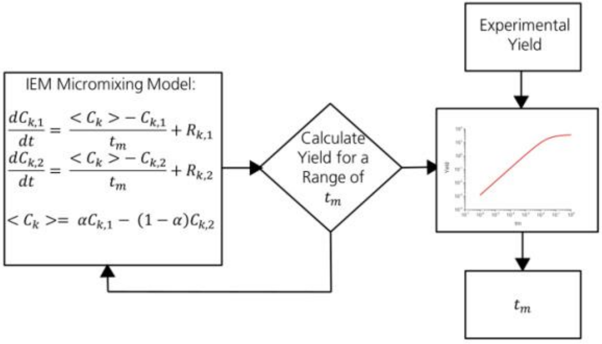

Figure 1: Determination of mixing times using the IEM micromixing model

As mentioned in the motivation, data from several papers were analyzed with the goal of comparing T, Dean, split and recombine and interdigital mixers [12-16]. The mixing performance of optical characterizations is given in terms of mixing lengths, times or as the number of elements required for complete mixing. These measures were all converted to mixing times. The results from competitive reaction systems are given as yields of the secondary reaction. These were then converted to micromixing times using the IEM model.

The efficiency was calculated by determining the energy dissipation from the pressure drop data, converting it into the Batchelor time scale, and then setting it into relation to the mixing time. In addition, two graphs were calculated to compare the experimental data with a mixing process with constant shear and mixing by diffusion only. The energy dissipation for pipe flow is given by the Hagen-Poiseuille equation [2]:

$$\varepsilon = \frac{32\, \nu\, u_m^2}{d^2} \tag{7}$$

where u_m is the mean velocity and d is the diameter of the pipe. The diffusion time can be estimated by:

$$t_D = \frac{d^2}{D} \tag{8}$$

resulting in an efficiency of:

$$\eta' = \frac{t_b}{t_D} = \frac{1}{4\sqrt{2}} \frac{D}{u_m d} = \frac{1}{4\sqrt{2}} \frac{1}{Pe} \tag{9}$$

showing a reciprocal dependency on the Peclet number Pe. By applying (4) from Baldyga and Bourne [2], assuming that the total shear rate participates in mixing and that the initial striation thickness is $d/2$, the efficiency for constant shear is:

$$\eta' = \frac{t_b}{t_D} = \frac{2\sqrt{2}}{\operatorname{arcsinh}(1.52\, Pe)} \tag{10}$$

showing only a weak dependency on the Peclet number.

RESULTS

In figure 2 and 3, the efficiencies of the mixers are shown. It can be seen that multilamination and split and recombine mixers show more gradual change in efficiency with an almost constant value in some cases, similar to the ideal case of constant shear.

T and Dean micromixers show a strong increase in efficiency above a certain Peclet number. Below that critical value the mixers show a similar slope as the efficiency by diffusion only. An interesting exception is the caterpillar mixer which, while being based on the split and recombine principle, shows a behavior similar to a T micromixer. However, the behavior at low Reynolds numbers is unknown.

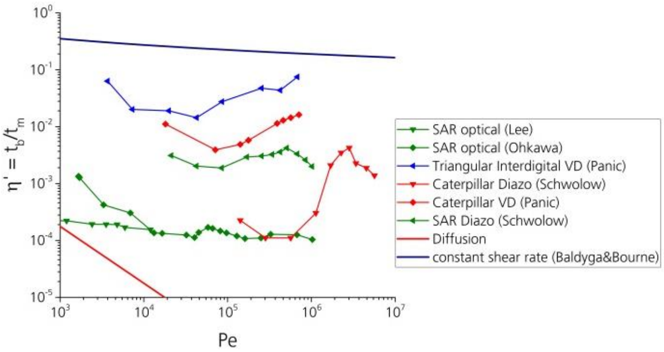

Figure 2: Efficiency of interdigital and split and recombine micromixers

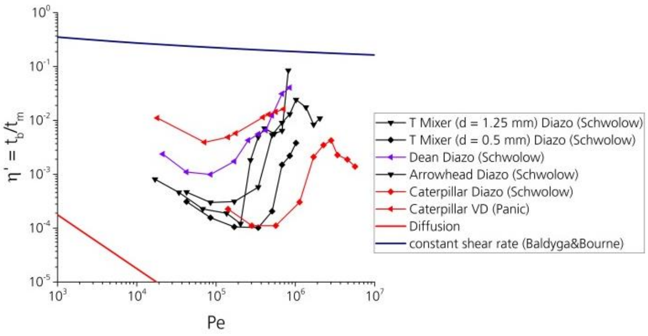

Figure 3: Efficiency of T, Dean and the caterpillar mixer

DISCUSSION

Perhaps the most surprising result is the behavior of the caterpillar micromixer which shows a dependence upon a critical Peclet number while being based on the split and recombine principle. This change is probably due to the formation of vortices inside the mixing structure at higher flow rates. The behavior at lower Peclet numbers is unknown, however other split and recombine mixers don’t show a sudden increase in efficiency at higher flow rates. This emphasizes the need to classify mixers according to their mixing performance rather than their mixing principle.

The mixers can be classified into two groups: inertial and laminating micromixers. Inertial micromixers require the formation of vortices inside the mixing structure and thus require flow rates/Peclet numbers above a critical value. Below that value the efficiency show the same slope as mixing by diffusion only. Laminating mixers such as the split and recombine and multilamination mixers already mix at lower flow rates and show a more gradual change in performance, similar to mixing with constant shear.

It is still difficult to find the most efficient mixer for a specific flow rate, as there is a large spread between the data. Sources for these deviations probably stem both from the characterizations themselves as well as from the later analysis. For the analysis the reaction kinetics have to be well-known. However, there is an ongoing discussion concerning the reaction kinetics of the popular Villermaux-Dushman reaction used in some of the characterizations analyzed in this paper [11]. Furthermore, the IEM mixing model describes the mixing process by a phenomenological approach which does not necessarily give a good representation of the mixing process. The micromixing time from the model can also differ from optical data, depending on the threshold value used to determine mixing times in the optical measurements. These deviations can also explain the offset between inertial micromixers at low flow rates and the efficiency of mixing by diffusion. For the constant shear rate case and the laminating mixers, the difference also stems from assuming an ideal process for the constant shear case.

SUMMARY

An efficiency measure was developed for the analysis of data from experimental characterizations of micromixers from the literature. It was shown that the efficiency is antiproportional to the mixing time and proportional to the Batchelor time scale, which depends on the pressure drop. The efficiencies of the analyzed micromixers show that the mixers can be classified into inertial micromixers, which show a strong increase in performance above a critical flow rate, and laminating mixers with a more gradual change in performance. The advantage of this classification is shown by the caterpillar mixer, which shows the behavior of an inertial mixer while being based on the split and recombine principle also found for laminating micromixers.

REFERENCES

[1] S. Wiggins, J.M. Ottino, “Foundations of chaotic mixing”, Phil. trans. Series A, Math., phys.& Eng. Sci. 362 (1818), pp. 937–970, 2004

[2] L. Falk, J.-M. Commenge, (2010): “Performance comparison of micromixers”, Chem. Eng. Sci. 65 (1), pp. 405–411, 2010

[3] N.-T. Nguyen, Z. Wu,“Micromixers—a review”, J. Micromech. Microeng. 15 (2), pp. R1-R16, 2005

[4] V. Hessel, H. Löwe, F. Schönfeld, “Micromixers—a review on passive and active mixing principles”,Chemical Engineering Science 60 (8-9), pp. 2479–2501, 2005

[5] C.-Y. Lee, C.-L. Chang, Y.-N. Wang, L.-M. Fu, “Microfluidic Mixing: A Review” IJMS 12 (12), pp. 3263–3287, 2011

[6] J.M. Ottino, J.M, W.E. Ranz, C. W. Macosko, “A lamellar model for analysis of liquid-liquid mixing”, Chem. Eng. Sci. 34 (6), pp. 877–890, 1979

[7] J. Bałdyga, R. Pohorecki, “Turbulent micromixing in chemical reactors - a review”, Chem. Eng. J. & Biochem. Eng. J. 58 (2), pp. 183–195, 1995

[8] F. Raynal, J.-N. Gence, “Energy saving in chaotic laminar mixing”, International Journal of Heat and Mass Transfer 40 (14), pp. 3267–3273, 1997

[9] P. Regenfuss, R. M Clegg, M. J. Fulwyler, F. J. Barrantes, T. M. Jovin,”Mixing liquids in microseconds”,Rev.Sci. Instrum. 56 (2), pp. 283, 1985

[10] J. Aubin, M. Ferrando, V. Jiricny,”Current methods for characterizing mixing and flow in microchannels”, Chem. Eng. Sci. 65 (6), pp. 2065–2093., 2010

[11] M. Jasińska, “Test Reactions to Study Efficiency of Mixing” Chem. &Proc. Eng. 36 (2), 2015

[12] S. Panić, S. Loebbecke, T, Tuercke, J. Antes, D. Bošković, “Experimental approaches to a better understanding of mixing performance of microfluidic devices”, Chem. Eng. J. 101 (1-3), pp. 409–419, 2004

[13] S. W. Lee, D. S. Kim, S. S. Lee, T. H. Kwon, “A split and recombination micromixer fabricated in a PDMS three-dimensional structure”, J. Micromech. Microeng. 16 (5), pp. 1067–1072, 2006

[14] K. Ohkawa, T. Nakamoto, Y. Izuka,Y. Hirata, Y. Inoue,”Flow and mixing characteristics of σ-type plate static mixer with splitting and inverse recombination”, Chem. Eng. R&D 86 (12), pp. 1447–1453, 2008

[15] S. Schwolow, J. Hollmann, B. Schenkel, T. Röder,”Application-Oriented Analysis of Mixing Performance in Microreactors” Org. Process Res. Dev. 16 (9), pp. 1513–1522, 2012

CONTACT

*Thomas Kretzschmar,
Thomas.Kretzschmar@imm.fraunhofer.de

TOWARDS A BETTER UNDERSTANDING OF THE RISKS OF MULTI INFUSION

Peter Lucas[1], Menne Schakel[1], Elsa Batista[2], Anders Niemann[3], and Roland Snijder[4]

[1] VSL – Dutch Metrology Institute, Delft, The Netherlands
[2] IPQ – Instituto Portugues da qualidade, Caparica, Portugal
[3] DTI – Danish Technology Institute, Aarhus, Denmark
[4] UMCU - University Medical Center Utrecht, Utrecht, The Netherlands

There is a significant risk associated with infusion technology in the critical care setting. Due to limited vascular access, clinicians typically connect multiple infusion pumps to one infusion set and catheter. This practice is called multi-infusion.

Within the completed Metrology for Drug Delivery (MeDD) project [1], we have gathered ample evidence that multi-infusion is associated with dosing errors due to ambiguous physical effects. Despite the fact that many of these dosing errors are due to technical properties, they can be mitigated or even prevented if multi-infusion users are given proper and comprehensive training.

A follow up project on MeDD has therefore started to disseminate the results developed in this project. The objectives aim at implementing the know-how and expertise in the calibration practices used in European hospitals as well as further educating those active in (multi)infusion technology in the risk associated. Hereto an E-learning module is being developed and the results are disseminated to two technical committees working on a revision of two relevant ISO/IEC standards.

The E-learning will contain ten clinical and two metrology cases. The topics range from basic drug concentration and flow rates relationships, to a profound understanding of the implication of the common (dead) volume. The two metrological cases discuss how traceability is important for the health care industry.

The clinical cases represent actual clinical situations. Because clinicians typically assess a clinical situation by observing vital signs it is desirable to present the effects of drug administration by infusion in terms of vital signs wherever possible. By doing so, we are able to create awareness that certain effects may have a technical/physical origin besides a clinical origin. For example, even though norepinephrine has an almost instantaneous effect, the pharmacokinetic/ pharmacodynamic modeling relations still predict an onset time of several minutes. Nevertheless, if after 15 minutes the expected effects are still not observed, this delay may be caused by the technical/physical aspects of the infusion setup.

The important physical effects that can be distinguished are the 1) push out effect, 2) pressure compliance and start-up delays, 3) syringe or infusion bag exchange, free and backflow and 4) impact of gravity in gravity driven infusion.

There are different methods to calibrate infusion devices: the Infusion Device Analyzer method, the gravimetric method and the water front tracking method. The first one is probably the most common method used by hospital technicians whereas the second by technicians at the National Metrology Institutes. The latter method is more applicable for very low flow rates as for example encountered for implanted infusion devices.

The Infusion Device Analyzer method is in fact a flow rate, or volume, measuring device and can be used to calibrate and/ or verify the error of an infusion device, for example a syringe pump. An Infusion Device Analyzer (IDA) is therefore nothing more than a 'comparing machine': it compares a flow rate, or volume, with its own reference. Consequently an analyzer needs to be calibrated by a primary method, for example the gravimetric method.

The final calibration uncertainty of the syringe pump follows from the following components: the IDA calibration uncertainty, water temperature, expansion coefficient of the disposable syringe, standard deviation of the measurements and the resolution.

Figure 1: Infusion pump analyzer (on the left) and a syringe pump (on the right) during a calibration

The working principle for the gravimetric method consists of a precision scale, a stopwatch and a flow generator. A measurement beaker, placed on the scale, is collecting the dispensed water. The water can be dispensed into the beaker in different ways, which will be described later. In any way, it is important to limit evaporation or to correct for the evaporated water during calibration. Moreover, it is very important to avoid unsteady conditions and dripping of water into the beaker as it will affect the measurement uncertainty.

The scale reads the amount of water dispensed in a certain amount of time, measured by the stopwatch. The average mass flowrate is then calculated as the quotient $\Delta m/\Delta t$. The volume flow can be calculated by dividing the results with the density of water at the measured water temperature. The working principle is indicated in figure 3. However, in order to arrive at a low measurement uncertainty various corrections need to be performed

.

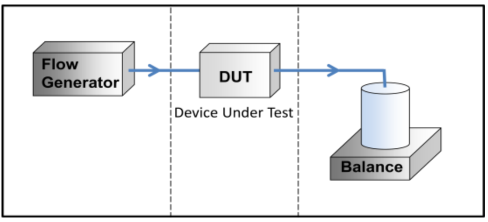

Figure 2: general working principle for the gravimetric method

References

1. Lucas P. MeDD - Metrology for drug delivery, EU-funded research project 2012 - 2015 Available at: www.drugmetrology.com

3D FRACTALS AS SERS SUBSTRATES FOR DETECTION OF NEUTOROTOXIC AGENTS IN GAS PHASE

M. Lafuente[1]*, E. J. W. Berenschot*[2]*, R. M. Tiggelaar*[2]*, R. Mallada*[1,3]*, M.P. Pina*[1,3]*, J. Santamaría*[1,3]*, N. R. Tas*[2]

[1] Nanoscience Institute of Aragon, University of Zaragoza, Department of Chemical & Enviromental Engineering, Edif I+D+I, Campus Rio Ebro, C/Mariano Esquillor, s/n, 50018, Zaragoza, Spain.

[2]Mesoscale Chemical Systems, MESA+ Institute for Nanotechnology, University of Twente, P.O. Box 217, 7500 AE Enschede, The Netherlands

[3] Networking Research Center on Bioengineering, Biomaterials and Nanomedicine, CIBER-BBN, 28029 Madrid, Spain.

Tackling terrorist access to CBRN material is currently considered a key priority under both the European Union Counter-Terrorism Strategy and the Organization for the Prohibition of Chemical Weapons (OPCW). The nerve agent Sarin (Propan-2-yl methyl phosphono fluoridate) is widely recognized as one of the most toxic chemical warfare agents (CWA), Figure 1. In addition to its neurotoxicity, the simplicity and relatively low cost of its manufacturing raises public concern about potential uses by terrorist groups or rogue nations. Sarin acute exposure guideline level (AEGL-3) is 0.064 ppm [1] for an exposure of 10 min, *i.e.* the persons exposed above this concentration for this period could experience life-threatening health effects or death.

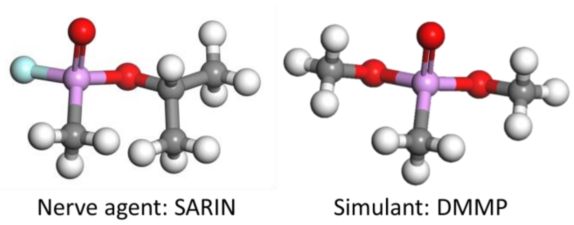

Figure 1. Structure and name of nerve agent sarin and its simulant: DMMP.

Presently, there are a number of competing technologies for the detection and identification of chemical agents. All detection and sensing systems deviate from the ideal in their limited capacity to optimize factors such as size, cost, sensitivity, speed, specificity, accuracy, reversibility and reusability. On the contrary, Surface Enhanced Raman Scattering (SERS) outstands as one of the most interesting and rapidly developing analytical tool for label-free ultrasensitive vibrational fingerprinting of a variety of molecular compounds [2]. SERS detection combines the vibrational Raman scattering from molecules with plasmonics from metal nanostructures. In a recent revision paper on explosives and chemical threat detection [3], SERS has been identified as key technique because it combines several attractive features such as ultrasensitivity, high speed, comparatively low cost, multiplexing detection capability (narrow bands of vibrational Raman scattering) and portability.

SERS is characterized by its surface selectivity as strongly enhanced Raman scattering only occurs in very close vicinity (ca. <10nm) to the metal substrate. It is also well known that chemical warfare agents (CWAs) are poor Raman scatterers with cross-sections in the range of 10^{-29} cm^2 sr^{-1} $molecule^{-1}$ thus precluding any possibility of analyte detection at low concentration levels without special enhancement processes. The degree of control and reproducibility of commercial as well as research based SERS substrates are still questionable and significant improvements in terms of performance, process standardization and sample to sample reproducibility need to be done. In this context, the development of robust and cost-effective SERS substrates that contain the so-called electromagnetic "hot-spots" is therefore a key requirement towards the widespread use of SERS as reliable tool. The magnitude of the SERS enhancement depends on the chemical nature of the analyte and on the metal surface (size, shape and structure). Precise control of both, the shape and

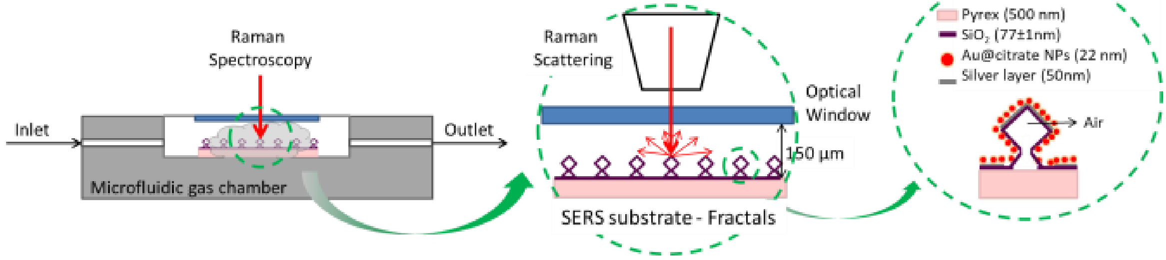

Figure 2. Experimental set-up for continuous SERS measurements using 3D fractals as SERS substrates

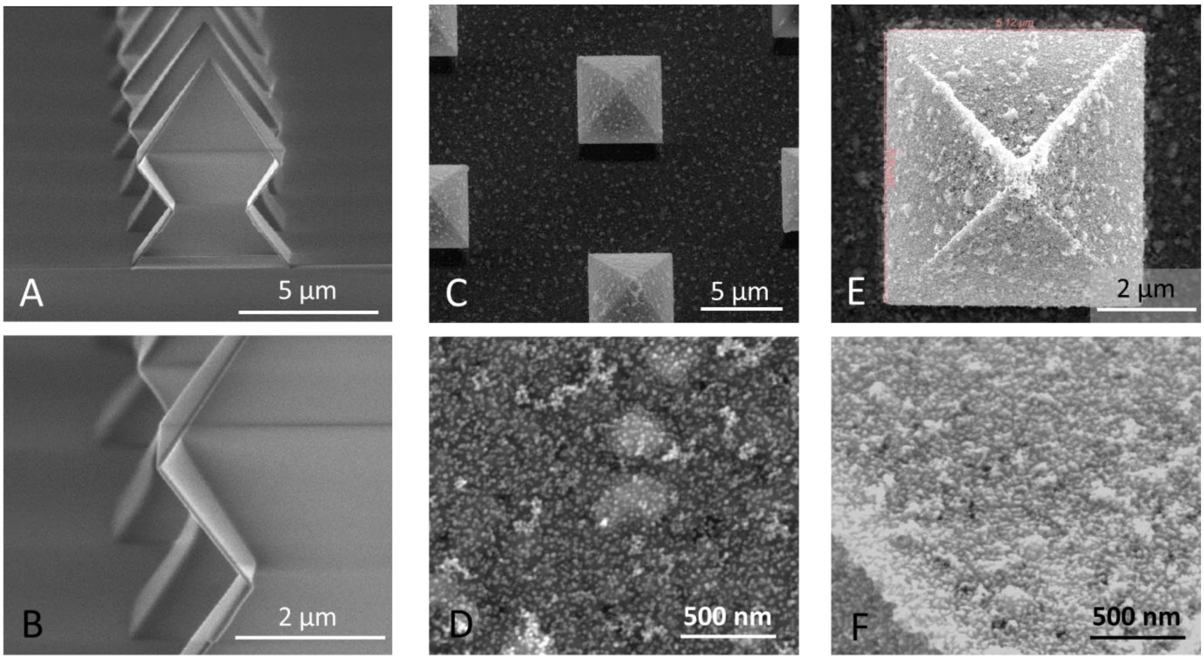

Figure 3. SEM image of naked 1G fractals: cross section (A) general view, (B) magnification. Top view of Ag 1G fractals coated Au NPs: (C) general view, (D) magnification of the ground level (z=0), (E) and (F) magnification of the top surface.

geometrical symmetry/periodicity of metallic structures by tow-down approaches has becoming an active focus of research [4-5]. In this way, the fabrication of ordered structures, i.e. pillars, array substrates, is more uniform and reproducible and easy for scaling-up. In addition, these SERS substrates reveal ideal for theoretical modelling.

Accordingly, this work explores the use of 3D fractals with metallic coatings as SERS active substrates for label free detection [6] of Sarin gas simulant, ethyl methylphosphonate (DMMP), Figure 1. In particular, SERS detection of DMMP in gas phase at low ppm level on silver 3D fractals coated with gold nanoparticles has been fully investigated (Figure 2). The method of engineering of a 3D fractal structure is based on a combination of anisotropic etching of silicon and corner lithography developed by E. J. W. Berenschot et al [7-8]. To facilitate the handling of 3D fractal surfaces, anodic bonding with MEMPAX glass wafer (500 µm thick) was performed before its release by back-etching of Si.

The first generation (1G) fractals (5 µm width and 20 µm pitch) were firstly coated with 50 nm of silver using electron beam evaporation (Edwards auto-500, $3{\cdot}10^{-7}$ mbar, 75 mA, 5.3 KV). The roughness of the silver coating is 2.61 ± 0.2 nm. In a second step, spherical citrate capped Au nanoparticles (22 ± 5 nm), Au@citrate NP, synthesized via a modified version of the Turkevich-Frens method were assembled on the Ag coated 3D fractals by electrostatic interactions. For such purposes, the silver substrates were incubated in a poly(diallyldimethilammonium) chloride aqueous solution (PDDA), 0.2% wt for 4 hours; followed by rinsing with deionized water. Afterwards, the substrates were immersed in Au@citrate nanoparticles solution (0.19 mg/mL) for 16 hours at 4ºC. SEM images of the Ag 1G fractals coated with Au@citrate NPs are shown in Figure 3. This procedure yielded homogeneous monolayer of Au@citrate NPs with a surface density on Ag fractals of 650 NPs/µm^2.

SERS experiments were performed with an Alpha 300 Raman spectrometer of WITec using 785nm excitation laser coupled through x20 objective (spot diameter 1.9 µm) or x50 objective (spot diameter 1.2 µm) respectively. Acquisition conditions were 50s and power at the sample 5 mW, unless otherwise indicated. For measuring DMMP in gas phase, the SERS substrate was mounted on the gas chamber and placed at an angle of 90º with respect to the laser excitation beam. The experimental set-up is illustrated in Figure 2. A nitrogen stream (10 STP cm^{3}min^{-1}) containing DMMP, 1.2 ppmV, was fed to the exposure cell, and SERS measurements were immediately performed without any stabilization period.

Recently, plasmonic systems consisting of metal nanoparticles separated from metal films by nanometer scale gaps have attracted great attention as SERS substrates, because the precise gap regions between metal nanoparticles and the films can also provide reproducible hot spots with large SERS enhancements. Theoretical and experimental studies have shown that the plasmonic properties of such systems are strongly dependent, among others, on the dielectric properties of both substrates. Accordingly, SERS measurements were firstly performed on flat Pyrex glass surfaces with and without Ag coating (see Table 1). On both samples, the deposition of Au@citrate nanoparticles was mediated by PDDA, leading to coverage density values above 600 AuNP/µm^2.

Table 1. Substrates prepared for this work.

Sample	Substrate material	Ag layer	Density AuNP@citrate (AuNP/µm^2)
Pyrex	Pyrex	-	623 ± 08
Pyrex_Ag	Pyrex	50 nm	633 ± 30
Ag 1G fractal	Pyrex	50 nm	619 ± 04
Ag 3G fractal	Pyrex	50 nm	561 ± 16

Figure 3 shows the DMMP Raman spectra measured on Pyrex and Pyrex_Ag substrates under identical conditions upon exposure to DMMP vapors in gas phase. On the silver coated sample, i.e. Pyrex_Ag, a peak located at 706 cm^{-1} corresponding to the P-C vibrational mode from DMMP is clearly observed. On the contrary, only broad bands in the region 1100 to 1700 cm^{-1}, attributed to amorphous carbon, are observed on the Pyrex sample. The carbon formation agrees with the photodecomposition of the citrate molecules covering the Au NPs. A possible explanation could rely on the dielectric environment of the plasmonic material. Our hypothesis is that in the case of Pyrex sample, the temperature of the substrate increases up to levels for the organics photodecomposition due to the poor thermal conductivity of the Pyrex substrate (1 W/K·m) compared to Pyrex_Ag counterparts (Ag 410 W/K·m). This effect is especially noticeable in experiments where the analyte concentration is ultralow.

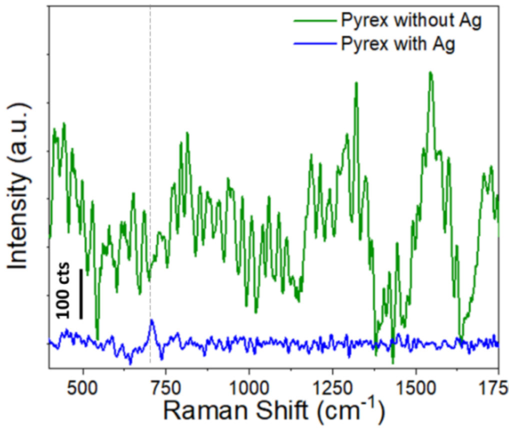

Figure 3. Raman spectra of DMMP vapors (1.2 ppmV) on Pyrex and Pyrex_Ag samples coated with Au@citrate NPs. Green line indicates the position of the characteristic P-C vibrational mode of DMMP molecules. Conditions: x50, 5mW and 1s.

Thus, Pyrex_Ag samples are preferred for SERS sensing applications due to clear spectral profiles, although less intense, are obtained. Accordingly, the 3D fractal structures studied in this work were coated with 50 nm of silver.

Figure 4 comparatively shows the recorded SERS spectra on Ag 1G fractals coated with AuNP upon exposure to DMMP vapors in gas phase (1.2 ppmV) with the focus plane at two z positions: 0 µm (bottom part of the fractal) and 5 µm (top part of the fractal). Once again, the most intense signal appearing at 706 cm^{-1}, tentatively assigned to the P-C stretching mode and used as Raman reference line is observed on Ag 1G fractals. However, when focused at z=0 the signal to noise ratio hinders its proper identification. In addition, the characteristic peak at 780 cm^{-1}, attributed to PO$_2$ bending of DMMP, is clearly observed on the top of the fractal. Both peaks are shifted with respect to normal Raman of DMMP in liquid phase. This observation agrees with the formation of weak interactions between citrate from the gold nanoparticles and DMMP molecules [9]. Our previous studies confirm the citrate coating as effective trap of the DMMP molecules on the immediate vicinity of the Au nanoparticle surface where the electromagnetic enhancement is maximum.

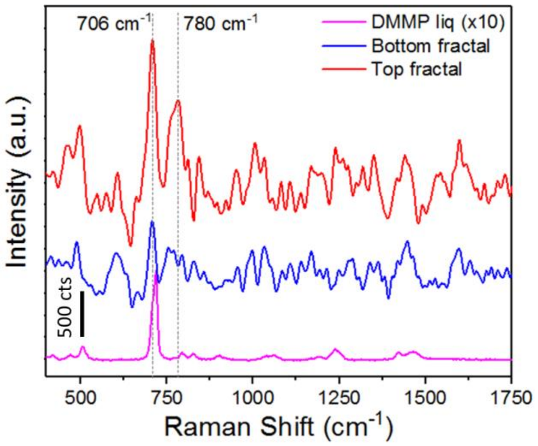

Figure 4. SERS spectra recorded on top and bottom of the Ag 1G fractal coated with AuNP upon exposure to 1.2 ppmV of DMMP in gas phase (Raman spectra of DMMP in liquid phase is include for comparison). Conditions: 5mW and 50s.

Based on these preliminary SERS results in gas phase, we fabricated third generation (3G) fractals and coated with 50 nm of silver and Au@citrate NPs (see Figure 5 (A) and (B)) to provide intense SERS hot spots for DMMP identification at sub-ppmV level. Initially we recorded the Raman spectra upon exposure to DMMP vapors in gas phase (1.2 ppmV) with the focus plane at different z positions of the 3G fractal: 5, 8, 10 and 12 µm from the bottom part. At each z position, a mapping area of 20x20 µm (1spectrum/µm) comprising 1 single 3G fractal structure was analyzed. The experimental conditions were 1mW, 1s. Figure 5 (C) shows the Raman map at z=8 µm, for which the highest signal was recorded. Bright areas, which correspond to the higher SERS intensity values at 706 cm^{-1}, are clearly located at the external surface are of the 3D fractal. Figure 5 (D) shows the recorded SERS spectrum on Ag 3G fractal with the focus plane at z=8 µm. The characteristic peak at 706 cm^{-1} of DMMP is clearly observed, and the registered SERS intensities are higher than those for Ag 1G fractals. The presence of the amorphous carbon background in the region 1000 to 1400 cm^{-1}, due to the photocombustion of the sample, indicates that further optimization of the acquisition conditions is still required.

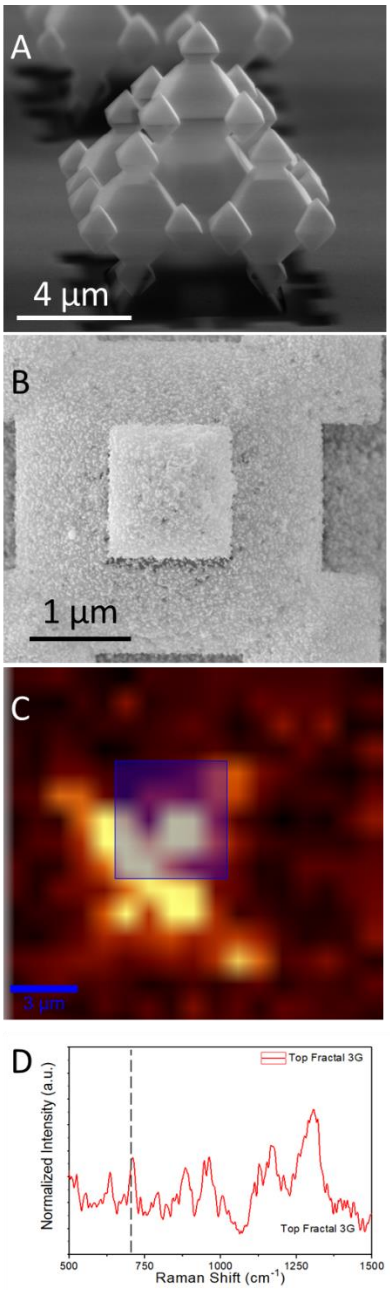

Figure 5. Ag 3G fractals coated with AuNPs: SEM images of (A) cross section, (B) top view; Raman map at 706 cm^{-1} across a 20x20 µm and 8 µm height from the botton surface (C); SERS spectrum upon exposure to DMMP vapors (D). Conditions: 5mW and 5s.

The fact that a measurable SERS signal is obtained even at lower number of gas phase molecules, indicates that a higher surface concentration has been achieved, and proves the effectiveness of the SERS substrates developed. Further efforts are focused on the analysis of the inverted·3D fractals as plasmon cavities with field enhancements controlled by the coupling to incoming laser and intracavity plasmon absorption.

REFERENCES

[1] Agent GB (Sarin) Results - AEGL Program https://www.epa.gov/aegl/agent-gb-sarin-results-aegl-program, accessed June 2017.

[2] K. A. Willets, R. P. Van Duyne, "Localized Surface Plasmon Resonance Spectroscopy and Sensing," Annual Review of Physical Chemistry, 58 (1), pp. 267-297, (2007).

[3] A. Hakonen, P.O. Andersson, M.S. Schmidt, T. Rindzevicius, M. Käll, "Explosive and Chemical Threat Detection by Surface-Enhanced Raman Scattering: A Review," Analytica Chimica Acta, 893, pp. 1-13, 2015.

[4] X. Liu, S. Lebedkin, H. Besser, W. Pfleging, S. Prinz, M. Wissmann, P.M. Schwab, I. Nazarenko, M. Guttmann, M.M. Kappes, "Tailored Surface-Enhanced Raman Nanopillar Arrays Fabricated by Laser-Assisted Replication for Biomolecular Detection Using Organic Semiconductor Lasers", ACSNano, 9 (1), pp. 260-270, 2014.

[5] M. Hu, F.S. Ou, W. Wu, I. Naumov, X. Li, A.M. Bratkovsky, R.S. Williams, Z. Li, "Gold Nanofingers for Molecule Trapping and Detection". Journal of the American Chemical Society, 132 (37), pp. 12820-12822, 2010.

[6] N. Taranenko, J-P. Alarie, D.L. Stokes, T. Vo-Dinh, "Surface-Enhanced Raman Detection of Nerve Agent Simulant (DMMP and DIMP) Vapor on Electrochemically Prepared Silver Oxide Substrates". *Journal of Raman Spectroscopy, 27* (5), pp. 379-384, 1996.

[7] E.J.W. Berenschot, H.V. Jansen., N.R. Tas, "Fabrication of 3D fractal structures using nanoscale anisotropic etching of single crystalline silicon" Journal of Micromechanics and Microengineering, 23, 1-10, 2013.

[8] E.J.W. Berenschot, R.M. Tiggelaar, J. Geerlings, J.G.E. Gardeniers, N.R. Tas, M. Malankowska, M.P. Pina, and R. Mallada. "3D-fractal engineering based on oxide-only corner lithography". in Symposium on Design, Test, Integration and Packaging of MEMS/MOEMS, DTIP 2016. 2016

[9] M. Lafuente, I. Pellejero, V. Sebastián, M.A. Urbiztondo, R. Mallada, M.P Pina, J. Santamaría. "Highly sensitive SERS Quantification of Organophosphorous Chemical Warfare Agents: A Major Step towards the Real Time Sensing in the Gas Phase". Submited.

LAB-ON-CHIP FOR DNA CONCENTRATION AND SEPARATION WITH A RESOLUTION LENGTH OF 6 BP

B. Chami[1]*, M. Socol*[1] *and A. Bancaud*[1]
[1] LAAS-CNRS, Toulouse, France

ABSTRACT

DNA separation and analysis has advanced over the last years benefiting from microfluidic systems that reduce sample volumes and analysis cost. We recently developed a microfluidic device that separates and analyzes nucleic acids using bidirectional actuation with a hydrodynamic flow and a counter electrophoretic force in viscoelastic polymer solutions. In this paper, we provide an analytical model of DNA transport by combining hydrodynamics and statistical mechanics capable of predicting the device performances as a function of the experimental control parameters; namely the pressure, the voltage and the fluid rheological properties. The model proves to be in quantitative agreement with the experiments. We finally define conditions for optimal DNA separation in terms of microchannel geometry, fluid viscoelastic properties and electro-hydrodynamic actuation that result in a resolution length (RSL) down to 6 bp.

KEYWORDS

DNA separation, viscoelasticity, resolution, resolution length (RSL).

INTRODUCTION

Transport in viscoelastic flow is gaining interest for particle and cell separation in continuous flow. Viscoelastic fluids have been exploited in the laminar regime or with inertial flows, depending on the throughput requirement of the experiment.

DNA molecules have also been conveyed in viscoelastic flows, showing similar behaviors to nano-objects. We recently showed that the application of a counter electric field offered a solution for high performance size separations as well as enrichment for channels with a funnel geometry [1]. So far, this technology has been applied to the separation of molecules in the size range 200-10000 bp, and we reasoned that its operation principle could be improved for low MW molecules.

Here we provide a quantitative model of DNA transport by combining hydrodynamics, finite-element methods, and statistical mechanics. We observe a very good agreement between our data and the model. One of the purposes of our study is to develop the µLAS device to be able to analyze low molecular weight DNA. This development follows three different roots; development of the channel design, working on the rheological properties of the viscoelastic fluid, and playing with the actuation parameters.

MATERIALS AND METHODS

The design of the microfluidic chips, which are processed by silicon/glass manufacturing[2], consists of a single straight channel with a funnel, as shown in Fig. 1. We define x as the longitudinal axis along the flow direction, y is along the channel width, and z the channel height. The width of the channel is then defined as $A_m x^m$ with m the power law of the constriction. The viscoelastic liquid flows in the chip by means of a pressure controller operating in the range 1-10 bar in either direction of the constriction. The electric field is generated using a DC voltage supply operating in the range 0-400 V. Image processing of fluorescence micrographs allows us to monitor the position of the DNA bands of a reference ladder (inset of Fig. 1). The position of the DNA bands is measured using the apex of the constriction as reference.

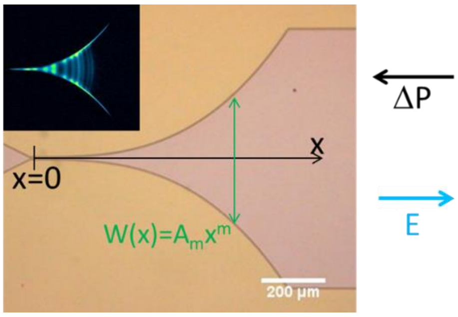

Figure 1: Bright field micrograph of a microchannel with a power-law profile (x^3-profile). The pressure and electric fields are actuated simultaneously in the same direction, but the negative charge of DNA induces an electrophoretic mobility in the opposite direction to the pressure flow. The inset represents a typical image of a DNA molecular weight ladder observed by fluorescence microscopy in the constriction. Each band is assigned to an accumulation position denoted x_{DNA}.

Various concentrations of the viscoelastic fluids used (PVP 1.3 MDa, PVP 40 KDa and PEG 10 KDa), are characterized using particle tracking microrheology[3] and are tested for the separation in different geometries and under several pressure and voltage conditions to determine the fluid resulting in the highest separation performance.

THE PHYSICAL MODEL

Our goal is to express the resolution of DNA separation experiments as a function of the electric and hydrodynamic actuation parameters and of the fluid viscoelastic properties. For this, we first derive an analytical expression of the transverse viscoelastic force for spherical tracers, and then validate its relevance with finite element simulations. Further, we use statistical physics to infer the distribution of tracers across the channel height, and come up with expressions that predicts the position, width and resolution of a DNA band. These predictions are compared to our experimental results.

Analytical calculation of the transverse viscoelastic force

Let us consider a particle of radius a conveyed by a Poiseuille viscoelastic flow of maximum speed V_{max} in a slit-like channel of height h (Fig. 2A). The shearing leads to an excess of elastic stress that results in transverse migration toward the channel centerline[4]–[6]. For a purely viscoelastic Maxwell fluid, the transverse force F_T reads:

$$F_T(\varepsilon) = -K \times 2\eta\tau \times \pi a^2 \times a \frac{\partial \dot{\gamma}(\varepsilon)^2}{\partial z} \qquad (1)$$

with $\dot{\gamma}$ the shear rate, η the viscosity, τ the fluid relaxation time, and ε the position of the particle. Note that according to the calculations of [5] the proportionality factor K is lower than one and greater than the Reynolds number, which is typically 10^{-4} in our experimental settings.

Considering the contribution of an electrophoretic velocity V_e oriented opposite to the hydrostatic flow and neglecting hydrodynamic interactions and finite-size effects, the velocity of the bead is $V_p(\varepsilon) - V_e$ with $V_p(\varepsilon)$ the hydrodynamic velocity at ε (Fig.2A). The transverse force becomes:

$$F_T^{el}(\varepsilon) = -32K \times \eta\tau\pi a \times \frac{V_p V_e}{h}\left\{1 - \frac{\varepsilon}{h/2}\right\} \qquad (2)$$

This equation applies for particles small compared to the channel height and neglecting pure hydrodynamic components.

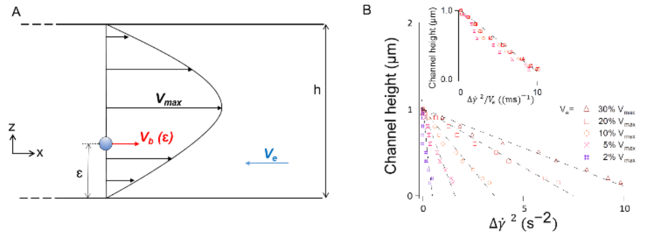

Figure 2: (A) Sketch of a bead at a vertical position ε in a slit-channel of height h. The Poiseuille flow is characterized by its maximum velocity V_{max} and the electrophoretic velocity is V_e. The velocity of the particle is V_b. (B) Using 3D finite element modeling, we measure the difference in square of the shear rate on the upper and lower apex of the particle. The channel height h is set to 2 µm, the particle radius a to 50 nm, the hydrodynamic maximum speed V_{max} to 75 µm/s and different electrophoretic speeds are modeled, as indicated in the inset. The set of data can be rescaled with the electrophoretic velocity (inset).

Validation with finite element simulations

Using 3D finite-element simulations performed with COMSOL, we checked the validity of Eq. (2) for a 100 nm particle flowing in a 2 µm-thick channel. We assumed the fluid to be Newtonian and set the maximum fluid velocity V_{max} to 75 µm/s. We used different electrophoretic velocities spanning 1.5 to 25 µm/s (Fig. 2B). In each condition, the particle was placed at different vertical positions, and we computed the difference between the square of the shear rate on the upper and lower apex of the particle. According to Eq. (2), we expect this data to scale linearly with the particle position and with the electrophoretic velocity. The prediction was quantitatively confirmed because the five simulation datasets could be rescaled with the electrophoretic velocity (inset of Fig. 2B).

Force close to the wall

Close to the walls, i.e. for distances $\varepsilon < 3a$, our analytical model is expected to be invalid as the gradient of flow velocity in between the wall and the particle is unknown. We noted that the COMSOL simulations indicated a reduction of the difference in square of the shear rate for distances in the range 50 to 150 nm (not shown). This result was qualitatively in agreement with the fact that the transverse viscoelastic force should drop to zero at the wall to insure zero-flux conditions. As a first order approximation, we assume that the force linearly drops to zero at the contact. The expression of the force near the wall then reads:

$$F_{T_{wall}}^{el}(\varepsilon) \sim -32K' \times \eta\tau\pi a \times \frac{V_{max} V_e}{h} \times \varepsilon \qquad (3)$$

with *K'* a dimensional constant equal to *K/l* with l the difference of slope in Eq. (2). This response is therefore analogous to an elastic spring retaining the sphere at the wall. We can then use Boltzmann statistics to extract the position and distribution of tracers at the wall as a function of the electrophoretic and hydrodynamic velocities.

Prediction for the position, width, and resolution of µLAS

Applying our analytical model, we can deduce the position of a DNA accumulation band, its width, and its separation resolution as shown by Eq. 4, Eq.5 and Eq.6, respectively.

$$x_{DNA}{}^{2m} = K' \times \frac{\eta\tau\pi^2 a h w_0^2}{k_B T A_m{}^2} \times \frac{V_{e,0}{}^3}{V_{max,0}} \qquad (4)$$

with w_0 the width of the channel at the apex, and $V_{max,0}$ and $V_{e,0}$ the maximum hydrodynamic and electrophoretic velocities at the apex.

$$B \sim \frac{3\,(\pi-2)^2}{8} K' \sqrt{\frac{\eta a h^3}{k_B T \tau}} \left(\frac{V_{e,0}}{V_{max,0}}\right)^{3/2} \qquad (5)$$

Finally, with the definition of the position of the bands and their breadth, it is possible to compute the resolution, as defined as:

$$\frac{Res_{1,2}}{\Delta a_{1,2}} \sim \frac{1}{2m*B_1} a_1^{\left(\frac{1}{2m}-1\right)} \times \left[\frac{K'\eta\tau\pi^2 h w_0^2}{k_B T A_m{}^2} \cdot \frac{V_{e,0}{}^3}{V_{max,0}}\right]^{\frac{1}{2m}} \qquad (6)$$

where $\Delta a_{1,2}$ the difference in size between two consecutive DNA bands. Note that we could also express the breadth B_1 using Eq. (5), but this additional calculation does not improve the fitting of our data. The right term in Equation (6) is the inverse of the resolution length (RSL) [7], which defines the minimal genomic distance between two consecutive peaks that can be separated with the technology.

RESULTS

Separation of 50-1000 bp DNA bands

By comparing the separation of a 50 bp DNA ladder in a linear versus a power-law geometry using the same viscoelastic solution PVP (40 KDa, 18% (wt%)) and under the same actuation parameters P-V (7 bar-300 V); at least a 25 bp RSL separation is possible with the power-law profile and not with the linear profile (Fig.4). The intensity profiles shown in Fig.4 (B) and (D) clearly show that the power-law profile allows the separation of DNA molecular weight lower than 200 bp.

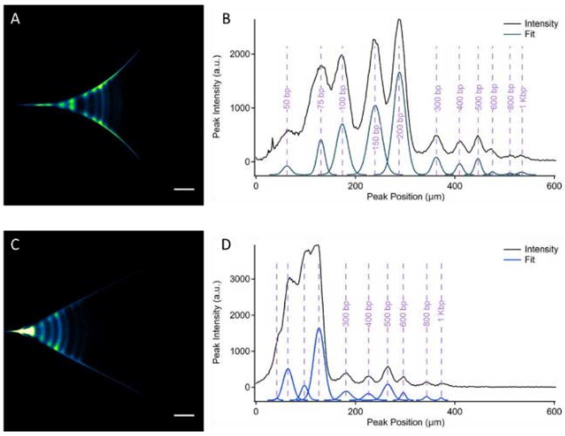

Figure 3: (A) and (C) The fluorescence images of a 50 bp DNA ladder separated in the power law profile and the linear profile, respectively (scale bar 100 µm). (B) and (D) The detected fluorescence intensity profiles of the DNA bands corresponding to (A) and (C), respectively.

Now that the power-law geometry has proved to be better than the linear one for separating low MW DNA, we use it to compare different polymer solutions. The rheological properties of all the tested solutions obtained using microrheology are displayed in Table 1.

Table 1: Viscosity (mPa.s) and Elasticity (Pa) of tested polymer solutions.

(MW)	(wt%)	Viscosity η (mPa.s)	Elasticity E (Pa)
PVP 40 KDa	10	6 ± 1.2	0.40 ± 0.07
	13	8 ± 1.3	0.50 ± 0.08
	15	9.5 ± 1.3	0.67 ± 0.13
	18	12 ± 1.25	0.85 ± 0.1
	20	14.5 ± 1.2	0.95 ± 0.3
PEG 10 KDa	20	12.7 ± 1.1	1.34 ± 0.3
PVP 1.3 MDa	2	6 ± 0.4	0.33 ± 0.08
	3	8 ± 1.3	0.45 ± 0.1
	4	19 ± 2	0.61 ± 0.1
	5	23 ± 1.25	0.50 ± 0.12

After testing all the viscoelastic fluids presented in Table 1 and choosing those that result in the best separations, the RSL obtained by each was calculated for all the DNA bands of the ladder and shown in Fig.4.

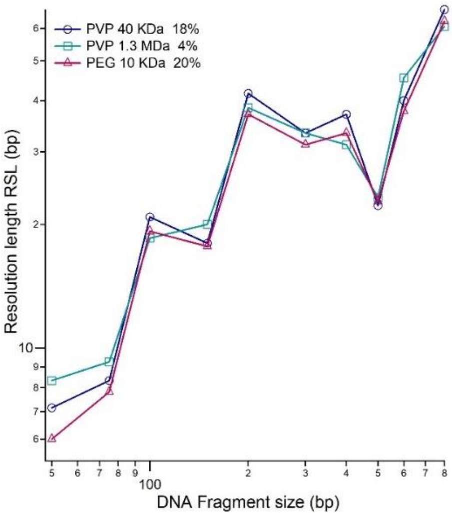

Figure 4: RSL for different polymer solutions at the optimal conditions of each.

From Fig.4 and the table, it can be concluded that the viscosity and the elasticity of the polymer solution play an important role in determining the separation performance of the device.

Validation of the physical model

The position and width of a DNA band

The data obtained from several experiments prove to fit the model perfectly as shown in Fig. 5 (A-D).

The slopes of the different fits change with the polymer solution showing a dependence on the rheological properties of the viscoelastic fluids as predicted by our model.

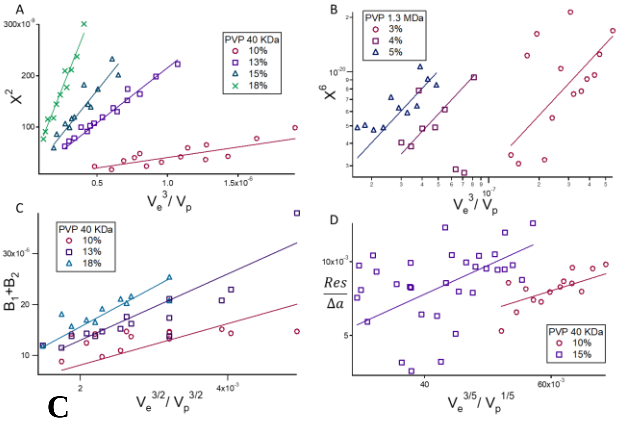

Figure 5: Model-Data fit. (A) The position of a 600 bp DNA band in a linaer geometry (m=1) for different concentrations of PVP 40 KDa. (B) The position of a 300 bp band in a power-law geometry (m=3) for different concentrations of PVP 1.3MDa. (C) The width of a 600 bp DNA band in a in a power-law geometry (m=2.5) in PVP 40 KDa at different concentrations. The inverse RSL of a 600 bp band in the power-law geometry (m=2.5) in PVP 40 KDa (10% and 15%).

CONCLUSION

The improvement of a new DNA separation and analysis technology, based on bidirectional electro-hydrodynamic actuation in viscoelastic fluids, was carried out through optimization of the microfluidic chip design and the viscoelastic fluid rheological properties. A physical model based on hydrodynamics and statistical mechanics and validated by finite element simulations enabled us to predict the device performance. A power-law chip design proved to be better than a linear design for the separation of DNA fragments smaller than 200 bp and a RSL of at least 25 bp was reached. Further improvement involving the viscoelastic fluid resulted in a RSL of 6 bp. Finally, the physical model fit the experimental data and provided insights for further developments.

REFERENCES

[1] H. Ranchon *et al.*, “DNA separation and enrichment using electro-hydrodynamic bidirectional flows in viscoelastic liquids,” *Lab Chip*, vol. 16, no. 7, pp. 1243–1253, 2016.

[2] B. M. Paegel, R. G. Blazej, and R. A. Mathies, “Microfluidic devices for DNA sequencing: sample preparation and electrophoretic analysis,” *Curr. Opin. Biotechnol.*, vol. 14, no. 1, pp. 42–50, Feb. 2003.

[3] T. G. Mason, K. Ganesan, J. H. van Zanten, D. Wirtz, and S. C. Kuo, “Particle Tracking Microrheology of Complex Fluids,” *Phys. Rev. Lett.*, vol. 79, no. 17, pp. 3282–3285, Oct. 1997.

[4] G. D’Avino, F. Greco, and P. L. Maffettone, “Particle Migration due to Viscoelasticity of the Suspending Liquid and Its Relevance in Microfluidic Devices,” *Annu. Rev. Fluid Mech.*, vol. 49, no. 1, pp. 341–360, Jan. 2017.

[5] B. P. Ho and L. G. Leal, “Migration of rigid spheres in a two-dimensional unidirectional shear flow of a second-order fluid,” *J. Fluid Mech.*, vol. 76, no. 04, p. 783, Aug. 1976.

[6] A. M. Leshansky, A. Bransky, N. Korin, and U. Dinnar, “Tunable Nonlinear Viscoelastic ‘Focusing’ in a Microfluidic Device,” *Phys. Rev. Lett.*, vol. 98, no. 23, Jun. 2007.

[7] Y. Yamaguchi, Z. Li, X. Zhu, C. Liu, D. Zhang, and X. Dou, “Polyethylene Oxide (PEO) and Polyethylene Glycol (PEG) Polymer Sieving Matrix for RNA Capillary Electrophoresis,” *PLOS ONE*, vol. 10, no. 5, p. e0123406, May 2015.

CRYSTALLIZATION OF ZINC(II) COMPLEX CONTAINING LYSOZYME BY SUPER WATER REPELLENT DOUBLY REENTRANT STRUCTURE UMBRELLA PILLAR ARRAY

D. Tanaka[1]*, W. Kawakubo*[1]*, D. H. Yoon*[1]*, T. Sekiguchi*[1]*, T, Akitsu*[2] *and S. Shoji*[1]
[1] Research Organization for Nano & Life Innovation, Waseda University
[2] Department of Chemistry, Faculty of Science, Tokyo University of Science

ABSTRACT

This paper reports the crystallization of a functional protein in the droplet on a super water repellent structure that consists of an umbrella-like pillar array. The structure provided certain participation of small volume reagents in the crystallization reaction. The crystallization conditions of functional protein were performed under room temperature and the atmosphere. Furthermore, the open structure allowed simple picking fragile crystals up. The umbrella-like pillar array structure was fabricated by soft MEMS process using SU-8 and polydimethylsiloxane (PDMS) simply. This research proposes a new crystallization technology for functional proteins, and the result of this research is useful for the analysis of functional proteins in the future.

KEYWORDS

Super repellent surface, Double reentrant structure, Surface tension, PDMS, Protein, Crystallization, Metal complex

INTRODUCTION

Functional proteins such as Zn(II) complex containing lysozyme are expected to be applied in a wide range of fields for tumor marker and electrode of fuel cell. For example, Nogala et al. reported the oxidation-reduction potential of laccase. They used a laccase and $Fe(CN)_6$ as a mediator to build a biologically safe biofuel cell [1]. Crystallization of functional proteins is an important technology for clarifying structure and characteristics. However, a stable crystallization technique of a functional protein has not been established yet. In recent years, microfluidic devices have been applied to the crystallization of functional proteins [2]. We have also conducted experiments for lysozyme crystallization in micro droplets using microfluidic device (Figure 1). The microfluidic devices were able to crystallize of lysozyme in micro droplets. However, crystals were easily broken when we practically picked them up or off from the closed devices. Therefore, we devised a simple crystallization method utilizing open air water repellent structure.

Already, many kinds of liquid repellent structures and materials are reported, and double reentrant structure showed the best performance with only structural feature [3]. We applied the double reentrant structure, umbrella pillar, to liquid repellent structure, as shown in Figure 2. The structure guarantees sphere shape of liquids, thus it is expected that a large proportion of liquids can participate in the reaction, even though the droplet has small volume and high wettability on the surface. Furthermore, the open structure allows simple experimental procedure for reagents' drop and collection of crystals.

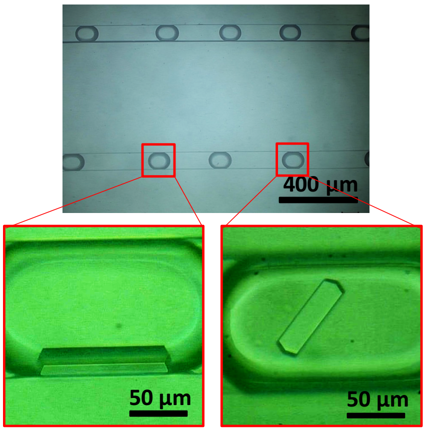

Figure 1: Crystallization of lysozyme by microfluidic device.

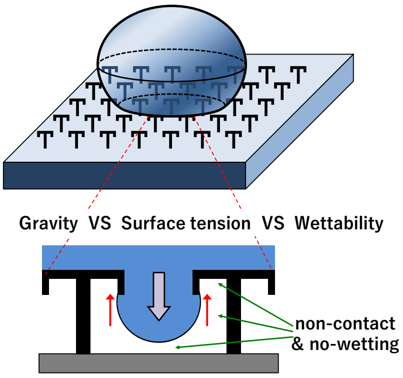

Figure 2: Water repellency principle of pillar array.

EXPERIMENTAL METHOD

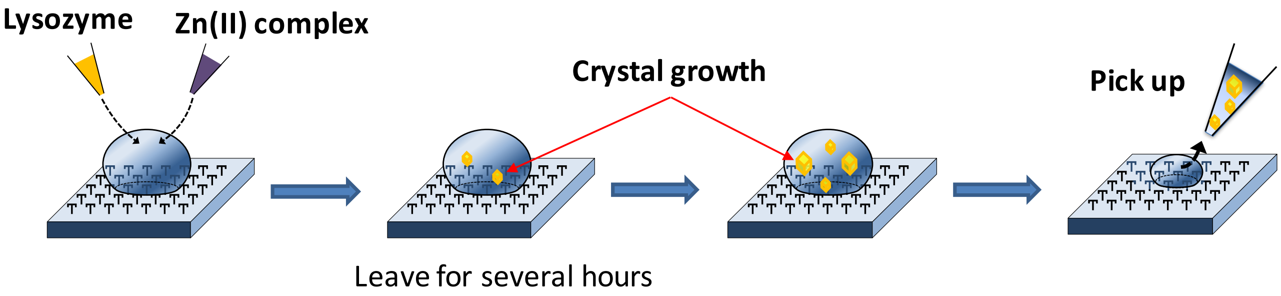

Figure 3: Outline of crystallization experiment

Figure 3 shows an outline of a crystallization experiment using an umbrella pillar array device. The functional protein crystallized and picks up with a pipette.

Fabrication Process

To fabricate the umbrella-like pillar array, Liu et al. used a silicon substrate and complicated etching and deposition process [4]. In this study we employed simple photoresist patterning and a transfer of the patterns using sacrificial layer and PDMS, as follows. (Figure 4).

① The sacrificial layer (LOR; Lift off resist) was coated on the Si substrate. ② SU-8 was exposed and coated separately in three stages and then developed. ③ The pillar array was bonded on PDMS film using uncured PDMS, and the PDMS for adhesion cured by heating ④ The sacrificial layer was dissolved and the Si substrate was removed.

Figure 5 is design dimensions of the pillar array and Figure 6 shows a scanning electron microscopy image (SEM; VE-7800, KEYENCE) after development.

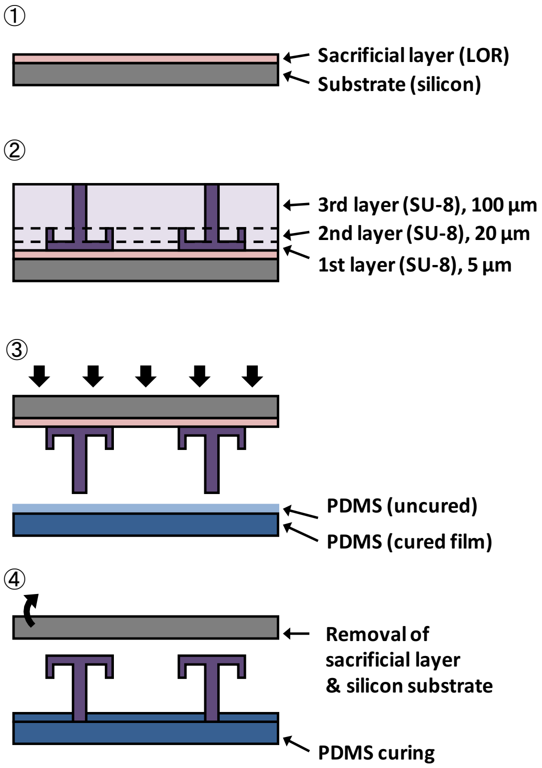

Figure 4: Procedure for fabricating doubly reentrant structure umbrella pillar array device.

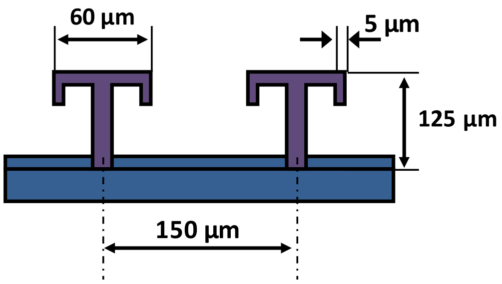

Figure 5: Design dimensions of pillar array device.

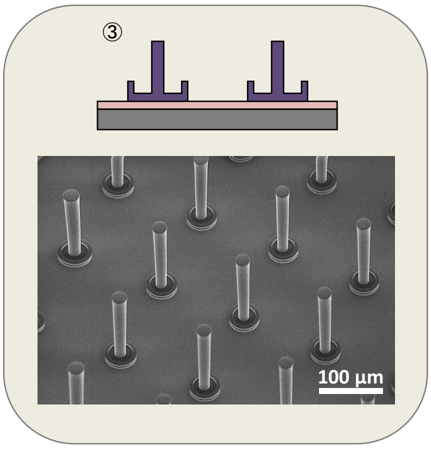

Figure 6: SEM image of pillar array.

Crystallization experiment

Figure 7 shows the synthesis and crystallization experiments of the Zn(II) complex and lysozyme. The crystallization experiment was carried out using Zn(II) complex (8 mmol/L) and lysozyme (10 mmol/L). Each reagent was dissolved with an aqueous citrate buffer solution. These aqueous solutions were dropped and mixed on an umbrella pillar array by pipettes, and crystallization experiment was conducted at room temperature (23°C) in the atmosphere. The crystallization time were 0 to 120 minutes. The crystallization was observed periodically by an optical microscope immediately after dropwise mixing. Crystallized materials were picked up by pipette and washing with pure water. After that, the crystals were analyzed by SEM (SU8240, Hitachi) and energy-dispersive X-ray spectroscopy (EDX; Genesis-AP2, EDAX).

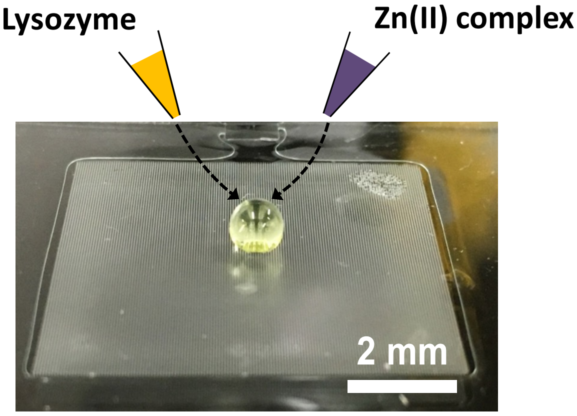

Figure 7: Crystallization experiment (Zn(II) complex and lysozyme).

RESULTS AND DISCUSSION

Figure 8 shows the obtained crystals that are expected to be Zn(II) complex containing lysozyme about 90 minutes later after dropping and mixing two aqueous solutions on the umbrella pillar array. The state of crystal growth was observable in real time by the optical microscope. This result informs that crystallization of Zn(II) complex containing lysozyme is possible even in droplets under atmospheric conditions, similar to droplets using microfluidic devices. Furthermore, the target crystal grows on a pillar array having water repellency, crystals of functional proteins could be easily picked up and off the umbrella pillar array device using a pipette.

Figure 9 shows EDX data with zinc peak. Therefore, crystallization of the Zn(II) complex containing lysozyme was successful.

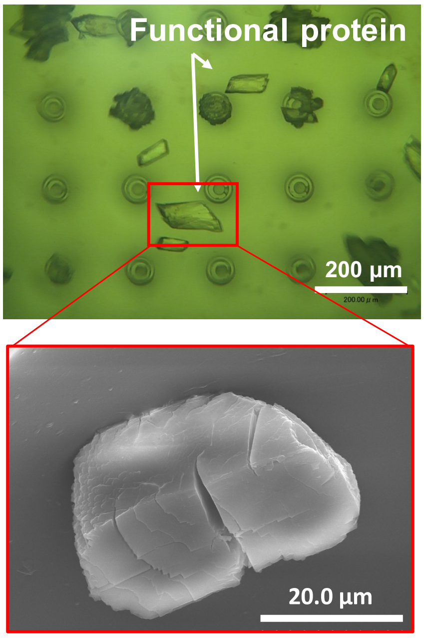

Figure 8: Observation of crystal by optical microscope and SEM.

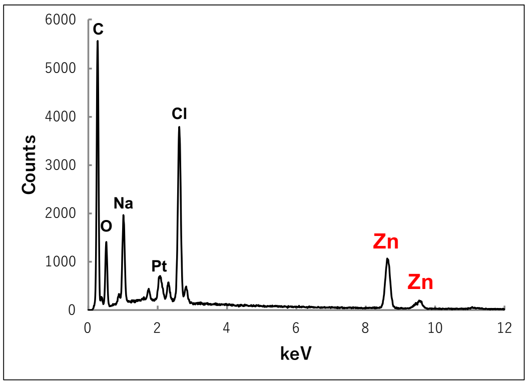

Figure 9. EDX analysis of the functional protein.

CONCLUSION

We succeeded in crystallization of Zn(II) complex containing lysozyme using a liquid repellent doubly reentrant structure fabricated by a lithography and pattern transfer process. Features of the umbrella-like pillar structure allowed a simple sample mixing and microcrystals formed on the structure could be easily taken out of the device without destruction by using a pipette.

In the future works, we will observe crystal growth by fluorescence microscopy and structural analysis of functional protein by XRD. Furthermore, we will apply this device and method to synthesizing and crystallizing functional proteins, albumin, which is expected to be applied to electrodes of fuel cells with high efficiency.

ACKNOWLEDGEMENTS

This work was partially supported by a Grant-in-Aid for the Scientific Basic Research (A) (No. 16H02349) from the Japanese Ministry of Education, Culture, Sports, Science and Technology (MEXT), and the authors would also like to thank the MEXT Nanotechnology Platform Support Project of Waseda University.

REFERENCES

[1] W. Nogala, K. Szot, M. Burchardt, F. Roelfs, J. Rogalski, M. Opalloa and G. Wittstock, "Feedback mode SECM study of laccase and bilirubin oxidase immobilised in a sol–gel processed silicate film", *Analyst*, 135, 2051–2058, 2010

[2] B. Zheng, L. S. Roach, and R. F. Ismagilov: “Screening of Protein Crystallization Conditions on a Microfluidic Chip Using Nanoliter–Size Droplets”, *J. AM. CHEM. SOC.*, Vol. 125, pp. 11170-11171, 2003

[3] K. Nakanishi, S. Minoshiro, D. H. Yoon, T. Sekiguchi and S. Shoji, "Development of low-cost mass production process of superrepellent surface using doubly reentrant structure pillar array", *The Journal of the Institute of Electrical Engineers of Japan*, E, No. 6, Vol. 138, 2017

[4] T.Y. Liu, and C.J. Kim: “Turning a surface superrepellent even to completely wetting liquids”, *Science,* Vol. 346, pp. 1096–1100, 2014.

CONTACT

* D. Tanaka, d.tanaka@aoni.waseda.jp

MICROFLUIDICS FOR THE ASSESSMENT OF THE EFFECTIVENESS OF NANOENCAPSULATED METHOTREXATE AGAINST OSTEOSARCOMA

O. Mitxelena-Iribarren[1], *Y. González-Fernández*[2,3], *E. Imbuluzqueta*[2,3], *M. Mujika*[1], *MJ. Blanco-Prieto*[2,3] *and S. Arana*[1]

[1] CEIT and Tecnun (University of Navarra), San Sebastián, Spain

[2] University of Navarra, Department of Pharmacy and Pharmaceutical Technology, Pamplona, Spain

[3]Instituto de Investigación Sanitaria de Navarra (IdiSNA), Pamplona, Spain

ABSTRACT

Cancer is a leading cause of mortality in the world, with osteosarcoma being one of the most common types among children between 1 and 14 years old. The use of lipid nanoparticles for controlled drug delivery shows promise as an effective and targeted treatment for osteosarcoma. However, the static nature of conventional techniques has prevented adequate *in vitro* testing of lipid nanoparticles. In this work, a microfluidic platform capable of determining the optimum dose of methotrexate-loaded lipid nanoparticles in osteosarcoma treatment is presented. Our results demonstrate higher effectiveness of osteosarcoma treatment with encapsulated methotrexate compared to treatment with free drug.

KEYWORDS

Microfluidic; methotrexate; nanoparticle; osteosarcoma; cancer therapy

INTRODUCTION

According to the World Health Organization, cancer is one of the main mortality causes all over the world. It has been estimated that the number of people diagnosed with cancer will increase up to more than 13 million deaths in 2030. Moreover, by the year 2050, 27 million new cancer cases will be diagnosed, among which 17.5 million will die [1]. Osteosarcoma, an uncontrolled growth of malignant cells produced in immature bone tissue, is one of the most common types of cancer among 1 to 14 year-old children [2]. Its current treatment is based on preoperative chemotherapy, surgery and postoperative chemotherapy [3]. However, their several side-effects and lack of tumor specificity have made the development of alternative treatment modalities necessary. Those new treatments should offer an efficient and targeted therapy to avoid all these limitations.

The use of lipid nanoparticles for controlled drug delivery shows promise as an effective and targeted treatment for osteosarcoma [4]. However, the static nature of conventional techniques has prevented adequate *in vitro* testing of lipid nanoparticles: static conditions involve a series of problems, such as the sedimentation of particles. This sedimentation hides the real effect of the nanoparticles and, therefore, their true cytotoxicity cannot be determined.

Microfluidics has shown to be of great utility in the development of alternative technologies for dynamic biomedical applications [5-11]. Besides, microfluidic platforms offer new alternatives for the *in vitro* characterization of the effect of the nanoparticles, since they allow a significant reduction of reagents and the possibility to modify cell environment in a controlled way [12].

Considering all the above mentioned facts, a validated microfluidic platform (Figure 1) that allows for optimized cell culture under dynamic conditions was used to perform the current set of experiments [14]. The design was previously optimized to allow an appropriate cell culture under dynamic conditions and the utility of it in cancer treatment characterization improvement was demonstrated [13]. The objective of this work was to validate the capability of the microfluidic platform to determine the optimum dose of methotrexate-loaded lipid nanoparticles in osteosarcoma treatment, analyzing the effect of different lipid nanoparticle types and concentrations under dynamic conditions. This makes dynamic microfluidic platforms a promising alternative to current nanoparticle characterization assays.

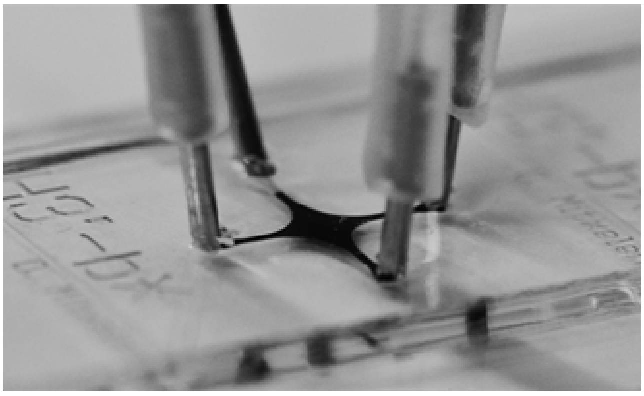

Figure 1: Real PDMS-glass microfluidic platform filled with ink and with the corresponding connectors [14].

MATERIALS AND METHODS

Fabrication of the microfluidic device

Microfluidic devices were fabricated in Polydimethylsiloxane (PDMS, Sylgard 184, Dow Corning) by replica-molding techniques using molds fabricated by conventional UV photolithography on 4” silicon wafers with SU-8 100 photoresist, as previously described [13].

Reagents for cell culture, methotrexate and methotrexate-lipid nanoparticle preparation

U-2 OS (ECACC 92022711, ATCC HTB-96) osteosarcoma cell line was used in this study. Cells were cultured using RPMI 1640 with Ultraglutamine 1 (RPMI 1640 with U1, Life Technologies, UK) supplemented with 10%(v/v) fetal bovine serum (FBS, Life Technologies, UK) and 1% of PenStrep (Gibco®, UK) at 37ºC in a humidified 5% CO_2 atmosphere. For subculturing, cells were washed with PBS, trypsinized with 0.5% trypsin-EDTA 1X (Gibco®, UK) and, once mixed with supplemented medium, centrifuged at 1500 rpm for 5 minutes. After this procedure, cells were used for subculturing (performed three times a week) or seeded in the microfluidic devices for the experimental procedures.

Free methotrexate (kindly provided by Dr. A. Aldaz, from the Department of Pharmacy of Clínica Universidad de Navarra, Spain) and both types of lipid nanoparticles (previously described by González-Fernández et.al [14]) were conveniently dissolved in RPMI 1640 for each concentration.

Experimental set-ups and procedures

Effects on the viability of a U-2 OS osteosarcoma cell line exposed to cell media, free methotrexate and Lec-PVA and Lec-TWEEN lipid nanoparticles (blank or containing methotrexate [10]) were quantified under dynamic assay conditions.

To achieve this, cells were seeded in a PDMS-glass microfluidic platform [13] at a concentration of $7 \cdot 10^4$cells/µL, using an in-line injection port (ibidi) and Tygon MHSL2001 tubes (ID = 0.38mm). Once adhered to the bottom of the 10mm^2 device chamber, the cell monolayer was subjected to the treatments in a set-up including a transmission Nikon Eclipse Ti microscope with a high resolution monochrome Hamamatsu camera under controlled environmental conditions. Recirculation of the different treatments (cell media, free methotrexate and two types of blank or methotrexate loaded lipid nanoparticles) at 15 µM, 150 µM or 1.5 mM methotrexate concentrations was performed with an IPC peristaltic pump at 2.15 µl/min for 72 hours.

Statistical analysis

Statistical analysis was performed with the cytotoxicity values. One-way analysis of variance (ANOVA) followed by post-hoc Bonferroni’s test or its non-parametric equivalent test (Kruskall-Wallis test) was performed when comparing more than two groups. When comparing only two groups, independent student’s t-test (or Mann-Whitney-U tests) was performed. For every comparison performed significant difference was determined as not significant ($P > 0.05$), significant ($0.01 < P < 0.05$), very significant ($0.001 < P < 0.01$) or extremely significant ($P < 0.001$).

RESULTS AND DISCUSSION

In order to assess the capability of the microfluidic platform to optimize the cytotoxic effect of drug-loaded nanoparticles, cells underwent different treatments. All cell assays consisted in four steps: (i) cell insertion, (ii) cell adhesion under static conditions for 24 hours, (iii) cell proliferation under corresponding dynamic treatment, and (iv) evaluation of the cytotoxic effect during 72 hours.

The cytotoxic effect of drug-loaded nanoparticles was assessed by first subjecting cells to regular cell media recirculation. As previously reported by this group [14] and depicted in Figures 2 and 3 with the striped line, cells proliferated as expected during the 72 hours period and withstood damage caused by the shear stress of the continuous flow rate.

Once the influence of the flow rate was proven to be negligible, assays for the quantification of the effect of methotrexate in osteosarcoma cells were performed. Thus, in order to verify that inside the microdevice the increasing amount of methotrexate had an increasing cytotoxic effect, cells were subjected to different concentrations of recirculating free methotrexate. As expected, the use of increasing free drug concentrations demonstrated a statistically very significant cytotoxic effect (p-values < 0.002) as cell population decreased gradually in 72 hours when increasing the concentration from 15 µM to 150 µM and 1.5 mM. Cells under 15 µM free methotrexate recirculation (Figure 2, straight line) kept proliferating, but with a lower growth rate than with media, due to the toxicity effect of the drug. This demonstrated a cytostatic but not cytotoxic effect of the free drug with this concentration. On the other hand, cell concentration was reduced to 55% (150 µM) and 28% (1.5 mM) after 72 hours of free drug recirculation.

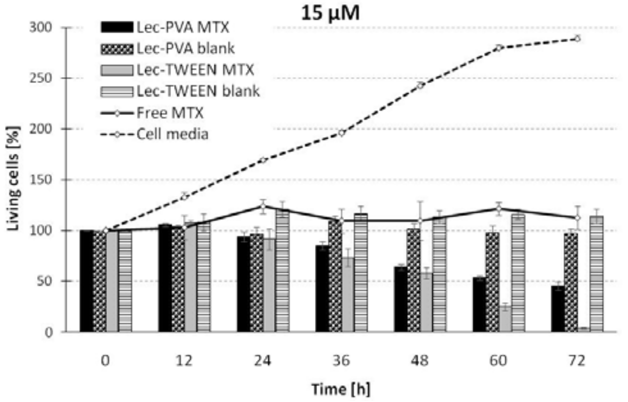

Figure 2. Living cell percentage under different cytostatic treatments in a 15µM concentration.

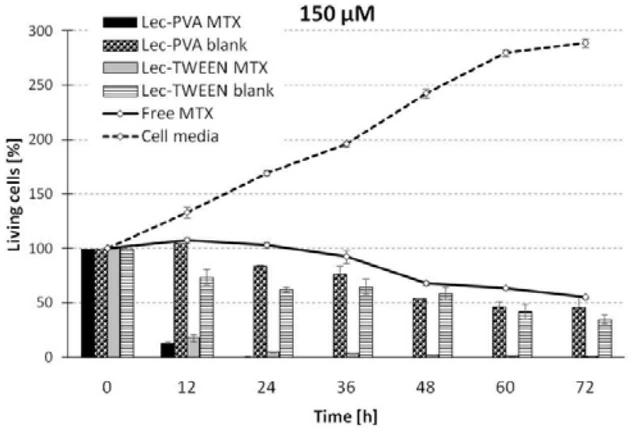

Figure 3. Living cell percentage under different cytostatic treatments in a 150µM concentration.

Afterwards, both types of lipid nanoparticles were circulated over the cells. As described before, cells were subjected to both circulating free and encapsulated methotrexate in order to assess the effectiveness of methotrexate-lipid nanoparticles, as well as to blank lipid nanoparticles to assess the effect of just adding a vehicle as a treatment. It has to be mentioned that for both lipid nanoparticles, the amount of vehicle needed to obtain the 1.5 mM concentration of the drug was too high, making the image so blurry that no cell could be distinguished. Therefore, this concentration was discarded for the study.

No difference was observed between Lec-PVA and Lec-Tween blank lipid nanoparticles, since both kept cell population in similar percentages. As shown by the dotted and striped bars in Figure 2, cell percentage remained around 115% under the equivalent weight of 15µM-loaded nanoparticles, but did not grow as much as under cell media, due to the higher shear stress produced by the nanoparticles on the cells. This shear stress effect was more clearly observed with the 150µM concentration of both blank nanoparticles (Figure 3), where the cell number was reduced by half. That is to say, when recirculating the equivalent nanoparticle amount of 15µM of both LEC-PVA and LEC-Tween blank nanoparticles, cell populations were kept after 72 hours up to 100% and 115%; these percentages were reduced to 45% and 35% though when using the equivalent of a 150 µM dose.

Finally, behavior of the cells under the recirculation of methotrexate-lipid nanoparticles was analyzed. As proven before with an 11 µM [13] methotrexate concentration, no nanoparticle sedimentation was observed during the 72 hours of each study in any of the three concentrations, as the study was carried out dynamically. Thus, as opposed to the results obtained with static traditional *in vitro* assays, with the use of the proposed microfluidic platform for dynamic cell analysis the real effect that these nanovehicles had over the cells was observed.

According to the cytotoxic effect, it was demonstrated that under the encapsulated methotrexate the efficiency of the treatment was much higher than under the free methotrexate: the higher effectivity of the loaded lipid nanoparticles (Figures 2 and 3, black and grey bars) against osteosarcoma cells was statistically significant already after 24 hours under 15 µM concentration. This efficiency was measured with the lowest concentrations.

Focusing on the different effects of the two encapsulated drugs, by the end of the assay, when exposed to 15µM, cells were reduced to less than the half for Lec-PVA nanoparticles and to around 4% for Lec-TWEEN. This higher toxicity rate for the Lec-Tween nanoparticles was not observed under the 150µM concentration, as both nanoparticle treatments reduced cell population nearly to zero after the 72 hours of recirculation, demonstrating that the cytotoxic effect of the encapsulated methotrexate was faster for higher drug concentrations. Knowing that the drug amount and the mechanisms with which the nanoparticles enter into the cells are exactly the same for both nanoparticles [14], the difference observed between both treatments could be due to the higher shear stress that Lec-Tween nanoparticles produce on the cells. This was because as these nanoparticles had a lower drug-load than the Lec-PVA ones, a higher amount of them was needed in order to have the same drug concentration.

Therefore, the results obtained indicate that for the same drug concentration the cytotoxicity for both loaded lipid nanoparticles is higher than that of free methotrexate, being even higher the one of the Lec-Tween formulation. With the use of the proposed microfluidic platform for dynamic cell analysis it was demonstrated that among the considered treatments, encapsulated methotrexate is the one with the highest efficacy in an osteosarcoma cell line.

CONCLUSIONS

Overall, the obtained results demonstrate that methotrexate-lipid nanoparticles are more effective at killing osteosarcoma cells than free drug treatment. In experiments under the same drug concentration, nanoparticles have shown to kill a higher amount of cells in shorter time, what could potentially reduce several side effects to the patients and therefore improve their quality of life.

This study demonstrated not only the effectiveness of the proposed nanovehicles, but also the effectiveness of the presented platform to dynamically analyze different nanoparticles at different concentrations. This microfluidic device shows promise in the research of new cancer treatments, as the dynamics of the platform reflects *in vivo* conditions better than the static well plates. Thus, the use of this platform will lead in the search of a personalized cancer treatment with nanoparticles.

ACKNOWLEDGEMENTS

Finally, authors would like to thank the Center of Biomedical Engineering of the University of Navarra and the Spanish Association against Cancer (AECC) for giving the financial support to accomplish this work. Also, the PREDOC program of the Basque Government for financing Oihane Mitxelena's PhD studies is acknowledged.

REFERENCES

[1] World Health Organization website http://www.who.int/

[2] R. Peris-Bonet, D. Salmeron, M.A. Martinez-Beneito, J. Galceran, R. Marcos-Gragera, S. Felipe, V. Gonzalez, J. Sanchez de Toledo Codina, "Childhood cancer incidence and survival in Spain", Ann. Oncol, Vol 21 Suppl 3, pp 103–110, 2010.

[3] J. Majó, R. Cubedo, N. Pardo, "Tratamiento del osteosarcoma. Revisión", Rev. Esp. Cir. Ortop. Traumatol, Vol 54, pp 329–336, 2010.

[4] B. Lasa-Saracibar, A. Estella-Hermoso de Mendoza, M. Guada, C. Dios-Vieitez, M. J. Blanco-Prieto, "Lipid Nanoparticles for Cancer Therapy: State of the Art and Future Prospects", Expert Opin Drug Deliv, Vol 9, pp. 1245–1261, 2012.

[5] A. Estella-Hermoso de Mendoza, M.A. Campanero, H. Lana, J.A. Villa-Pulgarin, J. de la Iglesia-Vicente, F. Mollinedo, M.J. Blanco-Prieto, "Complete inhibition of extranodal dissemination of lymphoma by edelfosine-loaded lipid nanoparticles", Nanomedicine, Vol 7, pp 679–690, 2012.

[6] A.M. Streets, Y. Huang, "Microfluidics for biological measurements with single-molecule resolution", Curr. Opin. Biotechnol, Vol 25, pp 69–77, 2014.

[7] I.U. Khan, C.A. Serra, N. Anton, T. Vandamme, "Microfluidics: a focus on improved cancer targeted drug delivery systems", J. Control. Release, Vol 172, pp 1065–1074, 2013.

[8] C. Rivet, H. Lee, A. Hirsch, S. Hamilton, H. Lu, "Microfluidics for medical diagnostics and biosensors", Chem. Eng. Sci, Vol 66, pp 1490–1507, 2011.

[9] R. Riahi, A. Tamayol, S.A.M. Shaegh, A.M. Ghaemmaghami, M.R. Dokmeci, A. Khademhosseini, "Microfluidics for advanced drug delivery systems", Curr. Opin. Chem. Eng, Vol 7, pp 101–112, 2015.

[10] N.S. Bhise, J. Ribas, V. Manoharan, Y.S. Zhang, A. Polini, S. Massa, M.R. Dokmeci, A. Khademhosseini, "Organ-on-a-chip platforms for studying drug delivery systems", J. Control. Release, Vol 190, pp 82–93, 2014.

[11] D. Huh, B.D. Matthews, A. Mammoto, M. Montoya-Zavala, H.Y. Hsin, D.E. Ingber, "Reconstituting organ-level lung functions on a chip", Science, Vol 328, pp 1662–1668, 2010.

[12] O.C. Farokhzad, A. Khademhosseini, S. Jon, A. Hermmann, J. Cheng, C. Chin, A. Kiselyuk, B. Teply, G. Eng, R. Langer, "Microfluidic system for studying the interaction of nanoparticles and microparticles with cells", Anal. Chem, Vol 77, pp 5453–5459, 2005.

[13] O. Mitxelena-Iribarren, C.L. Hisey, M. Errazquin-Irigoyen, et al., "Effectiveness of nanoencapsulated methotrexate against osteosarcoma cells: in vitro cytotoxicity under dynamic conditions", Biomed Microdevices, 19:35, 2017.

[14] Y. González-Fernández, M. Zalacain, E. Imbuluzqueta, L. Sierrasesumaga, A. Patiño-García, M. J. Blanco-Prieto, "Lipid Nanoparticles Enhance the Efficacy of Chemotherapy in Primary and Metastatic Human Osteosarcoma Cells", J Drug Deliv. Sci. Technol, Vol 30, pp. 435–442, 2015.

CONTACT

* O. Mitxelena-Iribarren, omitxelena@ceit.es

3-DIMENSIONAL FRACTAL GEOMETRY FOR GAS PERMEATION IN MICROCHANNELS

M. Malankowska[1,2], *S. Schlautmann*[1], *E. J. W. Berenschot*[1], *R. M. Tiggelaar*[1], *M. P. Pina*[2], *R. Mallada*[2], *N. R. Tas*[1], *and H. Gardeniers*[1]

[1]Mesoscale Chemical Systems, MESA+ Institute for Nanotechnology, University of Twente, P.O. Box 217, 7500 AE Enschede, The Netherlands

[2]Department of Chemical and Environmental Engineering and Aragon Nanoscience Institute, Campus Rio Ebro, C/ Mariano Esquillor s/n, 50018 Zaragoza, Spain

ABSTRACT

The integration of non-leaky membranes in microfluidic devices is a challenging task, in particular in case of gas-systems. In this work, the novel concept of a microfluidic silicon/glass chip with an integrated siliconoxide membrane in the form of three-dimensional fractal geometries with nanopores is presented. The permeation of oxygen and carbon dioxide are measured and validated theoretically. The results show a high permeation flux due to low resistance for mass transfer because of the hierarchical branched structure of the fractals, infinitesimal thickness of the pores and the high number of open pores. The developed chip is an interesting alternative for gas-liquid contactors that require harsh conditions such as microreactors or microdevices for energy applications.

KEYWORDS

Nanonozzles, gas permeation, integrated membrane chip, corner lithography

INTRODUCTION

The importance of membranes in microfluidic systems is reflected in the various applications that include membranes in microdevices. Among them we can find the detection of chemical reagents and gases, drug screening, cell growing, protein separation, microreactors, electrokinetical fluid transport and pump and valve fluid transport [1, 2]. In particular when the role of the membrane is to act as a gas-liquid interface, effective gas absorption and minimal gas leakage is required [3].

The key step for the combination of membranes and microfluidics is the sealing for avoiding leakages, especially in the case of gases. The most convenient strategies for the incorporation of membranes in microfluidics, which solve the key issue of sealing, include i) the preparation of the membrane as part of the silicon chip fabrication and ii) the use of the membrane properties of chip polymeric material [1]. In the case of biological applications this last option has been adopted in most of the cases using PDMS chips, it is well known that this polymer has high oxygen permeability [4]. However, when chemical or temperature resistance is needed, the use of silicon chips would be preferred.

In recent years the MCS-group of the University of Twente has developed an elegant fabrication method, based on a combination of anisotropic etching of silicon and corner lithography, to create small nanoapertures of around 80-100nm [5, 6]. The important features of this process are the possibility to easy scale up to wafer level and the ability to taylor the number of apertures and thus control the diffusion of gases through them. These apertures are distributed on the corners of pyramids which are part of a 3D fractal structure that could be replicated, see Figure 1. This fact adds an additional advantage that could not be achieved in other 2D materials such as porous silicon or anodized alumina. The 3D fractal structure could be embedded in a microfluidic channel which results in larger interfacial area and higher surface to volume ratio. The embedded structure would help to decrease mass transfer limitations, which often are encountered on the liquid side of the channels.

In summary the concept of membranes made of fractals containing nanoapertures would result in effective gas absorption without leakage of gases. In this paper we integrate the 3D fractal structure containing nanoapertures in a microchannel, then we evaluate the leaks and measure the gas permeation through the pores to estimate the ability of different gases, i.e. oxygen and carbon dioxide, to diffuse through these membranes. The measured values are validated with a model that considers molecular flow regime as the dominant mechanism for diffusion through the nanonozzles.

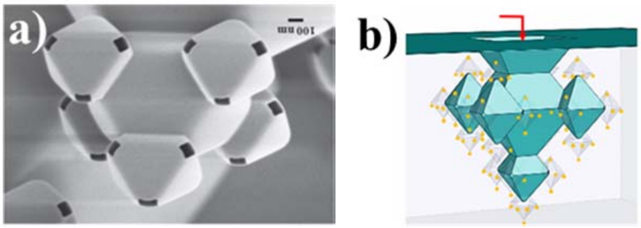

Figure 1. a) SEM image of 3rd *generation open fractals b) Schematic representation of fractal structures created by corner lithography.*

EXPERIMENTAL

Fractal fabrication

The method of engineering of a 3D fractal structure is based on a combination of anisotropic etching of silicon and corner lithography as developed by E. J. W. Berenschot et al. [6]. Corner lithography is a technique that allows production of truly three-dimensional features. It uses conformal deposition of layers of silicon nitride by low-pressure chemical vapor deposition (LPCVD), and thermal oxide and partly back-etching of a silicon nitride layer that is placed inside the octahedral silicon pits in order to form dots in sharp concave corners. The crystalline property of silicon and a gradual etching characteristic of its (111) planes result in the formation of octahedral cavities. Repeated corner lithography, in combination with anisotropic etching, results in the construction of 3D octahedral fractals where the number of layers can be controlled. Nevertheless, it has to be taken into account that the dimensions of the fractal structure levels scale down, by about a factor 2 for every next generation and the number of fabricated octahedra increases fivefold at the same time. The fabricated fractals are robust and possess well defined repetitive structures.

In order to maximize gas diffusion and increase surface to volume ratio, in this work the fractals with three generations have been selected. Figure 1 show the SEM photograph of 3rd generation fractal geometry with apertures in the range of 80 to 100 nm. The schematic drawing of this structure and how it evolves is presented in Figure 1b). The blue octahedral structures in the fractal correspond to 1st and 2nd generation and the transparent structures correspond to the 3rd generation that will be created after a corner lithography process, containing pores represented by the yellow dots. The fractal structures are hollow ("empty inside") which enables the gas to enter to the geometry (see red arrow in Figure 1b) and to permeate through the nanonozzle.

Chip design

The main considerations in the design of a proposed chip for gas diffusion in a channel are: 1) the number of fractal levels fabricated, that is directly connected with the number of openings, 2) the number of fractals in the channel, 3) the space among them and 4) the distance from one phase to another, i.e. the depth of the channel which is related to the diffusion distance.

The fractal structures were fabricated in a channel 3.5 cm long and 300 (Chip 1) or 500 (Chip 2) microns wide, containing a total of 244 (Chip 1) and 308 (Chip 2), 3rd generation fractals, unevenly distributed along the channel. Before the experiments, the total number of fractals containing open pores was evaluated by optical microscopy; the final number of estimated pores and characteristics of the chips is presented in Table 1. The total surface area of the channel was assumed as the active surface area of the membrane. The porosity was calculated as the volumetric porosity by dividing the volume of the pores by total volume of the structure.

The channel containing fractal structures was anodically bonded to a glass wafer with powder blasted holes and assembled together with another wafer containing a single channel 500 µm in height and same width and length as the fractal channels. Figure 2 shows a schematic representation of the final chip, containing a single free-hanging fractal for simplicity.

Table 1: Properties of fabricated fractal chips

	Chip 1	**Chip 2**
Channel width (µm)	500	300
Number open fractal structures	244	308
Surface area [m^2]	$1.75\ 10^{-5}$	$1.05\ 10^{-5}$
Volumetric porosity ε	$3.72\ 10^{-6}$	$3\ 10^{-6}$

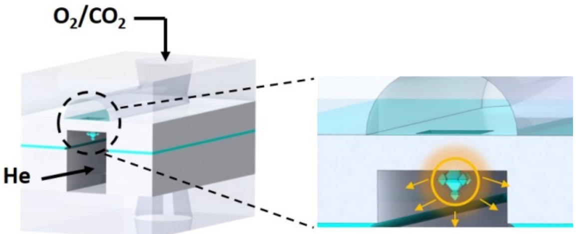

Figure 2. Schematic representation of the silicon nanonozzle chip vertical cross-section

Gas permeation measurements

The chip was placed in a holder (fabricated in RapidShape S30L) that enabled connecting it to the external capillary through the nanoport fitting. The holder was made of two parts that were connected to each other by two pins with 1.5 mm diameter (see central part of Figure 3. The experimental system for gas permeation measurements (Figure 3) consists of: 1) gas source, 2) mass flow controllers (Brooks, 5850 TR, USA), 3) pressure transducer (Panasonic, DP2-41E, Spain), 4) microfluidic fractal chip, and 5) micro-Gas Chromatograph (Micro – GC, Varian CP-4900, EVISA, USA). Two bubble flow meters were placed at the retentate and permeate side, respectively in order to measure the gas flow rates to ensure that there were no leaks in the system.

The permeation of two gases was measured: O_2 (purity grade 99.999% Praxair, Spain) and CO_2 (high-purity grade 99.998% Praxair, Spain). One of these two gases was introduced to the feed side at a given flow rate, controlled by mass flow controller (MFC). The pressure on this side was measured by a pressure transducer (PI). The sweep gas (He, purity grade 99.999% Praxair, USA) was introduced to the other chamber of the fractal microfluidic chip at a constant flow rate, 10 mL STP/min. The gas permeated through the nanoapertures to the permeate side and the mixture He + gas (CO_2 or O_2) was analysed in the Micro GC equipped with two modules, one with a M5A mole-sieve column and the other with Pora PLOT Q (PPQ) column. He was used as carrier gas in both columns. The micro-GC was calibrated in the range of 2.5 to 4.5% in volume for CO_2 and O_2.

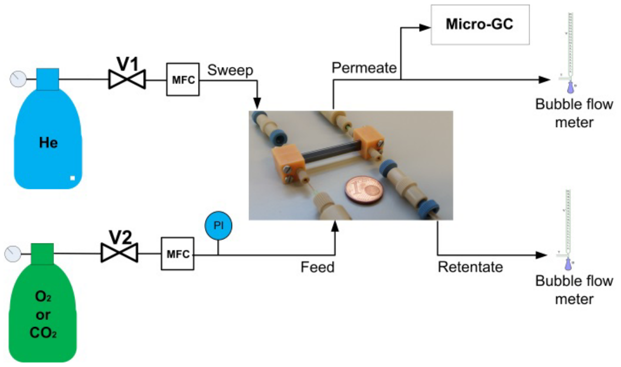

Figure 3 Experimental system for gas permeation measurements.

The permeation was calculated according to equation (1):

$$P = \frac{F_{perm}\, C_g}{100\, A\, \Delta P} \qquad (1)$$

where P is the permeance [mol/m^2sPa], F_{perm} is the total molar flow of the permeate [mol/s], C_g is the permeating gas (O_2 or CO_2) concentration expressed in percentage, and ΔP corresponds to the driving force for permeation and is the pressure difference between the feed side pure gas and the partial pressure of the permeating gas in the permeate side [Pa].

RESULTS

To evaluate the permeation through the pores of the fractal geometry two possible permeation mechanisms occurring simultaneously could be considered: molecular flow (or Knudsen) and viscous flow (or Poiseuille) [7, 8]. Different flow regimes were described by Knudsen who introduced the dimensionless Knudsen number: $Kn=\lambda/d$, being λ the mean free patch of the molecule and d the diameter of the pore. According to the Kn number the gas flow behaviour can be divided into viscous ($Kn < 0.01$), transition ($0.01 < Kn < 1$) and molecular ($Kn > 1$) flow regime. In our case, the Knudsen number is around 1.4 thus we considered that molecular flow will be more important.

Figure 4 shows two different sets of experimental points for permeation of oxygen versus mean pressure obtained for Chip 1 and Figure 5 corresponds to the permeation of for oxygen and carbon dioxide in Chip 2. In both figures the dashed line corresponds to the theoretical model used for the description of the permeation in the nanonozzles presented below.

All the permeation experiments show that there is no significant increase of the permeance with the mean pressure, which means that the viscous flow is negligible through these small nanoapertures [9]. Therefore, the molecular (Knudsen) flow regime was considered as the dominant flow through the nanonozzles, similar to previous work describing the flow through nanopillars of 62 nm height and described by equation (2) [8]:

$$F_{mol} = \frac{A \cdot \varepsilon\, w(x)}{\sqrt{2\pi M R T}} \qquad (2)$$

Where, F_{mol} is the flow conductance in the molecular flow regime i.e [mol s^{-1} Pa^{-1}], A is the total membrane surface area [m^2], ε is the porosity, M is the gas molecular weight [kg mol^{-1}], R is the gas constant [J $mol^{-1}K^{-1}$], T is the temperature [K] and w(x) is the Clausing function that considers the collisions of gas molecules with the walls of the pore and it is related to its geometry. In our case we have considered a pyramidal geometry corresponding to the 3rd generation open fractal structure.

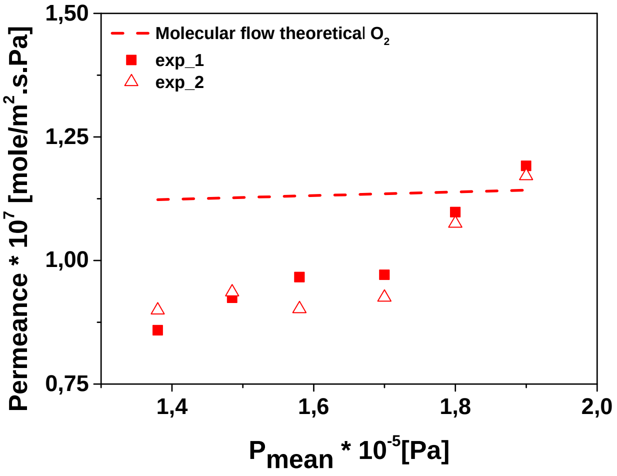

Figure 4. Experimental and theoretical permeation of O_2 in Chip1.

The Clausing function w(x), for conical orifices according to the conical geometry described by Lobo et al. with the angle of the pyramid 30 degrees, and

(L=495nm, R_0=100nm) has a value of 0.90814. [7, 10]. This value is higher compared to the one for cylinders, which means that the probability to exit the cone is higher compared to cylinder.

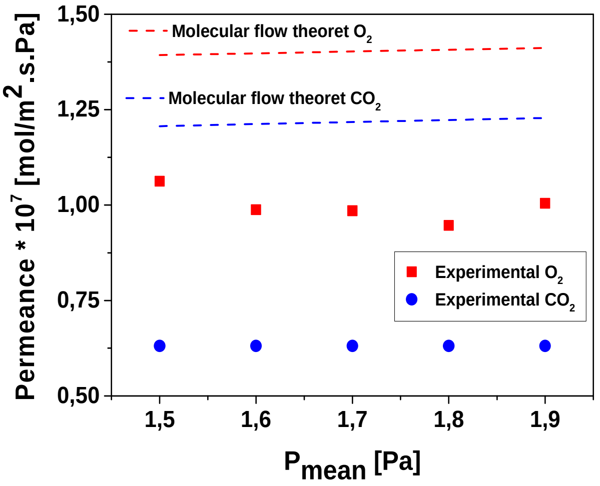

Figure 5. Experimental and theoretical permeation of O_2 and CO_2in Chip2.

The theoretical calculations showed that the experimental values are approximately 30-40% lower than the predicitions (see Figure 4 and Figure 5). This might be due to the difficulty in estimating the real amount of truly open apertures/nanonozzles. Some nanonozzles could be closed or not fully opened due to the fabrication procedure. Also, as expected in the Knudsen regime the diffusion of smaller molecules through the pores is faster than larger molecules, i.e. oxygen is faster than carbon dioxide. According to equation (2) the ideal selectivity of O_2 over CO_2 should be 1.2, whereas we found a slightly higher value of 1.6.

The permeation values obtained, in the order of 10^{-7} mol/m^2 s Pa are high if we compare this to polymeric materials such as PDMS. Considering a permeability value for PDMS of 620 Barrer for oxygen [4], a membrane film of just 1-4 micrometers would be required to get the same permeation flux as the nanonozzles presented here (but such thin PDMS membrane cannot be handled).

CONCLUSIONS AND FUTURE WORK

In this work we have validated the concept of a new 3D membrane structure incorporated in a chip for gas transfer to a microfluidic channel. We measure experimentally and calculated theoretically the permeation of oxygen and carbon dioxide.

Other applications apart from the single gas permeation tested here include gas-liquid contactors, where the 3D structure presents an advantage due to the higher surface to volume ratio compared to 2D membranes, and also applications requiring high temperatures and gas distribution or removal such as micromembrane microreactors [11].

CONTACT

* R. Mallada, rmallada@unizar.es

REFERENCES

[1] J. De Jong, R.G.H. Lammertink, M. Wessling, “Membranes and microfluidics: A review”, Lab on a Chip - Miniaturisation for Chemistry and Biology, 6 pp. 1125-1139, 2006.

[2] X. Chen, J. Shen, “Review of membranes in microfluidics”, Journal of Chemical Technology and Biotechnology, 92, pp 271-282, 2017.

[3] X. Ren, H. Lu, J.G. Zhou, P.L.G. Chong, W. Yuan, M. Noh, “Porous Polydimethylsiloxane as a Gas-Liquid Interface for Microfluidic Applications”, Journal of Microelectromechanical Systems, 26 pp. 120-126, 2017.

[4] K.S. Houston, D.H. Weinkauf, F.F. Stewart, “Gas transport characteristics of plasma treated poly(dimethylsiloxane) and polyphosphazene membrane materials”, Journal of Membrane Science, 205, 103-112, 2002.

[5] N. Burouni, E. Berenschot, M. Elwenspoek, E. Sarajlic, P. Leussink, H. Jansen, N. Tas, “Wafer-scale fabrication of nanoapertures using corner lithography”, Nanotechnology, 24, 2013.

[6] E.J.W. Berenschot, H.V. Jansen, N.R. Tas, “Fabrication of 3D fractal structures using nanoscale anisotropic etching of single crystalline silicon”, Journal of Micromechanics and Microengineering, 23 055024 10pp, 2013.

[7] R.P. Iczkowski, J.L. Margrave, S.M. Robinson, “Effusion of gases through conical orifices”, Journal of Physical Chemistry, 67, pp. 229-233, 1963.

[8] S. Unnikrishnan, H.V. Jansen, F.H. Falke, N.R. Tas, H.A.G.M. Van Wolferen, M.J. De Boer, R.G.P. Sanders, M.C. Elwenspoek, “Transition flow through an ultra-thin nanosieve”, Nanotechnology, 20, 2009.

[9] K. Keizer, R.J.R. Uhlhorn, R.J. Van vuren, A.J. Burggraaf, “Gas separation mechanisms in microporous modified γ-Al_2O_3 membranes”, Journal of Membrane Science, 39, 285-300, 1988.

[10] J. Gómez-Goñi, P.J. Lobo, “Comparison between Monte Carlo and analytical calculation of the conductance of cylindrical and conical tubes”, Journal of Vacuum Science and Technology A: Vacuum, Surfaces and Films, 21 pp. 1452-1457, 2003.

[11] X. Zhang, E.S.M. Lai, R. Martin-Aranda, K.L. Yeung, “An investigation of Knoevenagel condensation reaction in microreactors using a new zeolite catalyst”, Applied Catalysis A: General, 261 pp. 109-118, 2004.

EXTREMELY EFFICIENT AND NON-HAZARDOUS BROMO GROUP ADDITION REACTION USING SIMPLE MICROFLUIDIC DEVICES

W. Kawakubo[1]*, D. Tanaka*[1]*, D. H. Yoon*[1]*, T. Sekiguchi*[1]*, K. Takahashi*[2]*, T. Akitsu*[2]*, S. Shoji*[1]
[1] Research Organization for Nano & Life Innovation, Waseda University, Tokyo, Japan
[2] Department of Chemistry, Faculty of Science, Tokyo University of Science, Tokyo, Japan

ABSTRACT

Highly toxic and corrosive bromo group addition reaction was performed under highly efficient and non-hazardous conditions using a simple microfluidic method.

No atmosphere control was required because proposed silicon/glass structure prevented leakage and circulation of internal and external gases. The harmful bromine containing gas for the reaction was confined in the isolated microchannel of the device.

The small scales synthesis reduced the reaction time to within a few seconds, while the conventional methods took around 4 hours. Approximately 1/7000 times reduction was achieved by the proposed device. Both products synthesized by microfluidic method and conventional beaker works were compared and evaluated.

KEYWORDS

Microfluidic device, Chemical synthesis, Bromo groups, Laminar flow, Reduced reaction time

INTRODUCTION

Bromo groups have high electron withdrawing, thus those are expected to be adopted in several fields such as electronics, for example, to expand light absorption rate of dye sensitized solar cell.

However, conventional bromo groups addition reaction is hazardous due to toxicity and corrosiveness of bromine. Moreover, low reaction rate of bromination makes the reaction complicate.

In contrast, various microfluidics based chemical synthesis methods have been studied. Specificities of micro-scale reactor enabled the reactions to increase its reaction rate and to improve recovery rate of objective substance [1]. Our previous research accomplished synthesis of metal complex using microfluidic devices that can decrease reaction time and omit temperature and atmospheric control [2]. These studies indicated that use of microfluidic devices in chemical synthesis can realize various complicate reactions more efficiently.

Bromination reaction using microfluidic device was reported by Cygan et al. [3]. In the study, chemical reaction was attempted in the microdroplets generated in the device and objective substance was extracted from the microdroplets. However, the device fabricated by resin material was affected by swelling and corrosion from bromine and most of organic chemicals. Therefore, problems of chemical resistance still remain for use in bromination reaction. Furthermore, manual extraction process was finally necessary to obtain objective substance.

Hence, we presented a synthesis process using a simple Y-shaped microchannel and highly solvent-resistive silicon/glass device materials. Furthermore, the synthesis results and efficiency were evaluated by comparison to the conventional method.

DEVICE FABRICATION

Convenitonal bromination reaction

Conventional bromo group addition reaction methods are shown in Figure 1. $CHCl_3$ solution of bromine (0.15 mol L^{-1}, 10 mL) was added dropwise in the 1-Hydroxy-2-naphthaldehyde (0.050 mol L^{-1}, 20 mL, in $CHCl_3$) for 30 minutes and stirred for 4 hours at room temperature. Then, objective substance, 4-Bromo-1-hydroxy-2-naphthaldehyde, was extracted from the solution [4].

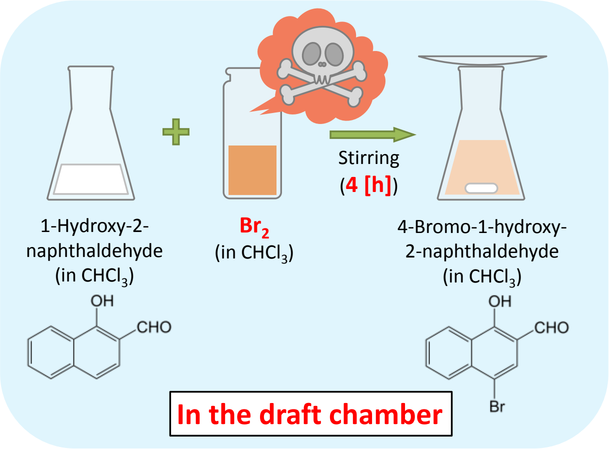

Figure 1: Conventional method of bromo groups addition

Bromination using microfluidic device

Figure 2 shows the design of microfluidic device using simple Y-shaped channel and a scheme of bromo groups addition reaction in the channel.

A $CHCl_3$ solution of 1-Hydroxy-2-naphthaldehyde and bromine were injected into different inlets, respectively. A laminar flow of each solution was formed at the channel junction, and the synthesis of the objective substance was performed. The objective substance was synthesized at the interface between

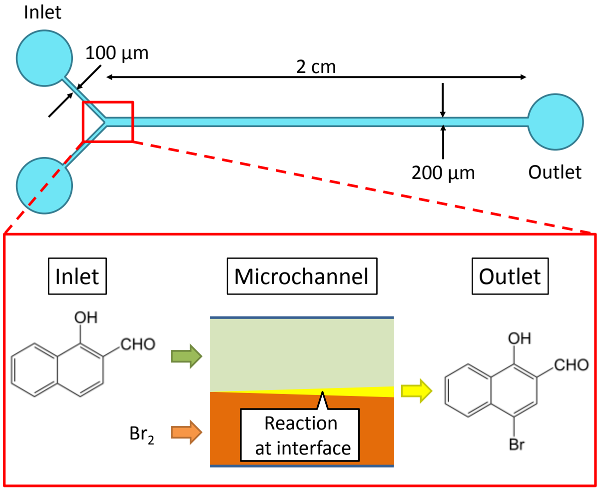

Figure 2: Bromo groups addition using microfluidic device

two liquids.

Device fabrication

Device fabrication process is shown as Figure 3. Silicone and glass was adopted as the material to ensure chemical resistance of the device to bromine and $CHCl_3$.

The microchannel was fabricated from silicon substrate. At first, a positive photoresist, OFPR (TOKYO OHKA KOGYO CO., LTD.), was spin-coated on the silicon substrate and device pattern was transferred on the resist using UV lithography process. Then, microchannel was formed using dry etching process, deep reactive ion etching. Inlets and outlet of the devices was formed in the same process. Finally, the silicon substrate and glass substrate were bonded by anodic bonding process.

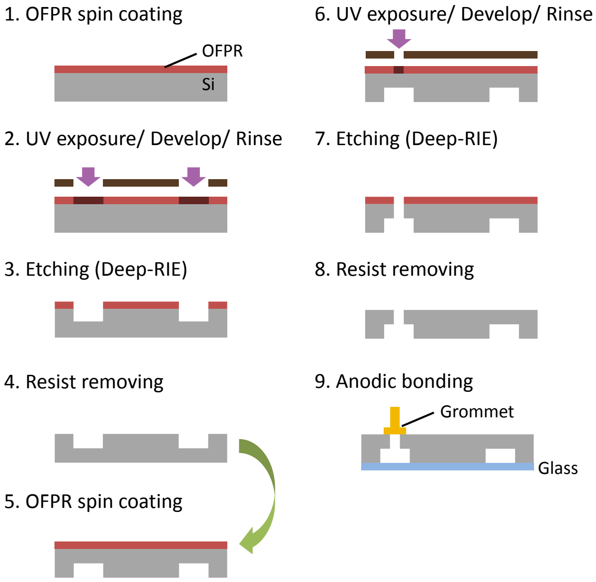

Figure 3: Fabrication process of the device

RESULTS AND DISCUSSION

Experimental procedure

In the synthesis using microfluidic devices, each reagent was injected by syringe pump (KDS210、KD Scientific). After synthesis, solution including samples was collected on filter paper and products were obtained by driving off the solvents. Each flow rate of the reagents was set at 10.0 µL min^{-1}. Conventional synthesis methods were performed as above.

The products synthesized using a microfluidic method and conventional method were analyzed by SEM (SU8240, Hitachi), EDX (Genesis V6.44J, EDAX), FTIR (FT/IR-6200, JASCO) and FAB-MS (JMS-BU25, JEOL) to confirm objective substance.

Results of the synthesis

Figure 4 shows obtained samples using each synthesis methods. Complete sealing of the silicon/ glass device realized the synthesis process without leakage of the hazardous reagents. Furthermore, as shown Figure 4-(c), laminar flow was correctly formed at the channel junction of the device. In the microchannel, reaction which took 4 hours in conventional methods was performed in a few seconds (1/7000 times decrease).

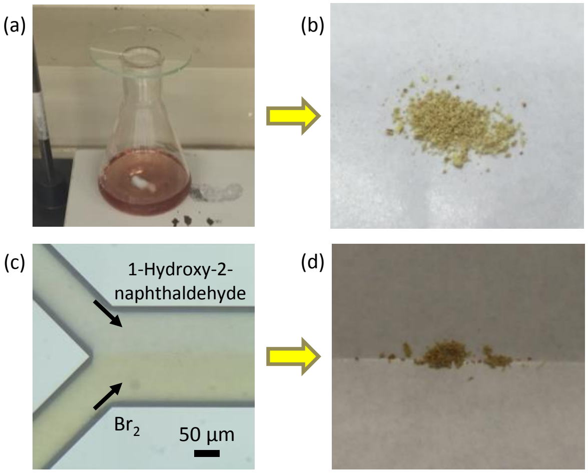

Figure 4: Results of synthesis (a) Synthesis based conventional method (b) Products obtained by conventional metod (c) Synthesis using microfluidic device (d) Peoducts obtained from device

Results of the analysis

First, SEM and elemental analysis using EDX was performed to confirm bromine contained in the samples. Results are shown as Figure 5. SEM images showed that each obtained samples was similar needle crystals. In addition, EDX spectra confirm that bromine is included in the samples.

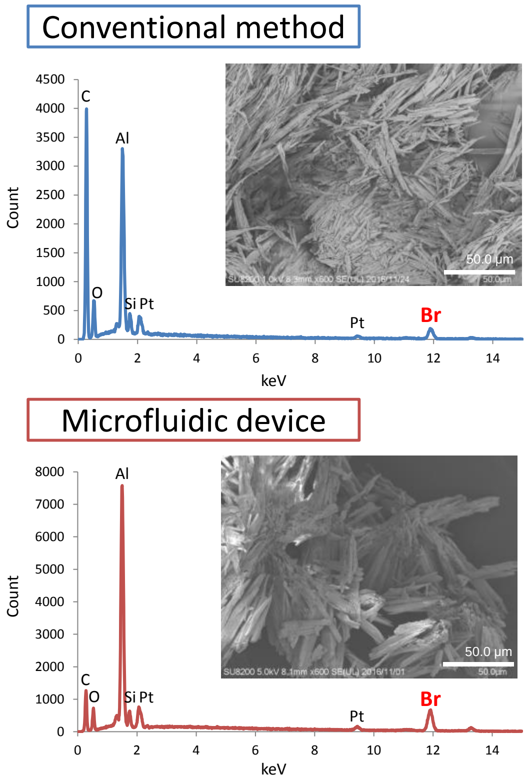

Figure 5: Elemental analysis of the products

Second, IR spectra were analyzed to confirm C-Br chemical bond included in the samples (Figure 6). In Figure 6, spectrum of 1-Hydroxy-2-naphthaldehyde was added for comparison. If C-Br chemical bond is in the sample, spectrum shows the peaks around 515-690 cm $^{-1}$ [5]. As shown in Figure 6, each spectrum of the samples had peaks at 541.9, 681.7 cm^{-1}, which were not shown in the spectrum of raw material. Therefore, this result indicates that obtained samples had C-Br chemical bond.

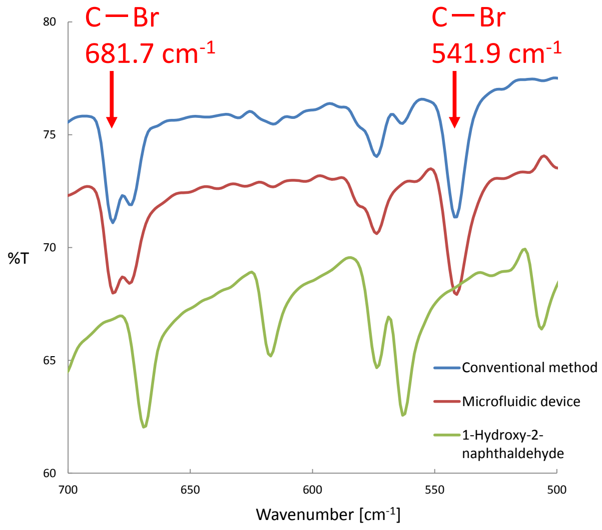

Figure 6: Infrared transmission spectra of the products

Finally, mass spectra of the products obtained by FAB-MS are shown in Figure 7. The spectra have peaks around 252 that are mass to charge ratio of the protonated molecular which comes from 4-Bromo-1-hydroxy-2-naphthaldehyde.

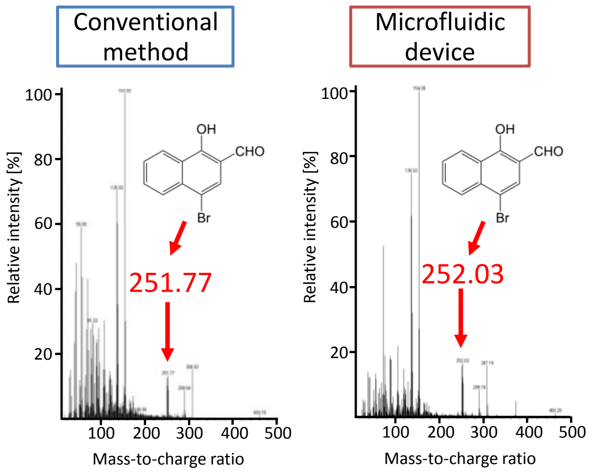

Figure 7: Mass spectra of the products

These three analysis results indicate that bromination reaction was successfully performed in the simple microfluidic device and the method allowed very rapid but non-hazardous reaction without complicated environmental controls.

CONCLUSION

Bromo groups addition reaction using simple Y-shape microfluidic device fabricated by silicon/glass was developed. In the micro-scale synthesis, reaction time was reduced by 1/7000 times without complicated environmental control. Moreover, analysis results using SEM, EDX, FTIR and FAB-MS confirmed that the products similar to the conventional method were obtained by the microfluidic method.

In this research, we achieved synthesis of single bromo group addition reaction. As a next step, we are investigating synthesis methods and conditions to realize the multiple bromo groups addition reaction.

ACKNOWLEDGEMENT

This work was partly supported by Japan Ministry of Education, Culture, Sports Science & Technology (MEXT) Grant-in-Aid for Scientific Basic Research (A) No. 16H02349 and the authors thank for MEXT Nanotechnology Platform Support Project of Waseda University.

REFERENCES

[1] K. S. Elvira, X. C i Solvas, R. C. R. Wootton and A. J. deMello: “The past, present and potential for

microfluidic reactor technology in chemical synthesis", *NATURE CHEMISTRY*, Vol.5, pp.905-915, 2013

[2] D. Tanaka, W. Kawakubo, E. Tsuda, Y. Mitsumoto, D. H. Yoon, T. Sekiguchi, T. Akitsu and S. Shoji: "Microfluidic synthesis of chiral salen Mn(II) and Co(II) complexes containing lysozyme", *RSC Advances*, Vol.6, pp.81862-81868, 2016

[3] Zuzanna T. Cygan, Joaõ T. Cabral, Kathryn L. Beers, and Eric J. Amis "Microfluidic Platform for the Generation of Organic-Phase Microreactors", *Langmuir*, Vol.21, pp. 3629-3634, 2005

[4] Y. Wang, M. Wang, Y. Wang, Y. Chen, and L. Sun:" SYNTHESIS OF NEW CHIRAL SCHIFF BASES CONTAINING BROMO- AND IODO-FUNCTIONALIZED HYDROXYNAPHTHALENE FRAMEWORKS" , *Synthetic Communications* , Vol.41 pp.1381-1393, 2011

[5] Robert M. Silverstein, G. Clayton Bassler and Terence C. Morril, "SPECTROMETRIC IDENTIFICATION OF ORGANIC COMPOUNDS THIRD EDITION", *WILEY*, pp. 144, 1974

CONTACT

* W. Kawakubo,
kawakubo@shoji.comm.waseda.ac.jp

DYNAMIC MODEL FOR INVESTIGATION OF INSTABILITIES IN MICROCHANNEL EVAPORATORS

F. K. Leube[1], K. S. Drese[2] and P. Stephan[3]
[1] Fraunhofer ICT-IMM, Carl-Zeiss-Straße 18-20, 55129 Mainz, Germany
[2] Institute of Sensor and Actuator Techology, HS Coburg, Coburg, Germany
[3] Institute of Technical Thermodynamics, TU Darmstadt, Darmstadt, Germany

ABSTRACT

Microchannel evaporators are widely used for both cooling applications and for vapor generation in process engineering. They allow high heat transfer rates within minimal space. However, the massive changes of the fluids properties during evaporation can trigger different types of instabilities. These mostly undesired effects are caused by complex interactions of heat conduction, heat transfer and fluid flow within the evaporator. A comprehensive dynamic model is developed to obtain a deeper understanding of the effects occurring her. Experimental validations show that the model is capable of correctly predicting the pressure drop behavior of practical microchannel evaporators.

KEYWORDS

Microchannel evaporator, heat transfer, two phase flow, pressure drop

INTRODUCTION

Microchannel evaporators are used both for vapor generation and cooling applications. A typical microchannel evaporator which is used in laboratory-scale applications is shown in figure 1. It consists of several parallel channels which connect the inlet and the outlet manifold. These microchannels are fabricated by laser ablation. Due to their high surface to volume ratio, these devices allow high heat transfer rates in very small spaces. However, microchannel microchannel evaporators are prone to several types of instabilities, such as flow oscillations or maldistribution. These undesired effects are caused by miscellaneous interactions of pressure-drop, heat transfer and compressibility of the fluid and heat conduction in the solid material. This work focuses on the development of robust evaporator designs for small scale applications, in which a steady vapor flow is crucial.

For this purpose, a comprehensive dynamic system model is developed to obtain a deeper understanding of the occurring effects.

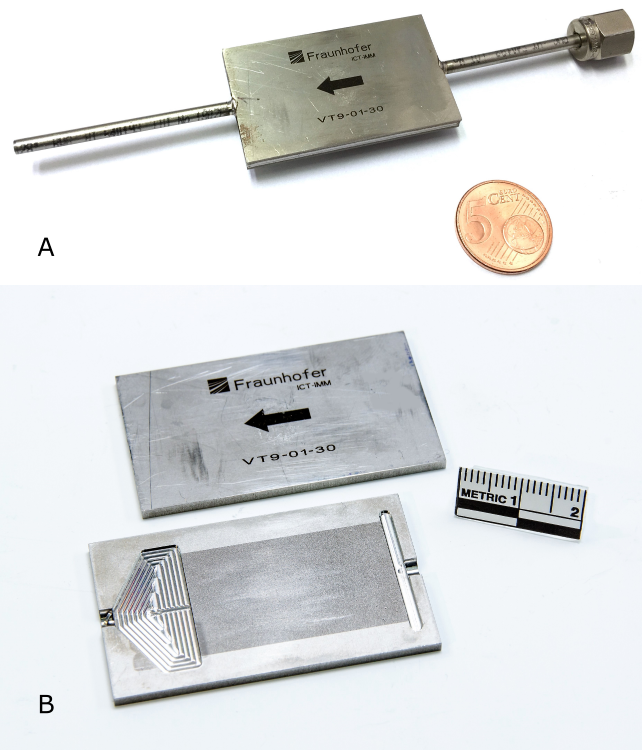

Figure 1: Example of a microchannel evaporator used for vapor generation in laboratory-scale applications. A): complete complete evaporator an B): internal structure.

MODELING APPROACH

In order to realictically describe the dynamic behavior of microchannel evaporators, the mass, momentum and energy balances of the fluid need to be modeled. Furthermore, the energy balance of the solid region needs to be taken into account, since the fluid thermally interacts with the solid walls surrounding it. For this type of problem several different modeling approaches exist, ranging from rather simple lumped parameter models [1] over more complex one dimensional models [2, 3] to full three-dimensional CFD codes [4]. Due to the large range of relevant length scales, it is not possible to simulate complete microchannel arrays using conventional 3D-CFD codes with currently available computers. Therefore, a simpler one-dimensional approach is chosen.

The present model is similar to the work of Saenen and Baelmans [2] and is capable of describing a three-dimensional array of microchannels. The fluid region is described by the area-averaged one-dimensional conservation laws for mass, momentum and energy using the diffusion model [5]. When neglecting axial heat conduction in the fluid, the resulting balances lead to equations 1 to 3:

$$A\frac{\partial \rho}{\partial t} + \frac{\partial \dot{m}}{\partial z} = 0 \tag{1}$$

$$\begin{aligned} &\frac{1}{A}\frac{\partial \dot{m}}{\partial t} + \frac{1}{A}\frac{\partial}{\partial z}\left(\frac{\dot{m}^2}{A\rho'}\right) \\ &\quad + \frac{\partial p}{\partial z} + \dot{m}\frac{2Po}{D_\mathrm{h}^2 A}\nu_\mathrm{mix} = 0 \end{aligned} \tag{2}$$

$$\frac{\partial \rho h^*}{\partial t} + \frac{1}{A}\frac{\partial \dot{m} h}{\partial z} - \frac{\partial p}{\partial t} = q''\frac{P}{A} \tag{3}$$

Here A is the cross-sectional area of the channel, D_h is the hydraulic diameter, P is the heated perimeter of the channel, $\dot{m}$ is the mass flow, x is the vapor fraction, ε is the void fraction, and h is the mass averaged specific enthalpy of the mixture. Furthermore q'' describes the heat flux which is transferred at the channel wall.

The density of the two phase mixture ρ can be calculated from the void fraction ε and the density of the liquid and the vapor phase:

$$\rho = \varepsilon\rho_\mathrm{V} + (1-\varepsilon)\rho_\mathrm{L} \tag{4}$$

In equation 2, ρ' indicates the momentum density, which takes into account that both phases do not move with the same velocity [5].

$$\rho' = \left(\frac{(1-x)^2}{\rho_\mathrm{L}(1-\varepsilon)} + \frac{x^2}{\rho_\mathrm{V}\varepsilon}\right) \tag{5}$$

The mixture specific enthalpy h^* can be calculated by:

$$h^* = \frac{\rho_\mathrm{L}(1-\varepsilon)h_\mathrm{L} + \rho_\mathrm{V}\varepsilon h_\mathrm{V}}{\rho} \tag{6}$$

Since the flow regime in microchannel evaporators is usually laminar, the frictional pressure drop is expressed via the Hagen-Poiseuille law. The Poiseuille Number is the product of the fanning friction factor and the Reynolds number: $Po = fRe$ [6].

The Poiseuille number is calculated by solving the flow profile for the corresponding microchannel geometry, which was determined by SEM microscopy (figure 2) to account for randomly shaped microchannels.

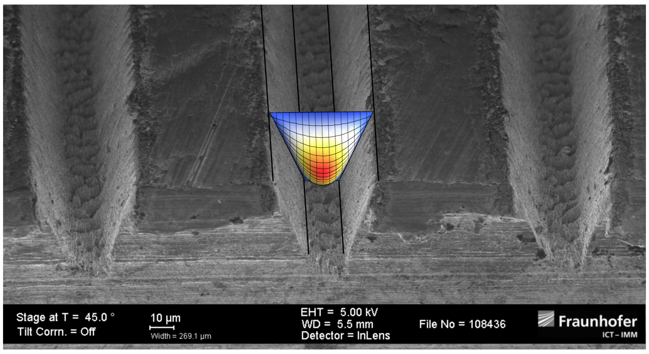

Figure 2: SEM image of a microchannel array. The simulated Hagen-Poiseuille flow profile is used to calculate the Poiseuille number Po, which allows the calculation of the single phase frictional pressure drop.

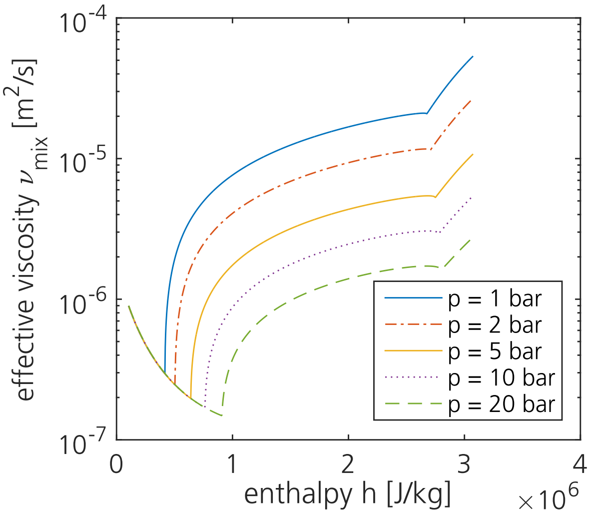

Figure 3: Effective mixture viscosity ν_mix of water assuming laminar annular flow in circular channels.

The effective viscosity ν_mix in equation 2 is used to express the frictional pressure drop in two phase flow. Since laminar annular flow is assumed to be the dominant flow regime, the void fraction ε and the effective mixture viscosity are both calculated using an annular flow model in the two phase region [7]. In figure 3, the effective mixture viscosity is plotted versus the specific enthalpy at different pressure levels. Since the liquid viscosity is decreasing with increasing temperature, and practically pressure independent, at low enthalpies, the viscosity increases with increasing enthalpy. When the fluid reaches the boiling temperature, the higher specific volume of the vapor phase will cause the effective viscosity to sharply increase. In two-phase and overheated vapor region, the pressure level has a strong impact on the pressure drop and thus on the effective viscosity. This is also mainly due to the increasing specific volume of the gas phase at decreasing pressure.

The distribution of the temperature T within the

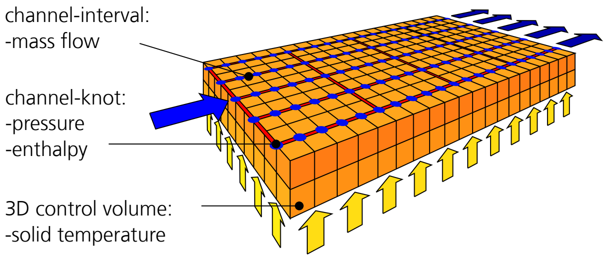

Figure 4: Exemplary simulation grid for a microchannel evaporator consisting of five parallel microchannels with three cross connecting channels.

solid region of the evaporator is described by the Fourier law:

$$\rho c_{\mathrm{p}} \frac{\partial T}{\partial t} - \lambda \nabla^2 T = q''' \tag{7}$$

Here, c_{p} is the specific heat capacity and λ is the thermal conductivity of the evaporator material. Furthermore, the term q''' describes the emitted heat per volume, which can either be negative in case of the supplied heat from the heating cartridge or positive in case of heat transferred to the fluid. The heat transfer is described using the correlation of Kim and Mudawar [8]. This correlation is chosen and implemented due to its broad range of validity for micro- and minichannels.

All balances are dynamically modelled using the finite volume method (FVM). The mass- momentum und energy balances of the fluid (equations 1, 2 and 3) are discretized on a staggered grid consisting of channel knots which are connected by channel intervals. The pressure and enthalpy are both evaluated in the channel knots whereas the mass flows are evaluated on the channel intervals. This approach allows a straightforward implementation of various flow geometries. The heat conduction in the solid region (equation 7) is modeled on a full three-dimensional grid. An exemplary simplified simulation grid is shown in figure 4.

Time stepping is done fully implicit to allow for rather large time steps and pressure-velocity coupling is realized using the PISO algorithm [9].

EXPERIMENTAL VALIDATION

To obtain data for validation, a test rig was installed (figure 5). It consists of two thermal jaws which are heated by four electric cartridge heaters. Between the thermal jaws different microchannel evaporators can be inserted. As working fluid, deionized and degassed water is supplied from a pressurized tank via a thermal mass flow controller. The inlet and outlet pressures

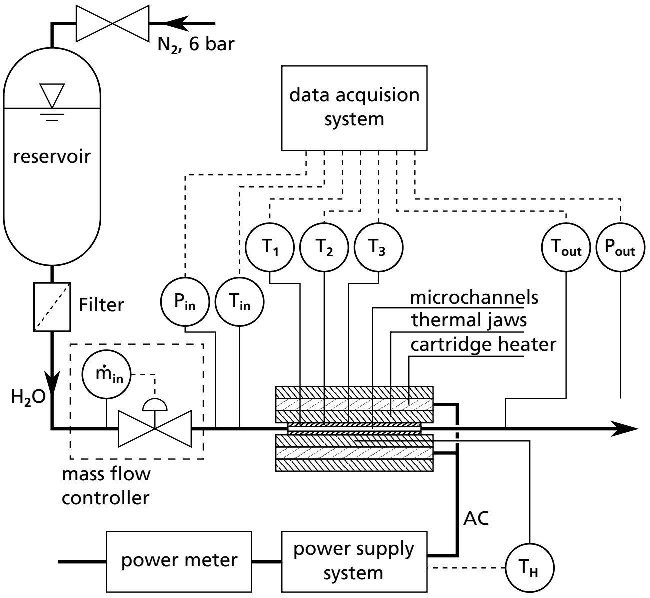

Figure 5: Experimental setup for characterizing microchannel evaporators. The microchennel evaporator is fixed between two thermal jaws, which are heated by electric cartridge heaters.

as well as several temperatures are recorded by a LabVIEW based data logger. During the experiments, the temperature of the thermal jaws was set to a certain value and controlled by a power supply system. The water mass flow was stepwise increased.

RESULTS AND DISCUSSION

In figure 6 A, the measured pressure drop data of an evaporator consisting of 50 parallel 84 µm channels is presented. It can be seen, that at increased mass flows, the pressure drop of this evaporator begins to fluctuate severely, indicating the occurrence flow instabilities. In figure 6 B, the mean pressure drop values are plotted over the mass flux G and compared to numerical results from the model. It can be seen, that the model is capable of realistically describing the pressure drop behavior. This implies, that the assumption of annular flow characteristics is justified. Accordingly, the model can be used for designing and dimensioning of microchannel evaporators in practical applications. However, for dynamic simulations the numeric stability needs further improvements.

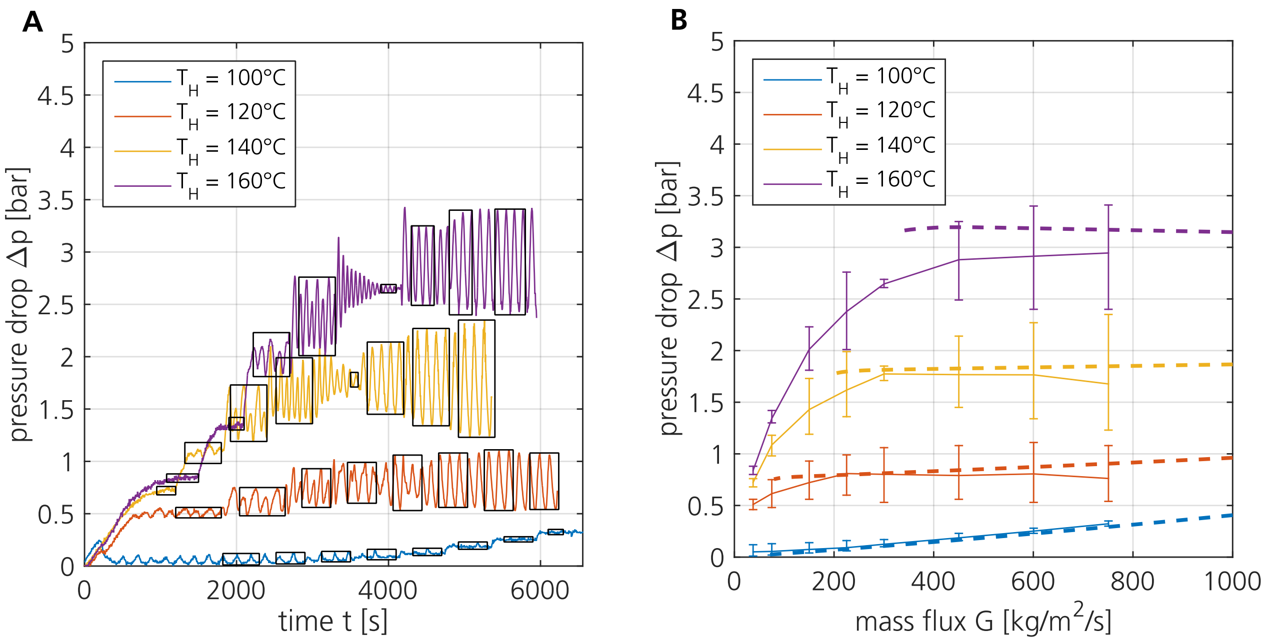

Figure 6: Pressure drop data for a 84 µm microchannel evaporator operated with water at a stepwise increasing mass flow. A): measured pressure drop values. B): time averaged pressure drop versus inlet mass flux. The solid lines show the experimental results whereas the dashed lines represent the simulated data.

REFERENCES

[1] TieJun Zhang, Yoav Peles, John T. Wen, Tao Tong, Je-Young Chang, Ravi Prasher, and Michael K. Jensen. Analysis and active control of pressure-drop flow instabilities in boiling microchannel systems. *International Journal of Heat and Mass Transfer*, 53(11-12):2347–2360, 2010.

[2] Tom Saenen and Martine Baelmans. Numerical model of a two-phase microchannel heat sink electronics cooling system. *International Journal of Thermal Sciences*, 59:214–223, 2012.

[3] Leonardo Carlos Ruspini, Carlos A. Dorao, and M. Fernandino. Two-phase flow instabilities in boiling and condensing systems. *Journal of Power and Energy Systems*, 6(2):302–313, 2012.

[4] A. Mukherjee and Satish G. Kandlikar. Numerical study of the effect of inlet constriction on bubble growth during flow boiling in microchannels. *Proceedings of ICMM2005 3rd International Conference on Microchannels and Minichannels*, 2005.

[5] Herbert Oertel, editor. *Prandtl - Führer durch die Strömungslehre*. 13 edition.

[6] Satish G. Kandlikar, Suresh Garimella, Dongquing Li, Stéphane Colin, and Michael R. King. *Heat Transfer and Fluid Flow in Minichannels and Microchannels*. Elsevier, 1 edition, 2006.

[7] Antonio C. Bannwart. Modeling aspects of oil–water core–annular flows. *Journal of Petroleum Science and Engineering*, 32(2-4):127–143, 2001.

[8] Sung-Min Kim and Issam Mudawar. Universal approach to predicting saturated flow boiling heat transfer in mini/micro-channels – part i. dryout incipience quality. *International Journal of Heat and Mass Transfer*, 64:1226–1238, 2013.

[9] R. I. Issa. Solution of the implicitly discretized fluid flow equation by operator - splitting. *Journal of Computational Physics*, 62:40–65, 1985.

CONTACT

Felix K. Leube, felix.leube@imm.fraunhofer.de

FLOW RATE INDEPENDENT MICROFLUIDIC GRADIENT GENERATOR

S. Höving[1], D. Janasek[1] and P. Novo[1]
[1] Leibniz-Institut für Analytische Wissenschaften - ISAS - e.V., Dortmund, Germany

ABSTRACT

A flow rate independent microfluidic gradient generator is presented. The channel architecture consists of a typical mixing tree and includes herringbone micromixers at each channel branch, which ensure mixing of solutions at high flow rates. Flow rates up to 200 µl/min are demonstrated to generate equal concentration gradients of a fluorophore molecule. Linear and mirrored linear gradients are shown.

KEYWORDS

Flow rate independent, microfluidic gradient generator, linear fluorophore concentration gradient

INTRODUCTION

The use of microfluidic gradient generators (∇G) [1] has greatly enhanced experimental throughputs in diverse fields, such as in biology [2,3], chemistry [4], and biosensors [5]. Thenceforward, several works demonstrated different device configurations and applications. For instance, the generation of linear and other concentration functions have been developed [6]. The use of microfluidics not only offers high control at setting the referred gradients, but it also allows for direct integration with other functions, such as in perfusion systems [7,8]. However, work in the field has been strongly application dependent. Especially, the set of flow rates (and/or diffusion coefficients) used to generate a given concentration gradient are very limited and in the order of nl/min [9] to low µl/min [10]. The development of a flow rate insensitive ∇G is of extreme importance to enable applicability in diverse fields with minimal chip design adaptation challenges. The simple scaling of channel lengths or cross section dimensions is not sufficient to achieve such goal. The reason is that as flow rates increase and diffusion coefficients decrease, a dramatic increase in mixing time is required which would ultimately result in massive microchip footprints and huge pressure drops during operation (see later analysis in the results and discussion section).

Here we present a flow rate independent ∇G that circumvents the above referred limitations by the use of herringbone micromixers [11] at each branch of a mixing tree. The device generates equal gradients independently of flow rate, tested up to 200 µl/min which is a value about two orders of magnitude higher than any work in the literature.

MATERIALS AND METHODS

General Layout

The device architecture is presented in Fig. 1A. It has three inlets (*L*, *M* and *R*) and 33 outlets which are connected to a common chamber (Fig. 1C). Each mixing level adds an exponentially increasing number of channel branches. Each of the branches is a herringbone micromixer. The dimensions of each of the micromixers was designed to ensure full mixing of solutions flowing therein (based on finite element modelling), and to divert flow in such a way that linear gradients are obtained at the outlets of the ∇G. The use of three inlets allows to obtain linear or mirrored linear concentration gradients as it will be presented hereafter.

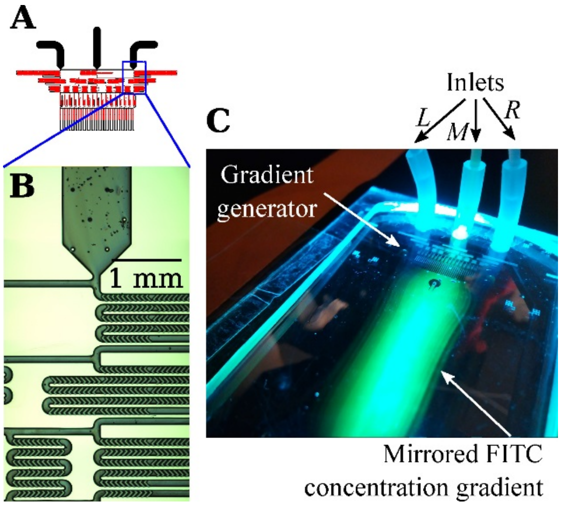

Figure 1. Schematic of the gradient generator architecture. A) Top view of the mixing tree having three inlets and 33 outlets. Each channel branch is a herringbone micromixer. B) Micrograph of the SU8 mold (from the indicated region in A) used for the fabrication of the PDMS devices. C) Photograph of the microfluidic device used in the generation of a mirrored FITC concentration gradient. Related results are presented in fig. 3(Mirrored).

Fabrication

The ∇G device was fabricated out of PDMS via soft-lithography techniques and using a two-level SU8 mold. The first layer (50 µm high) includes the main fluidic network, whereas the second defines asymmetric v-shaped grooves (30 µm high) for the micromixer (Fig. 1B). The SU-8 mold was fabricated on top of a silicon wafer using SU-8 25. The first level was spun at 1100 rpm baked at 95 °C for 10 min. Then, a mask defining the overall fluidic network was aligned using chromium marks, and the SU-8 was exposed for 13 s. Following, the second SU-8 layer was directly spun on top of the previous one at 2200 rpm and baked at 95 °C for 10 min. A second mask, including only the positions for the asymmetric v-shaped structures, was aligned with the existing structures using chromium marks, and the SU-8 was exposed for 13 s. Following, the two layers were baked at 95 °C and then developed in mr-Dev 600 (Microresist, Germany) with manual stirring. PDMS (Elastosil RT 601, Wacker, Germany) chips were prepared by mixing prepolymer to curing agent at a 10:1 ratio and by polymerization at 80 °C on top of the SU-8 molds. Inlets/outlets were created by the use of blunt syringe tips and a custom designed PMMA mold. Microfluidic chips not having the second SU-8 layer were also fabricated to conduct control experiments. The fabrication procedures were similar to those mentioned above simply by skipping the second SU-8 layer fabrication step. The controlled delivery of solutions contained within plastic syringes and connected to the PDMS chip via Teflon tubing was performed using syringe pumps (neMESYS, Cetoni, Germany).

Characterization of concentration gradients

Fluorescent molecules and fluorescence microscopy were used for simplicity of characterization of the concentration gradients generated by the microfluidic device. A XC30 CCD camera coupled to an inverted fluorescence microscope (IX71, Olympus) were used to acquire fluorescence images using the appropriate fluorescence filters as a function of fluorophore of interest (FITC or rhodamine B as presented hereafter).

ImageJ was used to quantify the fluorescence intensity as a function of specific image color channels (green for FITC, red for rhodamine, as it will be shown hereafter) and to conduct image transformations (case of the middle picture of Fig. 2B).

RESULTS AND DISCUSSION

Tests on mixing of difference fluorescent and non-fluorescent solutions are presented in Fig. 2. Fluorescein isothiocyanate (FITC), water and rhodamine B solutions were injected at inlets *L*, *M* and *R*, respectively, and at the relative flow ratios of 15-70-15 (Fig. 2A) and 35-30-35 (Fig. 2B) µl/min, respectively. The red and green image channels in the case of Fig. 2B(inlet M) were merged for easy identification of the mixing of both fluorescent solutions. As it can be observed, especially in the case of the middle micrograph of Fig. 2B, full mixing of the solutions flowing in the respective branch is achieved. This figure also indicates that different gradients can be generated by changing the flow ratios. In this work, we were especially interested in testing the device's performance at generating linear or mirrored linear concentration gradients. For that purpose, only FITC and water solutions were used. In the case of simple linear gradients (Fig. 3 top), FITC was injected at inlet *L* and water at inlet *R* (inlet *M* was not used and kept closed). In the case of mirrored linear gradients (Fig. 3 bottom), FITC was injected at the central inlet *M* and water at the remaining inlets *R* and *L*. The normalized fluorescence intensity results of each of the experiments at each of the ∇G outlets are presented in Fig. 3. The flow rates employed are indicated in the figure and the corresponding results plotted as dots using the same color as that of the legend. As it may be observed, the gradients generated are linear (R^2=0.98), independent of flow rate and reproducible (inter-assay coefficient of variation of 1.1%). The flow rates used (and consequently fluid velocity within the microchannels) are about two orders of magnitude higher than those available in the literature. In order to further stress the novelty of the work and the need for micromixers to ensure flow rate independent gradient generation, we performed control experiments using devices having the same fluidic network but without the v-shaped grooves. The results are plotted as black lines in Fig. 3. As expected, without enhanced mixing, high flow rates lead to non-linear concentration profiles at the exit of the ∇G, because the residence time within each channel branch is not sufficient to ensure full mixing.

In order to ensure full mixing of solutions at each channel branch and consequently linear gradient formation using a device having only simple channels instead of the micromixers, the channels would have to be at least 67 m long (a 95% mixing level was considered as full mixing and the analysis [1] performed for FITC/Rhodamine with $D = 4 \times 10^{-10}$ m^2/s [12]). This length is further increased to several hundreds of meters in the case of other large molecules of extreme biological significance such as signaling molecules (such as EGF [13]) with diffusion coefficients in the order of 10^{-11} m²/s or less. This analysis further confirms the need for accelerated mixing strategies as demonstrated through Figs. 1-3.

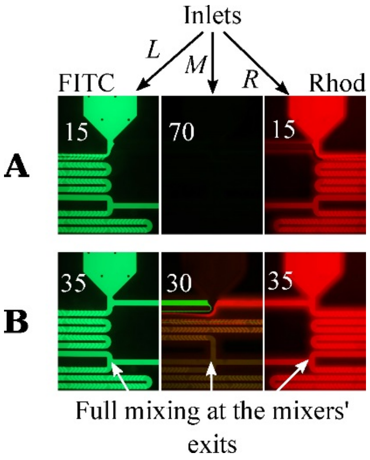

Figure 2. Fluorescence micrographs of the gradient generator at the inlet and first mixing level regions. FITC, water and rhodamine B were injected at inlets L, M and R, respectively, at different relative flow rates (indicated in µl/min on each photo). A) Due to the flow ratio, water streamed into the channel branches immediately after inlets L and R. B) Due to the flow ratio, FITC and rhodamine B streamed into the middle channel branch immediately after inlet M.

CONCLUSIONS

A microfluidic gradient generator consisting of a mixing tree including herringbone micromixers at each channel branch was presented. The fabrication was carried out using a two level SU-8 mold and soft-lithography of PDMS. The micromixers ensured full mixing of the solutions flowing within each channel branch of the mixing tree and the flow was equality distributed across 33 outlets in order to generate linear concentration gradients. The gradients generated were identical at different flow rates tested to values up to 200 µl/min, which is about two orders of magnitude higher than any publication in the literature. In conclusion, this work presented a device of general applicability which may be easily adapted to integrate other microfluidic operations, namely in perfusion-based applications.

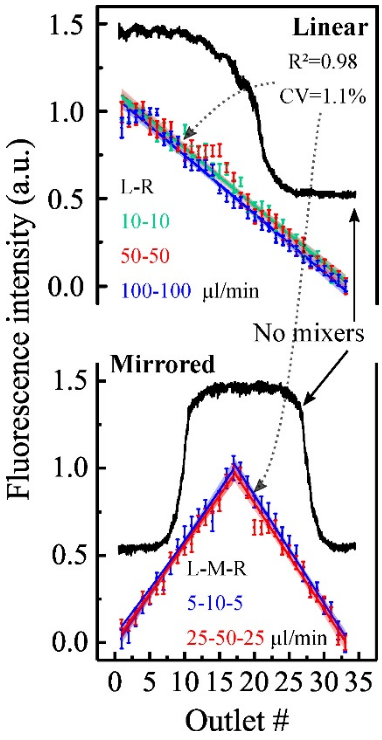

Figure 3. Fluorescence intensity gradients as a function of the ∇G outlets' and flow rates applied. The dots are the fluorescence intensity at the gradient generator outlets. The black lines are the fluorescence intensity profiles at the exit of the ∇G outlets when no enhanced mixing was applied. Linear fits to the data and the 95 % confidence bands are presented.

ACKNOWLEDGMENTS

This study was supported by the Ministerium für Innovation, Wissenschaft und Forschung des Landes Nordrhein-Westfalen, the Regierende Bürgermeister von Berlin - inkl. Wissenschaft und Forschung, and the Bundesministerium für Bildung und Forschung. Pedro Novo also thanks for ISAS strategic funds. ISAS's workshop is gratefully acknowledged.

REFERENCES

[1] N. L. Jeon, S. K. W. Dertinger, D. T. Chiu, I. S. Choi, A. D. Stroock, G. M. Whitesides, "Generation of solution and surface gradients using microfluidic systems", *Langmuir*, 16, pp. 8311–8316, 2000

[2] J. T. S. Fernandes, S. Tenreiro, A. Gameiro, V. Chu, T. F. Outeiro, J. P. Conde, "Modulation of alpha-synuclein toxicity in yeast using a novel microfluidic-based gradient generator", *Lab. Chip*, 14, pp. 3949–3957, 2014

[3] C.-G. Yang, Y.-F. Wu, Z.-R. Xu, J.-H. Wang, "A radial microfluidic concentration gradient generator with high-density channels for cell apoptosis assay", *Lab. Chip*, 11, pp.3305-3312, 2011

[4] C.-G. Yang, Z.-R. Xu, A. P. Lee, J.-H. Wang, "A microfluidic concentration-gradient droplet array generator for the production of multi-color nanoparticles", *Lab. Chip*, 13, pp. 2815–2820, 2013

[5] B. Hong, P. Xue, Y. Wu, J. Bao, Y.J. Chuah, Y. Kang, "A concentration gradient generator on a paper-based microfluidic chip coupled with cell culture microarray for high-throughput drug screening", *Biomed. Microdevices*, 18, pp.1-8, 2016

[6] S. K. W. Dertinger, D. T. Chiu, N. L. Jeon, G. M. Whitesides, "Generation of gradients having complex shapes using microfluidic networks", *Anal. Chem.*, 73, pp. 1240–1246, 2001

[7] D. Choudhury, D. van Noort, C. Iliescu, B. Zheng, K.-L. Poon, S. Korzh, V. Korzh, H. Yu, "Fish and chips: a microfluidic perfusion platform for monitoring zebrafish development", *Lab. Chip*, 12, pp. 892–900, 2012

[8] D. Choudhury, D. van Noort, C. Iliescu, B. Zheng, K.-L. Poon, S. Korzh, V. Korzh, H. Yu, "Fish and chips: a microfluidic perfusion platform for monitoring zebrafish development", *Lab. Chip*, 12, pp.892-900, 2012

[9] D. Irimia, D.A. Geba, M. Toner, "Universal microfluidic gradient generator", *Anal. Chem.*, 78, pp.3472-3477, 2006

[10] J.T.S. Fernandes, S. Tenreiro, A. Gameiro, V. Chu, T.F. Outeiro, J.P. Conde, "Modulation of alpha-synuclein toxicity in yeast using a novel microfluidic-based gradient generator", *Lab. Chip*, 14, pp.3949-3957, 2014

[11] N.-T. Nguyen and Z. Wu, "Micromixers - a review", *J. Micromech. Microeng.*, 15, pp.R1-R16, 2005

[12] P.-O. Gendron, F. Avaltroni, K. J. Wilkinson, "Diffusion Coefficients of Several Rhodamine Derivatives as Determined by Pulsed Field Gradient - Nuclear Magnetic Resonance and Fluorescence Correlation Spectroscopy", *J. Fluoresc.*, 18, pp.1093-1101, 2008

[13] R.G. Thorne, S. Hrabětová, C. Nicholson, "Diffusion of epidermal growth factor in rat brain extracellular space measured by integrative optical imaging", *J. Neurophysiol.*, 92, pp.3471-3481, 2004

CONTACT

* P. Novo, pedro.novo@isas.de

GAS DENSITY AND VISCOSITY MEASUREMENT WITH A MICROCANTILEVER AND DETERMINATION OF WOOBE INDEX, CALORIFIC VALUE AND TOTAL INERT GAS CONTENT OF NATURAL GAS

C. Huber[12]**, P.Reith*[1] *and A. Badarlis*[2]
[1] TrueDyne Sensors AG, Reinach, Switzerland
[2] Endress+Hauser Flowtec AG, Reinach, Switzerland

ABSTRACT

TrueDyne Sensors AG is developing and producing sensors to measure thermophysical properties of liquids and gases from which fluid quality information can be deduced. Principally we are working with MEMS resonators like oscillating micro tubes [1,2] or micro cantilevers [3,4,5] to measure density and viscosity of fluids.

Here we present our latest work on a micro cantilever sensor that is highly sensitive and allows to measure density and viscosity of low pressure gases with accuracies in the range of 1%. Furthermore we show the potential of such a sensor using for online monitoring of combustion gas mixtures. The most popular of these mixtures is natural gas.

KEYWORDS

Density, viscosity, micro cantilever, natural gas, Wobbe index, calorific value, inert gas

INTRODUCTION

Fluid density in process or in a lab is traditionally measured using resonating structures made of stainless steel or glass where the frequency can be associated with density and the quality factor can be used to get information about the viscosity of the fluid. However, accurate measurement of gas density and viscosity in a low pressures range of < 5 bar abs remains a challenge since the sensitivity of the sensing device must be very high. The smaller the oscillating structure the higher the sensitivity to small changes of the surrounding fluid. In this study an atomic force microscopy Si-cantilever is used, shown in Fig.1. It has a length of 310 microns, a width of 110 microns and a thickness between 3 and 5 microns. The eigenfrequency of the first flexural mode is found between 30 to 50 kHz. The quality factor in air is about 200. The density sensitivity of the frequency of this mode is in the order of 250 Hz m^3/kg.

By measuring density, viscosity, temperature and pressure of natural gas, one can deduce the average molar mass M_{NG}, energy (Wobbe index WI and calorific value CV) and composition (total inert gas content) information of the analyzed gas mixture using correlation methods.

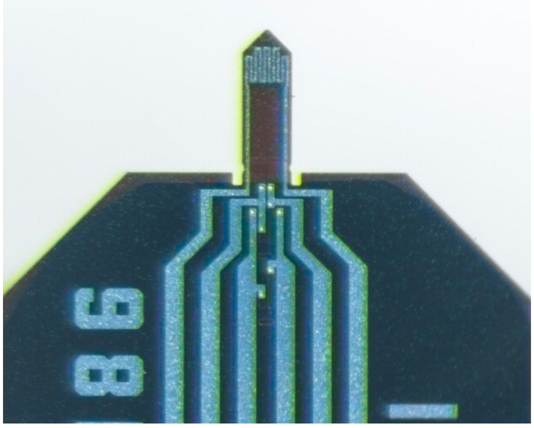

Figure 1: The atomic force microscopy Si-cantilever beam used in this study. The tip has a length of 310 microns, a width of 110 microns and a thickness between 3 to 5 microns.

CANTILEVER PHYSICS

The modeling of the cantilever sensor was based on the model proposed in literature by Sader [6] and Hosaka et al. [7]. In this approach, the sensor is considered as simple harmonic oscillator and the viscous and inertia effects of the gas are modeled with the help of a hydrodynamic function, which can be found in the resonance frequency and in the viscous quality factor.

The fluid-structure interaction effect has an impact on the resonance frequency in the form of resonance frequency shift. This frequency shift can be calculated from Sader's analysis [6]. The parameters b, ρ_b and h represent the width, the density and the thickness of the beam respectively.

$$\omega_0 = \frac{\omega_{0,vac}}{(1+\bar{G}\rho\,\Gamma_r(Re))^{0.5}} \tag{1}$$

$$\bar{G} = \frac{\pi b}{4\rho_b \mathrm{h}} \tag{2}$$

$$Re = \frac{\rho\omega b^2}{4\mu} \tag{3}$$

Due to the complicated form of the hydrodynamic function Γ, a simplified form proposed by Maali et al. [8] was used.

$$\Gamma_r(Re) = a_1 + \frac{a_2}{\sqrt{Re}} \tag{4}$$

Besides, the temperature dependency of the sensor was compensated adapting the Young's modulus of the cantilever beam, which is found in the vacuum resonance frequency ($\omega_{0,vac}$) and is a function of the temperature.

On the other hand, the dominant dissipative mechanism is the fluid interaction and the quality factor that is related to the fluid was modeled using the quality factor equation proposed by Hosaka et al. [7].

$$Q = \frac{\rho_b h b^2 \omega_0}{3\pi b\mu + 0.75\sqrt{2}\pi b^2\sqrt{\rho\mu\omega_0}} \tag{5}$$

Adding calibration parameters to the models, the discrepancy between the model and the real response of the sensor was significantly eliminated. This calibrated model was then used for the extraction of gas density and dynamic viscosity.

The cantilever was calibrated and validated with various gases in a temperature range of 20 to 50°C and a density range between 0.5-2.0kg/m^3. As illustrated in Fig. 2, we achieved accuracies of 1% and 1.5% for density and dynamic viscosity, respectively. This measuring performance is also achieved with combustion gas samples as listed in Table 1.

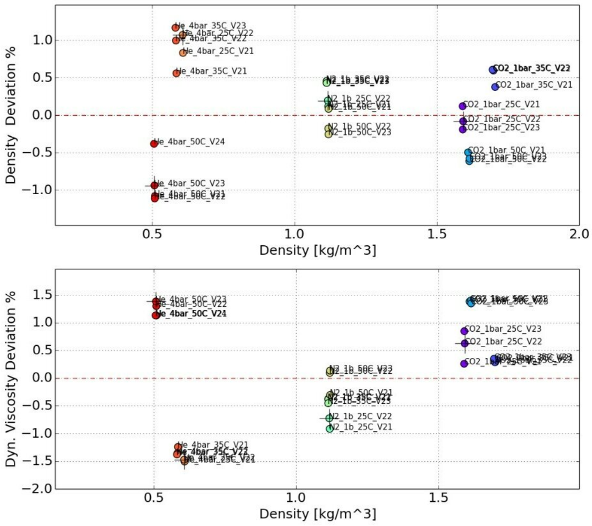

Figure 2. Calibration measurements of micro cantilever with CO_2, N_2 and He at different temperatures and pressures.

COMBUSTION GAS MONITORING

Smart sensors for fast online monitoring of combustion gases become more and more important since gas composition in gas grids is subject to fast changes which can have a big influence on burner or engine performance.

Natural gas is not a binary mixture. It consists of hydrocarbon gases such as methane, ethane, propane, butane, pentane, etc. and inert gases such as nitrogen, carbon dioxide and oxygen. The exact composition varies from one source to another. In Fig.3. typical composition ranges of natural gas are shown.

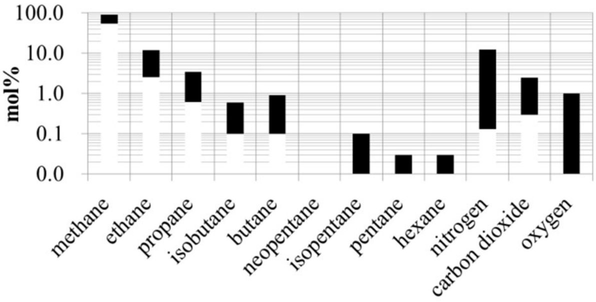

Figure 3. Typical composition ranges of natural gas used for the correlations in this study.

To analyze natural gas the micro cantilever was placed in a gas tight flow cell together with a temperature and a pressure sensor. With this setup we were able to measure density (ρ), dynamic viscosity (μ), temperature (T) and pressure (p) of the gas sample in the cell. These four physical properties were then used as input parameters of correlation models in order to characterize the gas [5].

Physical Properties at STP

First of all the measured physical properties are transformed to standard reference conditions (STP: T_{STP} =0°C, p_{STP} = 1.01325 bar) using expressions in the form of equations 6 to 8, respectively were M_{NG} the average molar mass , SG_{STP} the specific gravity and μ_{STP} is the dynamic viscosity of the measured gas sample at STP–conditions.

$$M_{NG} = \sum_{i=0}^{n} b_i \cdot \mu^{\beta 1_i} \cdot p^{\beta 2_i} \cdot T^{\beta 3_i} \tag{6}$$

$$SG_{STP} = \frac{M_{NG}}{M_{Air}} \tag{7}$$

$$\mu_{STP} = \sum_{i=0}^{n} c_i \cdot \mu^{\gamma 1_i} \cdot p^{\gamma 2_i} \cdot T^{\gamma 3_i} \tag{8}$$

Energy Information

Thereafter, energy information can be deduced. As shown in Fig.4. the dynamic viscosity of natural gas at reference conditions can be nicely correlated with the Wobbe index. The accuracy of this correlation is in the order of 2% (2σ) for a gas samples matching the composition ranges of Fig.3.

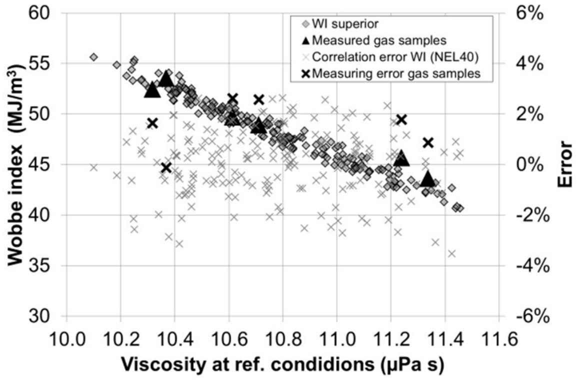

Figure 4. Correlation of Wobbe index with the dynamic viscosity at standard reference conditions of natural gas and corresponding correlation error. Black triangles are measured gas samples from Table 1.

Knowing the Wobbe index and the average molar mass of the gas sample the calorific value can be derived easily according to equation 1 with a similar accuracy.

$$WI = \frac{CV}{\sqrt{SG_{STP}}} = \frac{CV}{\sqrt{M_{NG}/M_{Air}}} \qquad (8)$$

Composition Information

Additionally, we found a way to determine the total inert gas content (the sum of CO_2, N_2 and O_2) in the natural gas sample. The correlation input is given in equation 9. It is basically the ratio of a potential calorific value (assuming only hydrocarbons like methane, ethane, propane, butane etc. are present and therefore the calorific value is directly proportional to the molar mass) and the real calorific value of the sample gas mixture deduced from the correlation with viscosity described above.

$$Corr.input = \frac{d_0 + d_1 \cdot M_{NG}}{CV} - 1 \qquad (9)$$

In Fig.5. the found correlation of the total inert gas content with is shown. This correlation is valid for total inert gas contents of up to 30%. The accuracy is in the order of 2 mol% (2σ).

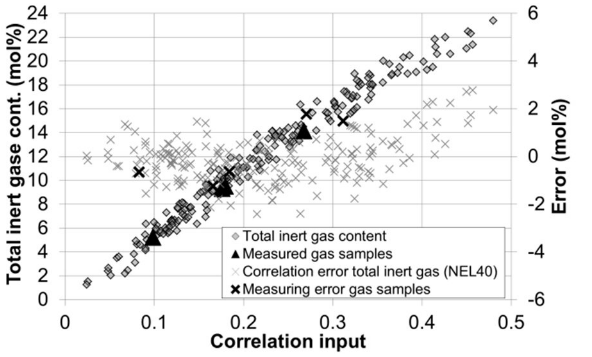

Figure 5. Correlation of the total inert gas content of natural gas and corresponding correlation error. Black triangles are measured gas samples from Table 1.

Hydrogen Content

So far we focused on pure natural gas mixture according to Fig.1. containing inert gases but no hydrogen. However, hydrogen contents of up to 10% will become more and more usual in European gas grids due to hydrogen injection of power to gas plants. Unfortunately hydrogen behaves differently than hydrocarbons and with the two parameters molar mass and dynamic viscosity a detailed and accurate characterization of the combustion gas mixture is not possible anymore.

Therefore, we extended the measuring setup with a thermal conductivity sensor [9]. The sensor chip is placed in the same fluidic cell as the other sensors. The thermal conductivity of hydrogen enriched natural gas nicely correlates with its hydrogen content as shown in Fig..6. allowing to compensate the effects of hydrogen.

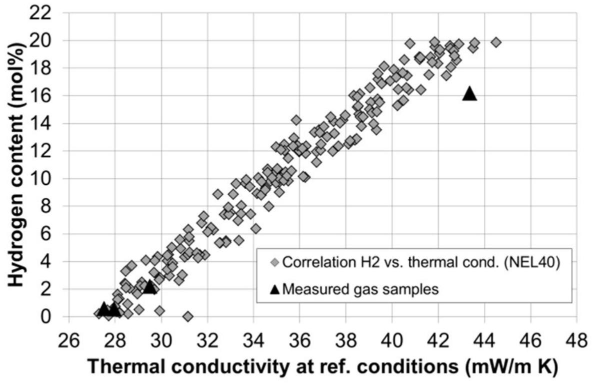

Figure 6. Correlation of the hydrogen content with the thermal conductivity at standard reference conditions of hydrogen enriched natural gas. Black triangles are measured gas samples from Table 1.

Table 1. Validation of the new sensor concept. 6 reference combustion gas samples measured at atmospheric pressure. Notation: measurements results (meas), derived energy and composition information based on correlation methods (corr), reference values (ref), relative errors of reading versus reference (re). Note that these errors include measurement and correlation uncertainties.

Sample	Temp	Density	Molar mass		Viscosity		Th. cond.	Wobbe index		Inert gas cont.		H_2 cont.
	meas /°C	meas /kg/m^3	corr /g/mol	re /%	meas /µPa s	re /%	meas /mW/m K	corr /MJ/m^3	re /%	ref /mol%	re /%	ref /mol%
1	24.50	0.6506	16.04	0.0	11.19	0.1	31.17	53.5	-0.1	0.0	-0.9	0.0
2	24.10	0.7297	17.96	0.7	12.10	-0.8	30.13	43.6	0.8	15.0	-0.7	0.0
3	24.23	0.7920	19.58	0.0	11.13	0.2	28.04	52.4	1.7	5.0	0.1	0.0
4	24.17	0.8201	20.24	0.6	11.37	-0.4	27.75	49.7	2.7	10.0	-0.7	0.0
5	24.34	0.7831	19.36	0.2	11.50	-0.3	30.19	48.9	2.6	10.0	-0.8	3.0
6	24.20	0.5821	14.40	0.1	12.04	-0.4	46.82	45.7	1.7	10.0	-2.0	20.3

CONCLUSIONS AND OUTLOOK

Using technology which is readily available and applying the corresponding physical models, we presented a sensor concept for measuring properties of natural gas, such as density and viscosity. Based on a MEMS cantilever which for example, can be found in an atomic force microscope we obtain the density and the viscosity from its resonance frequency and the quality factor. In a physical model which is based on correlations, quantities like the calorific value, the content of inert gas and the Wobbe index can be determined. Additionally, taking into account the thermal conductivity, the hydrogen content of the natural gas was measured. We have shown accuracies 1% on the gas density measurement, 1.5% on the viscosity measurement, leading to a 2 to 3% accuracy on the further processed values like Wobbe index, calorific value or inert gas content.

Currently we are working on a demonstrator unit in order to perform tests of the cantilever sensor in field applications. A CAD-drawing of the lid is shown in Fig.7. All electronics and the sensor unit inside a gas cell is placed inside a 3d-printed enclosure. Controlled is the demonstrator with a touchscreen in the lid.

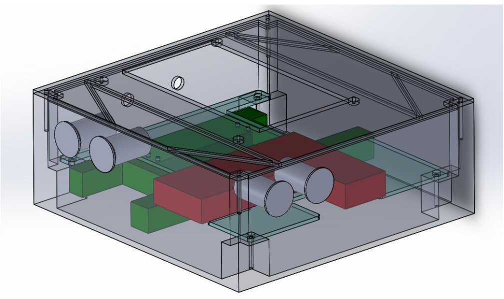

Figure 7. CAD-Drawing of future demonstrator. All electronics and the sensor unit is placed inside a 3d-printed enclosure. The unit is controlled via touchscreen which is located in the lid.

REFERENCES

[1] C. Huber, “MEMS-based Micro-Coriolis Density and Flow Measurement Technology”, tm-Technisches Messen, 83(3), 157-162, 2016

[2] C. Huber, “Density and Concentration Measure-ment Applications for Novel MEMS-based Micro Densitometer for Gas”, 18.GMA/ITG-Fachtagung Sensoren und Messsysteme, 2016

[3] A. Badarlis, A. Pfau, A. Kalfas, “Gas Density and Viscosity Measurement Using Micro-Cantilerver Sensor”, AMA Conference, 2015

[4] A. Badarlis, A. Pfau, A. Kalfas, “Measurement and Evaluation of the Gas Density and Viscosity of Pure Gases and Mixtures Using a Micro-Cantilever Beam”, Sensors, 15(9), 24318-24342, 2015

[5] C. Huber, A. Badarlis, “A method for determining properties of a hydrocarbon-containing gas mixture and device for the same”, DE102015117468, 2015

[6] J. E: Sader. "Frequency response of cantilever beams immersed in viscous fluids with applications to the atomic force microscope." Journal of applied physics 84.1 (1998): 64-76

[7] H. Hosaka, S, Kuroda. "Damping characteristics of beam-shaped-micro-oscillators." Sensors and Actuators A: Physical 49.1-2 (1995): 87-95.

[8] A. Maali, et al. "Hydrodynamics of oscillating atomic force microscopy cantilevers in viscous fluids." Journal of Applied Physics 97.7 (2005): 074907.

[9] Xensor Intergration bv, Thermal Conductivity Sensor XEN-TCG3880, www.xensor.nl

CONTACT

* C. Huber, christof.huber@truedyne.com

INLINE SIZING OF NANO PARTICLES USING ULTRASOUND

G.J.A. van Groenestijn[1], *A.W.F. Volker*[1], *N.M.M. Meulendijks*[2], *P.L.M.J. van Neer*[1], *G.L.G. Pierre*[3], *C. Julien*[3]
[1] TNO, The Hague, The Netherlands, [2] TNO, Eindhoven, The Netherlands, [3] Sonaxis, Besançon, France

ABSTRACT

The growth of Silica particles during a Stöber reaction is followed online using an ultrasound nanoparticle sizer. In the Stöber reaction and in validation measurements on standardized nanoparticles Silica particles in the 100 nm and 700 nm mean-diameter range and mass concentrations of 0.02 % till 2 % are measured.

KEYWORDS

particle sizing, nanoparticle sizing, ultrasound spectroscopy, transmission spectroscopy, Stöber reaction, silica particle.

INTRODUCTION

Today, nanoparticles and nanodroplets can be found in a variety of products, such as coatings, paints, medicines, etc. To optimize the production of nanoparticles and nanodroplets in-line quantitative measurements of their size, density, and concentration are needed. Ultrasound methods are a logic choice for particle and droplet sizing; they are non-destructive, non-invasive, fast, relatively cheap, and can measure high particle-concentrations and opaque dispersions. We have built an ultrasound nanoparticle sizer (UNPS) [1], shown in Figure 1, and are reporting in this abstract on its validation test on standardized particles and an online measurement of Silica (SiO_2) particle growth during a Stöber reaction.

THEORY AND METHOD

The speed and attenuation of ultrasonic waves are altered by the presence of nanoparticles in a dispersion. The alteration depends, amongst others, on the particle size, density, and the concentration of the nanoparticles. This dependency is used in the measurement method.

Figure 1: The UNPS probe with a diameter of 18 mm.

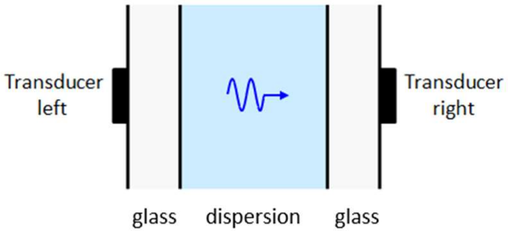

Figure 2: Sketch of the basics of the method to measure the speed of sound and attenuation of ultrasonic waves in a dispersion.

Figure 2 shows the basics of the UNPS. The left transducer sends an ultrasonic wave through a glass wall, the dispersion, and another glass wall, to the right transducer that records the wave. From the recording the speed and attenuation of the wave are determined as a function of frequency (see the blue circles in Figure 3). Using the known values of the speed and attenuation of the ultrasonic wave in the dispersing medium, the frequency dependent change in speed and attenuation can be obtained. An inversion algorithm fits these changes in speed and attenuation (see the red stars in Figure 3) by estimating the mean particle-size, particle density, and concentration of the particles that caused them.

RESULTS

The UNPS system and its algorithm were first validated by static measurements using two samples of standardized Silica nanoparticles in water; Nist490 and Nist730. The specifications of the samples are given in table 1. The UNPS probe has been placed both in a measuring cup filled with an undiluted Nist490 dispersion and in a measuring cup filled with an undiluted Nist730 dispersion. The results of the measurements can be seen in Table 1.

Table 1. UNPS calibration on two samples of standardized Silica nanoparticles in water; specified versus measured values.

	Nist490		Nist730	
	Specific.	Meas.	Specific.	Meas.
diameter (nm)	490 ± 20	462	730 ± 20	708
density (kg/m^3)	1830	1852	1980	1979
mass volume	2%	1.95%	2%	1.90%

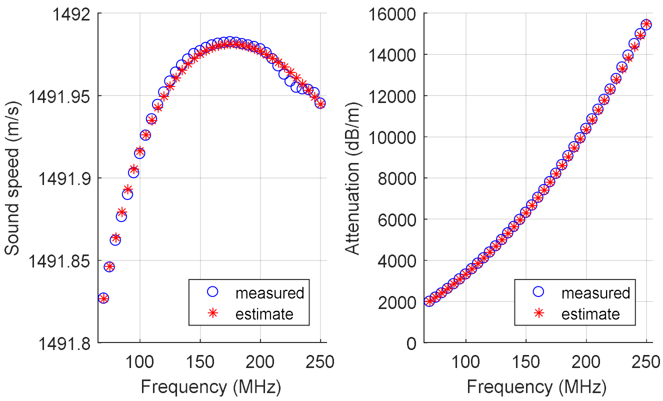

Figure 3: Measured speed of sound (left) and attenuation (right) *for the Nist490 dispersion.*

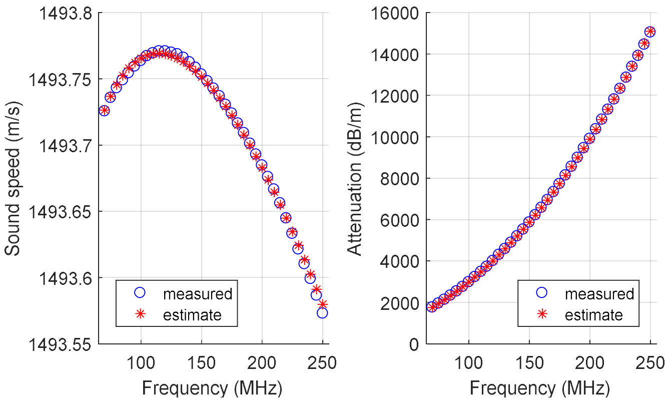

Figure 4: Measured speed of sound (left) and attenuation (right) *for the Nist730 dispersion.*

Comparing the specifications and the measured values, it is concluded that all values are within a 6 % error margin. It might be interesting to note that, Figure 3 and Figure 4 show the measured and estimated speed of sound and attenuation for a Nist490 sample and Nist730 sample, respectively.

Next, the UNPS is used to follow the growth of Silica particles in a Stöber reaction [2] for 60 minutes, performing a measurement every minute. Figure 5 shows the measured relative speed of sound (that is the speed of each frequency minus the average speed over all frequencies), and Figure 8 shows the measured attenuation in the dispersion. The changes in the relative speed of sound are a consequence of the particles growing in size (blue line in Figure 6) and mass concentration (Figure 9). Comparing Figure 5 till Figure 9 show that the changes in speed follow the changes in particle growth and mass concentration; a rapid change occurs in the first twenty minutes of the reaction, followed by a more gentle change in the next forty minutes. Figures 7, 10, and 11 show the measured speed of sound and attenuation, and their estimated fit at three selected times during the reaction.

The red line in Figure 6 shows the measured particle diameters by a DLS [3], an optical device that was also present during the Stöber reaction. Unfortunately, the DLS reports a hydrodynamic diameter that cannot be compared one on one with the diameter reported by the UNPS. However, both show the same behavior in particle growth. After the UNPS measurement was finished, the dispersion was left overnight in the reaction vessel. The next day the particles were dried and a scanning electron microscope picture was made (Figure 12). The mean diameter of the particles in the scanning electron microscope picture is around 264 nm.

CONCLUSION AND DISCUSSION

The validation measurements on standardized nanoparticles and inline measurements on a Stöber reaction have shown that the UNPS can measure Silica particles in the 100 nm and 700 nm mean-diameter range and mass concentrations of 0.02 % till 2 %. It is good to note that these ranges are not the limits of the UNPS. We are working on determining these limits and have already measured smaller and larger particles, and higher concentrations.

We learned that the success of the method relies for an important part on the substances in the dispersions;
- Some solvents can have a very high absorption that reduces the bandwidth at the high frequency side (note for example, that the frequency range used in Figures 3 and 4 where water was the solvent is larger than the more attenuative ethanol solvent in Figures 7, 10, and 11).
- In order to measure particles in reactions that (temporarily) consists of more substances, other than particles and solvent, the algorithm needs to be extended to incorporate this substance as well.

Currently, the UNPS has been applied to solid particles in liquids. We are interested in applying the UNPS to gas/liquid droplets in liquid as well, using existing theory (e.g. [4,5]) this should be feasible.

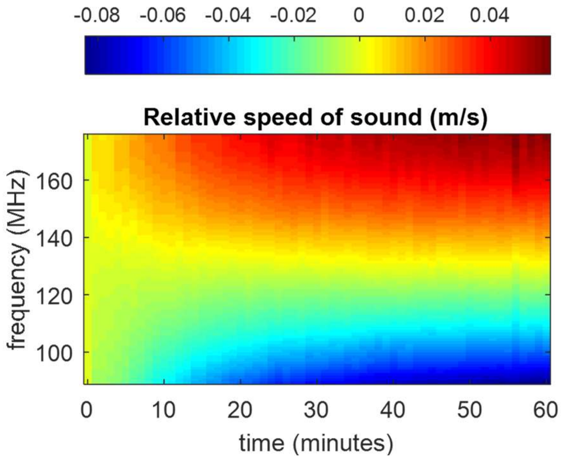

Figure 5: Relative speed of sound in the Silica dispersion measured by the UNPS during the Stöber reaction.

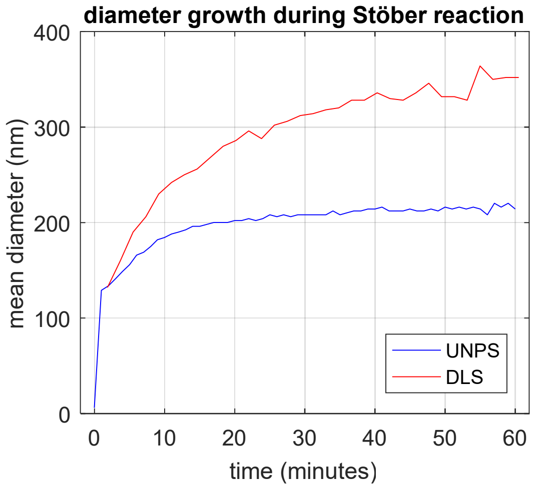

Figure 6: The mean diameter of the Silica particles measured by the UNPS (blue) and DLS (red) during the Stöber reaction.

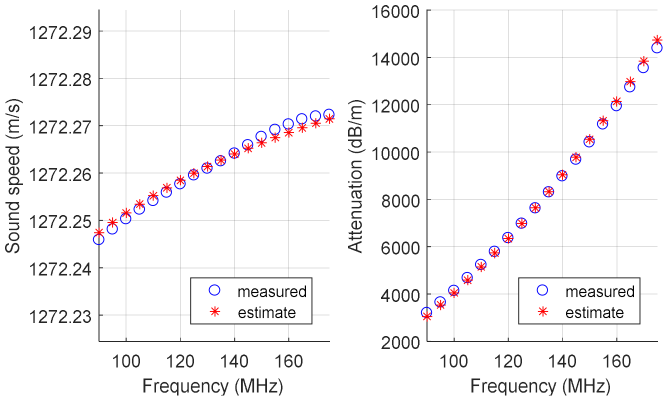

Figure 7: Measured speed of sound (left) and attenuation (right), 10 minutes after the start of the Stöber reaction.

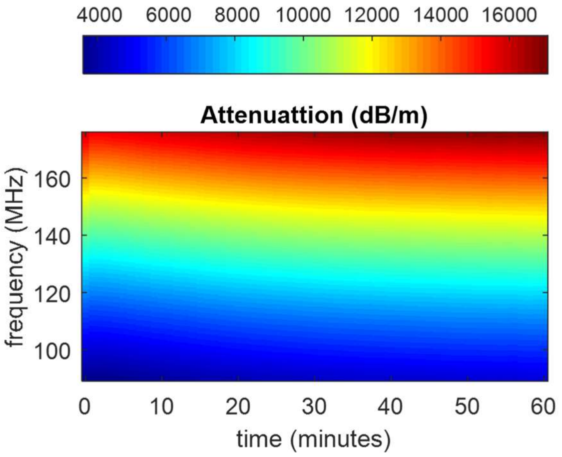

Figure 8: Attenuation in the Silica dispersion measured by the UNPS during the Stöber reaction.

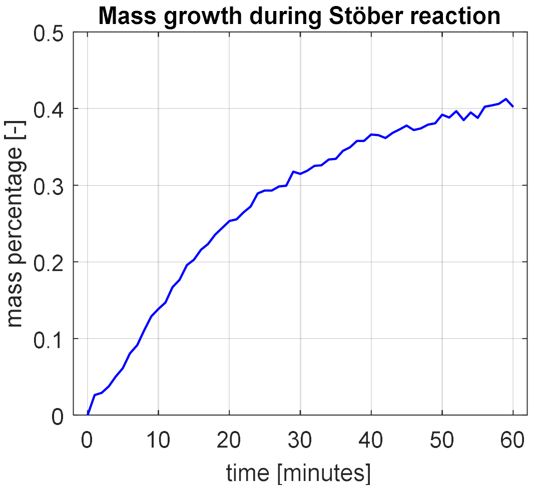

Figure 9: The mass percentage of the Silica particles measured by the UNPS during the Stöber reaction.

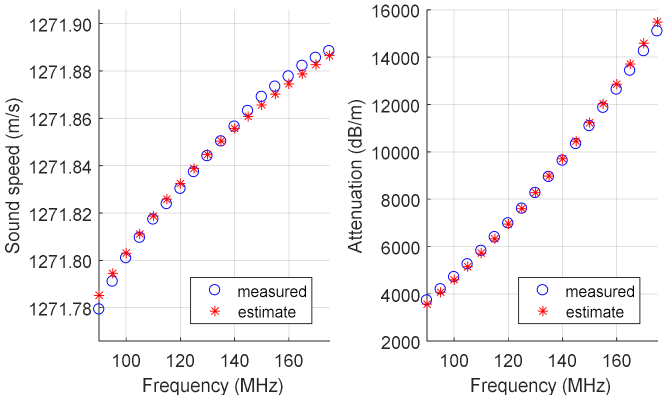

Figure 10: Measured speed of sound (left) and attenuation (right), 30 minutes after the start of the Stöber reaction.

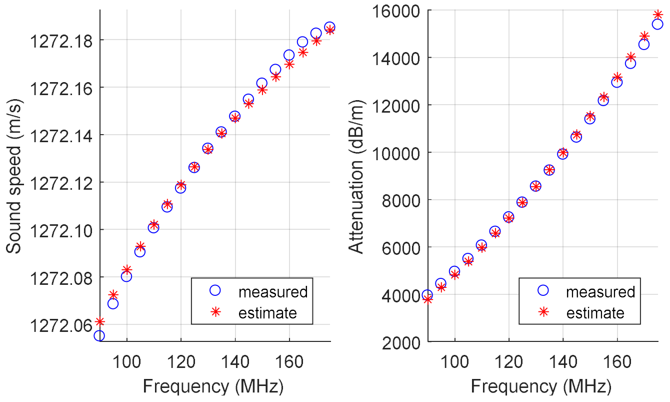

Figure 11: Measured speed of sound (left) and attenuation (right) Measured speed of sound (left) and attenuation (right), 50 minutes after the start of the Stöber reaction.

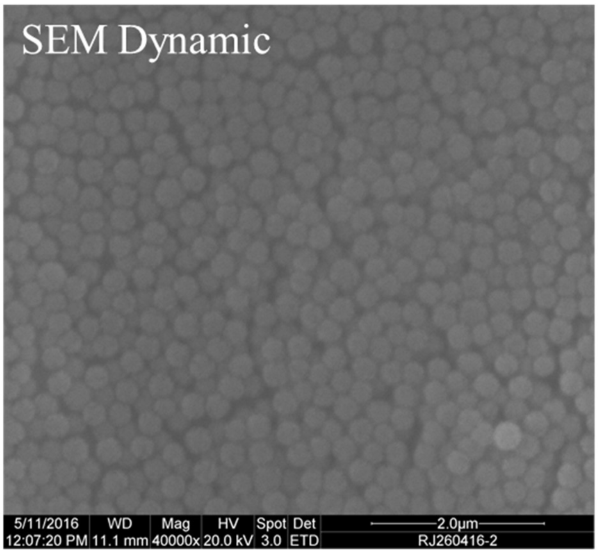

Figure 12. A scanning electron microscope picture of the silica particles created in the Stöber reaction.

REFERENCES

[1] van Neer, P.L.M.J., Volker, A.W.F., Pierre, G.L.G., Bouvet, F.L.D.M., Crozat, S. "Ultrasound transmission spectroscopy: In-line sizing of nanoparticles," 2014 IEEE International Ultrasonics Symposium, Chicago, IL, 2014, pp. 2454-2457. doi: 10.1109/ULTSYM.2014.0612

[2] Stöber, W., Fink, A., Bohn, E. 1968. "Controlled growth of monodisperse silica spheres in the micron size range". Journal of Colloid and Interface Science. 26 (1): 62–69. doi:10.1016/0021-9797(68)90272-5.

[3] Berne, B.J., Pecora, R. 2000. “Dynamic Light Scattering: With Applications to Chemistry, Biology, and Physics”, Mineola.

[4] Epstein, P. S., Carhart, R. R. 1953. "The absorption of sound in suspensions and emulsions. I. Water fog in air", The Journal of the Acoustical Society of America 25(3), 553-565.

[5] Allegra J. R., Hawley, S. A. 1972. "Attenuation of sound in suspensions and emulsions: theory and experiments", The Journal of the Acoustical Society of America 51(5), 1545-1564.

A NEW TYPE OF REACTOR SYSTEM: AEROGEL-BASED OPTOFLUIDIC MICROREACTOR WITH INTEGRATED OPTOFLUIDIC WAVEGUIDES

Yaprak Özbakır[1,2]*, Alexandr Jonáš*[3]*, Alper Kiraz*[2,4]*, Can Erkey*[1]
[1] Department of Chemical and Biological Engineering, Koc University, Istanbul, Turkey
[2] Department of Physics, Koc University, Istanbul, Turkey
[3] Institute of Scientific Instruments of the ASCR, v.v.i., Academy of Sciences of the Czech Republic, Královopolská, Brno, Czech Republic
[4] Department of Electrical and Electronics Engineering, Koc University, Istanbul, Turkey

ABSTRACT

A new type of aerogel-based optofluidic microreactor which we termed “Aerogel Optofluidic Microreactor with Waveguide (AOMW)” which consists of a single channel inside a monolithic aerogel block for photochemical reactions with light delivered to the reaction medium by optical waveguides based on TIR was demonstrated. Aerogel-based optofluidic waveguides were constructed by opening channels in silica aerogel blocks followed by hydrophobic surface treatment. Three different techniques were developed to fabricate channels in silica aerogels. Photochemical reactions of an organic model compound in fabricated channels in such a reactor were carried out and demonstrated for the first time.

KEYWORDS

Optofluidics, Optofluidic Waveguides, Optofluidic Microreactors, Porous Nanomaterials, Aerogels, Photochemistry, Photocatalyst.

INTRODUCTION

Accomplishment of uniform distribution of light through in photoreactors through reaction medium maintaining good interaction of light and fluid is important. An alternative way to deliver light to an optufluidic microreactor to address disproportionate light propagation through the reaction medium may be using optofluidic waveguides which enable distinctively guiding of light through its fluidic channels. In this approach, a suitable material confines core liquid within internal channels and, simultaneously, behaves like waveguide cladding. Here, we demonstrate a new type of chemical micro-photoreactor formed by a liquid-core optofluidic waveguide fabricated inside an aerogel monolith. Due to total internal reflection of light (TIR) at the interface between the aqueous waveguide core and the aerogel-based cladding, light can be carried in a controlled manner over extended distances in confined geometries. We demonstrate monolithic integration of microfluidics and waveguides to facilitate photochemical reactions of an organic model compound based on total internal reflection in the interface of the aerogel and the core liquid in the channel for the first time. For the propagation of non-lossy optical modes guided in the liquid by TIR from the channel walls, the cladding material should have a low absorption coefficient at working light wavelength and a lower refractive index than that of the core liquid ($n_{core}>n_{cladding}$) [1, 2]. In applications involving aqueous solutions, the refractive index of the core liquid is around 1.33 (refractive index of water). However, a limited choice of solid host materials with an index of refraction below that of water is available; thus it is a challenge to find a cladding material with a refractive index much lower than 1.33 to maintain a reasonable numerical aperture (NA). Most of the polymers, including those that are utilized in lab-on-a-chip devices such as PDMS, have higher refractive indices than water; thus, light cannot be confined and delivered by TIR in channels fabricated from these polymers.

Aerogels are nanostructured materials with an internal solid structure consisting of crosslinked polymers with a large number of air-filled pores between the solid polymeric chains. Because of their very high porosity, they are sometimes termed “solid air” and have refractive indices close to that of air. Aerogels are highly porous nanostructured materials with unique properties such as extremely low refractive index, high surface area to volume ratio, and high optical transparency [2, 3]. These properties, particularly the low refractive index of ~1.05, make aerogels a remarkable solid-cladding material without any additional coating since almost all liquids have refractive indices exceeding that of aerogel [2, 4].

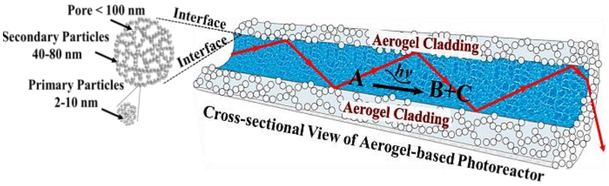

Figure 1: *Cross-sectional view of aerogel-based photoreactor*

Aerogel-based optofluidic waveguides are constructed by opening microchannels inside monolithic aerogel blocks. Following surface treatment, the microchannels are filled with a suitable liquid that serves as the waveguide core liquid. There is actually no restriction on the type of liquid and the type of aerogel that can be used, as long as the liquid can be confined inside the aerogel block without penetrating the aerogel network. As shown in Figure. 1.a microchannel in a silica aerogel is surrounded by a wall that is made up of interconnected secondary particles that are around 40 to 80 nm in size, with pockets of air in between them that constitute pores with sizes less than 100 nm. The secondary particles are formed from the primary particles, which are 2 to 10 nm in size. The air in the aerogel pockets is responsible for guiding light by total internal reflection (TIR) in the liquid-filled channel.

We present a new, straightforward technique that uses direct manual drilling to manufacture TIR-based liquid-core optofluidic waveguides in aerogel monoliths. This method is capable of producing channels with lengths significantly larger than those reported previously in the literature and it also provides relative flexibility in the channel shaping. To illustrate the potential of our technique, we demonstrate that both a straight channel and an L-shaped channel with the total length up to ~7.5 cm could be created. The resulting aerogel-based optofluidic waveguides exhibited efficient light guiding features, as verified by direct imaging of guided light modes and measuring the transmittance of the waveguides. The light is delivered to the liquid reaction medium inside the microchannel by an optical waveguide based on TIR to initiate the reaction, as shown schematically in Figure. 2. We show that our photoreactor is well suited for photochemical degradation of a model organic compound – methylene blue (MB) dye – and we characterize the efficiency of dye photoconversion as a function of the incident light intensity.

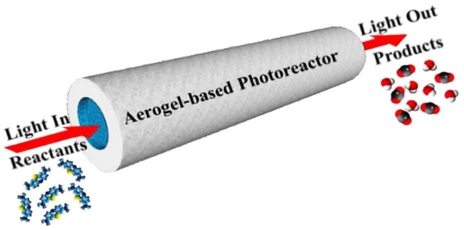

Figure 2: *Aerogel-based photoreactor*

MATERIALS AND METHODS

Preparation of Silica Aerogel Monoliths

Silica aerogels were synthesized using a conventional two step sol–gel process and aged in TEOS-containing aging solutions as shown in Figure. 2. TEOS (98% purity; AlfaAesar) was used as the silica precursor, hydrochloric acid (HCl) (37% purity; Riedel-de Haen) as the acid catalyst, and ammonium hydroxide (NH_4OH) (2.0 M in ethanol; Aldrich) as the base catalyst. TEOS, ethanol (99.9% purity; Merck), and water with a mass ratio of 1:0.89:0.26 were mixed together. After the addition of the acid catalyst, the solution was continuously stirred at room temperature for 60 min and transformed to a sol. Subsequently, the base catalyst was added to the sol to increase the rate of silanol condensation leading to gel formation. Before gelation, the solution was transferred into a polymethylmethacrylate (plexiglass) rectangular mold (height = 7 cm, length = 5 cm, width = 1.3 cm) or a cylindrical plastic mold with varying dimensions (diameter = 2.45 cm, height = 5 cm or diameter = 1.2 cm, height = 10 cm) tightly sealed to prevent evaporation of the solvent. After the gelation, the resulting alcogels were soaked in an aging solution (40 v/v % TEOS, 10 v/v % water, 50 v/v % ethanol) at 50 ºC in an oven for 24 h. The samples were further kept in TEOS aging solution at room temperature for varying times ranging from one day to seven days to obtain aerogels with different densities. The alcogels were then washed in fresh ethanol for 3 days to remove any impurities and water remaining in the pores of the alcogels. Finally, the alcogels were dried at 40 ºC and 100 bar with supercritical CO_2 ($scCO_2$) in Applied Separations Speed SFE unit for 6 h.

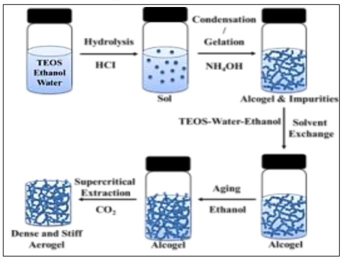

Figure 3: *Preparation of monolithic silica aerogels by aging silica alcogels in TEOS solution*

Surface Modification of Aerogels

Synthesized silica aerogel monoliths were treated with hexamethyldisilazane (HMDS) vapor in a tightly sealed beaker with a volume of 200 ml to render their surfaces hydrophobic and thus to confine within the channel fabricated in the aerogel without penetrating into the porous network of the aerogel. A stainless-steel screen was put in the middle of the beaker where liquid HMDS was placed to prevent contact between the aerogel and liquid HMDS. The beaker was then sealed and heated to 110 °C at ambient pressure. The aerogels were exposed to HMDS vapor for around 3 h. After reaction of surface silanol groups with HMDS vapor, hydrophobicity of the resulting silica aerogel monoliths was determined by measuring water contact angle on the aerogel surface.

Channel Formation in Aerogel Monoliths

Aerogel-based optofluidic waveguides were successfully constructed by opening channels in synthesized monolithic silica aerogel blocks followed by hydrophpobic surface tretatement as demonstrated before in our recent publication as shown in Figure. 4 [3-6]. In this study, three different techniques were developed to fabricate channels in silica aerogels. The first one allows formation of precise channels in monolithic silica aerogels by ablation with femtosecond laser pulses. Using fast scanning of the focused laser ablation beam synchronized with the motion of the aerogel sample, high-quality straight microchannels with controlled cross-sections (~500μm) inside monolithic aerogels were created. The second technique is based on extraction of CO_2 soluble fibers from alcogels in the supercritical drying step. We could create U-shaped channels with diameters around 1 mm using fibers made out of POSS. The third one is drilling of aerogels which required fabrication of aerogels which are mechanically stronger than conventional silica aerogels.

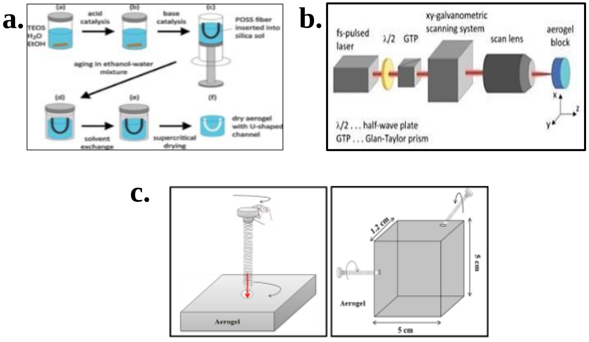

***Figure 4:** Microchannel formation in hydrophobic aerogel monoliths (**a.** scCO$_2$-soluble polymer channel preforms for U-shaped channels, **b.** femtosecond laser ablation **c.** drilling*

Experimental Setup for Photochemical Reactions

Figure. 5 shows a schematic diagram of the experimental setup that was employed for studying model photochemical reaction - degradation of MB in an aqueous solution contained inside the fabricated microchannel in the hydrophobic silica aerogel. The hydrophobic aerogel block with the inclined L–shaped channel was mounted on an adjustable metal holder and it was connected to a Union Tee adapter. Central port of the Union Tee was then connected to a syringe and the remaining end of the Union Tee was used to insert a solarization-resistant multimode optical fiber. This fiber served for delivering photoactivation light to the reaction volume and its end was held at a fixed position at the channel entrance. The channel was filled with the aqueous MB solution using the syringe. The MB solution could be confined within the channel without penetrating into its porous network due to hydrophobic walls of the channel. In order to initiate light-induced degradation of MB, we used a laser beam from a femtosecond-pulsed, tunable laser light source (Coherent Chameleon) with a maximal output power of 4 W. The laser beam was coupled into the free end of the multimode optical fiber with the aid of an objective lens. The operating wavelength of the laser was tuned to 388 nm corresponding to the wavelength of maximal MB absorption. The input power coupled into the optofluidic waveguide could be adjusted from the laser source. The intensity of light transmitted through the waveguide was visually monitored and measured at the outlet of the channel by a laser power meter. In order to monitor the progress of photodegradation of MB, samples with a volume of 10 μL were collected at various times from the end of the channel by a micropipette and subsequently analyzed by Nanodrop ND-1000 Spectrophotometer for absorbance-based quantification of MB concentration. Light-guiding experiments with aerogel-based optofluidic waveguides were also performed using the same experimental set-up shown in Figure. 5. The channel fabricated within the aerogel monolith was first filled by water and illuminated by laser light at 488 nm coupled into the horizontal channel through the optical fiber. The light power at channel input and output was measured.

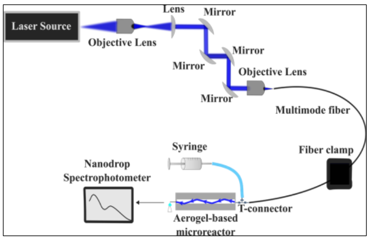

***Figure 5:** Schematics of experimental set-up used in characterization of light guiding and photochemical reactions in aerogel-based optofluidic microreactors*

RESULTS AND DISCUSSION

The refractive indices (n) of the aerogels were measured and were found to linearly increase with increasing density (ρ). The following relationship: $n = 1+\alpha\rho$, where α (~0.27 cm^3/g) is the wavelength-dependent constant was obtained. The synthesized samples retained their low refractive index (below ~1.09) and hence they could serve as suitable optical cladding materials for aqueous waveguide cores. Silica aerogel samples also had low absorption coefficients (~0.7) and high porosities (~ 85 %). Long channels (~7.5 cm) as straight and inclined L-shaped channels could be fabricated. Water-filled optofluidic waveguides in synthesized aerogels yielded high numerical aperture values (~ 0.8). Efficient guiding of light by total internal reflection in the water-filled channel in aerogels was visually revealed and characterized by monitoring power at channel output. The characterization of transmission indicated that propagation losses were lower than 2 dB cm^{-1}, demonstrating that liquid-core waveguides with drilled aerogel represent an attractive alternative in applications targeting controlled light routing along arbitrary paths (Figure. 6).

Table 1: *Properties of HMDS-treated aerogel samples with various density*

Sample	*Density (g/cm^3)*	*Porosity (%)*	*Measured Refractive Index*	*Critical Angle (°)*	*Absorption Coefficient (cm^{-1}) at 488 nm*
1	0.15	93	1.023±0.004	77.7±1.1	0.52
2	0.22	90	1.060±0.007	70.7±1.0	0.69
3	0.39	82	1.093±0.001	66.2±0.1	0.87

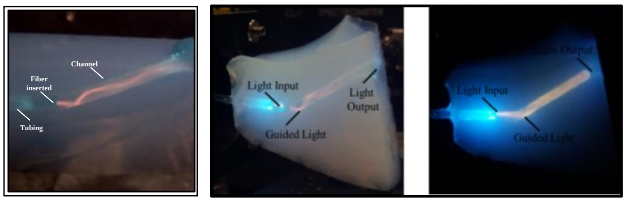

Figure 6: *Total internal reflection in the water-filled channel in monolithic aerogels.*

Photochemical reactions were then performed in dye solution-filled channels. In order to initiate the reaction, the light is delivered to the liquid reaction medium inside the microchannel by an optical waveguide based on TIR, as shown schematically in Fig. 1.a-b. We show that our photoreactor is well suited for photochemical degradation of a model organic compound –methylene blue dye– and we characterized the efficiency of dye photoconversion as a function of the incident light intensity (Figure. 7).

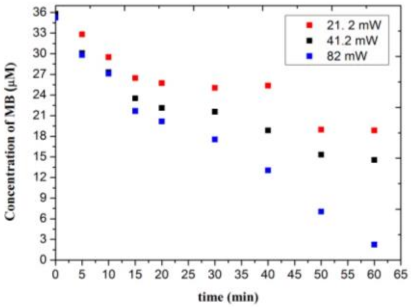

Figure 7: *Time variation of the concentration of aqueous MB solution in an aerogel channel under illumination at 388 nm with varying power of the incident light. The initial concentration of MB was 36 µM.*

CONCLUSIONS

We demonstrated a novel type of chemical photoreactor with integrated optofluidic waveguide which is formed by a liquid-filled channel fabricated in a monolithic aerogel block. The unique optical properties of aerogels - particularly, their low refractive index and low absorption coefficient- allow them to be used as the cladding material. Post-synthesis modification of the prepared aerogel monoliths rendered the aerogel surface hydrophobic. Thus, aqueous solutions of methylene blue serving both as the waveguide core liquid and the reaction medium could be confined inside a channel embedded in the aerogel, without being adsorbed on the channel walls or compromising the monolithic structure of the aerogel. We directly visualized TIR-assisted light propagation along liquid-filled channels fabricated in aerogel blocks and verified that light could be efficiently guided even along paths with a non-linear geometry. Consequently, we have successfully shown light-driven photolysis of methylene blue by the light guided along the full length of the photoreactor channel.

REFERENCES

[1] L. Xiao and T. A. Birks, "Optofluidic microchannels in aerogel," *Optics Letters,* vol. 36, no. 16, pp. 3275-3277, 2011/08/15 2011.

[2] Y. Özbakır, A. Jonas, A. Kiraz, and C. Erkey, "Aerogels for Optofluidic Waveguides," *Micromachines,* vol. 8, no. 4, p. 98, 2017.

[3] B. Yalizay *et al.*, "Versatile liquid-core optofluidic waveguides fabricated in hydrophobic silica aerogels by femtosecond-laser ablation," *Optical Materials,* vol. 47, pp. 478-483, Sep 2015.

[4] Y. Özbakır, A. Jonáš, A. Kiraz, and C. Erkey, "Total internal reflection-based optofluidic waveguides fabricated in aerogels," *Journal of Sol-Gel Science and Technology,* journal article pp. 1-13, 2017.

[5] G. Eris *et al.*, "Three-dimensional optofluidic waveguides in hydrophobic silica aerogels via supercritical fluid processing," *The Journal of Supercritical Fluids,* vol. 73, pp. 28-33, 2013/01/01/ 2013.

[6] B. Yalizay *et al.*, "Optofluidic waveguides written in hydrophobic silica aerogels with a femtosecond laser," in *Integrated Optics: Devices, Materials, and Technologies Xix,* vol. 9365, J. E. Broquin and G. N. Conti, Eds. (Proceedings of SPIE, 2015.

CONTACT

* yozbakir@ku.edu.tr